UNIVERSITÀ DEGLI STUDI DI TORINO

DIPARTIMENTO DI SCIENZE DELLA TERRA

DOTTORATO DI RICERCA IN SCIENZE DELLA TERRA – XXXIII CICLO

Paleoenvironmental change during the first stage of the Messinian salinity crisis: Insights from lipid biomarkers in the Primary Lower Gypsum unit (Piedmont basin, NW Italy)

CANDIDATO: **DAVEY JOEY STOLWIJK**

SUPERVISORI: **PROF. FRANCESCO DELA PIERRE**

DOTT. MARCELLO NATALICCHIO

CO-SUPERVISORE**:** **PROF. JÖRN PECKMANN**

COMMISSIONE VALUTATRICE: **DOTT. GIOVANNI ALOISI** (IPGP PARIS)

DOTT. ROCCO GENNARI (UNIVERSITÀ DEGLI STUDI DI TORINO)

DOTT. DANIEL BIRGEL (UNIVERSITÄT HAMBURG)

COORDINATRICE DEL CORSO DI DOTTORATO: PROF.SSA ANNA MARIA FERRERO

ANNO ACCADEMICO: 2020-2021

SETTORE SCIENTIFICO-DISCIPLINARE DI AFFERENZA: GEO/02

ABSTRACT

During the Messinian salinity crisis (5.97-5.33 Ma), the Mediterranean transformed into a giant saline basin and more than 1 million km^3 of evaporites were deposited on the Mediterranean seafloor. The first stage of the crisis resulted in the cyclic deposition of up to 16 shale/gypsum couplets (Primary Lower Gypsum unit) in marginal Mediterranean basins, which have been correlated with the precessional cycle. While the lower five gypsiferous cycles are typified by beds of vertically oriented twinned selenite crystals (massive and banded selenite lithofacies), the 6th cycle (~5.87 Ma) indicates an abrupt change in gypsum lithofacies, marked by the appearance of branching selenite and laminar gypsum, probably reflecting a significant change in environmental conditions. This thesis uses a biogeochemical approach to reconstruct the paleoenvironmental conditions during the first phase of the Messinian salinity crisis, from the 6th Primary Lower Gypsum cycle and beyond. The lipid biomarker content of seven consecutive shale/gypsum couplets (Primary Lower Gypsum cycle 6-12) from the Pollenzo section has been thoroughly analyzed, providing taxonomical and paleoenvironmental information on the Piedmont basin (northwestern Italy), the northernmost offshoot of the Mediterranean basin during the crisis. Lipid biomarkers have been extracted from the main lithologies of the Pollenzo section, shedding light on the chemical conditions in the water column and climatic conditions in and around the Piedmont basin.

For the first time, biomarker data has been obtained from Messinian gypsum samples, providing insight on paleoenvironmental conditions during times of gypsum deposition (corresponding to precession maxima). Compound specific carbon stable isotope ($\delta^{13}C$) measurements of long-chain *n*-alkanes have confirmed that precession controlled the cyclical deposition of the Primary Lower Gypsum unit. This is indicated by significant $\delta^{13}C$-excursions (up to ~6‰) over the course of individual Primary Lower Gypsum cycles, which are the reflection of terrestrial climate changes (and associated vegetation shifts) around the Piedmont basin. Tetrahymanol distribution across the Pollenzo section suggests that the precession affected freshwater budget of the Piedmont basin controlled the intensity of stratification in the water column, reflected by a vertically oscillating chemocline. Furthermore, the co-occurrence of archaeol and extended archaeol, in combination with high GDGT-0/crenarchaeol ratios, suggests that paleoenvironmental conditions in the water column were generally harsh and possibly hypersaline. Normal marine conditions in the upper water column seem to have only episodically returned during precession minima, as evidenced by diagnostic biomarkers (crenarchaeol, dinosterol and C_{30} 1,15-diol) indicating substantial primary productivity pulses.

Wetenschap is niet zozeer vasthouden aan wat je altijd dacht, maar leren van het nieuwe.

- *Maurice de Hond*

Where all think alike, no one thinks very much

- *Walter Lippmann (1889-1974)*

INDEX

Chapter 1 – General introduction and synopsis

Earth's interconnected oceans form a massive body of water that covers more than two-thirds of the Earth's surface. Although a layman might suspect that the Earth's oceans form a rather homogenous body of water, scientists are well aware of the fact that the physical properties and dynamic processes of the ocean vary significantly from location to location. Sea water properties such as temperature, oxygen concentration, salinity, pH and nutrient availability are among the variable factors that highly influence ecosystems at any given location in the ocean. In fact, these environmental conditions are largely responsible for the presence and biodiversity of marine ecosystems and have determined which ecological niches are occupied by which organisms, for millions of years (e.g. Twitchett, 2006; Danise *et al.,* 2015).

Habitats that are characterized by harsh environmental conditions are referred to as "extreme environments". Such environments are, generally speaking, inhospitable for life, because they are typified by extreme circumstances, e.g. very high or low temperatures, very acidic or basic conditions, reducing conditions and/or environments with high concentrations of heavy metals, high salinities at saturation levels, high pressures, high levels of ionizing radiation, desiccation, among others (Rothschild and Mancinelli, 2001). For a long time, it was thought that life could not exist under such extreme conditions. However, in the late sixties it became clear that somehow, a thermophilic bacterium (*Thermus aquaticus*) was able to survive the high temperatures (>70°C) of thermal springs in Yellowstone National Park (Brock and Freeze, 1969). After that, more discoveries of microorganisms that are able to thrive under a variety of extreme conditions followed. Archaea, bacteria and fungi that are able to survive in environmental conditions that we consider "extreme", are commonly known as "extremophiles", ever since Macelroy (1974) introduced this term. More specifically, extremophiles can be distinguished in groups such as thermophiles and psychrophiles, acidophiles and alkaliphiles, halophiles, barophiles and xerophiles. These groups relate to their uncommon adaptations, such since many extremophiles seem to have specialized in surviving at one specific extremity. However, some extremophiles are extreme in more than one dimension, e.g. archaea from the genus *Sulfolobus*, which are able to survive at around 85°C and a pH of ~2.0 (Plumb *et al.,* 2002). Also, certain (hyper)thermophilic methanogens are able to survive the extreme

environmental challenges that they are facing. These archaeal specialists have adapted in such a way that they are able to thrive at high temperatures in strongly reducing conditions near hydrothermal vents (e.g. Baumann *et al.,* 2018).

Although extremophiles are very good indicators for specific environmental conditions, body fossils of archaea and bacteria are rarely encountered in the geological record. Luckily, these microorganisms, and so do eukaryotic organisms (i.e. fungi, plants and animals), leave behind molecular fossils, specific molecules in the sedimentary archive that are to a large extent derived from cellular membranes (Schouten *et al.,* 2013; Briggs and Summons, 2014; Falk and Wolkenstein, 2017; Luo *et al.,* 2019). In **Chapter 2**, the use of molecular fossils or "lipid biomarkers" within the scope of biogeochemical research is discussed, in particular with respect to the reconstruction of paleoenvironments. Thus, lipid biomarker analysis can be a very helpful tool for the reconstruction of ancient (extreme) environments.

An evaporitic basin is an excellent example of an extreme environment. When evaporation exceeds the total input of freshwater (precipitation + river discharge), a marine basin can eventually transform into an evaporitic basin, an environment where evaporitic minerals precipitate. At such places, sea water salinities are able to reach very high levels, sometimes high enough for evaporite formation on a large scale. Such extremely saline settings leave little or no room for life to flourish, leading to an absence of body fossils in the sedimentary archive. This impedes taxonomical research, leaving lipid biomarker analysis as the most suitable option for direct reconstruction of paleoenvironmental conditions in ancient evaporitic basins. Today, the evaporitic basins on Earth are restricted to small scale coastal settings, where evaporites form in so-called "sabkhas" (supratidal saltflats) and evaporitic lagoons. There are no present-day examples of evaporitic basins where evaporites are being deposited on a massive scale, i.e. covering thousands of km^2 and with evaporite volumes in the order of thousands of km^3. However, Earth's stratigraphic record has demonstrated that in the past, enormous volumes of evaporites have formed in much larger marine settings than today (**Fig. 1**) (e.g. Evans, 2006; Haq *et al.,* 2020).

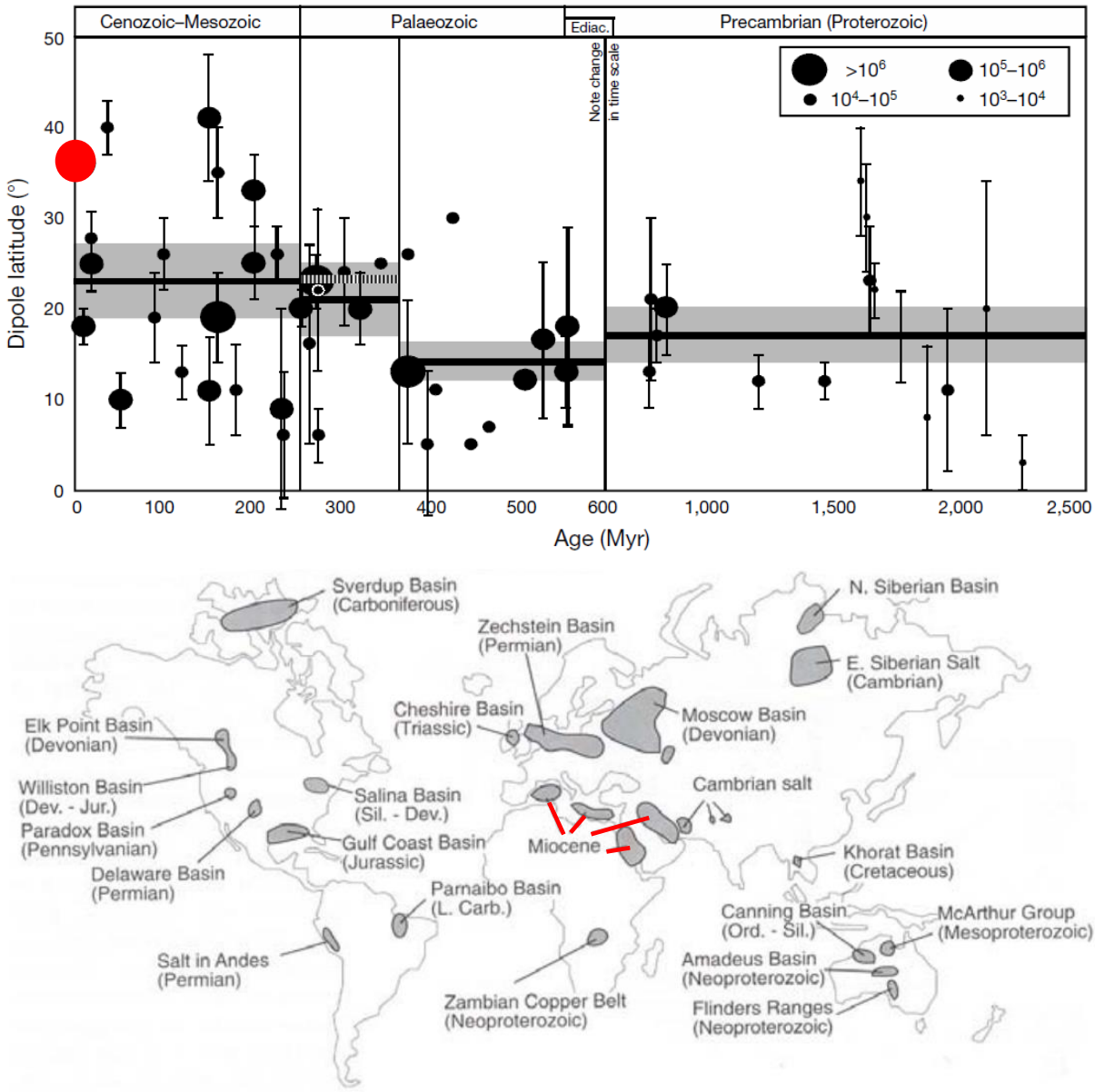

(Fig. 1): **TOP**: Overview of evaporitic basins or "salt giants" plotted against paleolatitudes trough time. Circle sizes indicate the volumes of individual evaporitic basins and are in km^3. The red circle indicates the evaporitic volume deposited in the Mediterranean basin during the Messinian salinity crisis. Figure modified from Evans (2006). Consult Evans (2006) for more detailed information regarding uncertainty limits of paleolatitudes, volume-weighted means and error envelopes (shaded bars). **BOTTOM**: Geographical map displaying the locations of some major evaporitic deposits. Red lines indicate Miocene deposits that have been deposited during the Messinian salinity crisis. Modified from Kendall (1992).

Currently, a popular expression which refers to the deposits of such large ancient evaporitic basins, is the term "salt giant". These salt giants represent hundreds of meters thick basin-filling deposits of evaporitic minerals that have precipitated from immense volumes of seawater. The largest and most recent salt giant on Earth has been deposited in the

Mediterranean basin, where a ~1.5 km-thick layer of evaporites lies buried below the present-day Mediterranean abyssal plain (Hsü *et al.,* 1973a,b; Camerlenghi and Aolisi, 2020). This thick layer of salts formed during a period when suitable chemical conditions for evaporite deposition existed in the Mediterranean, which is commonly referred to as the Messinian salinity crisis, a concept that has been introduced by Selli (1960). The Messinian salinity crisis is considered an extraordinary geological event that started about 6 million years ago, affecting the Mediterranean basin for more than 600 ka (Hsü *et al.,* 1973a; Manzi *et al.,* 2013; Roveri *et al.,* 2014). The concept and chronology of the Messinian salinity crisis, as well as the causes for this paleoceanographic event and the consequences for life in the Mediterranean, are discussed in **Chapter 3**.

When a body of water is evaporating and the ion concentration progressively increases, a certain succession of evaporitic minerals will form during the evaporation process. This was first described halfway the 19th century by the Italian chemist Usiglio, who evaporated a body of Mediterranean seawater and recorded in which order minerals precipitated from the evaporating seawater (Usiglio, 1849a,b). This sequence is now known as the "Usiglio sequence", and is directly related to the solubility of the evaporitic minerals (**Fig. 2**).

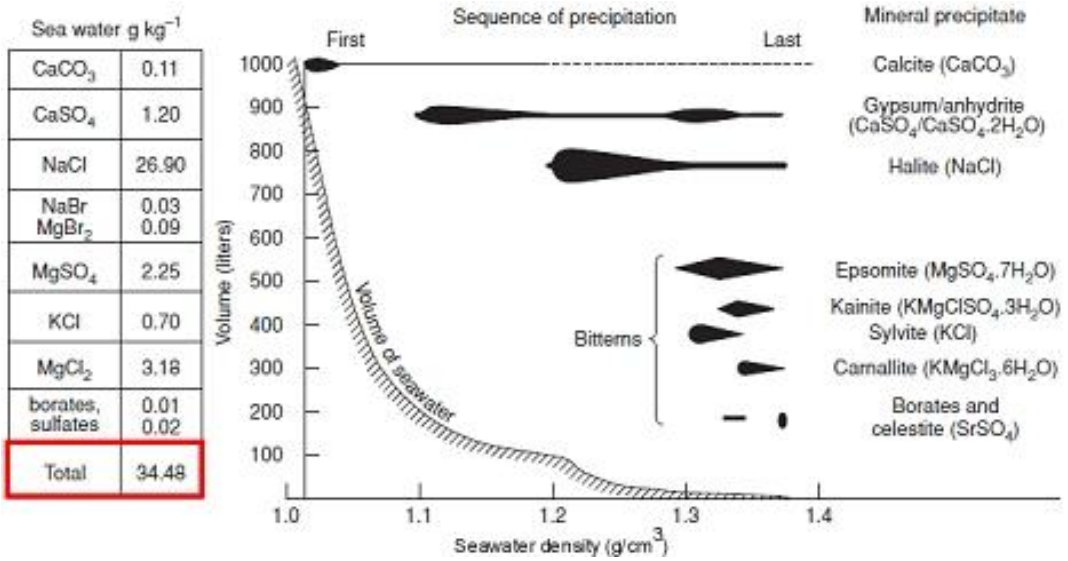

(Fig. 2): The paragenetic sequence of evaporitic mineral precipitation from typical seawater. **Left**: Table that shows the chemical species that are dissolved in typical seawater. **Right**: The order of salts that precipitate from seawater when a body of typical seawater is evaporated. Note the curve that indicates the amount of seawater that needs to evaporate in order to consecutively precipitate each mineral. The K-Mg salts are formed from bitterns, hypersaline solutions that represent less than 5% of the original seawater. Modified from Guilbert and Park (1986).

The order of precipitation in the Usiglio sequence reflects a rise in solubility of the evaporitic minerals. In practice, this means that the least soluble salt precipitates first, which is calcium carbonate, followed by gypsum, halite and ultimately the K-Mg salts. Especially the early stages of evaporation that lead to gypsum and halite precipitation are well known, as is demonstrated by repetition of the Usiglio experiments (e.g. McCaffrey *et al.,* 1987) and empirical observations in marine solar saltworks (e.g. Orti *et al.,* 1984). During the later stages of evaporation, when K-Mg minerals precipitate from highly concentrated brines, some differences may occur that are mainly related to variations in physical parameters (Garrett, 1970; Braitsch, 1971). This demonstrates that the prediction of evaporite precipitation from a brine is not always a straightforward process. In fact, evaporite deposition is dependent on many factors, such as biology, temperature, pressure, the mixture of ion species, the replenishment of ions, the depositional environment, as well as seasonal and long-term climatic changes. Therefore, it is not surprising that scientists have strenuously debated the paleoenvironmental conditions in the Mediterranean during the Messinian salinity crisis, especially because evaporite deposition occurred on such a massive scale (Haq *et al.,* 2020).

The Mediterranean is a semi-enclosed marginal sea that communicates with the global ocean through the Strait of Gibraltar. The present-day salinity of the Mediterranean is higher than the average salinity in the global ocean, because high evaporation rates in the Mediterranean area are not compensated by the input of freshwater from rivers that drain the surrounding region (Mariotti *et al.,* 2002). This means that the connection with the open ocean (Gibraltar strait) and the continuous inflow of Atlantic seawater prevents the desiccation of the Mediterranean. This inflow of Atlantic seawater causes a west-east salinity gradient and downwelling of saltier and denser seawater in the Eastern Mediterranean (Lascaratos *et al.,* 1999). Although the major-ion composition in seawater has changed over time, the most abundant ions in modern seawater are Na^+ and Cl^- ions, while SO_4^{2-}, $Mg^{2+,}$ Ca^{2+}, K^+ and HCO_3^- ions are present in smaller quantities (**Fig. 3**).

Major Ion	Eocene-Oligocene seawater (36-34 Ma)	Serravallian-Tortonian seawater (13.5-11.8 Ma)	Messinian seawater (6-5 Ma)	Present-day seawater[a]
Na^+	488	488	486	485
K^+	11	11	11	11
Ca^{2+}	16 (11-20)	13 (8-16)	12 (7-15)	11
Mg^{2+}	36	44	48	55
Cl^-	565	565	565	565
SO_4^{2-}	19 (14-23)	24 (19-27)	26 (21-29)	29
Mg^{2+}/Ca^{2+}	2.3	3.4	4.0	5

(Fig. 3): The major-ion composition of Cenozoic seawater. All values are given in millimolal (millimoles per kg of H_2O). [a]Present day seawater composition from Holland (1984). Modified from Brennan *et al.* (2013).

As the concentration of ions in a body of water increases and moves towards the point of saturation with respect to a certain mineral, supersaturation ultimately occurs and the respective mineral may precipitate. The resulting minerals are called primary evaporites and their precipitation changes the composition of the remaining brine. Often, the inflow/outflow of water in an evaporitic basin is the main factor that determines which salt precipitates, as this factor controls the maximum salinity and may limit the precipitation of certain minerals, particularly those that precipitate during the later stages of evaporation (i.e. the K-Mg salts). Moreover, this factor controls the replenishment of minerals in the basin, which is required for the deposition of thick layers of evaporites, such as the thick gypsum and halite layers that were deposited during the Messinian salinity crisis (Topper and Meijer, 2013). It is important to realize that this factor is crucial for the establishment of a system where evaporation and mineral replenishment continuously take place, balancing the environment in such a way that it can operate for thousands of years, while a thick layer of evaporites is being deposited. If such a system would not be in place, the evaporation of a kilometer of typical seawater would lead to less than 20 m of evaporitic deposits, while during the Messinian salinity crisis, hundreds of meters of evaporites have been deposited (Lugli *et al.*, 2010).

Gypsum (calcium sulfate dihydrate; $CaSO_4{*}2H_2O$) is one of the evaporative minerals that precipitated on a massive scale during the Messinian salinity crisis. It is one of the most

valuable nonmetallic resources on Earth and therefore actively mined for numerous construction purposes. If the temperature is below ~42°C, calcium sulfate precipitates as gypsum under natural sedimentary conditions (Hardie, 1967). After burial, gypsum is dehydrated into anhydrite ($CaSO_4$) if the temperature exceeds ~42°C, after which it can be hydrated back to gypsum during uplift and exposure to water. Gypsum may precipitate from brines that have an ion concentration of ~3.8 times that of seawater, while halite starts to precipitate when the brine reaches a concentration factor of ~10.6 (McCaffrey *et al.,* 1987). In terms of salinity, this means that gypsum precipitation mainly occurs between ~140-200 ‰ and 290-320 ‰, although minor amounts of gypsum are also formed beyond that salinity range, since the field of gypsum precipitation overlaps with the lower end of the halite crystallization field (Logan, 1987; Babel and Schreiber, 2014). Especially during the first phase of the Messinian salinity crisis, an enormous amount of primary gypsum was deposited in the Mediterranean basin (Lugli *et al.,* 2010). These gypsum deposits are present across the entire Mediterranean area and outcrop at numerous places (Krijgsman *et al.,* 2001; Rouchy and Caruso, 2006; Lugli *et al.,* 2010). **Chapter 4** describes and discusses the so-called "Primary Lower Gypsum unit", the stratigraphic unit to which these primary gypsum deposits belong. Among the discussed topics are the sedimentary cyclicity and different lithologies, including the different evaporative facies that are present. Furthermore, different scenarios for the formation of gypsum are discussed, as well as the main factors that controlled the deposition of this stratigraphic unit. The chapter concludes with an overview of climate modeling and lipid biomarker studies related to the Primary Lower Gypsum unit, which together summarize the current state of the art concerning the paleoenvironmental conditions during deposition of this stratigraphic unit.

Due to the extreme transition and the relative recent occurrence of the Messinian salinity crisis, the change of the Mediterranean basin from a marginal sea into an evaporitic basin (Roveri et al., 2014) has been of great interest to scientists ever since its discovery. Nevertheless, many issues are still unknown, especially because modern analogues for the crisis are absent. Key issues still under debate are the depth of deposition of the evaporites, the chemical composition of the Mediterranean water column and the redox conditions at the bottom of the water body (e.g. Dela Pierre et al., 2014). The consequences of the prevailing chemophysical parameters and the biological impact of the event have already

been the main focus of a large number of studies on the Messinian salinity crisis. This extraordinary event led to extreme conditions for life in the Mediterranean and terminated the ecological niche of many organisms or pushed them to the brink of extinction. However, some microorganisms flourished despite the harsh conditions (e.g. Dela Pierre et al., 2012; 2014 & 2015) and it is of critical importance to unravel the exact impact of changing chemophysical parameters (e.g. hypersalinity, anoxia and/or eutrophication) in the marine environment, causing the nearly inhospitable conditions of the Mediterranean seawater during the MSC. Although most studies have focused on a restriction between the Mediterranean and the Atlantic Ocean as the main cause for the Messinian salinity crisis and the deposition of evaporites (e.g. Duggen *et al.,* 2003; Flecker *et al.,* 2015), it has recently been suggested that perhaps a more complex situation might have influenced the Mediterranean basin throughout the crisis (Grothe *et al.,* 2020). In fact, a strong influence of freshwater appears to have been present during the crisis, as is strongly implied by the salinities of fluid inclusions from gypsum crystals (Natalicchio *et al.,* 2014; Evans *et al.,* 2015). Such studies are in great contrast with the classical view that Messinian gypsum was deposited under strictly hypersaline conditions and this apparent paradox needs to be thoroughly addressed.

This thesis uses a biogeochemical approach to tackle the main controversies that concern the paleoenvironmental conditions during the first phase of the Messinian salinity crisis. Biogeochemical tools are used to address key scientific questions related to the environmental conditions that were present in the Piedmont basin (northwestern Italy), the northernmost offshoot of the Mediterranean basin during the crisis. The Pollenzo section, which comprises the whole Messinian sedimentary succession, has been selected as the ideal section in the Piedmont basin to address these paleoenvironmental questions. The geological setting of the Piedmont basin, as well as the stratigraphy of the Pollenzo section are discussed in **Chapter 5**. By investigating the lipid biomarker content of sediments deposited during the first phase of the Messinian salinity crisis, this thesis aims to shed light on both the paleoceanographic and paleoclimatic conditions during deposition of the Primary Lower Gypsum unit. Lipid biomarker analysis has been performed on the hydrocarbon and alcohol fractions (**Chapter 6**) that has been extracted from the main lithologies of the Pollenzo section. All gathered data concerning the lipid biomarker analysis

of the Pollenzo sediments is presented in **Chapter 7**. The interpretation of this data, as well as their significance and implications for the Messinian salinity crisis, are discussed in **Chapter 8**.

The lipid biomarkers obtained from the Pollenzo sediments not only provide taxonomical information regarding the organisms that lived during the first phase of the crisis, but also reveal new information related to the chemical conditions in the water column and the climatic conditions in and around the Piedmont basin. More specifically, compound specific carbon stable isotope ($\delta^{13}C$) measurements of long-chain *n*-alkanes have been used in order to reconstruct changes in the source of terrestrial organic matter, which in turn can be directly related to changes in terrestrial climate (i.e. precipitation changes). In fact, this $\delta^{13}C$-analysis reveals distinct climatic fluctuations on both the short- and longer-term during the first phase of the Messinian salinity crisis. For the first time, biomarker data has been obtained from ancient gypsum samples, providing valuable information on the paleoenvironmental conditions in the Mediterranean water column during times of gypsum deposition. In general, the data presented in this thesis provides a reconstruction of the paleoenvironmental conditions during the first stage of the Messinian salinity crisis, as well as a better understanding of the cyclicity in the Primary Lower Gypsum unit. Furthermore, this lipid-centric thesis fills gaps in our understanding of the chemical conditions of the Mediterranean water column, in which stratification and episodical freshening of surface waters might have played a crucial role.

Chapter 2 – The use of lipid biomarkers in paleoenvironmental reconstruction

Lipid biomarkers, also called molecular or chemical fossils, biological markers or simply "biomarkers", are organic compounds that can be preserved in ancient deposits and contain valuable information related to their biological precursors (Falk and Wolkenstein, 2017 and references therein). Biomarkers that are found in sediments originate mostly from biogenic lipids. Lipids (both structurally intact and rearranged forms) are often used in biogeochemical research because they are more resistant to (bio)degradation (Tegelaar et al., 1989; Eglinton and Logan, 1991; Wakeham and Canuel, 2006; Schwarzbauer and Jovančićević, 2016) and are more stable (LaRowe and Van Cappellen, 2011) than other biological molecules like DNA and proteins, which in turn have the potential to provide more phylogenetic/taxonomic information (Briggs and Summons, 2014) (**Fig. 4**).

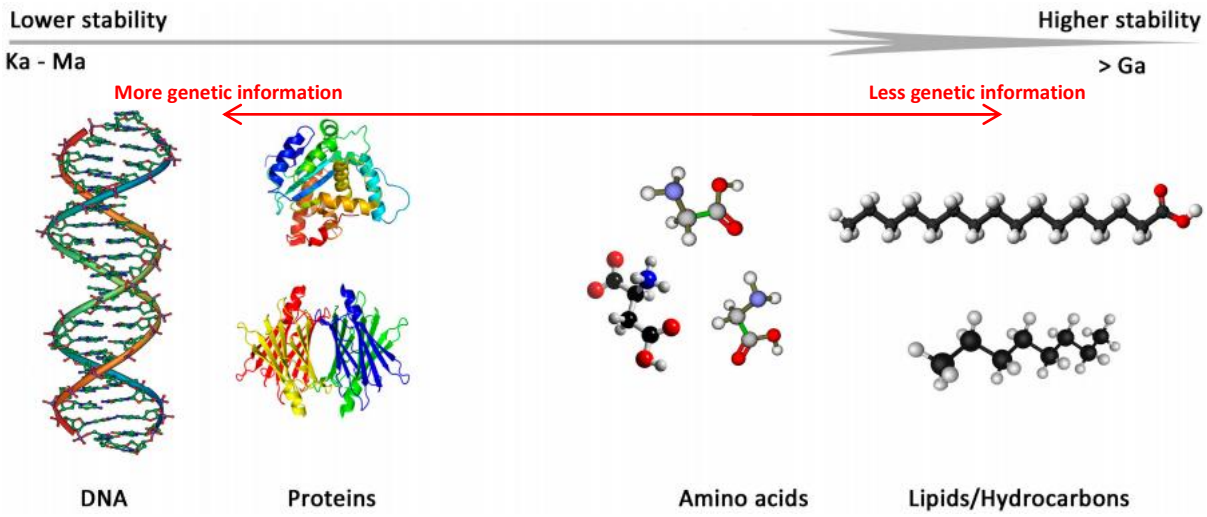

(Fig. 4): Several biological molecules and their inverse relationship between preservation potential and the amount of information they carry in their structure. Ka: thousand years. Ma: million years. Ga: billion years. Modified from Aerts et al. (2014).

Lipid biomarkers are a group of molecules that include e.g. fats, oils and waxes, which have important roles in the cells of all Earth's organisms, especially as the building blocks of cellular membranes. Research has shown that each of the three domains of life (Eukarya, Bacteria and Archaea) biosynthesizes characteristic lipid biomarkers (Briggs and Summons, 2014; Luo et al., 2019 and references therein). Some lipid biomarkers even have the potential to indicate the (former) presence of a specific group of organisms (e.g. Brocks, 2011), distinct environmental conditions and/or a type of metabolism (e.g. Sinninghe

Damsté and Schouten, 2006). With a laboratory technique called "chromatography", lipid biomarkers extracted from geological samples can be systematically separated according to the molecules' specific properties (size, weight, volatility, polarity etc.). A gas or liquid chromatograph (known as a "GC" or "LC", respectively) can automatically separate complex mixtures of lipid biomarkers. Chromatography is often coupled with mass spectrometry (e.g. Myher and Kuksis, 1995; Niessen, 1998; 2006) in order to identify and quantify lipid biomarkers, enabling large potential for biogeochemical research.

2.1) Paleoenvironmental applications of lipid biomarkers

Lipid biomarkers can be considered as informants or witnesses of the past, carrying information regarding Earth's history through time and space. Some of them are able to resist degradation for millions or even billions of years (Brocks and Summons, 2005). Lipid biomarkers can be used as indicators for the source organisms that biosynthesized them and/or link them to specific paleoenvironmental conditions in which these organisms lived. Although pioneering biomarker research was related to studies on oil samples (Philp and Lewis, 1987 and references therein), numerous applications of biomarkers in paleoenvironmental research have been developed over the years, including organic geochemical climate proxies (Eglinton and Eglinton, 2008; Sachs *et al.,* 2013; Luo *et al.,* 2019). The (relative) abundance and compound-specific isotopic composition of lipid biomarkers can be used to reconstruct various aspects of paleoenvironments, including but not limited to temperature (sea surface temperature; Prahl and Wakeham, 1987; Schouten *et al.,* 2002; Rampen *et al.,* 2012 and mean annual air temperature; Weijers *et al.,* 2007; Peterse et al., 2012; Vasiliev *et al.,* 2019), precipitation (Schefuß *et al.,* 2005; Tierney *et al.,* 2008; Sachse *et al.,* 2012 and references therin), (hyper)salinity (Rosell-Melé, 1998; Van der Meer *et al.,* 2007; Turich and Freeman, 2011; Dawson *et al.,* 2012), stratification and/or redox conditions (Sinninghe Damsté *et al.,* 1995a; Hughes *et al.,* 1995; Sinninghe Damsté and Schouten, 2006), terrestrial input (Eglinton and Hamilton, 1967; Hopmans et al., 2004), vegetation changes (Eglinton and Hamilton, 1963; Schefuß *et al.,* 2003; Rommerskirchen *et al.,* 2003; 2006a), elemental cycling (Hayes *et al.,* 1987; Pancost *et al.,* 2013; Isaji *et al.,* 2019) and other (ancient) biogeochemical processes (Hayes *et al.,* 1990). The lipid groups that are important for the reconstruction of paleoenvironmental aspects in this thesis are

discussed in the paragraphs below.

2.2) Long-chain *n*-alkanes

Because of their ubiquity in natural and geological samples and their straightforward identification, long-chain (usually C_{23} to C_{35}) *n*-alkanes are one of the most frequently reported terrestrial plant biomarkers in biogeochemical research (Eglinton *et al.,* 1962; Philp and Lewis, 1987; Gaines *et al.,* 2009; Bush and McInerney, 2013; Freeman and Pancost, 2014; Naafs *et al.,* 2019). Long-chain *n*-alkanes are major components of epicuticular leaf waxes of vascular plants, aiding in the protection of the plant against their external environment, while their apolar chemical structure helps to protect the leaves from water loss by evaporation (Bush and McInerney, 2013) (**Fig.5**).

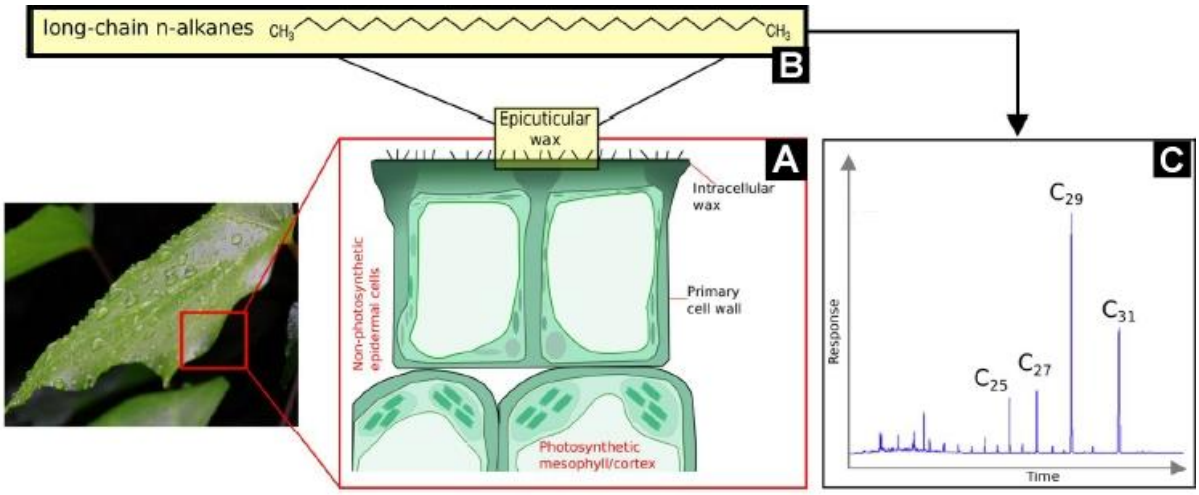

(Fig. 5): Schematic overview of the origin and chemistry of leaf wax derived n-alkanes: **A:** Epidermal cells of a plant indicating epicuticular wax alongside the external cell wall which contains long-chain *n*-alkanes. **B:** The chemical structure of a (C_{29}) *n*-alkane, often the most ubiquitous *n*-alkane in sedimentary samples that are rich in leaf wax derived *n*-alkanes of terrestrial higher plants. **C:** Chromatogram showing a typical distribution of *n*-alkanes in the sedimentary archive. The area of the peaks produced by the *n*-alkanes can be used for quantification. Modified from Eley and Hren (2018).

Besides their hydrophobic property, *n*-alkanes lack functional groups and reactive double bonds. Thus, the simplicity in their chemical structure not only makes them adequate leaf protectors, but also causes them to be relatively resistant against biodegradation, resulting in great preservation potential (Gaines *et al.,* 2009). During and especially at the end of the

plants' life cycle, the *n*-alkanes can be eroded from the plant material by water and wind, potentially transported for hundreds of kilometres to ultimately end up in the sedimentary archive (e.g. Conte and Weber, 2002; Wang *et al.,* 2009). This can complicate the interpretation of *n*-alkane data, because both erosion pathways need to be considered in terms of their relative contribution to the depositional site (Eglinton and Eglinton, 2008).

The study of long-chain *n*-alkanes in geological samples can provide valuable paleoenvironmental information, since the *n*-alkane signature (both the distribution and their isotopic composition) in geological samples is directly related to climate. Factors such as temperature, precipitation and wind strength, influence vegetation growth (and thus *n*-alkane biosynthesis) and/or the dominant type of erosion (and thus transport pathway) of the *n*-alkanes (Eglinton and Eglinton, 2008). When long-chain *n*-alkanes are utilized in paleoenvironmental studies, their distribution is typically described by reporting a specific carbon-number range (i.e. length of the carbon chains that occur), as well as the most abundant homologues that occur in the analysed samples, often complemented with compound specific stable isotope measurements ($\delta^{13}C$ and/or $\delta^{2}H$; e.g. Vogts *et al.,* 2009; Tipple and Pagani, 2010; Natalicchio *et al.,* 2019; Sabino *et al.,* 2020). In addition, biomarker proxies based on *n*-alkane distribution can be applied, like the commonly used Carbon Preference Index (CPI; Bray and Evans, 1961) and the Average Chain Length parameter (ACL; Poynter and Eglinton, 1990).

2.2.1) The Carbon Preference Index (CPI)

The CPI is based on the observation that higher plants predominantly biosynthesize odd numbered *n*-alkanes in comparison to even numbered carbon chains (Eglinton and Hamiltion, 1967). This proxy is frequently used to assess the quality (i.e. freshness) of terrestrial organic matter, by assessing the degree of *n*-alkane degradation in sediments (e.g. Bray and Evans, 1961; Schefuß *et al.,* 2003; Rommerskirchen *et al.,* 2006a,b; Natalicchio *et al.,* 2019). The CPI formula (Bray and Evans, 1961):

$$CPI = 0.5\left(\frac{C25+C27+C29+C31+C33}{C24+C26+C28+C30+C32} + \frac{C25+C27+C29+C31+C33}{C26+C28+C30+C32+C34}\right),$$

calculates the degree to which odd numbered *n*-alkanes dominate over even numbered *n*-alkanes, with values >4 indicating significant input of terrestrial higher plant material in sediments, while values near unity indicate petrogenic hydrocarbon contamination or the presence of recycled/degraded organic matter (Kennicutt *et al.,* 1987; Collister *et al.,* 1994; Jeng *et al.,* 2006). Thermal maturity of geological samples decreases CPI values, because during catagenesis (hydrocarbon formation), longer *n*-alkanes are cleaved into shorter ones and new *n*-alkanes are released from kerogen. This results in *n*-alkanes with shorter carbon chains and a loss of the predominance of odd-numbered *n*-alkanes (Tegelaar *et al.,* 1989; Peters and Moldowan, 1993).

2.2.2) The Average Chain Length (ACL) parameter

The ACL parameter (modified from Poynter and Eglinton, 1990):

$$ACL = \frac{(25\ X\ C25)+(27\ X\ C27)+(29\ X\ C29)+(31\ X\ C31)+(33\ X\ C33)}{C25+C27+C29+C31+C33},$$

is used to calculate the average chain length of odd numbered *n*-alkanes (C_{25} to C_{33}), basically providing a value for the molecular distribution of *n*-alkanes in a geological sample, which is broadly related to latitude (Poynter and Eglinton, 1990). The type of vegetation is the main influence on the average chain length of odd *n*-alkanes, with C3 plants producing shorter odd *n*-alkanes on average, while odd *n*-alkanes from grasslands (i.e. C4 plants) have longer chain lengths (Cranwell, 1973; Jeng *et al.,* 2006). It has been suggested that climate (which is strictly related to vegetation type) controls the distribution of odd numbered *n*-alkanes, with longer chain lengths reported from sources with warmer climates (Poynter *et al.,* 1989). Distributional variation of odd chain *n*-alkanes is also suggested to be related to aridity (Huang *et al.,* 2000; Schefuß *et al.,* 2003). Thus, the ACL is able to track changes in *n*-alkane distribution over time and has been applied as a proxy for both paleoclimate and paleovegetation (Diefendorf & Freimuth, 2017). However, the application of the ACL is complex, since both climate and biology seem to affect ACL values, while the exact way in which this happens remains unclear (Hoffmann *et al.,* 2013; Freeman and Pancost, 2014). Nevertheless, it seems most likely that the ACL is driven by changes in growing season temperature and/or aridity, rather than a change in the source of *n*-alkanes (McInerney and Wing, 2011; Bush and McInerney, 2015). A recent study has shown that the ACL may also

have paleoenvironmental potential in reconstructing the moisture state of the past atmosphere, because plants regulate their *n*-alkane production in response to osmotic stress (Eley and Hren, 2018).

2.2.3) Compound-specific carbon and hydrogen isotopes

Long-chain *n*-alkanes are frequently used plant wax biomarkers in paleoenvironmental reconstructions, but the interpretation of their distribution is complicated by factors related to paleoclimate, paleovegetation, transport and diagenesis (Diefendorf and Freimuth, 2017). Carbon ($\delta^{13}C$) and hydrogen ($\delta^{2}H$) stable isotope measurements of individual *n*-alkanes are able to provide fundamental information to improve the interpretation related to changes in paleoclimate, paleovegetation and paleohydrology (Sachse *et al.,* 2012; Vasiliev *et al.,* 2013; Sessions, 2016; Diefendorf and Freimuth, 2017). Isotopic measurements of specific *n*-alkanes concerning carbon and hydrogen are considered to be reliable, because the covalent bonds within the molecule (C-C and C-H) are highly stable, unless very high temperatures are experienced or specific enzymes are present (Eglinton and Eglinton, 2008). Compound-specific carbon isotope measurements have been successfully used as a proxy for C3 vs. C4 vegetation (e.g. Schefuß *et al.,* 2003; Castañeda *et al.,* 2009*).* Because C3 plants (-36‰ < $\delta^{13}C_{alk}$ < -30‰) are adapted to more humid conditions than C4 plants ($\delta^{13}C_{alk}$ > -26‰), both plant types produce long-chain *n*-alkanes with distinctly different $\delta^{13}C$-values, regulated by their distinctly different carbon fixation pathways (Schefuß *et al.,* 2003; Rommerskirchen *et al.,* 2006a; Naafs et al., 2012). When plants fix carbon during photosynthesis, the size of fractionation against the heavier carbon isotope (i.e. ^{13}C) depends on the metabolic pathway used by the plant, with C3 plants (Calvin-Benson cycle) having larger net fractionation than C4 plants (Hatch-Slack cycle) (Diefendorf and Freimuth, 2017*).* Thus, the $\delta^{13}C$ values of *n*-alkanes have the potential to reveal changes in paleohumidity and indicate paleoclimatic change *(e.g.* Pagani *et al.,* 1999*;* Huang *et al.,* 2000*).*

There are many other factors that need to be considered when it comes to interpreting the $\delta^{13}C$ of n-alkanes, from the atmospheric CO_2 level at the time of carbon fixation (Tipple *et al.,* 2010), until preservation in the sedimentary record. Such factors include photosynthetic

pathway-dependent fractionation (Calvin-Benson cycle vs. Hatch-Slack cycle; Castañeda *et al.,* 2009*;* Diefendorf and Freimuth, 2017 and references therein), plant-species-dependent fractionation during leaf wax biosynthesis (e.g. Diefendorf *et al.,* 2015a,b), the source of the *n*-alkanes (i.e. species mixture; Collins *et al.,* 2011; Vogts *et al.,* 2012 and *n*-alkane transport pathways; Schefuß *et al.,* 2003; Pancost and Boot, 2004) as well as contamination with older reworked *n*-alkanes (Schefuß *et al.,* 2016). Diagenesis does not seem to significantly affect the $\delta^{13}C$ of *n*-alkanes, at least in sediments with low to moderate thermal maturity (<250 °C; Diefendorf *et al.,* 2015c).

2.3) Glycerol Dialkyl Glycerol Tetraethers

Archaea, which represent one of the three domains of life, are single-celled microorganisms that biosynthesize characteristic membrane lipids. Being relatively resistant to degradation and commonly preserved in the sedimentary archive, archaeal membrane lipids provide excellent biomarker potential, contributing to our knowledge regarding Earth's history and its geological processes (Schouten *et al.,* 2013). Archaeal membrane lipids are composed of isoprenoid moieties linked to glycerol and have a unique stereochemistry (Koga *et al.,* 1993; Valentine, 2007), making them distinctly different from bacterial membrane lipids (**Fig. 6**).

A wide range of archaea (and a specific group of bacteria) biosynthesize membrane lipids that are called glycerol dialkyl glycerol tetraethers (GDGTs) and some of them are commonly used as biomarkers to indicate the presence and abundance of certain groups of archaea (and bacteria) that produce them (Schouten *et al.,* 2013 and references therein). GDGTs were originally thought to be exclusively produced by archaea adapted to extreme environments (De Rosa and Gambacorta, 1988), but we now know that they are also biosynthesized by archaea that live in moderate aquatic settings, after their identification in ocean (DeLong *et al.,* 1998; Vetriani *et al.,* 1998) and lake sediments (MacGregor *et al.,* 1997), as well as in terrestrial settings (Hershberger *et al.,* 1996). These discoveries triggered a wave of GDGT-related research, which led to important findings, such as the identification of branched GDGTs (brGDGTs; Sinninghe Damsté *et al.,* 2000), which are suggested to be produced mostly by *Acidobacteria* (Weijers *et al.,* 2009; Sinninghe Damsté *et al.,* 2011a), as well as crenarchaeol (Sinninghe Damsté *et al.,* 2002a), an isoprenoid GDGT (isoGDGT) that is

mainly biosynthesized by archaea of the phylum *Thaumarchaeota* (Brochier-Armanet *et al.,* 2008; Spang *et al.,* 2010) and is usually indicative for open marine conditions (Walker *et al.,* 2010).

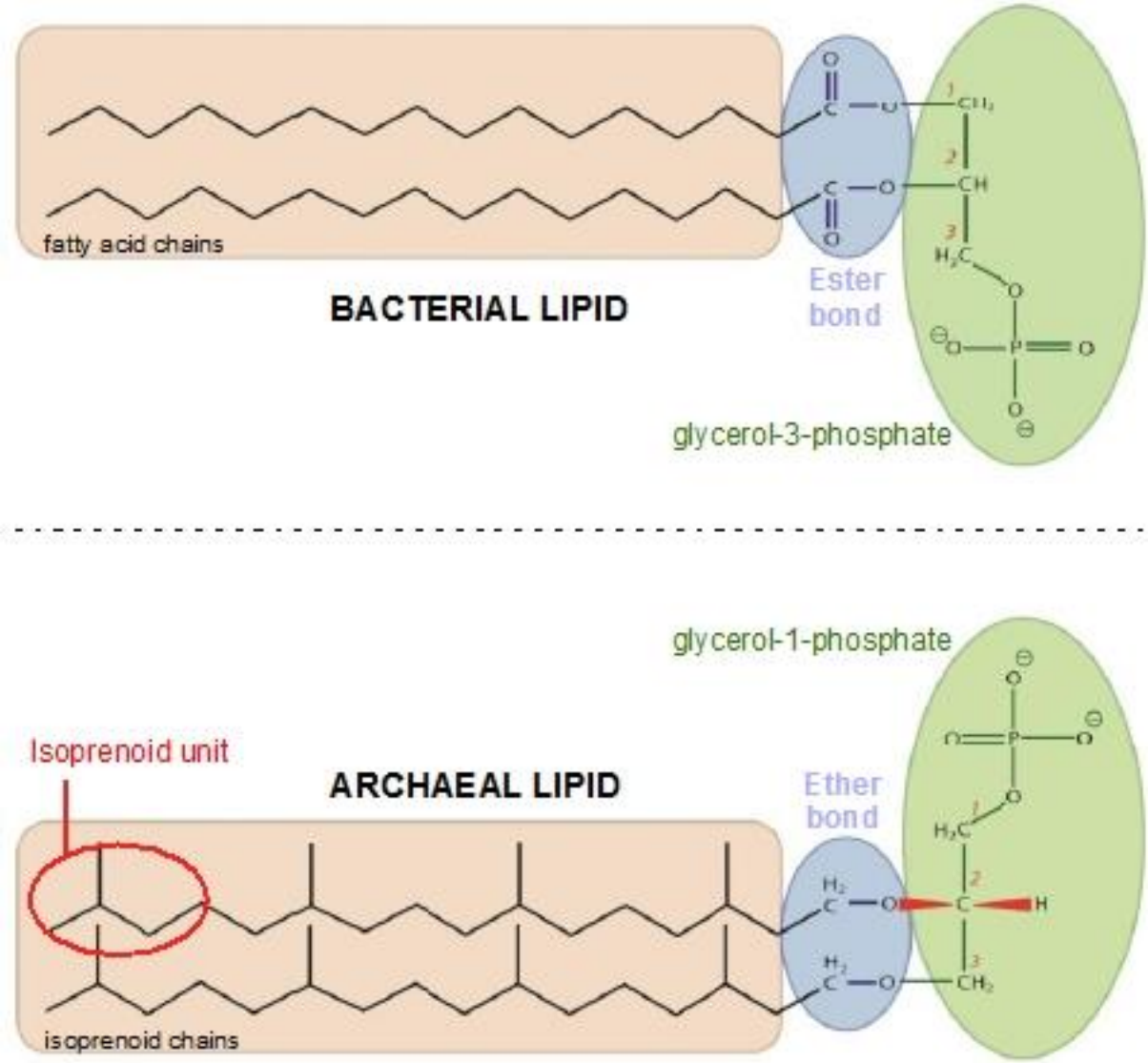

(Fig. 6): Structures of archaeal and bacterial membrane lipids and their main chemical differences. Bacterial membrane lipids consist of isoprenoid units bound to glycerol with ester linkages, while archaeal membrane lipids consist of fatty acids bound to glycerol with ether linkages. Note the stereospecific numbering of the glycerophosphate backbones, indicating a different stereochemical configuration of archaeal and bacterial membranes. Modified from Caforio and Driessen (2017).

2.3.1) Structures and sources of GDGTs

Both isoGDGTs and brGDGTs consist of two carbon chains that are bound with an ether linkage to glycerol on either side, forming a ring-like structure, but their structural differences are related to their core carbon skeletons (**Fig. 7**). The carbon skeleton of isoGDGTs is made up of isoprenoid units (5 carbon atoms arranged in a specific pattern), while the brGDGTs are composed of branched alkyl core units. The individual differences between isoGDGTs are to a great extant related to the amount of cyclopentane rings that are incorporated in the ring structure. It has been suggested by Schouten *et al.* (2013) to use the number of cyclopentane moieties in the nomenclature of the most common isoGDGTs (i.e. GDGT-x where 'x' indicates the number of cyclopentane rings). It should be noted that crenarchaeol is a very characteristic isoGDGT because there is also a cyclohexane ring incorporated in its structure (Sinninghe Damsté *et al.,* 2002a). BrGDGTs differ among one another in the number of branches (i.e. methyl groups) that they have attached to their alkyl core units (Sinninghe Damsté *et al.,* 2000), although they can also contain cyclopentane rings in their structure.

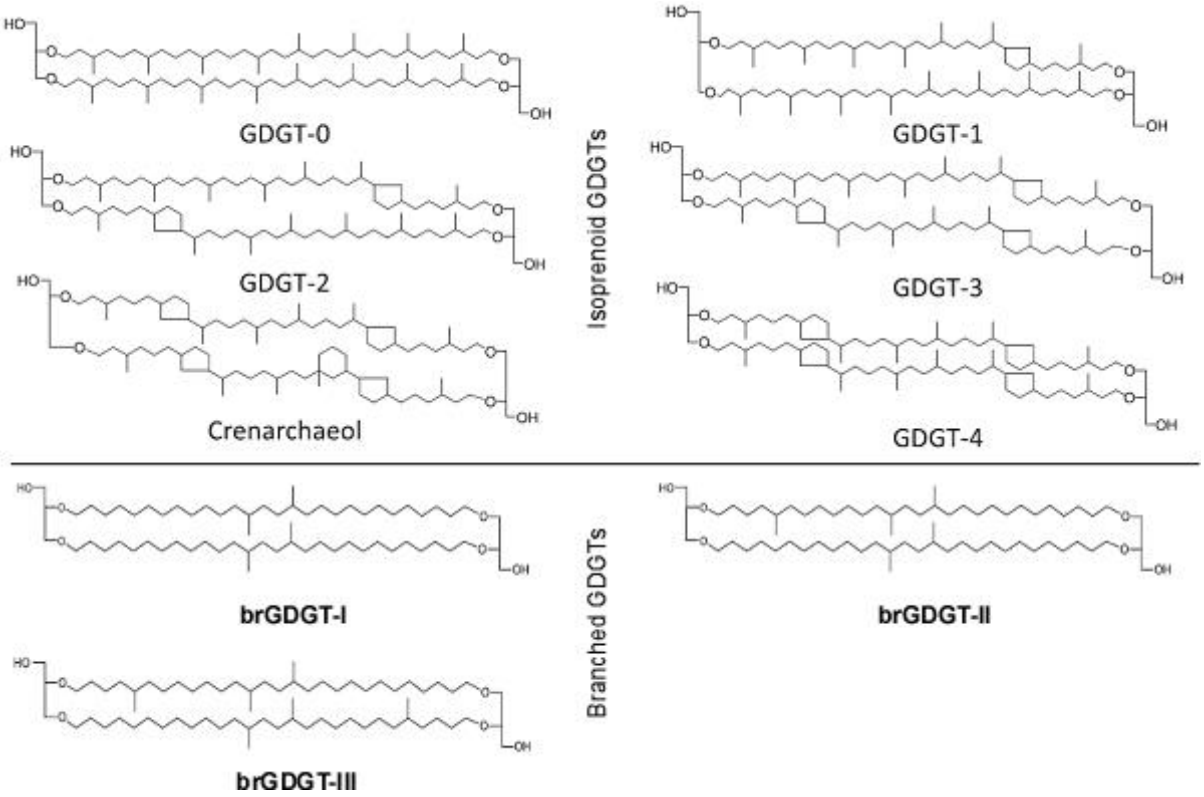

(Fig. 7): Structural differences between some common isoprenoid and branched GDGTs. Modified from Schouten *et al.* (2013).

As already mentioned earlier in this paragraph, brGDGTs are mainly produced by a specific group of bacteria (*Acidobacteria*; Weijers *et al.,* 2009; Sinninghe Damsté *et al.,* 2011a), while isoGDGTs are predominantly biosynthesized by archaeal source organisms, which include planktonic (e.g. Blaga *et al.,* 2009), as well as methanotrophic and methanogenic species (e.g. Blumenberg *et al.,* 2004).

The isoGDGT referred to as GDGT-0, also specified as caldarchaeol in some studies, is the most commonly reported GDGT in cultivated archaea (Schouten *et al.,* 2013). The biosynthesis of this cyclopentane-ring-lacking GDGT is not representative for a specific phylogenetic group within the Archaea and occurs in all major phyla (Schouten *et al.,* 2013). It is produced by mesophilic Thaumarchaeota (Sinninghe Damsté *et al.,* 2002b), by thermophilic Crenarchaeota and Euryarchaeota, as well as methanogens (anaerobic Euryarchaeota) (Koga *et al.,* 1993). The occurrence of GDGT-0 has also been linked to methanotrophic Euryarchaeota, by analyzing GDGTs at sites where active anaerobic oxidation of methane takes place, reporting a large depletion in ^{13}C of the carbon skeleton of GDGT-0 (Pancost *et al.,* 2001). Thus, GDGT-0 is encountered in cultivated species of all major phyla of Archaea, except in cultivated halophilic archaea (Schouten *et al.,* 2013). Interestingly, GDGT-0 is the only GDGT encountered in sediments that represent ancient hypersaline environments, although its source remains unknown (Turich and Freeman, 2011; Birgel *et al.,* 2014).

If Thaumarchaeota are the dominant source of GDGT-0, high amounts of crenarchaeol are also expected (Sinninghe Damsté *et al.,* 2002a; see also the GDGT-0/crenarchaeol ratio below). High abundances of GDGT-0 that are accompanied by low abundances of crenarchaeol (and GDGTs 1-3) have been linked to methanogens as the major source of GDGT-0 (e.g. Blaga *et al.,* 2009; Słowakiewicz *et al.,* 2016). The ubiquitous and metabolically more diverse Marine Group II archaea from the phylum *Euryarchaeota*, which generally prefer the photic zone and are less abundant in deeper waters (Rinke *et al.,* 2019), has also been suggested to be a source for GDGT-0 (Turich *et al.,* 2007). Strong evidence from preferably cultivated Marine Group II Euryarchaeota is needed to support this hypothesis, since a correlation between Marine Group II Euryarchaeota and the abundance of GDGT-0 appears to be absent in the North Sea (Wuchter, 2006; Herfort *et al.,* 2007). Recently, a

study on suspended particulate matter in the eastern tropical South Pacific has correlated several archaeal intact polar lipids (i.e. GDGTs + their polar headgroups still attached) to specific archaeal groups (Sollai *et al.,* 2019). The study concludes that both the Thaumarchaeota and Marine Group II Euryarchaeota could be responsible for GDGT-0 production, since the occurrence of archaea and the intact polar lipid of GDGT-0 (among others) is correlated in the upper water masses of the eastern tropical South Pacific (Sollai *et al.,* 2019).

GDGTs 1-4 are also biosynthesized by Thaumarchaeota, Crenarchaeota and some Euryarchaeota (Schouten *et al.,* 2013). The common occurrence of GDGTs 1-4 in cultivated Thaumarchaeota (Elling *et al.,* 2017) and the dominant presence of this archaeal group in aquatic environments (both marine and lacustrine; Auguet *et al.,* 2010), suggests that the Thaumarchaeota are a major source of these isoGDGTs in such environments. GDGTs 1-3 have also been encountered in significant amounts at sites where active anaerobic oxidation of methane takes place (Pancost *et al.,* 2001; Blumenberg *et al.,* 2004; Blaga et al., 2009). This suggests that methanotrophic Euryarchaeota can potentially be important producers of these isoGDGTs, especially if they dominate in concentration over crenarchaeol, since within the Thaumarchaeota, GDGTs 1-4 generally occur in low relative abundance compared to crenarchaeol and GDGT-0 (Schouten *et al.,* 2013). Methanogenic Euryarchaeota are unlikely to be an important source of GDGTs 1-4 in most environments, since these isoGDGTs were not reported from cultivated methanogenic archaea, with the exception of a single hyperthermophilic species (Schouten *et al.,* 2013).

GDGTs usually have great preservation potential unless severe maturation occurs and temperatures exceed 240 °C (Schouten *et al.,* 2004). They have been successfully extracted from sediments that date back as far as the Jurassic (Jenkyns *et al.,* 2012) and have been applied as a supplementary tool to identify the presence of specific phylogenetic groups of Archaea (e.g. Pitcher *et al.,* 2011), as well as for constraining carbon fixation pathways by measuring the carbon stable isotope composition of biphytanes (e.g. Pancost *et al.,* 2000). Futhermore, brGDGTs and isoGDGTs are now widely used biomarkers in several paleoenvironmental proxies (Schouten *et al.,* 2002; Hopmans *et al.,* 2004; Weijers *et al.,* 2007; Turich *et al.,* 2007; Peterse *et al.,* 2009; Zhang *et al.,* 2011).

2.3.2) Paleoenvironmental proxies and other indices based on GDGTs

The most renowned paleoenvironmental proxy based on GDGTs is undoubtedly the **TEX_{86}** (Schouten *et al.,* 2002), which stands for the "TetraEther indeX of tetraethers consisting of 86 carbon atoms":

$$TEX_{86} = \frac{[GDGT{-}II + GDGT{-}III + Cren\_isomer]}{[GDGT{-}I + GDGT{-}II + GDGT{-}III + Cren\_isomer]} \quad ,$$

where 'cren_isomer' signifies the crenarchaeol stereoisomer (Sinninghe Damsté *et al.,* 2018). After a while it became apparent that the original TEX_{86} was less successful in low-temperature oceans (Kim *et al.,* 2008) and two new GDGT indices were proposed by Kim *et al.,* 2010:

$$TEX^{H}_{86} = LOG \frac{[GDGT{-}II + GDGT{-}III + Cren\_isomer]}{[GDGT{-}I + GDGT{-}II + GDGT{-}III + Cren\_isomer]} \quad ,$$

where 'H' stands for high temperature regions and recommended for >15 °C:

$$TEX^{L}_{86} = LOG \frac{GDGT{-}II}{[GDGT{-}I + GDGT{-}II + GDGT{-}III]} \quad ,$$

where 'L' stands for low temperature regions and recommended for <15 °C. The TEX^{L}_{86} is also recommended when paleotemperatures are expected to encompass both above and below 15 °C. The TEX_{86} has been successfully applied as a proxy for sea surface temperature, even for GDGTs extracted from sediments that date back as far as the Cretaceous (Kuypers *et al.,* 2001; Schouten *et al.,* 2003; Jenkyns *et al.,* 2004; Forster *et al.,* 2007) or even the Jurassic (Jenkyns *et al.,* 2012). TEX_{86} is based on the number of cyclopentane rings that are incorporated in the GDGT structure, which is dependent on temperature (De Rosa *et al.,* 1980; Uda *et al.,* 2001). Although the TEX_{86} has shown to have a strong correlation with mean annual sea surface temperature, the TEX_{86} values can be affected by the input of soil-derived organic matter. Soil Thaumarchaeota biosynthesize GDGT 1-3, as well as crenarchaeol and its isomer, all of which are incorporated in the TEX_{86} formula and can therefore seriously bias TEX_{86}-derived temperatures (Weijers *et al.,* 2006, Sinninghe Damsté *et al.,* 2012). Another factor that can contaminate the original GDGT signature of sediments is the activity of methanotrophic Euryarchaeota (Pancost *et al.,* 2001, Blumenberg *et al.,* 2004; Blaga *et al.,* 2009), which biosynthesize GDGTs 1-3 and can substantially affect the

outcome of TEX_{86}-derived temperatures (e.g. Weijers *et al.,* 2011). In order to check if methanotrophic archaeal communities affected the GDGT signature of the Thaumarchaeota, Zhang *et al.,* (2011) developed the **Methane Index** (MI):

$$MI = \frac{[GDGT{-}I + GDGT{-}II + GDGT{-}III]}{[GDGT{-}I + GDGT{-}II + GDGT{-}III] + [Crenarchaeol] + [Cren\_isomer]} \quad ,$$

which takes advantage of the circumstance that a major group of methanotrophic Euryarchaeota (AMNE-1) does not produce crenarchaeol, but predominantly biosynthesizes GDGTs 1-3 (Pancost *et al.,* 2001; Blumenberg *et al.,* 2004). MI values >0.3 are considered as an indicator that AMNE-1 archaea living in anoxic waters and/or sediments influenced the GDGT pool (Zhang *et al.,* 2011).

To assess the relative abundance of soil-derived organic matter vs. marine organic matter, the **Branched and Isoprenoid Tetraether index** (BIT; Hopmans *et al.,* 2004) can be applied:

$$BIT = \frac{[brGDGT{-}I + brGDGT{-}II + brGDGT{-}III]}{[brGDGT{-}I + brGDGT{-}II + brGDGT{-}III] + [Crenarchaeol]} \quad ,$$

where brGDGT-I, II and III refer to the brGDGTs with m/z 1022, 1036 and 1050, respectively. The BIT index is based on the relative difference between the dominantly soil-derived brGDGTs and crenarchaeol, which is usually the most ubiquitous marine GDGT (Sinninghe Damsté *et al.,* 2002a). The application of the BIT index can potentially be complicated by minor production of brGDGTs in marine sediments and estuaries (Peterse *et al.,* 2009; Zhu *et al.,* 2011; Zell et al., 2015), while Thaumarchaeota (and thus crenarchaeol) also occur in soils (Weijers *et al.,* 2006). Thus, BIT values of analysed marine sediments and soil samples should rarely reach extreme values of 0 (no brGDGTs) or 1 (no crenarchaeol), respectively. In practice, BIT values for open marine surface sediment (where crenarchaeol predominates) are usually <0.15, while BIT values for surface soils (where brGDGTs predominate) are usually >0.5 (Schouten *et al.,* 2013). Although the BIT index is probably best applied when the results are qualitatively interpreted (by looking at trends in BIT records instead of absolute BIT values), values <0.2 should be related to a relatively low input of soil derived organic matter, while values >0.8 should corresponds to a strong soil organic matter imprint (Schouten *et al.,* 2013). The BIT index is often used in combination with the TEX_{86} in order to see if the TEX_{86} paleotemperatures could be biased by the input of GDGTs from soil Thaumarchaeota (e.g. De Bar *et al.,* 2018). Marine sediment samples with

BIT values >0.4 are considered as samples that experienced such terrestrial impact that derived TEX_{86} paleotemperatures are rendered unreliable (Weijers *et al.,* 2006).

Another GDGT-based index is the **GDGT-0/crenarchaeol ratio**, which has been applied to both recent (Turich *et al.,* 2007; Kim *et al.,* 2010) and ancient sediments (Schouten *et al.,* 2013; Natalicchio *et al.,* 2017), and is usually implemented in (paleo)environmental studies to recognize if methanogens contributed significantly to the GDGT pool. Blaga *et al.,* 2009 argued that if the GDGT-0/crenarchaeol ratio is >2, GDGT-0 must be derived from other archaea than just Thaumarchaeota, most likely methanogens. This application of the index is based on the reasoning that Thaumarchaeota biosynthesize similar amounts of GDGT-0 and crenarchaeol (ratio ~1; Turich *et al.,* 2007; Kim *et al.,* 2010), while methanogenic archaea biosynthesize GDGT-0 and do not produce crenarchaeol (Blaga *et al.,* 2009). However, it should be noted that the origin of GDGT-0 is not exclusive to Thaumarchaeota and methanogenic Euryarchaeota and is in fact widely distributed within the archaeal domain (Schouten *et al.,* 2007; Schouten *et al.,* 2013 and references therein; Sollai *et al.,* 2019). Thus, this approach is only applicable if Thaumarchaeota and methanogens are the most likely sources for GDGT-0 production. The GDGT-0/crenarchaeol ratio has also been proposed as a proxy that is suitable for tracking changes in the water column from normal marine to harsher conditions, possibly even indicating water column stratification (Zhang *et al.,* 2016; Natalicchio *et al.,* 2017). Recently, it has been suggested that elevated ratios of this index could be related to the production of GDGT-0 by halophilic Euryarchaeota, although the exact species are hitherto uncharacterized (Zang *et al.,* 2018).

A study based on a large set of globally derived soils, revealed that the distribution of brGDGTs has a strong correlation with mean annual air temperature and soil pH (Weijers *et al.,* 2007). In particular, the amount of methyl groups branching from the alkyl core units correlates negatively with temperature and pH, while the amount of incorporated cyclopentane rings correlates negatively with soil pH. Based on these findings, the **methylation of branched tetraethers** (MBT) and **cyclization of branched tetraethers** (CBT) ratios were proposed (Weijers *et al.,* 2007). A recalibration of the MBT-CBT proxy resulted in a generally better agreement with independent temperature proxies due to lower amplitude changes and absolute temperatures (Peterse *et al.,* 2012). The MBT-CBT proxy

has been successfully applied in marine sediments (e.g. Peterse *et al.,* 2009; Vasiliev et al., 2019), lacustrine sediments (e.g. Zink *et al.,* 2010) and the terrestrial realm (e.g. Hren *et al.,* 2010), although caution should be applied (Tierney and Russel, 2009; Huguet *et al.,* 2012; Zell *et al.,* 2014).

2.4) Dialkyl Glycerol Diethers

Dialkyl glycerol diethers (DGDs) are isoprenoid membrane lipids that are widespread in the archaeal domain, but thought to be predominantly biosynthesized by the Euryarchaeota (Koga *et al.,* 1993; 1998; Dawson *et al.,* 2012). The main difference that distinguishes DGDs from GDGTs is the fact that their structure is acyclic, linking a glycerolphosphate backbone to hydrocarbon chains on one side of the molecule, while the other end of the hydrocarbon chains remains "linkage free" (Koga *et al.,* 1993; Koga and Morii, 2007; Valentine, 2007; Dawson *et al.,* 2012; Caforio and Driessen, 2017) (**Fig. 8**).

(Fig. 8): Structures of DGDs often associated with halophilic archaea. Note the "linkage free" side of the molecule, which is the main difference between DGDs and GDGTs. Modified from Natalicchio *et al.* (2017).

The most commonly reported DGDs are archaeol (biphytanyl [$C_{20,20}$] glycerol) and extended archaeol (phytanyl-sesterpanyl [$C_{20,25}$] glycerol). Archaeol is biosynthesized by most groups in both major archaeal kingdoms (i.e. Euryarchaeota and Crenarchaeota) and is an important source for sedimentary phytane (Brocks and Summons, 2005). Common producers of archaeol are the Euryarchaeota (Koga *et al.,* 1993; 1998), but it can also be biosynthesized by halophilic (Dawson *et al.,* 2012), methanotrophic (Hinrichs *et al.,* 1999), methanogenic (Pancost *et al.,* 2011), and even normal marine Euryarchaeota (Sollai *et al.,* 2019). Thus, care should be taken when using archaeol as a biomarker. Although isoprenoidal DGDs are commonly encountered biomarker lipids in sedimentary environments, the identification of high amounts of both archaeol and extended archaeol in sediments are commonly associated with hypersaline environments (Wang, 1998; Grice *et al.,* 1998; Turich and Freeman, 2011; Dawson *et al.,* 2012; Birgel *et al.,* 2014), especially the

presence of extended archaeol, which is a robust biomarker for hypersaline conditions (Teixidor *et al.,* 1993; Tachibana, 1994; Wang *et al.,* 2007; Stadnitskaia et al., 2008).

One of the main source organisms responsible for DGD biosynthesis are the halophilic Euryarchaeota (e.g. Teixidor *et al.,* 1993; Grice *et al.*, 1998; Dawson *et al.,* 2012). GDGTs on the other hand, are found to be mostly absent in hypersaline environments (Turich *et al.,* 2007), with the exception of the cyclopentane ring-lacking GDGT-0, often referred to as caldarchaeol, which is reported to occur in sediments that represent ancient hypersaline environments (Turich and Freeman, 2011; Birgel *et al.,* 2014). Based on the excellent correlation between salinity and the relative amount of archaeol to GDGT-0 (caldarchaeol) in modern surface sediments from a wide range of environments (from brackish to hypersaline), Turich and Freeman (2011) developed the Archaeol and Caldarchaeol Ecometric (ACE) as a proxy for (paleo)salinity. In the same study, the ACE showed potential for reconstructing paleosalinity, since the analysis of samples prior to the onset of the MSC indicated that ACE-derived paleosalinities increased just before the onset of the crisis. Turich and Freeman (2011) attributed the correlation between the ACE and salinity to a change in the archaeal community, from a mixed community of Euryarchaeota and Crenarchaeota in normal marine waters to the dominant presence of halophilic Euryarchaeota in hypersaline waters (Casamayor *et al.,* 2002). However, care should be taken when it comes to archaeol and GDGT-0 abundances, since both compounds may also be derived from methanotrophic archaea involved in the anaerobic oxidation of methane (Blumenberg *et al.,* 2004; Pancost *et al.,* 2005), which can seriously bias salinity calculations. Terrestrial influence might also impact ACE-derived paleosalinities, since GDGT-0 is the most commonly occurring GDGT in non-halophilic archaea and could thus also be derived from a terrestrial source (Schouten *et al.,* 2013 and references therein). Wang *et al.,* 2013 argued that in situ production of archaeol and GDGT-0 in sediments might also complicate the utilization of the ACE, with in situ GDGT-0 production being the most plausible complicating factor. In fact, Natalicchio *et al.,* 2017 demonstrated the limited applicability of the ACE, arguing that the total amount of GDGT-0 in the sediments can also be impacted by planktonic thaumarchaeotal production of GDGT-0. To assess if Thaumarchaeota have contributed significantly to the total GDGT-0 pool, the GDGT-0/crenarchaeol ratio can be applied (e.g. Turich *et al.,* 2007; Kim *et al.,* 2010).

2.5) Sterols

Sterols are essential membrane lipids of all eukaryotic cells, including animals and plants (Nash *et al.,* 2005), but are also biosynthesized by microorganisms such as dinoflagellates (Withers, 1987), algae (Patterson, 1991; Volkman *et al.,* 1998), diatoms (Barrett *et al.,* 1995; Rampen *et al.,* 2010) and bacteria (Bouvier *et al.,* 1976; Wei *et al.,* 2016; Rivas-Marin *et al.,* 2019). Sterols can be referred to as being part of the larger group of steroids. In fact, sterols are also intermediate products in the biosynthetic pathway of the more oxidized steroids (Goad and Akihisa, 2012). The core of a sterol consists of four linked hydrocarbon rings, often referred to as the "steroid nucleus" (i.e. perhydro-1,2-cyclopentanophenanthrene nucleus; **Fig. 9**). Other characteristics are the hydroxyl group at the C-3 position of the steroid nucleus and a side chain may be located at C-17 (Volkman, 2005; Goad and Akihisa, 2012) (**Fig. 9**). The high structural diversity of sterols is related to: 1) various positions for possible methyl, ethyl and/or propyl groups, 2) the position and amount of double bonds in both the steroid nucleus and/or the side chain, 3) the degree and position of side chain alkylation, 4) additional hydroxyl groups and 5) differences in stereochemistry (Volkman, 2003).

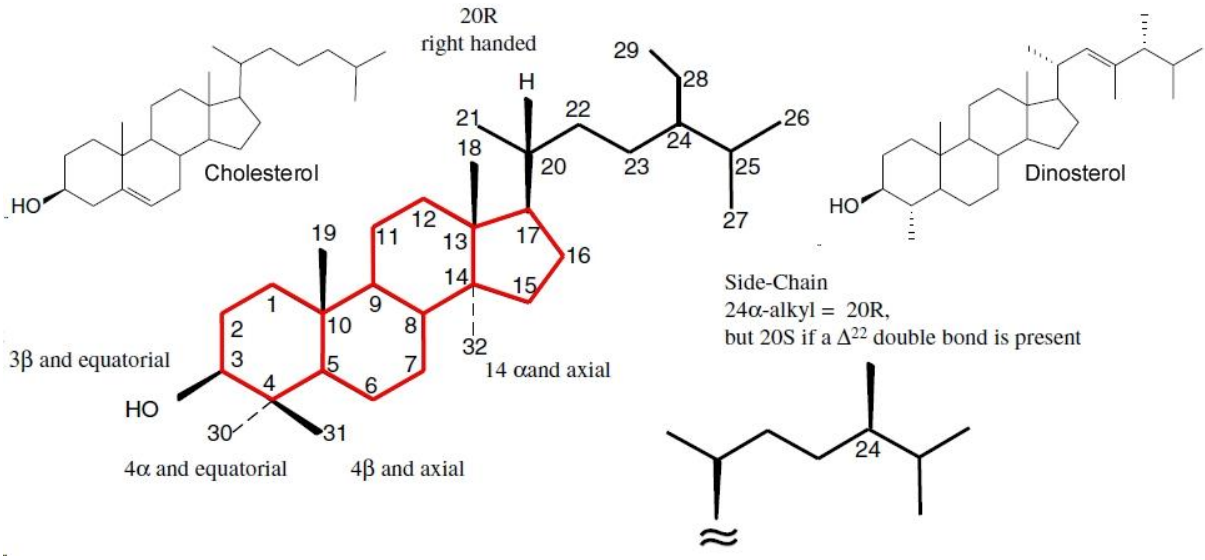

(Fig. 9): Structure and carbon numbering of a generalized sterol molecule. Red colours indicate the the central building block of all sterols, the perhydro-1,2-cyclopentanophenanthrene nucleus or "steroid nucleus". The structures of two characteristic sterols, cholesterol and dinosterol, are depicted in the upper left and right corner, respectively. Modified from Volkman (2005).

Some sterols are widely distributed and biosynthesized by numerous types of organisms, while other sterols are related to a very specific source and/or metabolism and have proven to be useful biomarkers (Schouten *et al.,* 2001; Volkman, 2005; Goad and Akihisa, 2012). Among the common sterols that are preserved in the sedimentary archive, cholesterol is one of the most abundant and it is the major sterol biosynthesized by all animal cells (Goad and Akihisa, 2012). Although cholesterol is biosynthesized specifically by some species of algae (Volkman, 1986; 2003), it usually indicates the presence of heterotrophic organisms and is often used as a biomarker proxy for zooplanktonic herbivory (Grice *et al.,* 1998). Other commonly encountered sterols in sediments are sitosterol, campesterol, stigmasterol, the three major sterols biosynthesized by plants (Goad and Akihisa, 2012) and dinosterol, which is almost exclusively produced by dinoflagellates (Withers, 1987).

The three major phytosterols (sitosterol, campesterol and stigmasterol) are widespread in higher plants (Moreau *et al.,* 2002) and are therefore sometimes used as biomarkers for riverine transported organic matter (e.g. McCallister *et al.,* 2006). Unfortunately, these sterols are not exclusively produced by higher plants, since e.g. sitosterol (the most common phytosterol; Goad and Akihisa, 2012) is also biosynthesized by some algae and cyanobacteria (Volkman, 1986; Volkman *et al.,* 1998). Therefore, the phytosterols are rather unspecific biomarkers and cannot be considered as unambiguous compounds of terrigenous organic matter or vascular plants, especially when most of the organic matter seems to have originated from marine organisms (Volkman, 1986). Conversely, when sitosterol is less abundant than stigmasterol and campesterol, one can be fairly confident that an algal source has been an important organic matter contributor (Volkman, 1986). Ratios of different sterols are sometimes used as a proxy to assess autochthonous vs. allochthonous organic matter (e.g. Nishimura, 1978; Prartono and Wolff, 1998). Medeiros and Simoneit (2008) use the cholesterol/(sitosterol + stigmasterol) ratio to indicate the input of phytosterols. Relatively low values indicate an apparent input of phytosterols, while relatively high values indicate a dominant input of algal-derived organic matter. This ratio is based on the assumption that the cholesterol in the organic matter is mainly derived from an autochthonous source (i.e. algal source), although it can also be derived from other organisms (Volkman, 1986; Goad and Akihisa, 2012). Phytosterol analysis is often compared with *n*-alkane distribution (Volkman, 1986), as well as with the presence of triterpenols such

as lupeol, α-amyrin and β-amyrin, other biomarkers that are used to indicate the input of higher plants to the organic matter pool (Otto and Wilde, 2001; Medeiros and Simoneit, 2008; Bataglion *et al.,* 2016).

Dinosterol is widely used as a biomarker for dinoflagellates (Boon *et al.,* 1979; Withers, 1983; 1987; Robinson *et al.,* 1984; Volkman et al., 1999), although it can also be produced, albeit in small quantities, by some diatom species (Volkman *et al.,* 1993). Nevertheless, it should be noted that not all dinoflagellate species biosynthesize high quantities of dinosterol (Withers, 1987) and some even lack it (Robinson *et al.,* 1987). The abundance of dinosterol and its diagenetic alteration product dinostanol have the potential to quantify dinoflagellate input to marine sediments (Mouradian *et al.,* 2007). The relative change of dinosterol abundance compared to other biomarker lipids can serve as a qualitative proxy to indicate changes in primary productivity over time. This approach has been successfully applied to show differences in primary productivity during Pliocene sapropel deposition (Menzel *et al.,* 2003; 2006), as well as more recent glacial/interglacial changes in primary productivity and/or composition of the phytoplankton community (e.g. Zhao *et al.,* 2006; Xing *et al.,* 2011; Mei *et al.,* 2019).

Chapter 3 – The Messinian salinity crisis

The Messinian salinity crisis (MSC), which occurred during the late Neogene, is one of the most dramatic paleoceanographic events in Earth's history. When this ecological crisis took place about 6 Ma, the Mediterranean was progressively isolated from the Atlantic Ocean due to the combined effect of tectonics and climatic changes, resulting in the deposition of more than one million km^3 of evaporative salts on the Mediterranean seafloor (Hsü *et al.,* 1973a,b; 1977; Ryan, 1976; Krijgsman *et al.,* 1999; Roveri *et al.,* 2014 and references therein). The deposition of this vast amount of gypsum, anhydrite and halite occurred in a time period of less than 700 ka, between 5.97 and 5.33 Ma (Manzi *et al.,* 2013; Roveri *et al.,* 2014). The geological relics of these ancient evaporites can be studied in numerous onshore sites where the deposits from marginal Mediterranean basins have been exposed (Roveri *et al.,* 2008; Lugli *et al.,* 2010; Dela Pierre *et al.,* 2011; 2016). However, the majority of the Messinian evaporites are still buried below the abyssal plains of the present day Eastern and Western Mediterranean Sea (e.g. Lofi *et al.,* 2011a,b; Roveri *et al.,* 2014; Güneş *et al.,* 2018), still awaiting a scientific drilling project that is able to recover cores that span the entire evaporite unit. Hitherto, only the top of the abyssal evaporite unit has been cored in the 1970s, leading to the original 'dessicated deep-basin model' for the MSC (Hsü *et al.,* 1973a; 1977; Ryan, 1976). This hypothesis became the prototype model for the MSC and remained largely unquestioned for decades. Since the early 2000s, studies appeared that suggested the persistence of deep-water conditions throughout the MSC (e.g. Hardie and Lowenstein, 2004; Manzi *et al.,* 2005; Garcia-Veigas *et al.,* 2018), an important suggestion that contributed to the general consensus on the MSC model. The gypsum deposits of the first phase of the MSC are now considered to be fully subaqueous, as supported by an absence of evidence for substantial sea level fall during this phase (De Lange and Krijgsman, 2010; Lugli *et al.,* 2010). Unfortunately, the absence of modern analogues hinders recognition of the exact mechanism behind this supposedly subaqueous gypsum precipitation. Therefore, this aspect and other features of the MSC remain elusive, emphasizing the necessity for additional research, in order to better constrain the paleoenvironmental settings during the MSC.

The MSC occurred at the end of a global period of cooling in the Late Miocene between about 7 and 5.4 Ma (Herbert *et al.,* 2016; Capella *et al.,* 2019). During this period, the continents endured a change to drier climatic conditions and experiencing greater seasonality, which had a significant effect on terrestrial plant communities, resulting in the expansion of C4 vegetation at ~7 Ma (Pagani *et al.,* 1999; Diester-Haass *et al.,* 2006). Superimposed on this Late Miocene cooling trend that resulted in drier conditions, significant climatic fluctuations were experienced during the MSC, which likely caused fluctuating evaporation rates and relative humidity, as concluded by research focussing on samples from a ~50 ka interval that likely deposited during the acme of the MSC (RLG; Stage 2), using the δ^2H of the C_{22} *n*-alkane and the biomarker 5α-cholestane (Andersen *et al.,* 2001). More recent biomarker research on the δ^2H of long-chain *n*-alkanes concluded that environmental conditions were probably less arid than previously argued, and that hydrological conditions were more likely similar to the present-day climate in the Mediterranean basin, at least during stage 1 of the MSC (Vasiliev *et al.,* 2017). However, this work also indicated that at specific stratigraphic levels the δ^2H-values suggested more arid conditions, similarly hinting to significant climatic fluctuation during the initial stage of the MSC.

3.1) Chronology of the Messinian salinity crisis

Since the discovery of the evaporites in the deeper Mediterranean basin, many studies have focussed on the diachronicity of the MSC events. Although several authors suggested a diachronous scenario for evaporite deposition in the Mediterranean basin (Rouchy, 1982; Butler *et al.,* 1995), it was difficult to test this hypothesis, since biostratigraphic and magnetostratigraphic approaches were unable to provide reliable age models for the MSC-related stratigraphic sections. After the development of an astronomical age model for several Messinian sedimentary successions (Hilgen *et al.,* 1995; Hilgen and Krijgsman, 1999; Krijgsman *et al.,* 1999; 2001; 2002), it became clear that at least the onset of evaporite deposition was synchronous in both the eastern and western Mediterranean basin. Although these cyclostratigraphic studies ended the debate on whether the onset of

evaporite deposition had a coeval origin or not, questions remained regarding the deposition in deeper settings, since none of the deep basinal evaporites have been exposed on land (Roveri *et al.,* 2014).

3.2) The stratigraphic model for the Messinian salinity crisis

After cyclostratigraphic studies were able to develop age models for pre-evaporitic cycles at a precessional-cycle-resolution, it was soon suggested that the subsequent cyclic deposition of gypsum beds during the MSC, was also related to precession (Krijgsman *et al.,* 2001), despite the lack of bio- and magnetostratigraphic evidence. After the proposition of a two-staged model for evaporite deposition in a desiccated Mediterranean basin (Clauzon *et al.,* 1996) and the doubts about the total evaporation of the seawater during evaporite formation (Manzi *et al.,* 2005), a consensus stratigraphic model was developed during a CIESM workshop, including the chronostratigraphy for all MSC events in a non-desiccated Mediterranean (CIESM, 2008) (**Fig. 10**). The CIESM consensus model consists of three separate stages (i.e. Stage 1, 2 and 3; Manzi et *al.,* 2013; Roveri *et al.,* 2014), each associated with specific evaporite bearing deposits. The original model has been slightly modified since then, by subdividing stage 3 into sub-stages 3.1 and 3.2 and including the different "Calcare di Base" types (Manzi *et al.,* 2011). The MSC stratigraphic framework is characterized by 5 key-surfaces, which define each MSC stage and are used to recognize MSC stages in the field (Manzi *et al.,* 2013) (**Fig. 10**).

Stage 1 of the MSC (5.97-5.6 Ma; Manzi *et al.,* 2013) and thus the onset of the crisis, is defined by the precipitation of primary gypsum in the relatively shallow-water peripheral basins (Roveri *et al.,* 2008; 2014), while shales and dolostones were depositing in the deeper settings of the Mediterranean (CIESM, 2008). Stage 2 (5.6- 5.55 Ma; Hilgen *et al.,* 2007) is regarded to as the climax or 'acme' of the MSC, during which enormous volumes of primary halite precipitated from dense brines in the deeper Mediterranean, as well as the development of the 'Messinian Erosional Surface' (MES) at the basin margins (Lofi *et al.,* 2005; Roveri *et al.,* 2008; Do Couto *et al.,* 2015) as a consequence of the tectonic uplift and tilt of the peri-Mediterranean orogens and the concomitant glacio-eustatic sea level drop (Roveri *et al.,* 2008). The tectonic pulse and the formation of the MES involved the

resedimentation of part of the gypsum that was deposited in stage 1 of the crisis and subsequently exposed and eroded.

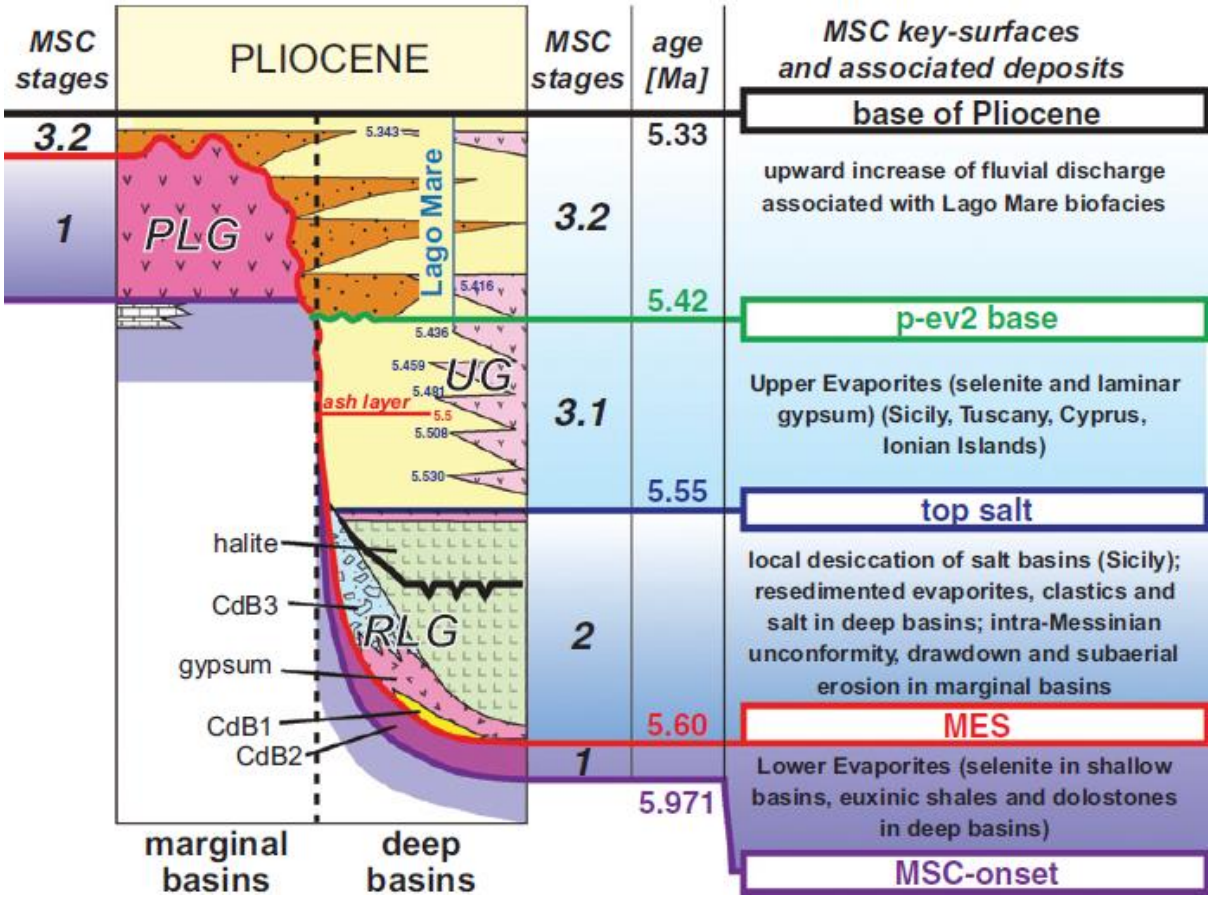

(Fig. 10): Modified version of the original CIESM consensus model (CIESM, 2008) depicting the chronostratigraphy of events during the MSC in the Mediterranean basin. Note that Stage 2 and sub-stage 3.1 are represented by a hiatus in the stratigraphic record of marginal Mediterranean basins. CdB: Calcare di Base. PLG: Primary Lower Gypsum unit. MES = Messinian Erosional Surface; RLG = Resedimented Lower Gypsum unit; UG = Upper Gypsum unit. Figure from Manzi *et al.* (2013).

The 3rd stage of the MSC (5.55-5.33 Ma; Van Couvering *et al.*, 2000; Hilgen et al., 2007) is characterized by the cyclical deposition of the 'Upper Evaporites' and 'Lago Mare' deposits (McCulloch and De Deckker, 1989; Krijgsman *et al.*, 1999; Fortuin and Krijgsman, 2003; Manzi *et al.*, 2009). The Lago Mare deposits are characterized by brackish to freshwater fauna and flora with Paratethyan affinities (e.g. Orszag-Sperber, 2006), although there is some controversy regarding the paleoenvironmental conditions during deposition of this unit, as indicated by reports of marine fish remains within the 'Lago Mare' deposits (Carnevale *et al.*, 2006). However, it is commonly suggested that freshening of

Mediterranean surface waters occurred, while locally marine conditions episodically returned, as evidenced by the rhythmic deposition of the 'Upper Gypsum', likely driven by precession (Roveri *et al.,* 2008; Manzi *et al.,* 2009; 2011). The deposits of MSC stage 3 are covered by marine Pliocene deposits, which represent the reestablishment of fully marine conditions in the Mediterranean and the end of the MSC, often referred to as the Pliocene or Zanclean flooding (Iaccarino *et al.,* 1999; Van Couvering *et al.,* 2000; Bache *et al.,* 2012; Micallef *et al.,* 2018).

Recently, a multidisciplinary study conducted on a sedimentary record recovered from an industrial drilling site in the deep Mediterranean basin (Levant basin), provided new insights that suggest the necessity for a new chronological model regarding the MSC (Meilijson *et al.,* 2019). According to this study, the lowest part of the MSC evaporitic sequence commences with deep basinal halite, which apparently deposited as early as ~300 ka before the currently assumed onset of the MSC (5.971 Ma; Manzi *et al.,* 2013). Seismic and cyclostratigraphic data suggests that halite deposition already occurred during the 1st stage of the MSC, rather than being limited to sea level low-stand phase in the 2nd stage of MSC (Lofi *et al*., 2011a,b). These findings imply that halite deposition in the deep Mediterranean Levant basin was coeval with deposition of the PLG unit in the marginal basins, and that the classic view of dense brines in a shallow desiccated Mediterranean is not required for halite deposition.

3.3) The ecological response to changing paleoenvironmental conditions related to the Messinian salinity crisis

The word "crisis" in Messinian salinity crisis refers to the drastic ecological changes in the Mediterranean ecosystem (Roveri *et al.,* 2014), which was greatly impacted before (pre-evaporitic phase) and around the onset of the MSC (Sierro *et al.,* 1999; 2003; Blanc-Valleron *et al.,* 2002). Biostratigraphic and sedimentologic evidence points to a general trend of increasing basin restriction from open marine conditions to a semi-enclosed Mediterranean over the course of roughly 1 million years, deteriorating paleoenvironmental conditions for (macro)biological life and reducing biodiversity in the Mediterranean ecosystems (Blanc-

Valleron *et al.,* 2002).

3.3.1) Prior to the Messinian salinity crisis

Before the evaporites of the MSC actually started depositing in the marginal Mediterranean basins, the ongoing restriction of the Mediterranean-Atlantic connection significantly affected the chemistry of the Mediterranean seawater, drastically increasing its salinity (Blanc-Valleron *et al.,* 2002; Garcia-Castellanos and Villaseñor, 2011). It has been suggested that the restriction was a stepwise process (Van Assen *et al.,* 2006), modulated by long-term orbital forcing (i.e. 400 ka eccentricity cycle; Kouwenhoven *et al.,* 2006), superimposed on the signal related to the gradual tectonic activity in the Gibraltar gateway area (Govers, 2009). The first evidence for basin restriction is indicated by a reduction of deep-water ventilation in the Mediterranean, as suggested by the increasing presence of stress tolerant benthic foraminiferal faunas around ~7 Ma (Kouwenhoven *et al.,* 1999; 2003; Kouwenhoven and Van der Zwaan, 2006). Around ~6.7 Ma, increased water column stratification started affecting (macro)benthic communities and sapropels started to form on the shelf of the Sorbas Basin and on the Mediterranean side of the African continent (Sierro *et al.,* 2003; Van Assen *et al.,* 2006). The next response to the reduced connectivity is displayed by a decrease in diversity of foraminifera and calcareous nannofossils prior to the MSC, probably related to enhanced salinities of Mediterranean surface waters during precession maxima as well as intensified stratification during precession minima (Sierro *et al.,* 1999; 2003; Blanc-Valleron *et al.,* 2002). In the period directly preluding the onset of the MSC (6.3-5.97 Ma), surface water salinities during precession maxima became too stressful for marine microfauna, resulting in the complete disappearance of planktonic foraminifera (Sierro *et al.,* 1999; 2003; Blanc-Valleron *et al.,* 2002).

3.3.2) During and after the onset of the Messinian salinity crisis

The onset of the MSC and its stressful paleoenvironmental conditions are well recorded in the sedimentary archive by the marine microfauna fossil record (Violanti *et al.,* 2013; Lozar *et al.,* 2010; 2018; Gennari *et al.,* 2018; Mancini *et al.,* 2020). In the Piedmont basin, just prior to the onset of the MSC, planktonic and benthic foraminifera decrease in size and

diversity, while the abundance of stress-tolerant species of calcareous nannofossils increases (Lozar *et al.,* 2010; Violanti *et al.,* 2013). At the onset of the MSC, both benthic and planktonic foraminifera disappear from the fossil record, followed after a few precessional cycles by calcareous nannofossils, which seem to be more stress-tolerant than foraminifera (Violanti *et al.,* 2013; Lozar *et al.,* 2018). After the onset of the MSC and the disappearance of calcareous plankton, few reports in the literature indicate evidence of marine life in the Mediterranean basin. Deposits interpreted as microbialites are reported in the anoxic deep-water counterparts of the selenitic gypsum that deposited in marginal Mediterranean sub-basins during the first stage of the crisis (Dela Pierre *et al.,* 2012). These microbialites show abundant evidence of spaghetti-like filaments, interpreted as *Beggiatoa*-like sulfide-oxidizing bacteria (Dela Pierre *et al.,* 2012; 2014). These filamentous fossils appear to be similar to the dense mazes of filaments reported from selenitic gypsum (Dela Pierre *et al.,* 2015), which were originally interpreted as algae or cyanobacterial remains (Vai and Ricci Lucchi, 1977; Rouchy and Monty, 2000; Panieri *et al.,* 2010). It has been suggested that the anoxic bottom water conditions also persisted after the first stage of the MSC, as supported by framboidal pyrite, the lack of benthic organisms, fine lamination and high U/Th ratios (Sampalmieri *et al.,* 2010). Some authors have suggested the presence of a diverse assemblage of calcareous plankton and benthic organisms even during the MSC, but it is unclear if these findings should be interpreted as evidence for normal marine conditions (Braga *et al.,* 2006) or are the result of reworking (Bassetti *et al.,* 2006). Nevertheless, normal marine conditions must have at least temporarily occurred locally, judging from the evidence of fish remains and other marine (micro)fossils that were found in sediments interbedded to selenitic gypsum from the first stage of the MSC (Carnevale *et al.,* 2008; 2019). It is clear that there is still a lot of uncertainty and controversy related to the paleoenvironmental conditions after the onset of the MSC, mainly because adequate micropaleontological research is hindered due to the lack or mixing of fossils of different environmental affinity. This points out the necessity for additional research from a different angle which can shed more light on paleoenvironmental conditions and (micro)biological communities. Lipid biomarker research might provide this essential information, contributing to the reconstruction of paleoenvironmental conditions in the Mediterranean water column during the MSC.

Chapter 4 – The Primary Lower Gypsum unit

In Mediterranean marginal sub-basins, the first phase of the MSC is represented in the stratigraphic record by the originally so-called Lower Evaporites (Krijgsman *et al.,* 1999), which refer to the primary sulfate evaporites that deposited during this period. This name was revamped when it became clear that the name 'Lower Evaporites' (or Lower Gypsum) was somewhat misleading, because at several sites this unit comprises both primary and resedimented (clastic) gypsum (e.g. Manzi *et al.,* 2005; 2007). Since the primary and resedimented gypsum represent two distinctly different and consecutive phases of the MSC (Roveri *et al.,* 2014 and references therein), the Lower Evaporites were subdivided into the Primary Lower Gypsum (PLG) unit and the Resedimented Lower Gypsum unit (RLG; Roveri *et al.,* 2008), representing the first and the second phase of the MSC, respectively.

4.1) Sedimentary cyclicity and lithologies of the PLG unit

The PLG unit is composed of up to 16 sedimentary cycles of shale/gypsum couplets, based on cyclostratigraphic correlations between the Sorbas basin (SE Spain; Krijgsman *et al.,* 2001) and the Vena del Gesso basin (Northern Apenines, Italy; Lugli *et al.,* 2010). The onset of gypsum sedimentation at a certain location in a marginal sub-basin can be delayed depending on the proximity to the basin margin. This is for instance indicated by a lateral transition of shale/gypsum to shale/marl couplets in the lower PLG cycles towards the basin depocenter of the Piedmont basin (Dela Pierre *et al.,* 2011). This demonstrates that the appearance of the first gypsum bed does not necessarily mark the onset of the MSC (Manzi *et al.,* 2007). The ideal evaporitic succession of a PLG cycle consists of a sequence of massive, banded and branching selenite facies, the latter appearing from 6th PLG cycle and commonly repeated in the consecutive PLG cycles, although some cycles may be exclusively composed of the branching selenite facies (Lugli *et al.,* 2010) (**Fig. 11**).The gypsum beds of the 3rd to 5th PLG cycle are basin-wide the thickest and only show the massive and banded selenite facies, while the first two PLG cycles are commonly the thinnest and solely consist of the massive selenite facies (Lugli *et al.,* 2010).

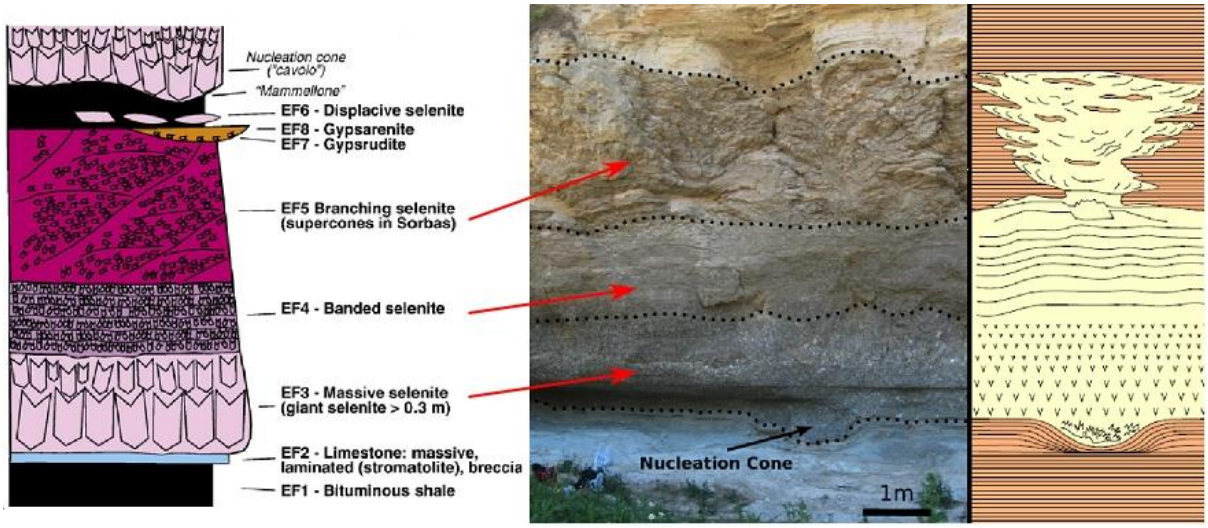

(Fig. 11): **Left:** the 'ideal depositional PLG cycle' and facies terminology from Lugli *et al.* (2010), most representative for the uppermost Vena del Gesso section (Northern Apennines, Italy). EF = evaporite facies. **Right:** photograph from Evans *et al.* (2015) of the 6th PLG cycle of the Río de Aguas section in the Sorbas basin (SE Spain), indicative for the successive facies change from massive selenite to banded selenite and branching selenite. The schematic diagram is after Dronkert (1977), emphasizing the evolution of gypsum facies, crystal morphology and structure.

The massive selenite facies (**Fig. 12A**) consists of decimeter-sized vertically oriented twinned crystals (often described as arrowhead or shallow-tail twin crystals), which are thought to be formed in a relatively deep basin permanently covered by moderately saturated brines (Schreiber & El Tabakh, 2000; Babel, 2002; 2007; Lugli *et al.*, 2010). Most gypsum beds in the PLG unit consist of larger selenite crystals in the bottom which gradually become smaller upsection, probably reflecting an increasing saturation level of the brine (Babel, 1999).

The banded selenite facies (**Fig. 12A-B**), which is typified by palisades of cm-sized crystals separated by mm-thick clay or carbonate layers, reflects more unstable conditions, likely controlled by continuous vertical fluctuation of the gypsum saturation zone (i.e. the pycnocline; Babel, 2007). These apparent fluctuations of the pycnocline repeatedly stop the growth of the gypsum crystals, as marked by the dissolution surfaces in the banded selenite, resulting in a stratified appearance of the selenite beds (Lugli *et al.*, 2010). Banded selenite has been interpreted by Lugli *et al.* (2010) as the acme of the precessional aridity peaks that are deemed responsible for the cyclical deposition of the PLG cycles.

The branching selenite facies (**Fig. 12C-E**), also described by Lugli *et al.* (2010), consists of mm- to cm-sized twinned selenite crystals with their long axis inclined or oriented horizontally. The crystals are arranged in cm- to dm-sized flattened conical structures that can be isolated or grouped to form larger, meter-sized cones. This crystal arrangement suggests that branching selenite cones grew laterally, outwards from a nucleation zone. When viewed from above, the cones have a circular to ellipsoidal aerial projection. The growth of the larger cones may be asymmetrical, with one side of the cone (branch) sometimes more developed than the other, hence the name branching selenite. The growth mechanism of the branching selenite facies and the reason behind its supposed Mediterranean scale appearance during the 6th PLG cycle remain under debate. Lugli *et al.* (2010) suggested that the asymmetrical lateral growth of branching selenite is promoted by brine currents, resulting in preferential growth towards the brine current, similar to the mechanism suggested for the growth of curved gypsum crystals from the Middle Miocene (Badenian) basin of Poland and Ukraine (Babel, 2002; Babel and Becker, 2006; Babel and Bogucki, 2007). The growth of superimposed branches could be related to a depressed but progressively rising pycnocline, limiting the vertical accommodation space and forcing the branching selenite to grow mainly laterally (Lugli *et al.,* 2010). However, many aspects of this puzzling gypsum facies remain enigmatic.

The branching selenite facies has been correlated with the 'supercones' of the Sorbas basin (SE Spain; Dronkert 1977, 1985). It was proposed that this gypsum lithofacies appeared synchronously at the Mediterranean basin scale within the 6th lithological cycle of the PLG unit (~5.870 Ma; Lugli *et al.,* 2010; Manzi *et al.,* 2013). According to this interpretation, the appearance of branching selenite can be used for the physical correlation of sections that are located hundreds of kilometers apart. In the Piedmont Basin the branching selenite facies is strictly associated with the laminar gypsum facies, representing a gypsum cumulate deposit. It consists of mm-thick laminae of fine-grained gypsum crystals separated by very thin veneers (>1 mm) of clay and organic matter (Schreiber *et al.,* 1976; Manzi *et al.,* 2012; Lugli *et al.,* 2015). The laminar gypsum facies is further discussed in the results section (**chapter 7.1**), as it is one of the dominant gypsum facies in the Pollenzo section and has been thoroughly investigated for the purpose of this thesis.

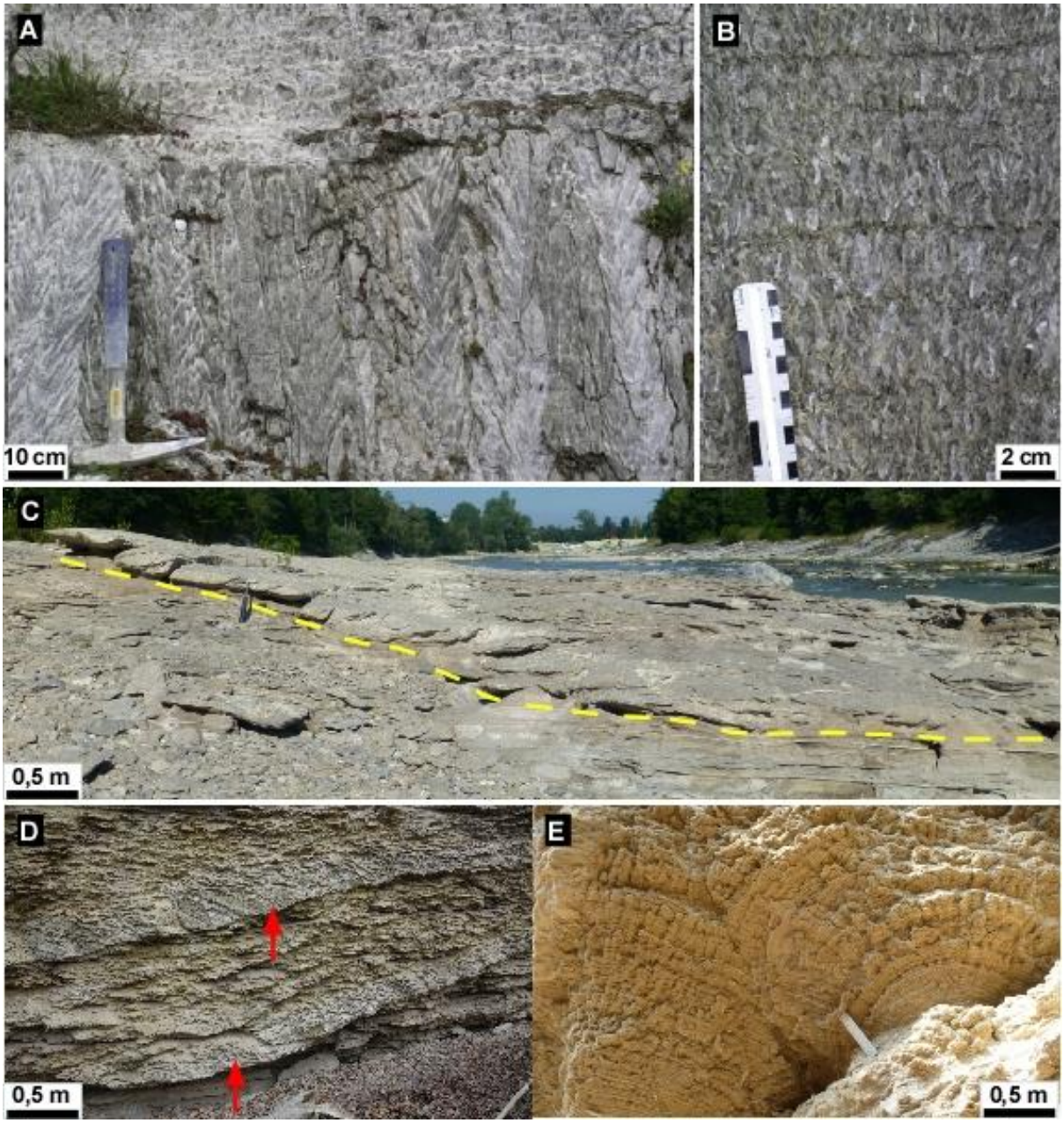

(Fig. 12): Different types of gypsum lithofacies in the PLG unit. **A:** Massive selenite (bottom), characterized by its large arrowhead-like crystals and the contact with the banded selenite facies (top) that consists of palisades of smaller selenite crystals. Photograph from Lugli *et al.* (2010), Rocca di Entella section, Sicily. **B:** Close-up of the banded selenite facies. Note the dissolution surfaces that give this facies its layered appearance. Photograph from Lugli *et al.* (2010) at Vita, Belice basin, Sicily. **C:** Branching selenite in the Sturani key-bed (PLG 6) at the Pollenzo section, Piedmont basin, NW Italy. Note the inclined development of a large 'branch' composed of superimposed conical structures (yellow dotted line). **D:** The branching selenite facies and its coalescent nature of flattened conical structures at the Arnulfi section, Piedmont basin, NW Italy. Note the development of some of the more dominant 'branches' (red arrows). **E:** Bottom-view of fairly symmetrical branching selenite cones, which grew outwards from their initial nucleation zone and collided at some point with one another, Pollenzo section, Piedmont basin, NW Italy.

4.2) The origin of the PLG unit

The presence of different gypsum lithofacies in the PLG unit and the locally delayed onset (or total absence) of gypsum deposition has raised many questions related to the mechanism that controls deposition of the PLG unit in peripheral basins. Several similarities among PLG deposits in the marginal Mediterranean basins have been identified, such as trends in the strontium content (Rosell *et al.,* 1998) and homogenous sulfate isotope compositions of gypsum ($\delta^{34}S$ = ~23‰ and $\delta^{18}O$ = ~14‰; Garcia-Veigas *et al.,* 2018), as well as the amount of gypsum-bearing cycles and the supposed appearance of the branching selenite facies in the 6th PLG cycle (Lugli et al., 2010). A unifying mechanism for gypsum deposition in the marginal Mediterranean basins was proposed by Lugli *et al.,* 2010, based on correlating PLG cycles between basins in the Apenines, Sicily and southern Spain. Based on this cycle-by-cycle correlation and the absence of sedimentary structures indicating subaerial exposure, a depositional setting at outer shelf depths (~100-200 m) was proposed for the gypsum deposition of the PLG units (Lugli *et al.,* 2010), while the absence of oxygen in permanently stratified basins likely prevented gypsum precipitation in the deeper parts of the basin (De Lange & Krijgsman, 2010). The latter is confirmed by studies on organic-rich shales and carbonates of deeper parts of the basin, which indicate that gypsum saturation was likely never achieved there, possibly due to the presence of prominent bacterial sulfate reduction (Dela Pierre *et al.,* 2012; Garcia-Veigas *et al.,* 2018; Sabino *et al.,* 2021). The scenario where gypsum precipitation occurs at moderate depths now seems to be the consensus model for the formation of the PLG unit, rejecting the original model that ascribes the precipitation of gypsum to very shallow water depositional environments (e.g. Hsü *et al.,* 1973a).

Up until now, it remains enigmatic which exact mechanism is behind the deposition of the PLG unit, particularly in relation to the chemical composition of the water column and where in the water column the gypsum precipitated. Normally, gypsum precipitation is associated with highly evaporative environments, with seawater reaching salt concentrations of at least 4 times higher than normal (~110‰; Warren, 2010). Studies on primary fluid inclusions incorporated in selenitic gypsum from the PLG unit in the Piedmont basin (Natalicchio *et al.,* 2014), Sorbas basin (Evans *et al.,* 2015) and Southern Apennines

(Costanzo *et al.,* 2019), revealed that the salinity of the gypsum parent water was probably lower than intuitively would be expected from seawater in an evaporitic basin. Relatively low salinities were measured in the water of the fluid inclusions, indicating that gypsum parent water was relatively low in sodium and chloride ions compared to modern seawater, although sulfate and calcium ions must have been enriched. This could have been related to a significant contribution of freshwater that transported ions from dissolved coeval marine gypsum to the basin (Natalicchio *et al.,* 2014). In agreement with this study, Evans *et al.,* 2015 also concluded that a source of freshwater must have had a significant influence during the formation of the PLG unit, judging from the low isotope values of gypsum hydration water ($\delta^{18}O$ and $\delta^{2}H$) and low salinity values from fluid inclusions in Messinian gypsum from the Sorbas basin. Nevertheless, the isotope values of gypsum hydration water and the measured salinities seem to be decoupled from the $^{87}Sr/^{86}Sr$, $\delta^{34}S$, and $\delta^{18}O_{SO4}$ signal, which all indicate a marine origin for gypsum. It was suggested that the recycling of previously deposited gypsum supplied the necessary ions for gypsum precipitation, leading to a marine signature for the primary sulfate deposits, while a mix between freshwater and marine water could have caused the low hydration water isotope and salinity values (Evans *et al.,* 2015).

More recently, another mechanism has been proposed, directly linking the Paratethys to the formation of PLG unit (Grothe *et al.,* 2020). Strontium isotope records evidence an establishment of the connection between the Paratethys and the Mediterranean as early as 6.1 Ma (Pontian Flood; Krijgsman *et al.,* 2010). It is proposed that Paratethyan waters caused the offset between strontium isotope ratios from gypsum and ocean water during deposition of the PLG unit, rather than regional discharge in marginal Mediterranean basins. According to the authors, the Paratethys freshened the surface water of the Mediterranean, creating a low salinity water layer that was unable to mix with underlying water due to the high-density contrast. This might have allowed a westward spreading of these low salinity surface waters towards the marginal Mediterranean basins, contributing to the formation of gypsum deposits by supplying the necessary calcium and sulfate ions (Grothe *et al.,* 2020).

4.3) Precessional control during deposition of the PLG unit

The sedimentary cyclicity in the PLG unit is assumed to be controlled by precession (Krijgsman *et al.,* 1999), one of the three Milankovitch cycles that accounts for the cyclical change in orientation of the Earth's rotational axis. The gypsum beds of the PLG unit are thought to be deposited under arid conditions during insolation minima (precession maxima), while shales probably deposited under more humid conditions during insolation maxima (precession minima) (Krijgsman *et al.,* 1999; 2001; Lugli *et al.,* 2010). The correlation of the sedimentary cyclicity with precession is primarily based on field observations and the tuning of individual cycles to the astronomical target curve (Krijgsman *et al.,* 1999; 2001). This target curve describes the precessional insolation quantity, using a numerical solution based on Earth's orbital data, solved by Laskar *et al.* (1993) and further improved by Laskar *et al.* (2004). The sedimentary cyclicity of the pre-evaporitic sediments, typified by alternations of organic rich shales (sapropels), marls and diatomites (Krijgsman *et al.,* 1999; Sierro *et al.,* 2001) changes into the gypsum/shale cyclicity of the PLG unit without any unconformities (Krijgsman *et al.,* 1999). Convincing evidence linking the pre-evaporitic cyclicity to the precessional cycle (Sierro *et al.,* 1996; 1999) and a good agreement between the number of cycles in the PLG unit and the astronomical target curve led to the consensus that the sedimentary cyclicity in the PLG unit was similarly controlled by precession. Adequate tuning of the cycles in the PLG unit to the astronomical target curve resulted in an age interval of 5.96-5.61 Ma for the first stage of the MSC (Krijgsman *et al.,* 1999). More recently, a re-assessment of the stratigraphic succession in the Sorbas basin led to the recognition of an additional gypsum-bearing cycle in the transitional interval encompassing the MSC onset, refining the tuning of the PLG cycles to the astronomical target curve. This resulted in a re-calibrated age for the onset of the MSC at 5.971 Ma (Manzi *et al.,* 2013). However, direct evidence confirming the assumption that precession is the main driver behind the sedimentary cyclicity during the first stage of the MSC has yet to be provided, especially for the gypsum bearing PLG cycles. Unfortunately, magneto- and biostratigraphic data cannot provide this confirmation, since the entire MSC succession occurred within a single reversed magnetic chron (C3r; Krijgsman *et al.,* 2001) and the absence or scarcity of calcareous microfossils impedes biostratigraphic correlation of MSC successions (e.g. Violanti *et al.,* 2013). Climate change has also been linked to precession by Evans *et al.,*

2015, based on isotopic and mineralogic observations over the course of one full PLG cycle.

4.4) Climate modeling during deposition of the PLG unit and strontium isotopes of primary evaporites

In the past two decades, numerous studies have used climate modeling to understand the relationship between the Atlantic-Mediterranean gateway(s), hydrological budget, evaporation, salinity, the strontium isotope ratio ($^{87}Sr/^{86}Sr$) of ocean water and the precipitation of evaporites (Flecker *et al.,* 2002; Topper *et al.,* 2011; 2014; Topper and Meijer, 2015; Simon and Meijer, 2015; Simon et al., 2017) . Even though the evaporative flux might be relatively small compared to the other fluxes affecting the Mediterranean hydrological budget, it controls salinity in mid-latitude settings such as the Mediterranean. Therefore, it is of great importance to include this evaporative flux into climatic models, in order to quantify the relationship between the $^{87}Sr/^{86}Sr$ and salinity (Flecker *et al.,* 2002). Reversely, $^{87}Sr/^{86}Sr$ and salinity data can be implemented in climate models in order to calculate relative changes in the fluxes contributing to the Mediterranean hydrological budget. By including the evaporative flux into the climate model, it was demonstrated that the total isolation of the Mediterranean is not a requirement to obtain salt concentrations which enable the precipitation of evaporites and to explain the strontium isotope anomalies of gypsum with coeval ocean water (Flecker *et al.,* 2002). Considerable improvements to the climate model revealed that the deposition of the PLG unit can be simply explained with a restriction of the Atlantic-Mediterranean gateway (Topper *et al.,* 2011). The dimension of this gateway has been approximated to be relatively shallow and narrow (30-45 m deep and 0.7-2 km wide; Simon and Meijer, 2015) during deposition of the PLG unit.

Climate modeling research has recently actively focussed on the question if the strontium isotope ratio of seawater can fluctuate as a result of a varying freshwater budget during a precessional cycle within a Mediterranean marginal basin. Indeed, even in settings within a large range of boundary conditions, including a varying precessional-forced freshwater input, strontium isotope and salinity fluctuations of the seawater are most certainly possible, indicating that a fluctuation of $^{87}Sr/^{86}Sr$ values should be a common feature in PLG

deposits (Topper *et al.,* 2014). Further climate modeling focussed on freshwater contribution in a restricted Mediterranean basin, concluding that the salinity of the Mediterranean seawater is quantitatively consistent with a precessional control, with salt concentrations fluctuating around a hypothetical concentration threshold suitable for gypsum precipitation (Simon *et al.,* 2017). The number of excursions in the modeled salinity curve (i.e. threshold exceedances) matches the amount of PLG beds found in the field (up to 16 gypsum beds; Roveri *et al.*, 2014), linking modeled salinity in the Mediterranean basin to the observed number of PLG cycles. The modeled salinity fluctuation can both be linked to a saltier (Lugli *et al.,* 2010) and a fresher (Grothe, 2016) Mediterranean seawater scenario, keeping the proposed model for PLG deposition (regarding gypsum precipitation threshold) open for discussion. Examining the phase relation between gypsum deposition and precessional forcing in a wide range of settings, model results indicate a significant phase lag of ~3.3 ka (±2.6 ka) for gypsum deposition in response to the precession signal (Topper and Meijer, 2015).

As predicted by climate modeling, strontium isotope measurements on planktic foraminifera from pre-evaporitic sediments reveal that the $^{87}Sr/^{86}Sr$ values make brief excursions in phase with precessional cyclicity (Modestou *et al.,* 2017). The obtained strontium isotope record was then used to model the hydrological conditions which are required to produce the observed $^{87}Sr/^{86}Sr$ record. The model results suggest that the strontium isotope anomalies are controlled by precessional freshwater pulses, resulting in limited exchange between marginal basins and the main Mediterranean basin due to the large density contrast between these water bodies (Modestou *et al.,* 2017). These findings furthermore implied that the hydrological budget in a marginal basin needs to be mainly positive in order to generate the strontium anomaly, in contrast to the negative hydrological budget of the main Mediterranean basin, a scenario which is in line with low salinity fluid inclusion measured in gypsum (Natalicchio *et al.,* 2014; Evans *et al.,* 2015; Costanzo *et al.,* 2019).

Strontium isotopes have also been measured across the onset of the MSC (Sorbas basin, SE Spain; Reghizzi *et al.,* 2017) and in individual gypsum beds from the PLG unit (Vena del Gesso basin, NW Italy; Reghizzi *et al.,* 2018). These studies confirmed that the

Mediterranean was likely never cut-off from the Atlantic Ocean during deposition of the PLG unit and that orbital forcing likely remained the main climate driver. Besides linking the fluctuations in the $^{87}Sr/^{86}Sr$ records to precessional forcing, the authors also suggested that the 100 ka eccentricity cycle had a significant influence on the hydrological budget of marginal basins (Reghizzi *et al.,* 2018). This is indicated by a gradual detachment of the strontium isotope values from the global ocean, with distinct detaching steps in the $^{87}Sr/^{86}Sr$ records correlating to eccentricity minima (Reghizzi *et al.,* 2018). Although this research clearly suggests that the Milankovitch cyclicity was influencing the seawater chemistry through the fluctuating input of freshwater during the MSC, these findings are yet to be confirmed by geochemical proxies that indicate climatic conditions in the terrestrial environment.

Climate modeling also suggests that the Piedmont Basin was likely influenced by precessional climate forcing, either due to changes in the intensity of the Mediterranean storm track (Kutzbach *et al.,* 2014) or the total precipitation budget over the Mediterranean region (Bosmans *et al.,* 2015). These precipitation mechanisms were likely of significant importance and able to affect the freshwater budget of the northern Mediterranean (Meijer and Tuenter, 2007), in phase with the African monsoon (Toucanne *et al.,* 2015), which in turn affected the eastern/southern Mediterranean freshwater budget (Rohling and Hilgen, 2007*;* Rohling *et al.,* 2015; Ziegler *et al.,* 2010; Grant *et al.,* 2016). Modeling studies have also indicated that precession-driven changes in strontium isotopes should be a common feature in the PLG deposits of the Mediterranean marginal basins (Topper *et al.,* 2014), which has been recently confirmed by studies on Messinian gypsum (Reghizzi *et al.,* 2017; 2018). Besides linking the fluctuations in the $^{87}Sr/^{86}Sr$ records to precessional forcing, Reghizzi *et al.,* 2018 also suggested that the 100 ka eccentricity cycle had a significant influence on the hydrological budget of the basin.

4.5) Lipid biomarkers in the PLG unit

Thus far, lipid biomarker studies on the PLG unit have been very sparse, hitherto limited to the Vena del Gesso and Piedmont basins (**Fig. 13A**).

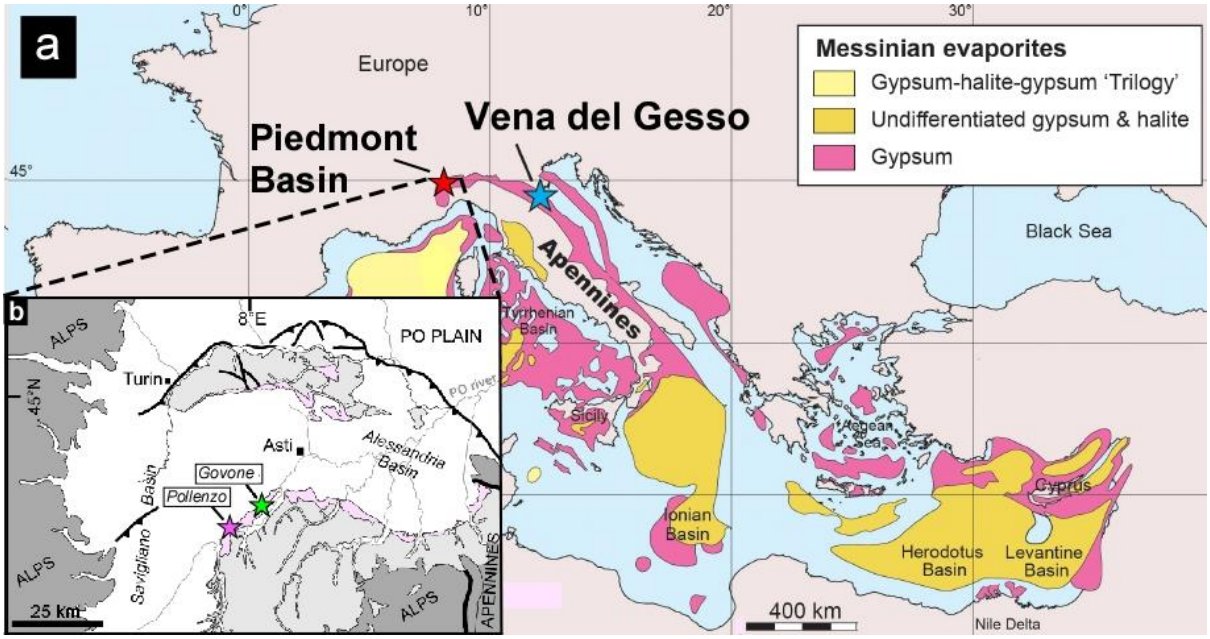

(Fig. 13): Map indicating the locations where PLG-unit-related biomarker studies have been performed. Locations have been marked with colored stars. **A:** Map indicating the distribution of Messinian evaporites, as well as the Vena del Gesso and Piedmont basins. Figure modified from Isaji *et al.* (2019). **B:** Map of the Piedmont basin in indicating the Pollenzo and Govone sections. Figure modified from Sabino *et al.* (2020).

At the end of the 20th century, pioneering studies on lipid biomarkers in the PLG unit have been performed in the Vena del Gesso basin. Here, biomarker analysis has been performed on the organic-sulfur rich marls deposited between the gypsum beds of the PLG unit. Environmental reconstructions were made based on the analysis of marls from up to 10 PLG cycles (Sinninghe Damsté *et al.,* 1995b; Keely *et al.,* 1995) or in more detail for a single PLG cycle (Kenig *et al.,* 1995; Schaeffer *et al.,* 1995). Large and varying suites of biomarkers were found, indicating a high diversity of organisms that lived in the water column inside a highly dynamic environment. The presence of isorenieratane (photic zone euxinia indicator) and gammacerane (water column stratification indicator) suggests that the Vena del Gesso basin was mostly an euxinic and stratified basin during marl deposition (Sinninghe Damsté *et al.,* 1995b; Kenig *et al.,* 1995), with these conditions probably being more prevalent at times when the middle of the marl sections deposited (Schaeffer *et al.,* 1995; Keely *et al.,* 1995). In the final stages of marl deposition, it is proposed that stratification collapsed due to shallowing of the basin, as indicated by the increased presence of cyanobacterial hopanoids and stromatolitic beds in the very top of the studied section (Kenig *et al.,* 1995). The authors found proof for the activity of primary producers such as diatoms, dinoflagellates,

coccolithophorids, cyanobacteria, green and purple sulfur bacteria, as well as considerably varying terrestrial *n*-alkane input (Sinninghe Damsté *et al.,* 1995b; Kenig *et al.,* 1995). The high degree of sulfurization of the organic matter is hypothesized to be related to a varying depth of the chemocline, with a shallower chemocline related to a higher degree of sulfurization since organic molecules are faster in reaching the anoxic zone (where reduced sulfur species await), making them less vulnerable to oxidation (Kenig *et al.,* 1995).

The Vena del Gesso basin was also studied in order to infer hydrological changes in the Mediterranean basin during the MSC, which were reconstructed using the hydrogen isotope compositions of long chain *n*-alkanes and alkenones (Vasiliev *et al.,* 2017). The δ^2H values of *n*-alkanes from the PLG unit of the Monte Tondo section suggest that hydrological conditions under which gypsum precipitated during the Late Messinian are similar to the current climatic situation in the Mediterranean region. Obtained δ^2H values range between -138‰ and -171‰, which are close to values measured in modern Italian lakes close to the Vena del Gesso basin (−159‰ to −167‰; Sachse *et al.,* 2004). Although likely cut-off from the Mediterranean, a severe period of drought in the adjacent Black Sea basin was identified between ~5.8-5.6 Ma (Vasiliev *et al.,* 2013; 2015), which likely also affected the Mediterranean basin. To further investigate this significant change in the hydrological regime during the first stage of the MSC, a detailed study on mean annual air temperatures was carried out, based on the relative abundance of brGDGTs in sediments of the Black Sea basin (Vasiliev et al., 2019). A marked decrease in mean annual air temperature was identified between ~6.2-5.8 Ma (from 16 to 8 °C), coinciding with the change towards considerably drier conditions. This period of cooling might be related to the Late Miocene cooling, which culminated with lowest sea surface temperatures between ~5.8-5.7 Ma (Herbert *et al.,* 2016) and transient glaciations of the northern hemisphere between ~5.8-5.5 Ma (Holbourn *et al.,* 2018).

A recent biomarker study on the PLG unit in the Vena del Gesso basin involved the analysis of geoporphyrins (derived from marine phototrophs) from shales representing the 4th and 5th PLG cycles (Isaji *et al.,* 2019). Structures of geoporphyrins and their carbon and nitrogen isotopic compositions have been analysed in order to provide paleoenvironmental information about the phototrophic community and the carbon and nitrogen cycles. The

study suggests that nitrogen-fixing microorganisms (diazotrophs) were favoured due to the density-stratified conditions in the basin during shale deposition, causing a lower N/P ratio and a diminished supply of nutrients. These diazotrophs might have had a symbiotic relationship with diatoms by supplying the necessary nitrogen, which resulted in the deposition of the organic-rich shales during formation of the PLG unit (Isaji *et al.,* 2019).

The Piedmont basin (**Fig. 13B**) has also been studied to deduce paleoenvironmental change from the distribution of lipid biomarkers. The accumulation of isoprenoidal DGDs and GDGTs throughout the Pollenzo section sharply increased across the onset of the MSC, suggesting the establishment of adapted archaeal communities, possibly including the emergence of halophilic archaea (Natalicchio *et al.,* 2017). Both crenarchaeol and tetrahymanol have been identified in sediments deposited after the onset of the MSC, indicating persisting normal marine water conditions in the upper water column, as well as stratified conditions (Natalicchio *et al.,* 2017). Further paleoenvironmental research on the same sediments of the Pollenzo section focussed on geochemical proxies based on elemental ratios and the distribution of long-chain *n*-alkanes. Several elemental ratios demonstrated a fluctuating input of fluvial and aeolian sedimentary particles, demonstrating the influence of precession-driven climate change (Natalicchio *et al.,* 2019). The distribution of *n*-alkanes and barium content (a paleoproductivity proxy; Tribovillard *et al.*, 2006) agree that during precession minima (insolation maxima) increased input of terrestrial organic matter and nutrients promoted phases of stratification and eutrophication in the Piedmont basin (Natalicchio *et al.,* 2019). Across the onset of the MSC, a lithological change occurred during precession maxima, from bioturbated marls to laminated marls. The presence of fossilized sulfide-oxidizing bacteria (Dela Pierre *et al.,* 2014) and tetrahymanol (Natalicchio *et al.,* 2017) in these laminated marls suggests that stratification likely persisted during precession maxima (insolation minima). This is interpreted as a continuous inflow of freshwater into an increasingly restricted Piedmont basin, increasing the sensitivity of the basin to water column stratification, preceding the onset of gypsum precipitation (Natalicchio *et al.,* 2019).

The Govone section, located a little more towards the depocenter of the Piedmont basin and thus representing deposition in a 'deeper' marine setting, has recently been the focus of paleoenvironmental studies related to the MSC. Sediments from this section have been thoroughly investigated in order to trace climatic and hydrologic variability across the onset of the MSC, using element distributions and carbon and hydrogen stable isotope compositions of long-chain n-alkanes (Sabino *et al.,* 2020). Confirming the outcome of previous studies in the Piedmont basin, this study also concluded that deposition at the Govone section was controlled by precession-driven climate fluctuations across the onset of the MSC. Interestingly, this study also mentioned that humidity likely increased after the onset of the MSC, with an overall increase in precipitation over the northern Mediterranean, as indicated by a decrease in several Al-based proxies (Ti/Al, Si/Al and Zr/Al) and an increasing trend in the abundance of plant-wax derived long-chain *n*-alkanes. The Govone section has also been the study site for research focusing on paleoenvironmental conditions across the onset of the MSC (Sabino *et al.,* 2021), using a multidisciplinary approach (lipid biomarker content, compound specific carbon and oxygen stable isotopes as well as petrographic data). The most important conclusion of this study is the recognition of the dominant role that the intensification of water column stratification (rather than increasing salinity) must have played during the first phase of the MSC, impacting environmental conditions in the Piedmont basin. The water column was likely divided into an upper water layer influenced by riverine input of freshwater, separated by a vertically oscillating chemocline from a saltier, denser and oxygen-depleted bottom water layer.

Chapter 5 – Geological setting and the Messinian succession of the Piedmont basin

The Piedmont Basin is a wedge-top basin developed upon an orogenic wedge of Alpine, Ligurian and Adria basement units, which is filled with sediments of Late Eocene to Messinian age (Rossi *et al*., 2009; Mosca *et al*.,2010; Rossi, 2017) (**Fig. 14A**). The Messinian sedimentary succession is exposed in the southern and northern basin margins (Langhe and Torino Hill-Monferrato regions, respectively), while it is buried below Pliocene to Holocene deposits in the depocentral zones (Dela Pierre *et al.,* 2011) (**Fig. 14B**).

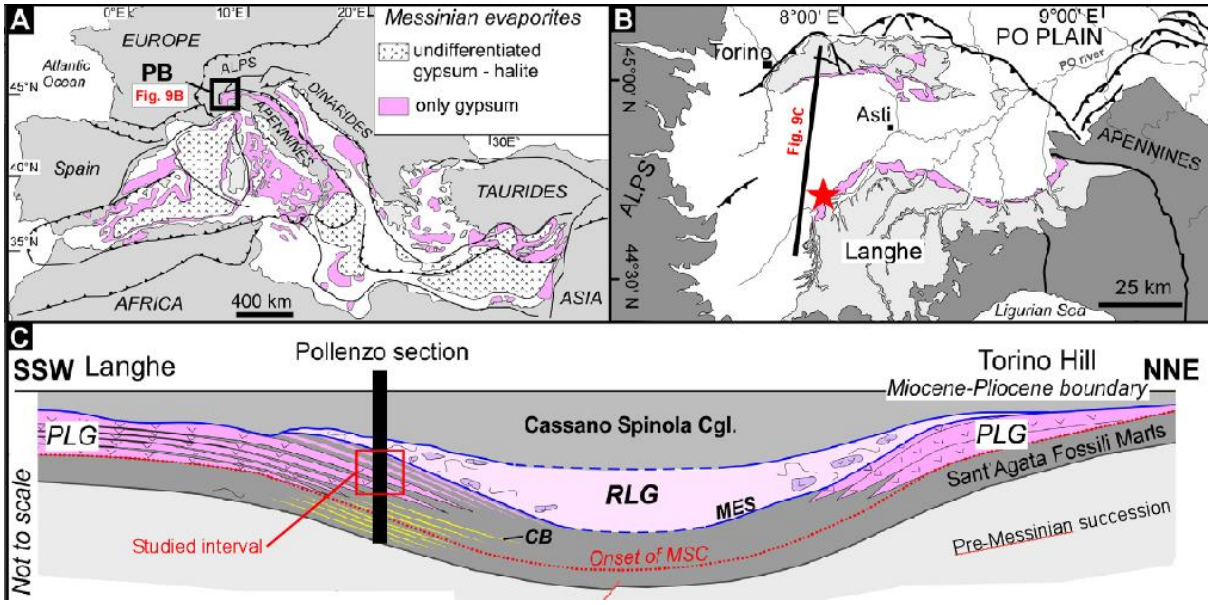

(Fig. 14): **A:** Distribution of Messinian evaporites in the Mediterranean basin. PB: Piedmont basin. **B:** Geological overview of the Piedmont basin (box in Fig. 9A). Pink colours indicate the distribution of Messinian deposits in the Piedmont basin. The red star indicates the location of the Pollenzo section (44°41'08"N; 7°55'33"E). The black line represents the transect visible in Fig. 9C. **C:** A NNE-SSW transect of the western Piedmont basin, showing the vertical distribution of the Messinian stratigraphic units and indicating the studied interval of the Pollenzo section. CB = carbonate-rich beds; MES = Messinian Erosional surface; RLG = Resedimented Lower Gypsum unit; PLG = Primary Lower Gypsum unit. Figure modified from Natalicchio *et al.* (2017).

The Messinian succession (**Fig. 14C**) starts with outer shelf to slope fine-grained sediments known as the Sant'Agata Fossili Marls (Tortonian-lower Messinian) that consist of a rhythmic alternation of shale/marl couplets (Dela Pierre *et al.,* 2011, 2012; Lozar *et al.,* 2010), which point to a progressive restriction of the basin, announcing the onset of the MSC. Thorough studies on the calcareous microfossil content in the Sant'Agata Fossili Marls

(planktonic and benthic foraminifera, calcareous nannofossils) indicate that the lithological cyclicity is strictly controlled by precessional-driven climate oscillations (Lozar *et al.,* 2010; Violanti *et al.,* 2013; Lozar *et al.,* 2018, Lozar and Negri, 2019) with shales and marls reflecting humid and arid climate conditions at precession minima and maxima, respectively. At the basin margins, the Sant'Agata Fossili marls are followed upwards by the shale (and marl) / gypsum couplets of the PLG unit (Dela Pierre *et al.,* 2011), which correspond to the first stage of the MSC (5.97–5.60 Ma; Manzi *et al.,* 2013). Towards the depocenter (Pollenzo and Govone sections), the PLG cycles make a lateral transition into shales and marls that belong (from the lithostratigraphic point of view) to the Sant'Agata Fossili Marls, with marls representing the deep-water equivalents of marginal gypsum layers (Dela Pierre *et al*., 2011; 2012). The PLG unit and its deep-water equivalents are followed by clastic and chaotic gypsum deposits known as the Valle Versa chaotic complex, which belongs to the RLG unit and records the second phase of the MSC (Dela Pierre *et al.,* 2007; 2011). These deposits are followed by fluvio-deltaic terrigenous sediments (Cassano Spinola Conglomerates) with Lago Mare fossil assemblages in the upper part (Sturani, 1973) that record the final stage of the MSC (Dela Pierre *et al.,* 2011).

The Pollenzo section (44°41'08"N; 7°55'33"E), located at the NW edge of the Langhe domain (**Fig. 14B**), has been the main focus of this thesis and comprises the whole Messinian sedimentary succession. The section starts with the Sant'Agata Fossili marls that consist of seven lithological cycles of shale/marl couplets (Dela Pierre *et al.,* 2011; 2012; Violanti *et al.,* 2013; Natalicchio *et al.,* 2017; 2019; Lozar *et al.,* 2018). The onset of the MSC has been placed within the Sant'Agata Fossili Marls at the base of the marls in cycle Pm5, according to cyclostratigraphic and biostratigraphic data (see **Fig. 15** and Dela Pierre *et al.,* 2011; Lozar *et al.,* 2018; Lozar and Negri, 2019; Natalicchio *et al.,* 2019 for more details). The Sant'Agata Fossili Marls are sharply overlain by the PLG unit, which consists of nine lithological cycles of shale/gypsum couplets, of which seven have been thoroughly studied for the purpose of this thesis (the studied interval is described in detail in **chapter 7.1**). The PLG unit is in turn overlain by a slumped mudstone interval enclosing meter-sized gypsum slabs. This unit is ~5 m thick and has been referred to as the Valle Versa chaotic complex, the local equivalent of the RLG unit (Dela Pierre *et al.,* 2011). It is bounded at the base by the MES and corresponds to the second stage of the MSC. The Pollenzo section ends with fluvio-deltaic and lacustrine

sediments with Lago Mare fossil assemblages (Cassano Spinola Conglomerates, MSC stage 3) in turn overlain by Zanclean marine marls (Argille Azzurre Fm.) (Dela Pierre *et al.,* 2011).

Chapter 6 – Materials & Methods

Fifty-three samples from the Pollenzo section, encompassing seven lithological cycles within the PLG unit (Pg3-Pg9) were excavated and analysed for their total organic carbon and lipid biomarker contents. Biomarker analysis and the measuring of geochemical properties has been performed at the Institute for Geology of the University of Hamburg (Germany). The analysed samples include 30 laminated shales, 17 gypsum samples (12 branching selenite and 5 laminar gypsum samples) and 6 homogenous marls. For a detailed description of the studied interval of the Pollenzo section, including the different lithologies, see **chapter 7.1**.

6.1) Total organic carbon analysis

The excavated samples were dried (45 °C) and subsequently powdered with a mortar and a pestle. Two aliquots were taken from the powdered sediments in order to measure the total organic carbon (TOC) content of each sample. The first aliquot was heated to 1350 °C to measure the total carbon (TC) content using a LECO SC-144DR Carbon Analyzer equipped with an infrared detector. The second aliquot was first heated to 550 °C for 5 hours to remove the TOC and subsequently heated to 1350 °C to measure the total inorganic carbon (TIC). Prior to the described measurements, a standard (Synthetic Carbon Leco 501-034; 1.01 ± 0.02 carbon%) was analysed for reference. The TOC was calculated by using the formula TOC = TC-TIC. The TIC can be expressed as percentage calcium carbonate (% $CaCO_3$) by applying the formula: $CaCO_3$ = TIC*8.33.

6.2) Lipid biomarker analysis

All shale, marl and laminar gypsum samples have been carefully cleaned by removing a few millimeter of sediment from the external surfaces with a knife. A more sophisticated cleaning procedure was applied to the 12 branching selenite samples, in order to fully remove weathered surfaces. The top few cm of these samples was removed with a hammer and chisel and subsequently rinsed with a solution of 10% HCl and Milli-Q water, respectively, in order to rinse off any possible contaminant. The branching selenite was then

broken into smaller pieces before drying. All samples were dried overnight in an oven (45 °C) and subsequently ground and homogenized with a mortar and a pestle. After being mixed with a few grams of extracted diatomaceous earth, the shales and laminar gypsum samples (~10 g dry weight) were extracted using accelerated solvent extraction (ASE), carried out by a DIONEX ASE 200 instrument, at 100 °C and a pressure of ~7*10^6 Pa, by using a mixture of dichloromethane (DCM) and methanol (MeOH) (9:1; v:v). The branching selenite samples (~175 g dry weight) were extracted via ultrasonication with the same mixture of DCM and MeOH (9:1; v:v). The ultrasonication procedure was repeated until the extracts became colorless. To establish quantification, internal standards were added before extraction of the samples, except for the 12 branching selenite samples, for which the internal standards were added to the total lipid extract (TLE). 5α-cholestane (100 mg/L) was used as the internal standard to quantify the long chain *n*-alkanes, while 1-nonadecanol (100.4 mg/L) and the dialkyl glycerol ether (DAGE) C_{18}/*n*-C_{18} (100.4 mg/L) functioned as the internal standards for the alcohol fraction. The amount of standard added to a sample was sometimes dependent on lithology. Shales, marls and branching selenite received 100 µl of 5α-cholestane, while laminar gypsum samples only received 50 µl of this internal standard. To the branching selenite samples, 400 µl of DAGE $C_{18:18}$ has been added, while 250 µl was added to the samples from the other lithologies. An equal amount of 1-nonadecanol (100 µl) was added to all samples. Peak area calculation of compounds of interest was established by using chromatographic equipment (see **chapter 6.3-6.5**), after which the internal standards were used to quantify these compounds. Abundances were normalized to the TOC content of each sample by using the formula:

$$Abundance\ compound\ x = \frac{Weight\ internal\ standard\ *\ Area\ compound\ x}{Area\ internal\ standard\ *\ TOC\ weight\ sample}.$$

After the extraction procedures, the TLEs were treated with activated elemental copper and DCM to remove elemental sulfur (S_8) and subsequently dried over anhydrous sodium sulfate (Na_2SO_4) to get rid of possible extant water. After these techniques, 40% of the TLE was then separated into asphaltene (DCM-soluble) and maltene (*n*-hexane-soluble) fractions. Maltene fractions were further separated into 4 different fractions of increasing polarity using aminopropyl-bonded silica gel column chromatography and a sequence of organic

solvents: 1) hydrocarbons using 4.5 ml of *n*-hexane, 2) ketones using 6 ml of *n*-hexane:DCM (3:1, v:v), 3) alcohols using 7 ml of DCM:acetone (9:1, v:v) and 4) carboxylic acids using 8 ml of DCM:formic acid (49:1, v:v). The ketones and carboxylic acids did not contain any compounds of interest and are not further discussed in this thesis.

6.3) Long-chain *n*-alkane analysis and quantification

The hydrocarbon fractions of all samples were re-dissolved in *n*-hexane prior to measuring on a gas chromatograph equipped with a flame ionization detector (GC-FID) in order to quantify the long-chain *n*-alkanes. The analysis was done on a Thermo Scientific TRACE 1310 GC, using a 30m Thermo Scientific TraceGOLD capillary column (TG-5MS, Diameter = 250 µm and film thickness 0.25 µm) and hydrogen as the carrier gas (kept at a constant flow pressure of 2ml/min). Long-chain *n*-alkane analysis started with an initial temperature of 50 °C (held for 3 min) and increased, with a rate of 25 °C/min to 230 °C (held for 3 min) and subsequently with a rate of 6 °C/min to 320 °C, at which it was held for 25 minutes.

Compound identification has been achieved by measurements with a GC coupled to a mass spectrometer (GC-MS), using a Thermo Scientific TRACE GC Ultra coupled to a Thermo Scientific DSQ II. Compounds were separated using a 30 m Agilent J&W capillary column (DB-5MS, Diameter = 250 µm and film thickness 0.25 µm) and helium as the carrier gas (kept at a constant flow pressure of 2 ml/min). The compound assignment of the different long chain *n*-alkanes was based on relative retention times and published mass spectral data.

An Agilent 6890 GC coupled to a Thermo Finnigan Combustion III inter to a Thermo Finnigan Delta Plus XL isotope ratio MS (GC-irms) has been used for the compound-specific isotope measurements of the long-chain *n*-alkanes. Samples were injected at 50 °C (held for 3 min), where after temperature was increased with 11 °C / min until a temperature of 325 °C. Carbon stable isotope values are expressed in standard δ-notation relative to Vienna Pee Dee Belemnite (VPDB) per mil (‰).

6.4) Lipid biomarker analysis and quantification of the alcohol fraction

The alcohol fractions were derivatized for 1 hour at 70 °C by adding a mixture of pyridine and N_2O-bis(trimethylsilyl)trifluoroacetamide (BSTFA) (1:1; v:v) to measure the alcohols as their TMS-derivatives (Birgel *et al.,* 2006). The analysis of the derivatized alcohol fractions was done on the day of silylation to prevent destabilization of the trimethylsilyl groups. The derivatized alcohol fractions of all samples were re-dissolved in *n*-hexane prior to analysis with a GC-FID (quantification) and GC-MS (identification), in order to investigate compounds of interest in the alcohol fraction, such as DGDs and sterols. For the analysis of the alcohol fraction, the same apparatus, columns and instrument conditions were used as described in section 5.3 for the analysis of the hydrocarbon fraction. The only difference in analytic conditions were related to the temperature program of the GCs, for which the final temperature of 320 °C was held for 35 instead of 25 minutes, in order to allow the complete removal of the alcohol fraction (more polar compounds) from the column. Compounds in the alcohol fraction were identified as their TMS derivatives by comparison with mass spectra from literature and/or the NIST mass spectral library.

6.5) GDGT analysis

Analysis of GDGT distribution in the alcohol fraction was done by using high-performance liquid chromatography – mass spectrometry (HPLC/MS) with a Varian MS Workstation 6.91 HPLC system coupled to a Varian 1200L triple quadrupole MS. GDGTs of each sample were directly measured from separated maltene fractions (5% TLE). Prior to injection in the HPLC, samples were re-dissolved in an appropriate amount of *n*-hexane and an internal standard (C_{46} GDGT; 12 mg/L) was added for quantification purposes (Huguet *et al.,* 2006). Samples were injected with a Varian Prostar Dynamax autosampler on a Grace Prevail 272 Cyano column (2.1 x 150 mm, 3 µm) and a guard column, which were held at a constant temperature of 30 °C. The method used for the GDGT analysis uses A (hexane) and B (hexane:isopropanol, 9:1; v:v) as the mobile phases. GDGT elution started with 97.5% A and 2.5% B, followed by a linear gradient to 8.5% B in the first 8 minutes, a linear gradient to 25% B between 8-35 minutes of run-time and then linearly to 100% B in the 5 minutes thereafter. The situation with 100% of solvent B was held for 8 minutes after which the

column was re-equilibrated for 12 minutes with the 97.5% A and 2.5% B solvent mixture. The solvent flow rate was kept constant (0.3 mL/min) during the 60-minute analysis.

GDGT identification was achieved with a triple quadrupole MS, equipped with positive ion atmospheric pressure chemical ionization (APCI) mode, capable of detecting the protonated ($[M + H]^+$) molecules of the various GDGTs. Conditions for the positive ion (APCI)-MS detection were: nebulizer pressure = 60 psi, vaporizer auxiliary gas temperature = 400 °C; pressure = 18 psi, drying gas temperature = 200 °C; pressure = 12 psi, capillary voltage = 90V, corona discharge current = 5 µA (~3.2 kV). The spectral range used to scan for iso- and brGDGTs was set at *m/z* 500-750 and *m/z* 950-1500. Identification of the anticipated GDGTs was achieved by selecting base peaks for each target mass *m/z*, including ions with ± 1.0 of the target mass *m/z*. Relative response factors were determined using a standard mixture containing synthetic archaeol (1,2-Di-*O*-phytanyl-*sn*-glycerol; CAS 99341-19-2), DAGE C18:18 (CAS 6076-38-6), DAGE C18:18-4ene (1,3-Dilinoleoyl-*rac*-glycerol; CAS 15818-46-9), and synthetic C46 GDGT (CAS 138456-87-8) in order to achieve appropriate quantification of the various GDGTs.

Chapter 7 – Results

7.1) Stratigraphy and facies description of the studied interval of the Pollenzo section

The studied interval of the Pollenzo section (**Fig. 15**) covers approximately 150 ka (5.87-5.72 Ma; Manzi *et al.,* 2013) and consists of seven lithological cycles that belong to the PLG unit, typically composed of shales alternated by different types of gypsum lithofacies (cycles Pg3 to Pg9, see **Fig. 16**). Cycles Pg1 and Pg2 were not sampled and studied for the purpose of this thesis, because these PLG cycles were already partly covered by Natalicchio *et al.* (2017; 2019), and by an unpublished dataset. The gypsum beds of the Pg1 and Pg2 cycles are composed of massive selenite, which is characterized by a very low organic matter content, unfavourable for biomarker analysis. Huge volumes of massive selenite (in the order of kilograms) would be necessary to collect an appropriate amount of lipids suitable for

biomarker analysis, making the analysis challenging. In contrast, the studied gypsum beds of Pg3 to Pg9 are made up of the branching selenite and laminar gypsum facies, which are richer in organic matter, especially the laminar gypsum (see **chapter 7.2**; **Table 1**).

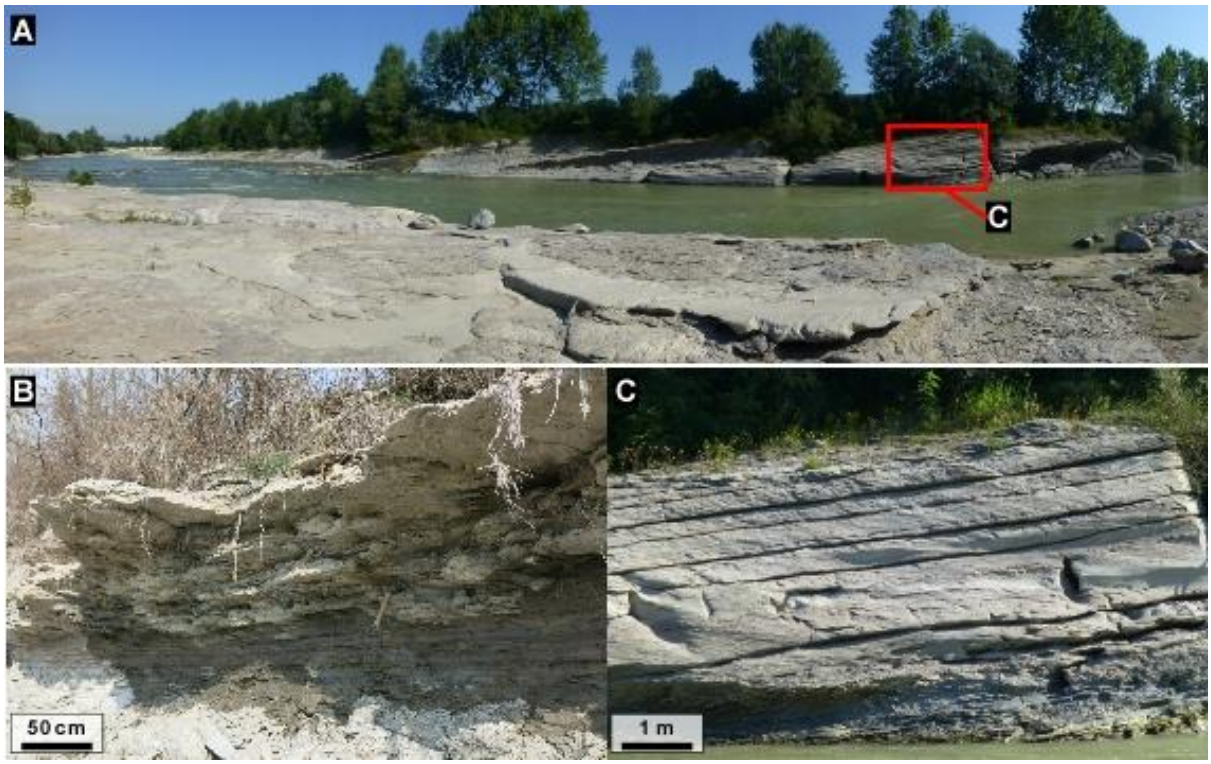

(Fig. 15): Outcrop views of the Pollenzo section. **A:** Overview of the Pollenzo section along the Tanaro river. **B:** Transition between the shale (bottom) and gypsum (top) hemicycles within a PLG cycle. **C:** Outcrop view of the Sturani key-bed (gypsum bed of the 6th PLG cycle).

The onset of the MSC is below the studied interval and placed within the Sant'Agata Fossili Marls at the base of the marls in cycle Pm5 (see **Fig. 16**; see Dela Pierre *et al.,* 2011 and Lozar *et al.,* 2018 for more details concerning the identification of the MSC onset). Thus, the seven studied PLG cycles (Pg3 to Pg9) are part of the first stage of the MSC and have been correlated to cycles PLG 6 to PLG 12 (see **Fig. 16**). The total thickness of the studied interval is 28.1 meters (Pg3 = 8.9 m, Pg4 = 2.8 m, Pg5 = 3.6 m, Pg6 = 2.85 m, Pg7 = 3.1 m, Pg8 = 4.35 m and Pg9 = 2.5 m).

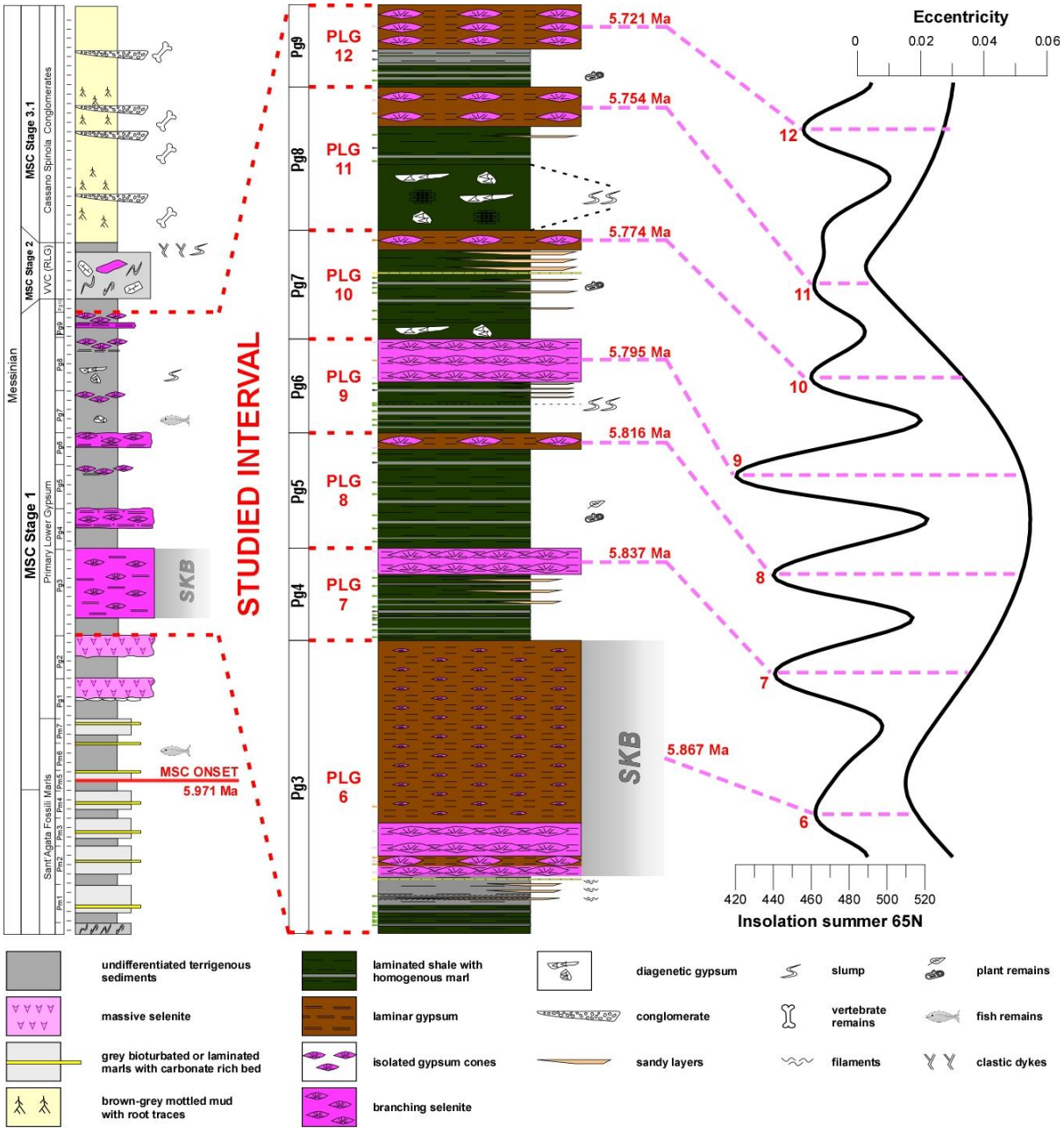

(Fig. 16): The stratigraphy of the Pollenzo section (**left**; modified from Dela Pierre *et al.*, 2011) and in more detail the studied interval of the Primary Lower Gypsum (PLG) unit (**middle**) that roughly covers 150 ka (~5.87-5.72 Ma). Ages represent gypsum midpoints correlated to precession maxima and eccentricity (**right**; sensu Manzi *et al.*, 2013; astronomical solution of Laskar *et al.*, 2004). SKB = Sturani key-bed; RLG = Resedimented Lower Gypsum; VVC = Valle Versa chaotic complex.

In more detail, each studied PLG cycle consists of an interval of fine-grained weakly consolidated sediments (referred to as the shale hemicycle), followed by a (more indurated) gypsum bed (referred to as the gypsum hemicycle) (**Fig. 15B**). The shale hemiycles are composed of layers of olive-green shales, which are finely laminated and irregularly interbedded with cm-thick light to dark grey silty marls and mm-thick sandy layers (**Fig.**

17A,C). Both the grey silty marls and thin sandy layers are interpreted as the product of flood events (Dela Pierre *et al.,* 2014). The lamination in the greenish shales is defined by an alternation of dark terrigenous layers and whitish layers rich in peloids and marine snow floccules (Natalicchio *et al.,* 2019). This lamination characterizes all shales throughout the studied intervals, although this lamination may be less defined in some specific intervals. The greyish layers of marl (1-10 cm thick) are homogenous (devoid of lamination) and more consolidated than the laminated shales. Some of the laminated shales may be normally graded (especially some of the thicker layers) and they are generally the most dominant lithology (thicker layers), although the homogenous marls may appear more frequently in the upper parts of the shale hemicycles. The thin layers of sand (1 mm to 2 cm thick) have a pale brown to rusty orange colour (**Fig. 17C**) and occur with different frequency and thickness throughout each shale hemicycle. Generally, the sandy layers are thinner and less frequent in the lower part, while they become more frequent and thicker in the upper parts of the shale hemicycles. In the uppermost part of the shale hemicycles, the laminated shales and homogenous marls start to contain mm-sized lenticular gypsum crystals, which gradually increase in number towards the appearance of the gypsum hemicycle. These transitional intervals are roughly between 15 and 40 cm thick. Occasionally, black/brownish silicate concretions identified as pieces of mineralized wood, as well as fossil leaves and the remains of fish (**Fig. 17D**), were encountered throughout the section. At the base of the shale hemicycles of cycles Pg7 and Pg8, meter-sized nodules composed of large limpid selenite crystals have been found, most likely of diagenetic origin. A slumped interval (2 m) occurs at the base of Pg8, deforming the laminated shales and impeding reliable sampling in this interval.

The gypsum beds exclusively consist of two distinctly different types of gypsum lithofacies: branching selenite and cumulate gypsum ("balatino" gypsum sensu Sturani, 1973) deposits, never observed in PLG cycles below the studied interval (Dela Pierre et al., 2011). The branching selenite facies, described by Lugli *et al.* (2010) and Dela Pierre *et al.* (2011), and discussed in **chapter 4.1**, appears to co-occur with cumulate gypsum deposits in the studied interval of the Pollenzo section (**Fig. 17B**). From here on, these cumulate gypsum deposits are referred to as the 'laminar gypsum' facies, named after its laminated appearance in the field (**Fig. 17F**). Laminar gypsum consists of alternating gypsum-rich and clay-rich laminae,

locally forming thick intervals that can be followed laterally for tens of meters. These intervals can be subdivided in cm-thick (up to ~50 cm) packets, separated by thicker terrigenous laminae. Each packet consists of numerous gypsum-rich laminae ranging in thickness from ~100 µm to 2 mm, separated by thinner clay layers (**Fig. 17F**). The gypsum-rich laminae are composed of a sutured mosaic of interlocked acicular (needle-like) crystals, ranging in size from a few µm up to 1 mm. Sedimentary structures related to tractive bottom currents (e.g. cross lamination) or oscillatory flows (e.g. hummocky cross stratification) have not been observed in the laminar gypsum, hinting towards deposition under relatively low hydrodynamic conditions. Plant remains and fossils of leaves have been frequently encountered in the laminar gypsum facies. Sturani (1973) has reported the remains of dragonfly larvae in this facies as well. Intervals of laminar gypsum may be cross-cut by the branching selenite facies and individual laminae of the laminar gypsum can be followed within the 'branches' of the branching selenite, indicating that these two facies were formed at the same time (**Fig. 17E**). The branching selenite can appear as isolated cones in a matrix of laminar gypsum, or grouped to form larger, meter-sized structures, a feature that is especially pronounced in the gypsum interval of cycle Pg3.

The lowest cycle of the studied interval (Pg3) is remarkable for several reasons. The shale hemicycle of this cycle starts with the usual greenish organic-rich shales and is succeeded by an interval of laminated marls (similar to Pm6-7 and Pg1; sensu Natalicchio *et al.,* 2019). These laminated marls are defined by an alternation of sub-mm thick grey and whitish laminae. While the grey laminae are mostly composed of silt-sized terrigenous material, the whitish laminae are rich in filamentous microfossils. These filaments are up to 2 mm long and 60–80 µm across, highly fluorescent when exposed to UV light, and possibly correspond to the remains of colourless sulfide-oxidizing bacteria (Dela Pierre *et al.,* 2012; 2014; 2015). These filaments, as well as the laminated marls, do not occur in the studied PLG cycles that succeed Pg3. Secondly, a relatively thick layer of gypsum (~7 m) was deposited on top of the laminated marl interval, which corresponds to the so-called 'Sturani key-bed' (SKB; Dela Pierre *et al.,* 2011; Caselle *et al.,* 2019). The thickness of the SKB is remarkable since it is at least five times thicker than the upper gypsum beds, which are between 60 to 135 cm thick.

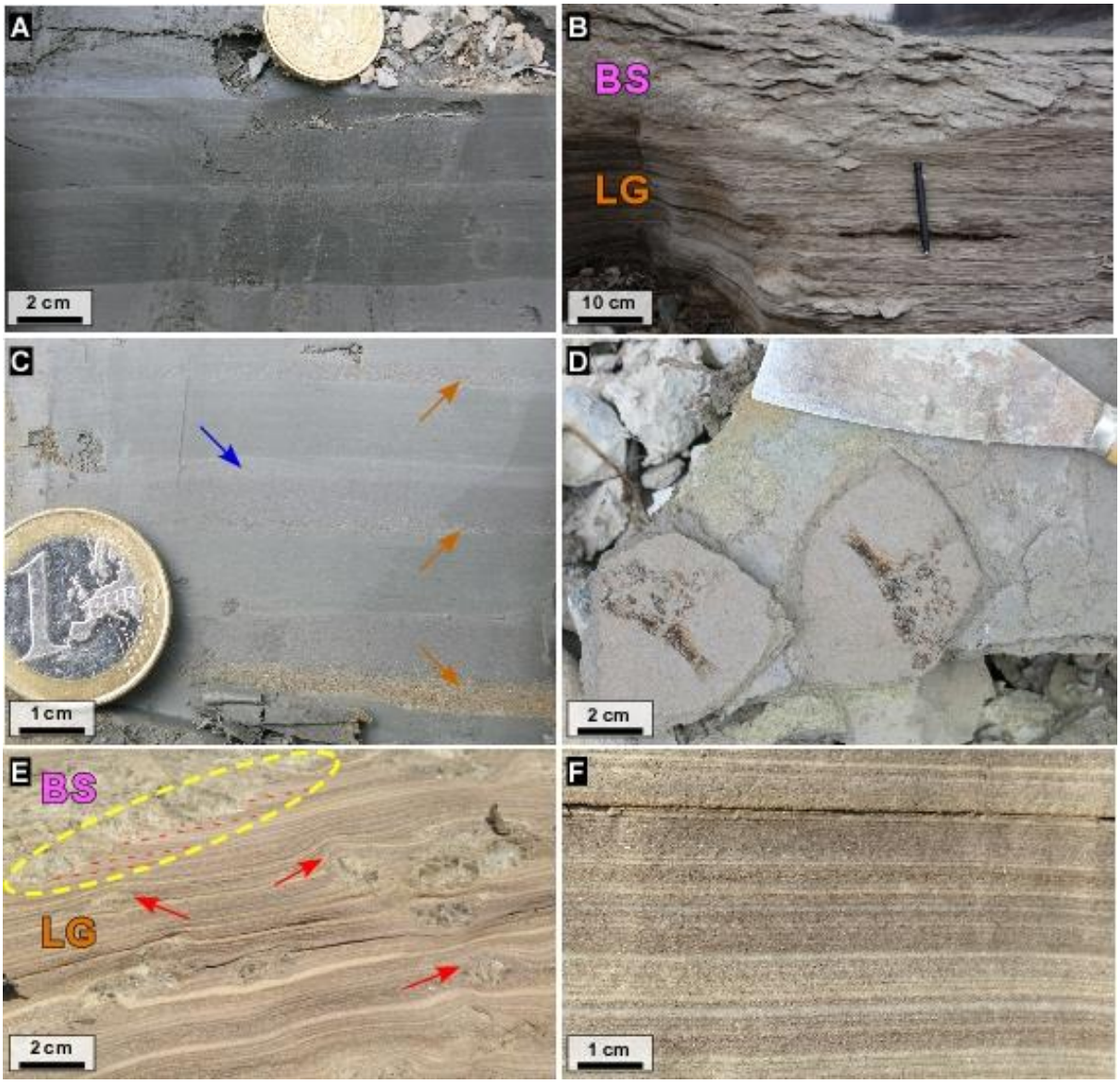

(Fig. 17): Sampled lithologies of the Pollenzo section **A:** Alternation of olive-green laminated shale (thick middle layer) and light grey homogenous marl (adjacent to the laminated shale). **B:** The interrelationship between laminar gypsum and branching selenite. Note pen for scale. **C:** Close-up of laminated shale, showing details in the lamination. Note the layer of homogenous marl (blue arrow) and sandy layers (orange arrows) **D:** Fish remains in laminated shale. **E:** Close-up of the contact between laminar gypsum and branching selenite. Note how the branching selenite cross-cuts the laminae of the laminar gypsum (yellow dotted oval). The red dotted lines indicate the orientation of the laminae that are cross-cut by the branching selenite. Red arrows indicate locations where the laminar gypsum 'drapes' the branching selenite. **F:** Close-up of laminar gypsum. Note the alternation of gypsum-rich and gypsum-poor layers. BS = branching selenite. LG = laminar gypsum.

The SKB is a distinct marker bed which can be traced within the Piedmont basin, marking a sharp lithofacies change in the PLG unit. This lithofacies change concerns the simultaneous appearance of the branching selenite and laminar gypsum in the 6th PLG cycle, never

observed in lower PLG cycles (Dela Pierre *et al.,* 2011). The branching selenite has been suggested to have formed synchronously in many western Mediterranean sub-basins starting from the 6th PLG cycle (Lugli *et al.,* 2010). This agrees with the correlation of cycle Pg3 (and the SKB) with PLG 6 (see **Fig. 16**), indicating that the studied interval (Pg3-Pg9) indeed corresponds to PLG 6 until PLG 12.

7.2) Total organic carbon and calcium carbonate content

The TOC content in the Pollenzo section roughly follows lithological cyclicity and ranges between 0.1 and 3.3% (**Fig. 18**). The highest average TOC content (see **Table 1**) is found in the laminated shales (average = 2.4%), with TOC values occasionally exceeding 3%. Lower TOC content is found in the homogenous marls (average = 1.5%) and the laminar gypsum (average = 1.1%). The branching selenite samples yielded the lowest TOC content, with samples containing no more than 0.2% TOC on average.

TABLE 1	Shale hemiycle		Gypsum hemicycle	
	Laminated shales	Homogenous marls	Branching selenite	Laminar gypsum
TOC (wt%)	2.4	1.5	0.2	1.1
$CaCO_3$ (%)	15.1	15.3	2.9	4.5
n-alkane abundance (µg/g TOC)				
C_{27} + C_{29} + C_{31} n-alkanes	130.7	129.0	32.4	124.1
n-alkane ratios				
CPI	6.8	7.6	6.5	8.6
ACL	29.3	29.3	29.5	29.2
No. of samples	30	6	12	5

(Table 1): Average TOC and $CaCO_3$ content, *n*-alkane abundance and *n*-alkane based ratios (CPI and ACL) per lithology of all samples (n = 53) in the studied interval of the Pollenzo section.

The $CaCO_3$ content in the Pollenzo section fluctuates between 0.48 and 43.69% (**Fig. 18**). Gypsum samples have relatively low $CaCO_3$ content (<7.6%) in comparison with the fine-grained sediments. The average $CaCO_3$ content (see **Table 1**) of branching selenite is slightly

lower (average = 2.9%) than that of laminar gypsum (average = 4.5%). The laminated shales and homogenous marls have an average $CaCO_3$ content of approximately 15.1 and 15.3%, respectively. The laminated shales in the Pollenzo section occasionally exceed a $CaCO_3$ content of 30%.

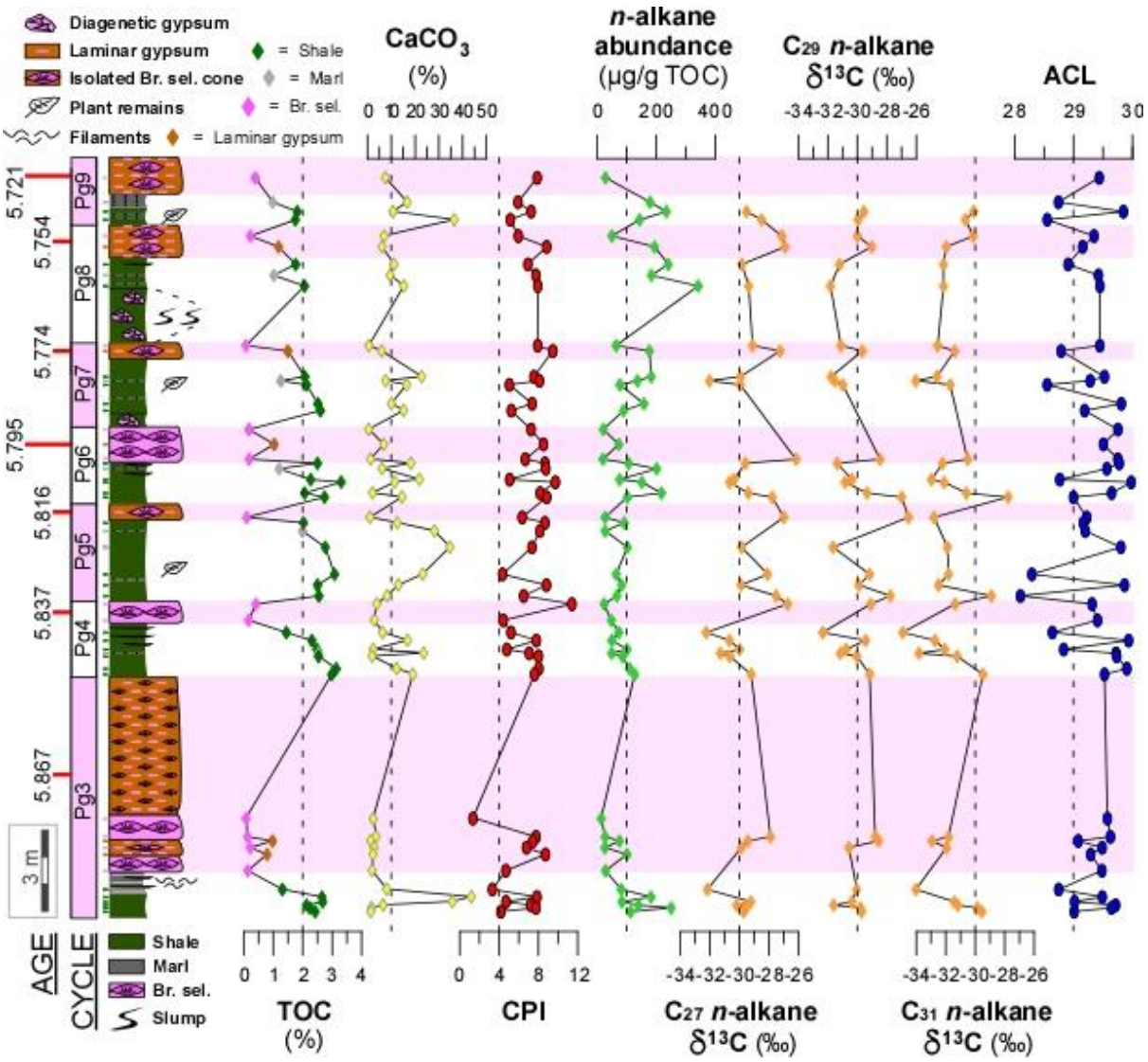

(Fig. 18): Graphs indicating from left to right: total organic carbon (TOC) content, calcium carbonate ($CaCO_3$) content, Carbon Preference Index (CPI; Bray and Evans, 1961), summed abundance of C_{27}-, C_{29}- and C_{31} *n*-alkanes (µg/g TOC), compound-specific carbon stable isotope values ($\delta^{13}C$) of C_{27}-, C_{29}- and C_{31} n-alkanes and the Average Chain Length (ACL; Poynter and Eglinton, 1990) of the Pollenzo section. Horizontal pink bars indicate gypsum intervals and the ages (Ma) next to the stratigraphic column represent gypsum midpoints (*sensu* Manzi *et al.*, 2013). Carbon isotope values are reported as per mil (‰) relative to the Peedee belemnite (PDB) standard. Br. sel. = branching selenite. Vertical dotted lines are reference lines.

7.3) Long-chain *n*-alkane results

7.3.1) Long-chain *n*-alkane abundance, Carbon Preference Index and Average Chain Length

The most abundant *n*-alkanes in the analysed samples are the C_{25}-C_{33} long-chain *n*-alkanes, with a predominance of the odd chain lengths, in particular the C_{27}, C_{29} and C_{31} long-chain *n*-alkanes. From here on, the term '*n*-alkane abundance' refers to the summed abundance of the C_{27}-, C_{29}- and C_{31} long-chain *n*-alkanes. Although the *n*-alkane abundance varies significantly between individual samples (from 19 to 324 µg/g TOC), it roughly follows lithological cyclicity and mirrors the trend of the TOC content (**Fig. 18**). The average *n*-alkane abundance (see **Table 1**) is highest in the laminated shales (average = 131 µg/g TOC), followed by homogeneous marls (average = 129 µg/g TOC) and the laminar gypsum (average = 124 µg/g TOC), while much lower content is found in the branching selenite (average = 32 µg/g TOC). Focussing on the shale hemicycle, maximum *n*-alkane abundance in a single sample has been measured in cycle Pg8 (324 µg/g TOC), while relatively low values (>50 µg/g TOC) have been measured in laminated shales and homogenous marls from cycle Pg4 and Pg5. This interval with relatively low *n*-alkane abundance in cycles Pg4 (average = 84 µg/g TOC) and cycle Pg5 (average = 72 µg/g TOC) is followed by a trend of increasing *n*-alkane contents in cycle Pg6-Pg9, reaching abundances that are three or four times higher in cycle Pg8 (average = 255 µg/g TOC) and Pg9 (average = 185 µg/g TOC).

The CPI of the analysed samples (**Fig. 18**) roughly ranges between 4 and 9 (average = ~7), with only few samples plotting outside this range of CPI values. Highest average CPI values (see **Table 1**) are calculated for the laminar gypsum samples (average = ~8.6), followed by the homogenous marls (average = ~7.6), while the lowest values are calculated for the laminated shales (average = ~6.8) and the branching selenite samples (average = ~6.5). No specific trends in CPI values are visible across the section.

The ACL of the analysed samples (**Fig. 18**) varies between 28.1 and 30.0, with an average value of 29.3. Looking at the different lithologies, there appears to be little difference. Both the laminated shales and the homogenous marls show average ACL values (~29.3), while the branching selenite shows slightly higher ACL values (average = ~29.5) and the laminar

gypsum shows slightly lower ACL values (average = ~29.2). Apart from these slight differences that can be attributed to lithology (see also **Table 1**), no trends are apparent in the ACL values.

7.3.2) Carbon stable isotopes of long-chain *n*-alkanes

Compound specific carbon stable isotope analysis of the main odd *n*-alkanes (C_{27}, C_{29} and C_{31}) shows a wide range of $\delta^{13}C$ values, between -34.9‰ and -26.2‰ (**Fig. 18**). At the scale of a single cycle, the three individual $\delta^{13}C$ records independently indicate shifts from lower values in shales, to higher values in gypsum samples (**Fig. 18**). In general, gypsum samples show higher $\delta^{13}C$ values, while laminated shales and homogenous marls tend to have lower $\delta^{13}C$ values. Exceptions to this observation concern the shales deposited immediately on top of the gypsum bed (i.e. the oldest shales of a younger PLG cycle). It appears that the *n*-alkanes in these shales have $\delta^{13}C$ values that are significantly higher than n-alkanes extracted from overlying shales in the same cycle. In fact, the $\delta^{13}C$ values are similar to (or even higher than) the $\delta^{13}C$ values of *n*-alkanes from the underlying gypsum, indicating that the $\delta^{13}C$ excursions are unrelated to lithology. The isotope excursions from lower to higher $\delta^{13}C$ values are observed in each of the fully analysed cycles (Pg3 to Pg8), with a magnitude that varies between ~1 and ~6‰ (**Fig. 18**). The $\delta^{13}C$ excursions are most prominent in cycle Pg3, Pg4 and Pg5, with isotope shifts between shales and gypsum of roughly ~5, ~4 and ~3‰, respectively (see **Fig. 18**).

7.4) Lipid biomarkers in the alcohol fraction

Substantial amounts of lipid biomarkers within the alcohol fraction have been detected in samples from the studied interval of the Pollenzo section. The dominant lipid groups within the alcohol fraction are isoprenoid alcohols (predominated by GDGTs and DGDs), brGDGTs and sterols. GDGTs and brGDGTs were analyzed by LC-MS, whereas the DGDs, sterols and other lipids of interest were measured by GC-FID (quantification) and GC-MS (identification). Some of the lipids in the alcohol fraction are particularly interesting within the scope of this thesis, among which are archaeol, extended archaeol, dinosterol, C_{30} 1,15-diol, tetrahymanol and the tentatively identified 4-methyl-ergosta-14-en-ol and ergosta-7-en-ol. Whereas most of these lipids have proven to be useful as molecular proxies and/or have diagnostic value, 4-methyl-ergosta-14-en-ol and ergosta-7-en-ol are relatively unknown and

poorly described in the scientific literature (see **section 7.4.6**). Therefore, these compounds are sometimes referred to as the "enigmatic sterols" throughout this thesis, always appearing conjointly if they are detected in the Pollenzo samples. Concerning the lipid biomarker signatures of the analyzed alcohol fractions, it appears that two types of signatures are dominant throughout the studied interval of the Pollenzo section (**Fig. 19**). Typically, the alcohol-fraction-chromatograms of laminated shales are dominated by a so-called "sterol hump" in which dinosterol and the C_{30} 1,15-diol are often the most abundant lipids (see **Fig. 19**), whereas gypsum samples are predominated by archaeol (and always associated with extended archaeol), as well as by the enigmatic sterols.

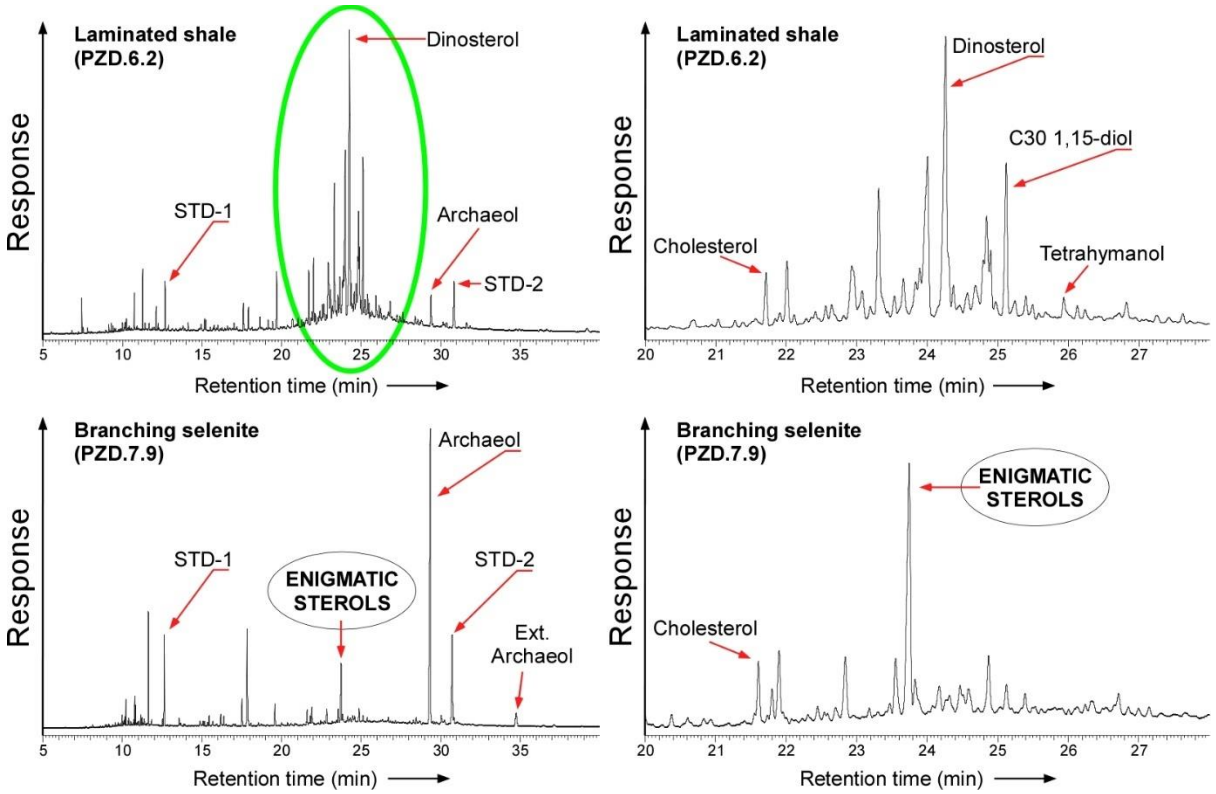

(Fig. 19): GC-FID chromatograms of the alcohol fraction concerning a typical laminated shale and a typical gypsum sample. Note that a typical laminated shale is characterized by a well pronounced sterol hump (green circle), often dominated by dinosterol and the C_{30} 1,15-diol. On the other hand, typical gypsum samples are dominated by archaeol and in lesser amounts the enigmatic sterols (4-methyl-ergosta-14-en-ol and ergosta-7-en-ol) and extended archaeol. Ext. archaeol = extended archaeol, whereas STD-1 (1-nonadecanol) and STD-2 (DAGE $C_{18:18}$) refer to the internal standards that were used for quantification.

Although the lipid signatures of the alcohol fractions depicted in **Fig. 19** are frequently encountered throughout the Pollenzo section, they are not exclusive to a specific lithofacies. For example, among the analyzed laminated shales are also samples that are dominated by

archaeol and the enigmatic sterols, whereas tetrahymanol has also been detected in laminated gypsum samples. In fact, the distribution of dominant lipids in the alcohol fraction (and their related environmental proxies) is highly variable across the Pollenzo section (see **Fig. 20**). However, a pronounced sterol hump and the detection of dinosterol and the C_{30} 1,15-diol, appears to be restricted to samples from the shale hemicycle, whereas the enigmatic sterols on the one hand, and dinosterol on the other hand, never co-occur in any of the analyzed samples.

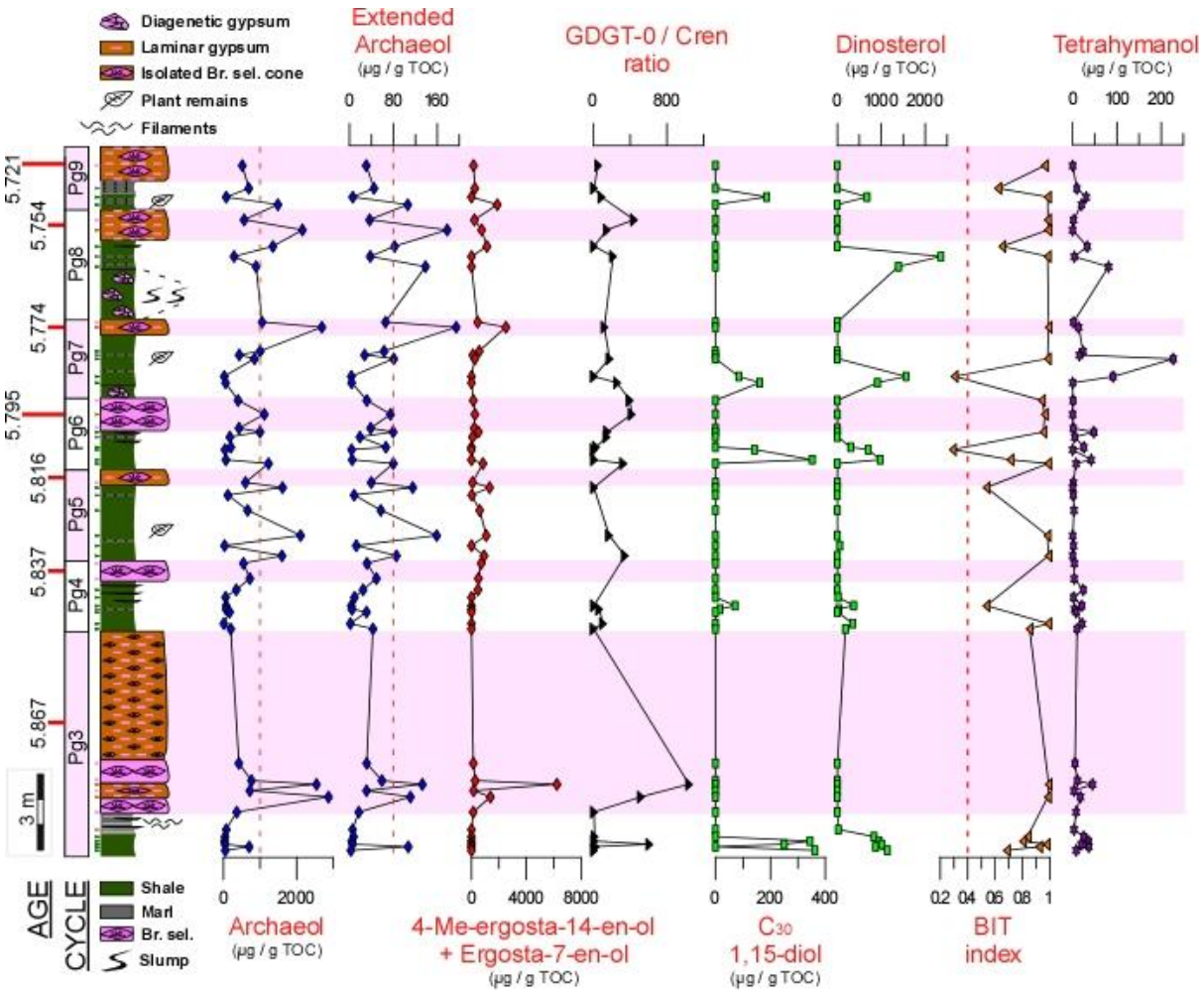

(Fig. 20): Graphs indicating the abundance of the main lipid biomarkers from the alcohol fraction and values for paleoenvironmental proxies across the Pollenzo section. From left to right: archaeol ($C_{20,20}$) abundance (µg/g TOC), extended archaeol ($C_{20,25}$) abundance (µg/g TOC), summed abundance of 4-methyl-ergosta-14-en-ol and ergosta-7-en-ol (µg/g TOC), GDGT-0/crenarchaeol ratio (Turich *et al.,* 2007), C_{30} 1,15-diol abundance (µg/g TOC), dinosterol abundance (µg/g TOC), the Branched and Isoprenoid Tetraether (BIT) index (Hopmans *et al.,* 2004) and tetrahymanol abundance (µg/g TOC). Horizontal pink bars indicate gypsum intervals and the ages (Ma) next to the stratigraphic column represent gypsum midpoints *sensu* Manzi *et al.,* (2013). Br. sel. = branching selenite. Vertical red dotted lines are reference lines.

7.4.1) Distribution of DGDs

Substantial amounts of DGDs are detected in the Pollenzo samples, in particular of archaeol and extended archaeol (see **Fig. 8** for their chemical structures and **Fig. 20** for their distribution). In fact, archaeol is the most abundant isoprenoid alcohol in the studied interval of the Pollenzo section, often even more abundant than the sum of total isoGDGTs (see Supplementary Information; **Table 2**). Archaeol abundances highly vary across the Pollenzo section, ranging from ~10 μg/g TOC up to ~2.87 mg/g TOC, with an average of ~687 μg/g TOC (see **Fig. 20** and **Table 2**). Extended archaeol is less abundant in the Pollenzo section than archaeol; abundances range from ~2 up to ~194 μg/g TOC, with an average of ~50 μg/g TOC (see **Fig. 20**). As can be seen in **Fig. 20**, archaeol and extended archaeol abundances follow a similar pattern across the Pollenzo section. High DGD abundances (archaeol >1 mg/g TOC and extended archaeol >80 μg/g TOC; see red dotted lines in **Fig. 20**) typify samples from gypsum intervals, or from shales adjacent to these intervals. An exception to this observation is cycle Pg5 (PLG 8), in which a high DGD abundance is also detected within the shale hemicycle.

7.4.2) Distribution of isoprenoid GDGTs and the GDGT-0/crenarchaeol ratio

In the studied interval of the Pollenzo section, all common isoGDGTs (GDGT 0-4; Koga *et al.*, 1993) have been detected, as well as crenarchaeol and its stereoisomer (see **Fig. 7** for their chemical structures and **Fig. 21** for their distribution). However, the distribution of these isoGDGTs is highly variable across the section, with 10 out of 53 samples devoid of isoGDGTs, while on the other hand, 12 out of 53 samples exceed a total isoGDGT abundance of >100 μg/g TOC (see **Fig. 23** and Supplementary Information; **Table 3**). Interestingly, the highest total isoGDGT abundances (>280 μg/g TOC) have been detected in gypsum samples, both in branching selenite (PZD.6.10, PZD.8.5 and PZD.9.5), as well as in laminar gypsum (PZD.3.11 and PZD.3.13) samples. The meaning of these sample codes is explained in the Supplementary Information. The absence of isoGDGTs in some samples from the Pollenzo section appears to be unrelated to lithology; all lithologies have samples amongst them that are devoid of isoGDGTs, with the exception of laminar gypsum.

IsoGDGTs are detected in most of the Pollenzo samples (43 out of 53 samples). GDGT-0 is evidently the most abundant isoGDGT, comprising at least ~44% of the total isoGDGT

abundance (see **Fig. 22**; **Table 3**). Sample PZD.4.1 is the sole exception to this observation, since GDGT-1 is the predominant isoGDGT in this sample. However, in 27 out of 53 samples, GDGT-0 comprises >90% of the total isoGDGT abundance (see **Fig. 22**; **Table 3**), with a maximum of ~1.0 mg/g TOC measured in sample PZD.8.5.

Another common isoGDGT across the Pollenzo section is crenarchaeol, which is detected in 34 out of 53 samples. In 10 out of these 34 samples, crenarchaeol comprises between ~13.5-25.5% of the total isoGDGT abundance (see **Fig. 22**; **Table 3**), with a maximum of ~31 µg/g TOC in sample PZD.8.3. In the other 24 samples, the total crenarchaeol abundance is ≤7.8% of the total isoGDGT abundance, of which 23 samples are ≤4.3%. High relative abundances of crenarchaeol (≤13.5%) are mostly found in laminated shale samples (see **Fig. 22**; **Table 3**), although high abundances of crenarchaeol have also been found in one branching selenite sample (PZD.3.10) and one homogenous marl sample (PZD.9.3). The crenarchaeol stereoisomer is detected in the same sample where crenarchaeol is also detected, unless the absolute abundance of crenarchaeol is below 0.3 µg/g TOC. For these samples, the chromatographic equipment is presumably not sensitive enough in order to detect the crenarchaeol isomer, since the abundance of the crenarchaeol isomer is at least an order of magnitude lower in most samples (see **Fig. 21**; **Table 3**).

GDGTs 1-4, as well as the crenarchaeol isomer, are much less abundant across the Pollenzo section than GDGT-0 and crenarchaeol (see **Fig. 21**; **Table 3**), with 16 out of 53 samples being devoid of these GDGTs. The assemblage of GDGTs 1-4 + crenarchaeol isomer usually comprises ≤11% of the total isoGDGT abundance (26 out of 37 samples), although in 10 out of 37 samples this isoGDGT assemblage makes up significantly higher percentages (~16-35%) of the total isoGDGT abundance (see **Table 3**). Samples with a relative high amount of GDGT 2-3 + crenarchaeol isomer also tend to have relatively high percentages of crenarchaeol. Among these less dominant isoGDGTs, the relative abundance of GDGT-1 (≤9.7%) and GDGT-2 (≤12.4%) tends to be higher than that of GDGT-3 (≤3.0%) and the crenarchaeol stereoisomer (≤2.9%).

Interestingly, when the abundance of crenarchaeol (and its isomer) peaks in the Pollenzo samples, GDGT 2-3 also appear to be more abundant (see **Fig. 21**). Moreover, the abundances of GDGT-2 and GDGT-3 largely mirror the distributional trend of crenarchaeol, whereas the abundance of GDGT-1 appears to follow the distributional trend of GDGT-0

(**Fig. 21**). Among GDGT 1-3 in the Pollenzo samples, GDGT-1 (average = ~4.5 µg/g TOC) is more abundant than GDGT-2 (average = ~3.1 µg/g TOC) and GDGT-3 (average = ~1.0 µg/g TOC). GDGT-4 is rarely detected in the Pollenzo samples, with the exception of two samples; a branching selenite (PZD.3.10; 0.07 µg/g TOC) and a laminated shale (PZD.7.2; 13.5 µg/g TOC). Sample PZD.4.1 appears to be an odd sample with respect to the general isoGDGT observations, since about ~91% of the total isoGDGT abundance of this sample consists of GDGT-1, and relatively low proportions of GDGT-0 and crenarchaeol are detected.

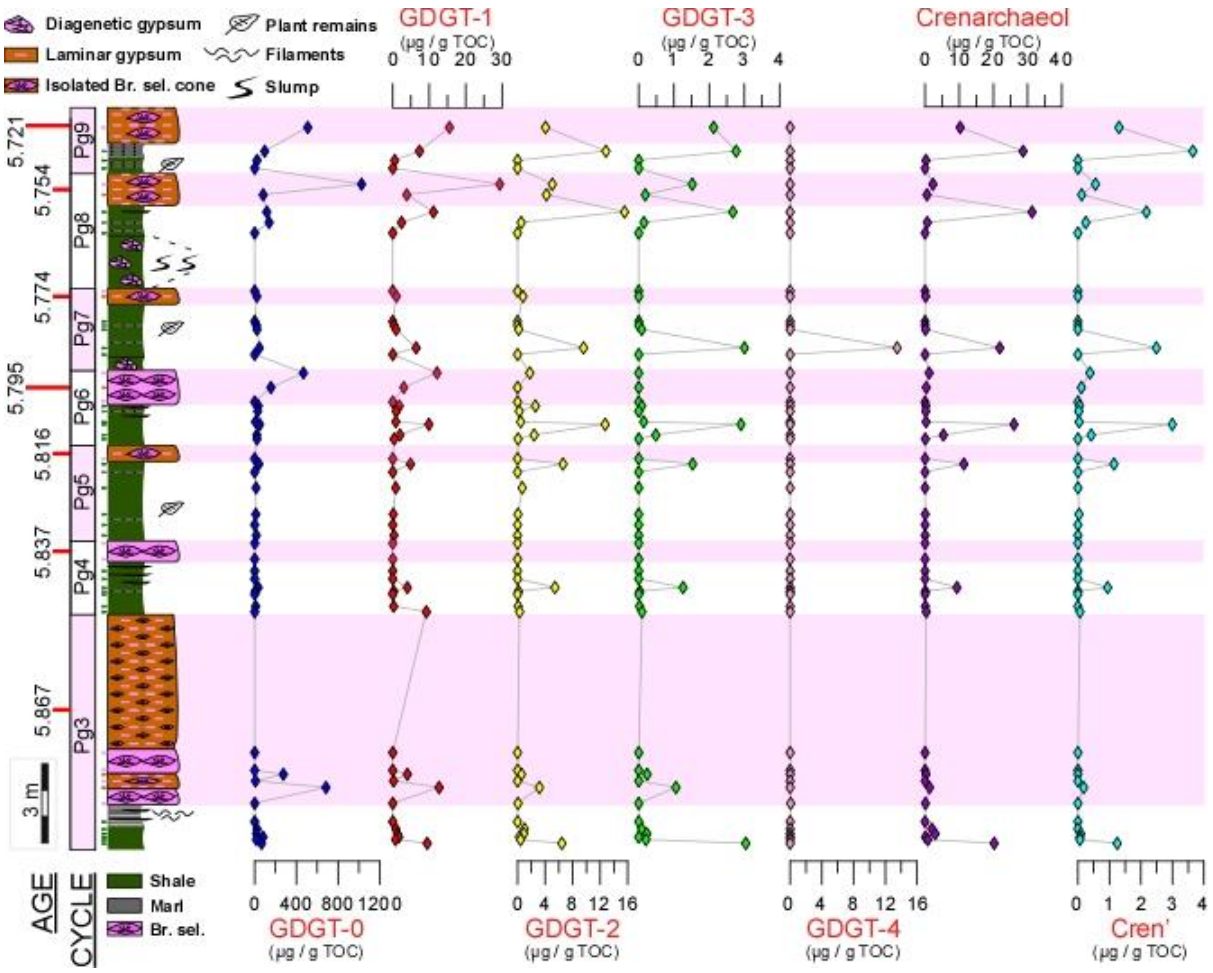

(Fig. 21): Graphs indicating the abundance (µg/g TOC) of individual isoprenoid glycerol dialkyl glycerol diethers (isoGDGTs) plotted against the Pollenzo stratigraphy. Horizontal pink bars indicate gypsum intervals and the ages (Ma) next to the stratigraphic column represent gypsum midpoints (*sensu* Manzi *et al.*, 2013). Br. sel. = branching selenite; Cren' = crenarchaeol isomer.

The GDGT-0/crenarchaeol ratio varies tremendously across the studied interval of the Pollenzo section, with values between 0.2 and 1043.5 (**Fig. 20**; **Table 3**). From the 34 out of 53 samples in which the GDGT-0/crenarchaeol ratio could be determined, 10 samples have

a ratio ≤3.8, from which only 3 samples have a ratio ≤2.0. The other 24 samples have GDGT-0/crenarchaeol ratios ≤5.6. These ratios show that the GDGT-0 abundance is often two or even three orders of magnitude higher than the crenarchaeol abundance, demonstrating that GDGT-0 is the predominant isoGDGT in the studied interval of the Pollenzo section.

7.4.3) Distribution of branched GDGTs

BrGDGTs have been detected in the Pollenzo samples, in particular brGDGT-I, brGDGT-II and brGDGT-III (see **Fig. 7** for their structures), although their occurrence and summed abundance varies highly across the Pollenzo section (Supplementary information, **Table 4**). In the 31 out of 53 samples where brGDGTs are detected, the summed abundance of brGDGT-I, brGDGT-II and brGDGT-III varies between 0.6-257.3 μg/g TOC, with an average of 29.9 μg/g TOC. The trends in abundance of the individual brGDGTs mirror one another, while their relative abundances fluctuate roughly between 25-40%, with brGDGT-I usually being less abundant than brGDGT-II and brGDGT-III (see **Table 4**). The absence of brGDGTs in the other 22 samples from the Pollenzo section seems unrelated to lithology. Similar to the absence of isoGDGTs, each lithology analysed in the Pollenzo section has samples that are barren of brGDGTs, with the exception of laminar gypsum. Interestingly, the highest summed abundances of brGDGTs are detected in gypsum samples that also have the highest absolute abundances of isoGDGTs (e.g. PZD.3.11, PZD.8.5 and PZD.9.5, see **Fig. 23** and **Table 2**).

The BIT index, a proxy that represents the relative abundances between brGDGTs and crenarchaeol (Hopmans *et al.,* 2004; see **section 2.3.2**), could be determined in 29 out of 53 samples from the Pollenzo section and varies between 0.99 and 0.29, with an average of 0.84 (see **Fig. 20** and **Table 2**). Either brGDGTs or crenarchaeol (or both) were not detected in the other 24 samples, rendering it impossible to determine BIT index in these samples. Out of the 29 samples for which BIT values could be determined, only two of them have BIT values <0.4 (PZD.6.4 and PZD.7.2, see **Fig. 20**), 6 of them have BIT values between 0.5 and 0.7, while the remaining 21 samples have BIT values ≥0.8. This indicates that only two samples (PZD.6.4 and PZD.7.2) can be considered as samples with a dominant marine signal (Weijers *et al.,* 2006), whereas all other samples have a high terrestrial influence.

7.4.4) Relative proportion of DGDs, isoGDGTs and brGDGTs

The predominant archaeal lipids in the studied interval of the Pollenzo section are unequivocally the DGDs. When the relative abundances between DGDs and isoGDGTs are compared to one another, the relative abundance of isoGDGTs is usually significantly lower (<5%; 32 out of 53 samples; **Fig. 22**). Samples with higher relative abundances of isoGDGTs (>5%; 21 out of 53 samples) have been detected in each of the analysed PLG cycles; with the exception of cycle Pg5. The isoGDGTs are more dominant (i.e. >50%) than the DGDs in 6 out of these 21 samples. Both cyclicity and lithology do not appear to be a factor that can be correlated to higher relative abundances of isoGDGTs, as all four sampled lithologies are among the samples with a relatively high isoGDGT abundance (>5%). Moreover, both laminated shales and branching selenite samples are among the 6 samples in which isoGDGTs predominate the DGDs.

In **Fig. 23**, both the absolute and relative abundances of DGDs, isoGDGTs and brGDGTs are compared with one another (see also Supplementary Information; **Table 5**). As already mentioned in **section 7.4.3**, it appears that peaks in the absolute abundance of brGDGTs can be correlated with higher abundances of isoGDGTs (**Fig. 23**). Moreover, when compared to the abundance of DGDs, it seems that a higher relative proportion of isoGDGTs often correlates with a higher relative proportion of brGDGTs. Apparently, if the relative abundance of isoGDGTs in the Pollenzo samples exceeds ~16%, the relative abundance of brGDGTs often exceeds ~5%. This observation holds true for 13 out of 16 samples that have a relatively high proportion of isoGDGTs (≥16.2%; **Table 5**).

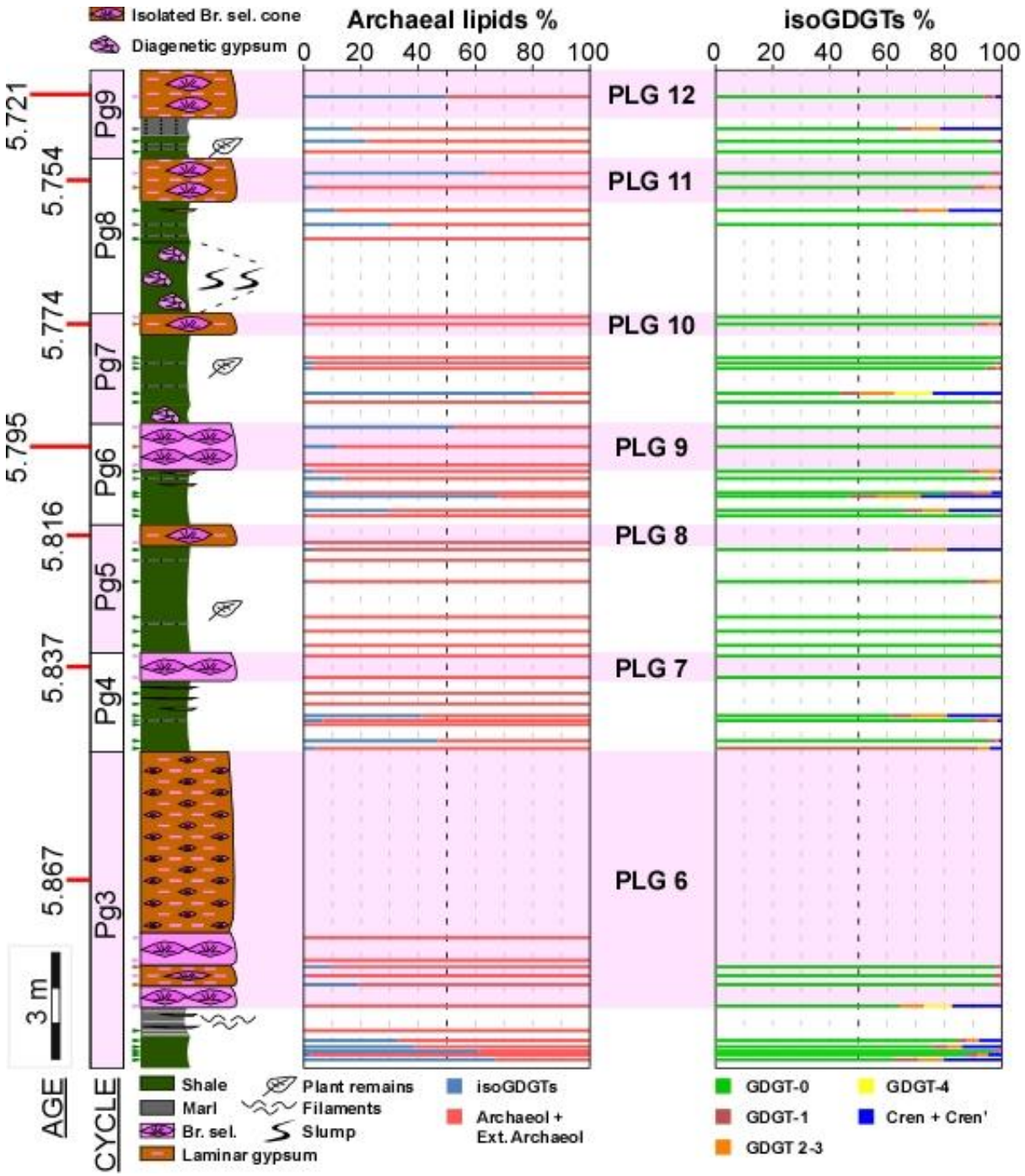

(Fig. 22): Figure indicating the relative abundances (%) of archaeal lipids (**left**) and isoprenoid glycerol dialkyl glycerol diethers (isoGDGTs) (**right**) across the studied interval of the Pollenzo section. Horizontal pink bars indicate gypsum intervals and the ages (Ma) next to the stratigraphic column represent gypsum midpoints *sensu* Manzi *et al.,* (2013). Br. sel. = branching selenite. Cren = crenarchaeol. Cren' = crenarchaeol isomer. Ext. archaeol = extended archaeol ($C_{20,20}$). PLG = Primary Lower Gypsum.

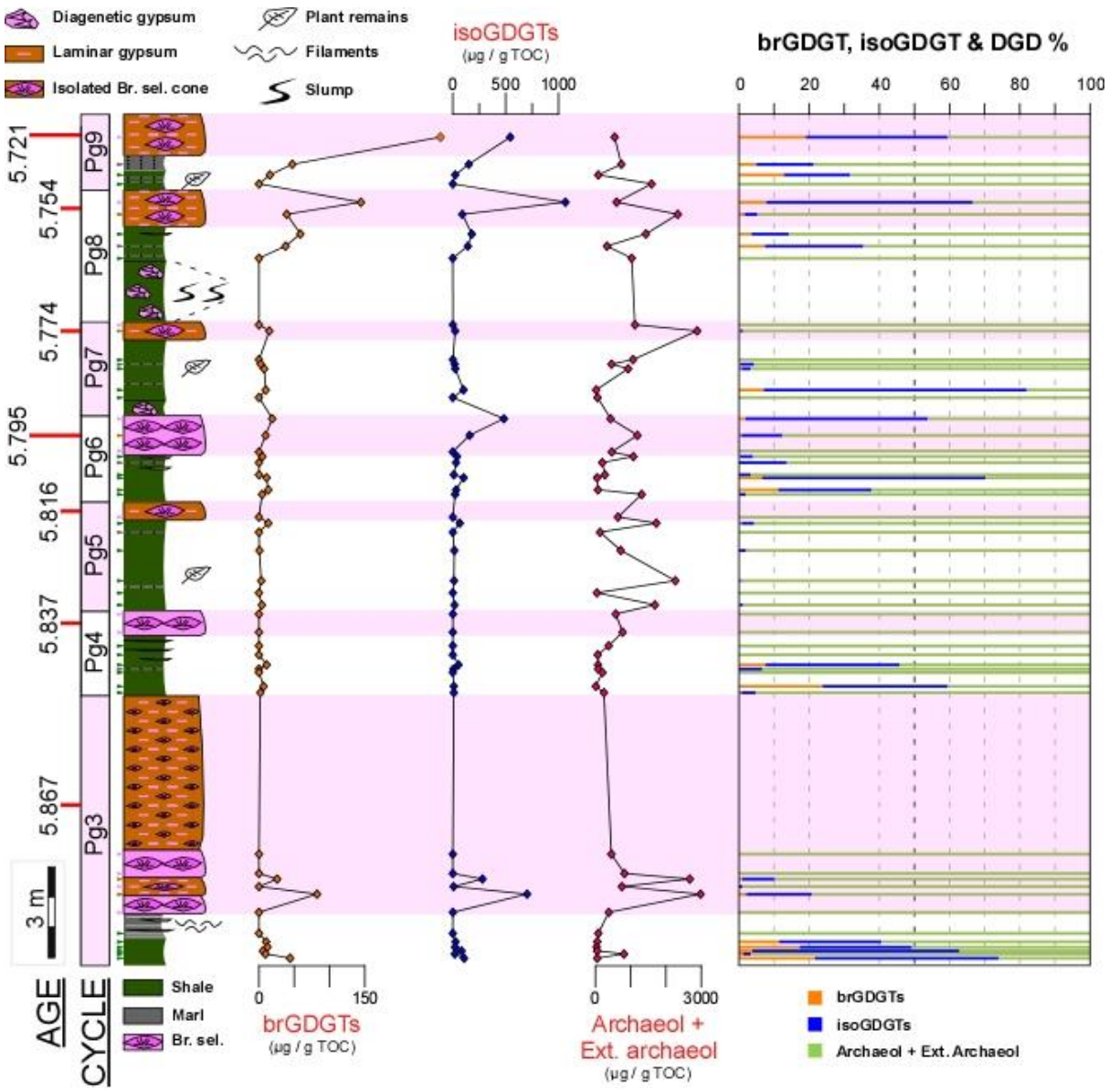

(Fig. 23): Comparison of the distribution of brGDGTs, isoGDGTs and DGDs across the Pollenzo section. The graphs indicate the summed abundances of brGDGTs, isoGDGTs and DGDs (archaeol + ext. archaeol) while the box on the right indicates the relative abundances between these lipid groups. Horizontal pink bars indicate gypsum intervals and the ages (Ma) next to the stratigraphic column represent gypsum midpoints (*sensu* Manzi *et al.,* 2013). Br. sel. = branching selenite; Ext. archaeol = extended archaeol ($C_{20,25}$).

7.4.5) Sterols and other prominent lipid biomarkers

Besides GDGTs and DGDs, additional abundant lipids in the alcohol fraction belong to the group of sterols, a sub-group of steroids (see **section 2.5** for background information). The identified sterols in the Pollenzo samples are derivatives of cholestane, ergostane and stigmasterane (**Fig. 24**).

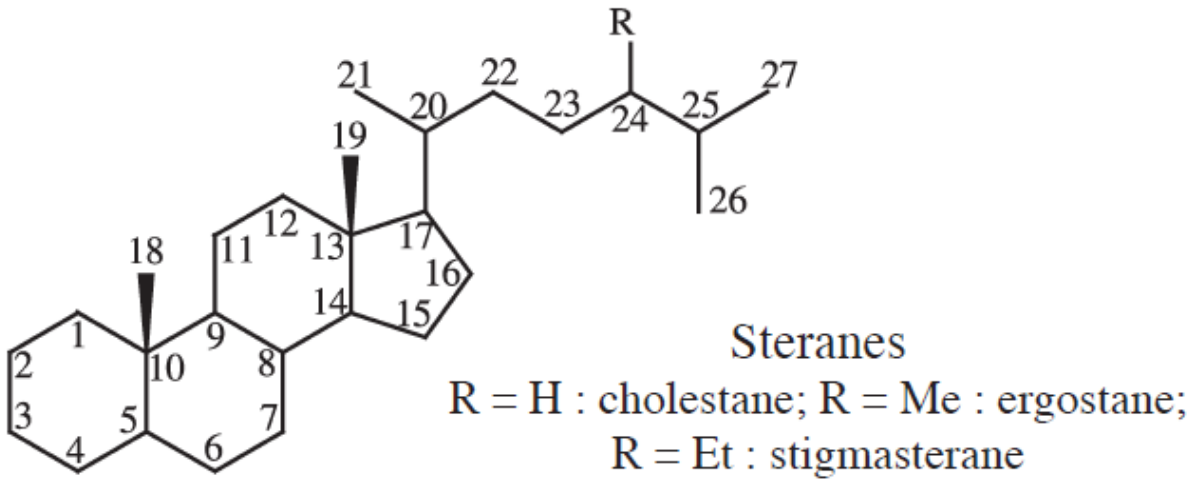

(Fig. 24): Chemical structure and carbon numbering of steranes. The identified sterols in this study are derived from these precursor structures. Modified from Stern (2009).

Among the predominant sterols in the Pollenzo samples are 4α,23,24-trimethyl-5α-cholest-22E-en-3β-ol (dinosterol), 4α,23S,24-trimethyl-5α-cholestan-3β-ol and 4α,23S,24-trimethyl-5α-cholestan-3β-ol (two dinostanol isomers; Harvey *et al.,* 1988), 24-methyl-5α-cholest-22E-en-3β-ol (brassicasterol), 24-ethyl-5α-cholest-22E-en-3β-ol, 24-ethyl-cholest-5α-en-3β-ol (sitosterol), cholest-5α-en-3β-ol (cholesterol), 5α-cholest-3β-ol (cholestanol), 24-ethyl-5α-cholest-3β-ol (stigmastanol or sitostanol), 4-methyl-24-ethyl-5α-cholest-3β-ol (4-methyl-stigmastanol) and 24-ethyl-5α-cholestane (stigmasterane). Additionally, two co-eluting sterols were tentatively identified as 4-methyl-ergosta-14-en-3β-ol (486 [M^+], 359, 269) and ergosta-7-en-3β-ol (472 [M^+], 345, 255, 94) (fungisterol; Tanret, 1908). Other prominent (non-sterol) lipids in the alcohol group are the long-chain C_{29}- and C_{30} *n*-alcohols, the C_{30} 1,15-diol (Volkman *et al.,* 1992; 1999), olean-12-en-3β-ol (β-amyrin, a common higher plant triterpenol; Otto and Wilde, 2001) and tetrahymanol (a pentacyclic triterpenoid; Mallory *et al.,* 1963).

7.4.6) Distribution of predominant sterols

From the identified sterols in the studied interval of the Pollenzo section, dinosterol and the tentatively identified 4-methyl-ergosta-14-en-ol and ergosta-7-en-ol are the most prominent. The aforementioned sterols therefore have been quantified and their abundances are shown in **Fig. 20** and **Table 2**. Since 4-methyl-ergosta-14-en-ol and ergosta-7-en-ol are co-eluting, these sterols have been quantified by calculating the areas within GC-MS chromatograms, by filtering for the dominant 269 and 255 fragments (M^+-SC-TMSOH),

respectively. Interestingly, dinosterol does not occur in samples where 4-methyl-ergosta-14-en-ol and ergosta-7-en-ol are detected and vice versa.

Dinosterol has been detected in 20 out of 53 samples (18 laminated shales and 2 homogenous marls) and does not occur in gypsum samples. The dinosterol abundance highly varies across the Pollenzo section; abundances range from ~16 μg/g TOC up to ~2.36 mg/g TOC, with an average of ~734 μg/g TOC (see **Table 2**).

The enigmatic 4-methyl-ergosta-14-en-3β-ol and ergosta-7-en-3β-ol are detected in 32 out of 53 samples, occurring in each of the four sampled lithologies. The abundance of both sterols is presented in **Fig. 20** as a summed total, since the abundances of these sterols do not show any variation in their distributional trends across the Pollenzo section. 4-methyl-ergosta-14-en-3β-ol is generally the more abundant sterol of the two, comprising about 44-73% of the summed total (see **Table 2**), while ergosta-7-en-3β-ol is generally less abundant, representing about 27-56% of the summed abundance. Sample PZD.6.6 (homogenous marl) is an exception with respect to the usual ratio between these sterols, with 77% comprised of ergosta-7-en-3β-ol and 23% of 4-methyl-ergosta-14-en-3β-ol. The summed abundance of 4-methyl-ergosta-14-en-3β-ol and ergosta-7-en-3β-ol varies from ~23 μg/g TOC up to ~6.22 mg/g TOC, with an average of ~754 μg/g TOC (see **Table 2**). The appearance of these enigmatic sterols is mostly restricted to the gypsum intervals, as they are detected in all gypsum samples, as well as in some of the laminated shales and homogenous marls adjacent to gypsum intervals.

7.4.7) Distribution of C_{30} 1,15-diol and tetrahymanol

Additional frequently detected lipid biomarkers in the alcohol fraction are the long-chain C_{30} 1,15-diol and the pentacyclic triterpenoid tetrahymanol (**Fig. 25**).

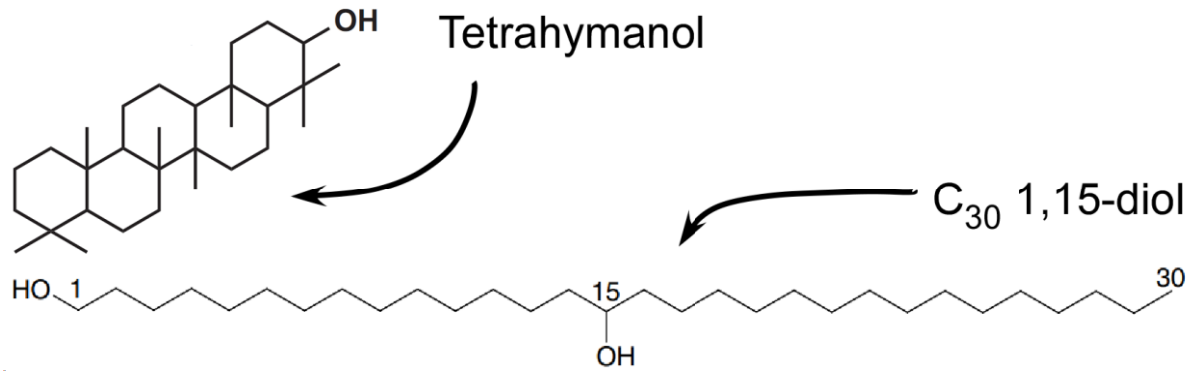

(Fig. 25): Chemical structures of tetrahymanol (a pentacyclic triterpenoid) and the C_{30} 1,15-diol (a long-chain diol), frequently detected biomarkers in the Pollenzo sediments. Modified from Rampen *et al.* (2007) and Banta *et al.* (2015).

The C_{30} 1,15-diol is detected in 10 out of 53 samples (9 laminated shales and 1 homogenous marl) and does not occur in gypsum samples. The C_{30} 1,15-diol always occurs conjointly with dinosterol, although the abundance of this long-chain diol is much less dominant. In the samples in which it is detected, the C_{30} 1,15-diol abundance varies between ~17 μg/g TOC up to ~363 μg/g TOC, with an average of ~197 μg/g TOC (see **Fig. 20** and **Table 2**).

Tetrahymanol is detected in 45 out of 53 samples and occurs (regardless of lithology) across the entire section. However, the abundance of tetrahymanol tends to be higher in laminated shales than in homogenous marls, branching selenite and laminar gypsum. Tetrahymanol is detected in 25 out of 30 laminated shales and varies in these samples from ~2 μg/g TOC up to ~227 μg/g TOC, with an average of ~34 μg/g TOC (see **Fig. 20** and **Table 2**). Tetrahymanol abundance exceeds 20 μg/g TOC in each of the studied PLG cycles, with the exception of cycle Pg5, in which the tetrahymanol abundance stays below ~4 μg/g TOC. The tetrahymanol abundance is >19 μg/g TOC in 17 out of these 25 laminated shales. In comparison, if tetrahymanol occurs in homogenous marls (6 out of 6 samples) or branching selenite (11 out of 12 samples), tetrahymanol abundances tend to be much lower (homogenous marls = ~7 μg/g TOC, and branching selenite = ~4 μg/g TOC). Interestingly, tetrahymanol abundance is relatively high in laminar gypsum samples (detected in 3 out of 5 samples), with an average of ~26 μg/g TOC.

Chapter 8 – Discussion

8.1) Input and source of terrestrial organic matter

Terrestrial organic matter is an important contributor to the TOC pool in marine coastal and deltaic deposits. On a yearly basis, thousands of kilotons of terrestrial organic carbon are globally transported to the marine realm by rivers and, in lower amounts, by aeolian dust (Schlünz and Schneider, 2000). Common components within terrestrial organic matter are the higher plant-derived long-chain *n*-alkanes, which are generally well preserved in sediments due to their refractory nature (Gaines *et al.*, 2009; Diefendorf and Freimuth, 2017). Therefore, the abundance of long-chain *n*-alkanes is a suitable and frequently used proxy to assess the input of terrestrial organic matter (Bush and McInerney, 2013).

In the studied interval of the Pollenzo section, the *n*-alkane abundance roughly mirrors the trend of the TOC record and tends to follow lithological cyclicity (**Fig. 18** and **Fig. 26**), showing higher abundances in laminated shales and lower abundances in branching selenite samples.

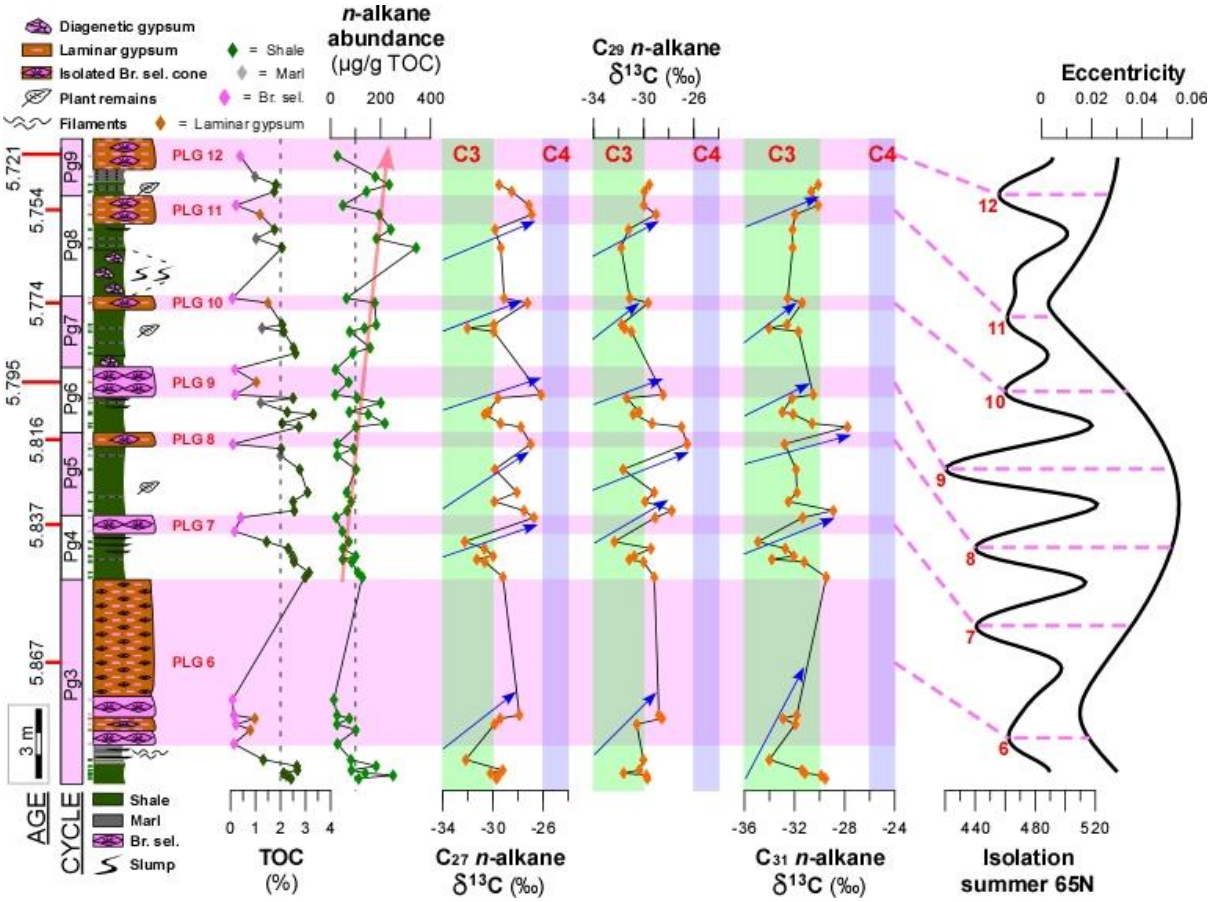

(Fig. 26): Tuning of the Pollenzo section and each of the Primary Lower Gypsum (PLG) cycles with precession and eccentricity (Manzi *et al.,* 2013) using the astronomical solution of Laskar *et al.,* 2004. Gypsum midpoints have been correlated with insolation minima (precession maxima). Pink shaded horizontal bars indicate gypsum beds. Green and blue shaded vertical bars indicate the range of $\delta^{13}C$ values of C3 and C4 plants, respectively (Rommerskirchen *et al.,* 2006a; Naafs *et al.,* 2012). Blue arrows indicate isotope excursions from negative to more positive values. The red shaded arrow indicates the gradual increase in *n*-alkane abundance from Pg4 to Pg9.

The differences in TOC content and *n*-alkane abundance between the shale- and gypsum hemicycles are well pronounced in each of the studied PLG cycles, indicating that during times of shale deposition, the input of terrestrial organic matter into the Piedmont basin increased. The higher TOC content and *n*-alkane abundance in the laminated shales could also be explained by increased preservation of organic matter, in turn controlled by low oxygen conditions in bottom waters. Such conditions agree with the absence of bioturbation and benthos in the Pollenzo section, as well as high pyrite contents (Natalicchio et al., 2019), altogether suggesting that reducing conditions favored the preservation of organic matter. In general, the fluctuation in TOC content and *n*-alkane abundance and its coherency with lithology, is in accordance with the assumption that lithological cyclicity in the PLG unit was controlled by precession driven climate change. In this view, the shale hemicycle would reflect the more humid climate during precession minima (enhanced input of terrestrial organic carbon by rivers), while the gypsum hemicycle would reflect the more arid climate during precession maxima (Lugli *et al.,* 2010; Dela Pierre *et al.,* 2011). This strong relationship between lithological cyclicity, TOC content and *n*-alkane abundance, already demonstrated for the Sant'Agata fossili marls in the lower part of the Pollenzo section (Natalicchio *et al.,* 2019), appears to be also valid for the gypsum-bearing cycles of the PLG unit (see **section 8.2**).

Interestingly, measured *n*-alkane abundances in the shale hemicycle (i.e. laminated shales and homogenous marls) are similar to those recorded in laminar gypsum (see **Table 1).** This is not surprising from the perspective of homogenous marls, since these deposits are generally interpreted as the product of flood events, composed of terrigenous grains and terrestrial organic matter transported by rivers (Dela Pierre *et al.,* 2014). However, this observation is quite surprising for the laminar gypsum facies, since from a stratigraphic

point of view, deposition of this facies seems to have been contemporaneous with the branching selenite, and yet these two facies do not show similar *n*-alkane abundances. Although the average *n*-alkane abundance in laminar gypsum is slightly lower than those measured in samples from the shale hemicycle, it is about four times higher than that of branching selenite. This could possibly be the result of a sampling bias. In fact, the fine lamination of laminar gypsum likely reflects annual variation from the humid to the dry season. Therefore, the *n*-alkane abundance in laminar gypsum samples would reflect a mixed signal of both the short-term humid and dry season. However, lower amounts of organic matter were incorporated in the branching selenite facies, although both facies were likely deposited under the same short-term climatic fluctuations. Branching selenite crystals, in contrast to those from laminar gypsum, formed at the bottom of the basin, with a crystal arrangement that suggests a dominant lateral growth orientation, outwards from a nucleation zone (Lugli *et al.,* 2010). Therefore, the displacive nature of laterally growing gypsum crystals could have pushed away part of the settling sediment (and organic matter). Moreover, post-depositional modification could have possibly enhanced this effect, if the overgrowth of gypsum crystals increased the volume of branching selenite, without entrapping sediment and organic matter. Consequently, the lower *n*-alkane abundance in the branching selenite could simply be the result of a different mode of gypsum formation with respect to the laminar gypsum, rather than different environmental conditions.

Looking at the *n*-alkane abundance in the Pollenzo section, a long-term increasing trend can be observed (see red shaded arrow; **Fig. 26**). Across the onset of the MSC, as described in Natalicchio *et al.* (2019), the long chain *n*-alkane abundances show a progressive increase, which has been attributed to an increased fluvial influx of terrestrial organic matter. Although the *n*-alkanes in the laminated shales show $\delta^{13}C$ values at the higher end (suggesting more arid conditions and less fluvial input), the authors put forward that the relatively low CPI values of the shales ($CPI_{average}$ = ~5) with respect to the marls ($CPI_{average}$ = ~6.5), suggest reworking of older organic matter, which might have slightly biased the $\delta^{13}C$ signature (Natalicchio *et al.,* 2019). Interestingly, the PLG cycles of the Pollenzo section (cycle Pg4-Pg9) studied for this thesis show a similar increasing trend in *n*-alkane abundances. The lower abundances in cycle Pg4-Pg5 and higher abundances towards cycle Pg8-Pg9 also suggest a long-term progressive increase in the input of terrestrial organic

matter to the basin. However, in the upper Pollenzo section (Pg6-Pg9), CPI values of the shales are relatively high (>5) and stable (average = 6.7), excluding extensive recycling of older sediments. Moreover, the absolute $\delta^{13}C$ values in the laminated shales are at the lower end, which agrees with the expected signal for increased fluvial input and more humid conditions (see **section 8.2**).

This raises the question how the *n*-alkane abundance (i.e. the input of organic matter) in the PLG cycles of the Pollenzo section can show a gradual increasing trend, while the $\delta^{13}C$ values of the individual *n*-alkanes do not reflect this gradual change to more humid climate conditions (i.e. lower $\delta^{13}C$-values, see **section 8.2**) . This apparent contradiction could be explained by a relative shallowing of the Piedmont basin, resulting in a closer proximity of the coastline and, hence, a higher input of terrestrial organic matter to the Pollenzo sediments. Shallowing is also suggested by the overall progradational stacking pattern of the PLG unit towards the Piedmont basin depocenter (Dela Pierre *et al.,* 2011). Thus, the observed gradual increase in *n*-alkane abundance in the Pollenzo section is not necessarily related to an increasing flux of terrestrial organic matter to the Piedmont basin, but might reflect a closer proximity of the discharging river systems instead. Another hypothesis that could possibly explain the gradual increasing trend of the *n*-alkane abundance is the 100 ka eccentricity cycle. Perhaps, the higher *n*-alkane abundances measured in Pg3 and Pg8-Pg9 are the reflection of eccentricity minima, suggesting that the increasing trend of *n*-alkane abundances are related to the cyclical variation of the 100 ka eccentricity cycle. In fact, Reghizzi *et al.* (2018) interpreted eccentricity minima as periods that are characterized by a more local Sr signal, which would agree with the isolation/shallowing of the Piedmont basin. Unfortunately, the time span of this dataset (~150 ka) is not large enough to clarify if eccentricity is the most plausible hypothesis to explain the gradual increasing trend of *n*-alkane abundances towards Pg8-Pg9.

8.2) Confirmation of the relation between orbital forcing and cyclicity of the PLG unit; insight from carbon stable isotopes of long-chain *n*-alkanes.

Extensive studies on sedimentary cyclicity before the MSC (Violanti *et al.,* 2013; Lozar *et al.,* 2018; Lozar and Negri, 2019, across the onset of the MSC (Natalicchio *et al.,* 2019; Sabino *et*

al., 2020) and after the MSC (Rohling *et al.,* 2015; Grant *et al.,* 2016) have concluded that the Mediterranean region was sensitive to orbital forcing. Climatic fluctuation driven by precession is also expected to be the main driver causing the cyclic deposition of the PLG unit, as suggested by several authors (Krijgsman *et al.,* 1999; 2001; Hilgen *et al.,* 2007; Lugli *et al.,* 2010), although hitherto, the scientific community is still awaiting confirmation of this assumption.

The $\delta^{13}C$ values of epicuticular leaf wax derived *n*-alkanes in sedimentary archives are commonly used to identify the relative amount of C3 and C4 plants in terrestrial organic matter (e.g. Huang *et al.,* 2000; Tierney *et al.,* 2010; Sinninghe Damsté *et al.,* 2011b). Therefore, $\delta^{13}C$ values of *n*-alkanes have the potential to indicate changes in humidity, since C3 plants (-36‰ < $\delta^{13}C_{alk}$ < -30‰) are adapted to more humid conditions than C4 plants ($\delta^{13}C_{alk}$ > -26‰) and both plant types produce long-chain *n*-alkanes with distinctly different $\delta^{13}C$ values due to their different carbon fixation pathways (Schefuß *et al.,* 2003; Rommerskirchen *et al.,* 2006a; Naafs et al., 2012).

Looking at the long-term progression of $\delta^{13}C$ values in each of the long-chain *n*-alkane records (C_{27}, C_{29} and C_{31}), it appears that average $\delta^{13}C$ values remain relatively stable during the first phase of the MSC. However, on the shorter term, distinct $\delta^{13}C$-excursions (up to ~6‰) between the shale- and gypsum hemicycles are present within each of the seven studied PLG cycles (Pg3-Pg9, see **Fig. 26**). The correlation of these isotope excursions with the lithological cyclicity of the PLG unit suggests that precessional forcing caused climatic conditions to fluctuate significantly during each PLG cycles, likely causing changes in the type of vegetation in the catchment area. This suggestion is strengthened by the observation that CPI values remain relative stable in the studied interval (see **Fig. 18**), indicating that these pronounced $\delta^{13}C$ excursions are unlikely to be the result of extensive reworking. Although the ACL proxy also has the potential to indicate a vegetation change over time (e.g. Rommerskirchen *et al.,* 2006a; Vogts *et al.,* 2009), there is no correlation between the ACL and the *n*-alkane $\delta^{13}C$ records (see **Fig. 18**). This observation suggests that for the Pollenzo samples in this study, the ACL is probably strongly influenced by factors other than climate. The ACL could be compromised by interspecies differences in long-chain *n*-alkane distribution (e.g. Hoffman *et al.,* 2013; Guo *et al.,* 2014; Diefendorf *et al.,* 2015a;

Bai *et al.,* 2019), perhaps as a result of genetical or environmental factors which are capable of causing variability in the *n*-alkane chain length (Jansen and Wiesenberg, 2017).

The *n*-alkane $\delta^{13}C$ records indicate that most shales have $\delta^{13}C$ values that are in the range of C3 plants (i.e. $\delta^{13}C_{alk} < -30‰$, see green shaded bars **Fig. 26**), while the gypsum samples, as well as the shales that were deposited immediately above gypsum, show values that lean more towards the range of C4 plants (Naafs *et al.,* 2012; Mayser *et al.,* 2017; Natalicchio *et al.,* 2019). This may suggest that during times of gypsum precipitation (precession maxima), the influence of C3 plants adapted to drier conditions became significantly higher (e.g. Hartman and Danin, 2010; Ma *et al.,* 2012; Chu *et al.,* 2014). Another possibility could be that the establishment of C4 plants took place (Edwards *et al.,* 2010; Marzocchi *et al.,* 2015; Mayser *et al.,* 2017) in the catchment area during precession maxima. The establishment of C4 plants could have caused $\delta^{13}C$ values to be in between the ranges for C3 and C4 plants (i.e. $-30‰ < \delta^{13}C_{alk} < -26‰$), if the long-chain *n*-alkane pool in the Pollenzo sediments is a mixture of C3 and C4 plants during precession maxima. As the deposition of gypsum-bearing cycles of the PLG unit progresses, drier climatic conditions seem to occur in the catchment area of the long-chain *n*-alkanes, as indicated by peaks in the $\delta^{13}C$ record that show relatively high $\delta^{13}C$ values between -27‰ and -26‰. So far, such high values are not shown by studies that analysed *n*-alkanes extracted from sediments that represent the onset of the MSC crisis, as demonstrated by Natalicchio *et al.,* 2019 and Sabino *et al.,* 2020, which report $\delta^{13}C$ values for long-chain *n*-alkanes that do not exceed -29‰ and -30‰, respectively. The increase in $\delta^{13}C$ values in the gypsum-bearing PLG intervals might be explained as a change in source region of the *n*-alkanes or as a reflection of more arid conditions during precession maxima (insolation minima).

During cycle Pg4-6, the high $\delta^{13}C$ values between -27‰ and -26‰ coincide with relatively large isotope excursions. These major isotope excursions can be tentatively correlated with an eccentricity maximum (see **Fig. 26**). Since the amplitude of precessional forcing is modulated by eccentricity (Huybers and Aharonson, 2010), it is very likely that the isotope excursions with higher magnitude can be correlated with a period where the amplitude of precession is greater and thus the differences between insolation maxima and insolation minima are largest, which results in climatic extremes (and likely in larger hydrological changes) leading to more pronounced vegetation shifts. Thus, for the first time, orbital

forcing on climate has been confirmed during stage 1 of the MSC, indicated by a molecular proxy that directly records climatic conditions in the terrestrial environment.

8.3) Water column stratification during deposition of the Primary Lower Gypsum unit

Climate induced stratification of the water column is thought to be an essential condition for the deposition of the pre-MSC sapropels (Sierro *et al.,* 1999; 2003), as well as for the basin-wide synchronous formation of the post-MSC sapropels in the Mediterranean (e.g. De Lange *et al.,* 2008; Rohling *et al.,* 2015), which have both been linked to precession minima. Stratification might have intensified in the Mediterranean water column across the onset of the MSC as a consequence of continued restriction of the Mediterranean basin (Sabino *et al.,* 2021). This is a realistic scenario according to a recent modeling study (Simon and Meijer, 2017) and supported by several studies which show that stratified conditions likely persisted well within the MSC (Christeleit *et al.,* 2015; Garcia-Veigas *et al.,* 2018).

The alleged intensification of water column stratification across the onset of the MSC has convincingly been deduced from paleoenvironmental reconstructions in the Piedmont basin, based on studies on the Pollenzo section (Natalicchio *et al.,* 2017; 2019), as well as the more distal Govone section (Sabino *et al.,* 2021). The main evidence for this conclusion is the presence of tetrahymanol (gammacer-3β-ol) in the Pollenzo and Govone sediments, a pentacyclic triterpenoid that is widespread in marine sediments (Ten Haven *et al.,* 1989). Tetrahymanol is biosynthesized by marine ciliates that feed on bacteria (Mallory *et al.,* 1963; Harvey and McManus, 1991), but other potentially important sources may be anoxygenic photosynthetic green sulfur bacteria (Kleemann *et al.,* 1990; Wakeham *et al.,* 2012) and aerobic methanotrophic bacteria (Banta *et al.,* 2015; Cordova-Gonzalez *et al.,* 2020). Ciliates biosynthesize tetrahymanol when they fully rely on sterol-lacking organisms as their primary food source (Harvey and McManus, 1991). Organisms in such a sterol-lacking diet may be autotrophic bacteria, which thrive in anoxic environments, or at the oxic/anoxic interface of such environments (i.e. at the chemocline; Degermendzhy *et al.,* 2010; Wakeham *et al.,* 2012). In fact, planktonic ciliates have been frequently encountered at the chemoclines of modern stratified environments (Fenchel *et al.,* 1990; Khromechek *et al.,* 2010; Degermendzhy *et al.,* 2010; Wakeham *et al.,* 2012), where they feed on organisms

such as phototrophic sulfur oxidizing bacteria (Zubkov *et al.,* 1992; Guhl and Finlay, 1993; Saccà *et al.,* 2009; Wakeham *et al.,* 2012). Since ciliates only produce tetrahymanol if their diet is lacking sterols (i.e. when chemocline-dwelling bacteria are the main food source), tetrahymanol and its derivative gammacerane (loss of the hydroxy group) are considered as reliable indicators of water column stratification (Schoell *et al.,* 1994; Sinninghe Damsté *et al.,* 1995a).

In the Pollenzo section, tetrahymanol makes its appearance right after the onset of the MSC (Natalicchio *et al.,* 2017). In contrast, tetrahymanol was already encountered in the more distal Govone section before the onset of the crisis (~6.069 Ma; Sabino *et al.,* 2021). This suggests that stratified conditions in the deeper part of the Piedmont basin were already established before the onset of the MSC. Moreover, these findings indicate that the stratified area in the deeper part of the basin likely expanded towards the basin margin around the onset of the crisis. This might have been related to an increase in humidity, possibly reflecting a hydrological change (i.e. increased precipitation) in the Mediterranean triggered by the continued restriction of the gateways between the Atlantic Ocean and the Mediterranean (Sabino *et al.,* 2020). The combined effect of increased freshwater input and ongoing isolation of the Piedmont basin might have resulted in an intensification of water column stratification (Natalicchio *et al.,* 2019), preceding the precipitation of gypsum.

Concerning the studied PLG unit, tetrahymanol continuously makes its appearance across the Pollenzo section, although in some samples tetrahymanol is lacking or abundances are low (see **Fig. 20**). The abundance of tetrahymanol is highest in the laminated shales, as is also the case for the analyzed shales from the Govone section (Sabino *et al.,* 2021). This observation likely reflects a more severe stratification of the water column as a result of more humid conditions (i.e. higher freshwater input) in the Mediterranean during precession minima (Natalicchio *et al.,* 2019; Sabino *et al.,* 2020). This is in agreement with the generally lower tetrahymanol abundances detected in gypsum samples, which are thought to be deposited during precession maxima, when river runoff is expected to be weakened as a result of dryer climatic conditions. Interestingly, relatively high tetrahymanol abundances are also detected in a few of the laminar gypsum samples, particularly those

from the thick laminar gypsum deposits in the SKB (cycle Pg3; PLG 6), in which tetrahymanol abundances are similar to those of laminated shales. This strongly suggests a marked stratification during the precipitation of laminar gypsum, at least during deposition of the SKB.

The common presence of tetrahymanol across the Pollenzo section indicates that water column stratification played a large role throughout the first phase of the MSC (both during precession minima and maxima), although it appears that the intensity of stratification (and associated position of the chemocline) was highly dynamic. This is not only indicated by the significantly varying tetrahymanol abundances across the section, but also by e.g. cycle Pg5, during which tetrahymanol abundance remains much lower during shale deposition in comparison with other PLG cycles (see **Fig. 20**). Moreover, some samples in cycle Pg5-Pg9 are barren of tetrahymanol (**Table 2**), which suggests that stratification could have been temporarily disrupted, or that ciliates have not been a consistent source of tetrahymanol production. This is interesting, because previous studies in the Piedmont basin suggested a persistence of stratified conditions after the onset of the MSC, based on reports of pyrite framboids (Natalicchio *et al.,* 2019; Sabino *et al.,* 2021) and sulfur-enriched compounds (Sabino *et al.,* 2021) in laminated shales. The extracted organic matter in the samples that have been analyzed for this study also show a similarly high degree of sulfurization. In fact, a desulfurization procedure needed to be performed on each sample (see **section 5.2**), because most samples contained enough sulfur to cause interference with the ion source during GC-MS analysis. The degree of sulfurization in the extracted organic matter might be related to the depth of the chemocline. A high degree of sulfurization might be related to a relatively shallow chemocline, since settling organic matter is able to reach the anoxic zone below the chemocline faster, where reduced sulfur species (such as H_2S) await and are able to bind to settling organic molecules, making them less prone to oxidation (Kenig *et al.,* 1995). Thus, taking into account the high degree of sulfurization of the Pollenzo sediments, the absence or lower abundance of tetrahymanol in gypsum and some laminated shales is more likely to be related to inhospitable environmental conditions for ciliates, rather than a full destabilization of stratified conditions down to the bottom of the basin. A less favorable habitat for ciliates could be related to a deeper position of the chemocline. If a trophic relationship was established between ciliates and photoautotrophic sulfur bacteria

(Wakeham *et al.,* 2012), a deeper chemocline (below the photic zone) would be disastrous for ciliate communities. Disappearance of an important food source would cause a decline in the number of ciliates, resulting in lower tetrahymanol abundances or even the absence of this biomarker if ciliates were unable to survive. It seems less likely that turbidity in the water column was responsible for a less favorable environment for ciliates, since relatively high tetrahymanol abundances are detected in laminated shales, which are deposited during precession minima, when river runoff (and thus terrigenous input) is expected to be larger than during precession maxima.

Thus, summarizing the main findings related to the tetrahymanol abundances in the studied interval of the Pollenzo section, it appears that tetrahymanol abundances are higher in the shale hemicycles than in the gypsum hemicycles. These findings indicate that stratification was generally more pronounced during precession minima (insolation maxima). However, tetrahymanol abundance is occasionally low or even absent in the Pollenzo section, even in some of the analyzed laminated shales, suggesting that the stratification was occasionally disrupted or the chemocline temporarily moved below the photic zone. Stratified conditions in the Piedmont basin may have been the result of an interplay between (1) a density gradient in the water column related to the riverine input of freshwater (2) oxygen consumption due to organic matter mineralization (i.e. development of an anoxic zone) and (3) a restriction of the basin resulting in limited water mass exchange. Several studies indicate that during precession minima, the input of freshwater to the Piedmont basin increased due to riverine discharge (Natalicchio *et al.,* 2019; Sabino *et al.,* 2020) or possibly Paratethian waters (Grothe *et al.,* 2020), causing a freshening of the upper water column. When the input of freshwater was high enough to keep pace with the effects of mixing in the upper water column, a 'low-salinity lid' may have been able to establish on top of a more saline water body (e.g. Schroeder *et al.,* 1990), leading to shutdown in the basin's overturning circulation and a density-stratified water column during precession minima. Increased riverine discharge into the Piedmont basin would not only lead to a higher input of terrestrial organic matter, but would also supply the basin with more nutrients (eutrophication), leading to an increase in the primary and exported productivity (see **section 8.4**). Increased primary productivity and terrestrial organic matter input (see **section 8.1**) would in turn have led to a higher flux of organic matter towards the seafloor, resulting

in higher oxygen consumption rates in the water column and at the seafloor (Suess, 1980). In a restricted marginal basin with limited water mass exchange, the mineralization of organic matter would gradually deplete the available oxygen from the bottom upwards, until eventually an anoxic zone would establish in the lower part of the water column, separated from an oxygenated and well mixed upper water column by an oxic/anoxic interface (oxycline). The depletion of oxygen in the Piedmont basin is supported by high TOC contents of laminated shales (average = ~2.4%). Over time, the oxycline likely developed into a chemocline, which in case of the Piedmont basin could be defined as the zone where H_2S appears and O_2 disappears in the water column. The development of a euxinic zone and associated chemocline is observed in modern marine anoxic basins (Sinninghe Damsté *et al.,* 1993; Wakeham *et al.,* 2012) and reconstructed for ancient evaporitic basins (Babel, 2004; Babel and Bogucki, 2007). The establishment of a chemocline in the Piedmont basin seems logical, since anoxic bottom waters would provide a suitable environment for the anoxic degradation of organic matter via bacterial sulfate reduction (which produces H_2S), as is already reconstructed for the Piedmont basin (Dela Pierre *et al.,* 2014) and supported by the high degree of sulfurization of the extracted organic matter in this study. The continuous deposition of organic matter in a stratified basin would eventually lead to a shallowing of the chemocline, theoretically up until the depth where the mixing forces of wind and waves are able to bring oxygen. Whenever the input of freshwater reduced and overturning circulation was restored in the Piedmont basin, this could have resulted in a deepening of the chemocline and less favorable conditions for the tetrahymanol-producing ciliates. However, full disruption of the stratified conditions seems unlikely, because modern (deep) saline basins show a nearly permanent zone of dense bottom brines, which do not permit downward flowing brines (produced by evaporation in surface waters) to reach the bottom of the basin directly (Babel and Bogucki, 2007). The ongoing isolation of the Piedmont basin (Natalicchio *et al.,* 2019; Sabino *et al.,* 2020), resulting in a limited exchange between the Piedmont and Mediterranean basins, would be ideal to keep the stratified water column with a vertically oscillating chemocline in place.

8.4) Environmental conditions in the marine water column after the onset of gypsum precipitation

In the Pollenzo section, calcareous nannofossil and foraminifer assemblages disappear from the stratigraphic record just a few meters below the first gypsum bed (Violanti *et al.,* 2013). Across the onset of the MSC, higher abundances of stress tolerant benthic foraminifera are observed, which indicates that increasingly extreme environmental conditions appeared in the Piedmont basin (Violanti *et al.,* 2013). The establishment of harsher conditions in the water column is confirmed by the lipid biomarker inventory of the Sant'Agata Fossili Marls, which clearly shows a change in the distribution of archaeal lipids one precessional cycle above the MSC onset (Natalicchio *et al.,* 2017). The most significant changes among the Archaea concern the distribution of major GDGTs (e.g. higher GDGT-0/crenarchaeol ratios), increasing concentrations of archaeol across the MSC onset, as well as the first appearance of extended archaeol and tetrahymanol after the beginning of the crisis (Natalicchio *et al.,* 2017). The changes in the GDGT- and DGD abundances mirror a pronounced change in the archaeal community, which could be related to the establishment of water column stratification, as suggested by the first appearance of tetrahymanol (Sinninghe Damsté *et al.,* 1995a).

After the onset of gypsum precipitation in the Piedmont basin, water column conditions generally remained relatively harsh, especially during times of gypsum deposition. This is indicated by the abundance of archaeol and extended archaeol, lipids that predominate in the Pollenzo sediments and peak during times of gypsum deposition (**Fig. 20**). The production of extended archaeol has been commonly attributed to hypersaline Euryarchaeota (Dawson *et al.,* 2012) and its dominance in the sedimentary archive (in combination with archaeol) has been linked to hypersaline environments (Birgel *et al.,* 2014), as are their isoprenoid derivatives (Grice *et al.,* 1998). Although the presence of archaeol is not very diagnostic for specific environmental conditions, it has been encountered in (extremely) halophilic archaea, capable of living in sulfide- and sulfur-rich environments (Elshahed *et al.,* 2004). Another indicator for extreme conditions during times of gypsum deposition is the ratio between GDGT-0 and crenarchaeol (Turich *et al.,* 2007), which peaks during or just after times of gypsum deposition (see **Fig. 20**). Note that for 19 of the analyzed samples in this study (most of which are gypsum samples or shales in the vicinity of gypsum deposits), the GDGT-0/crenarchaeol ratio could not be determined (see **Table 2**). This can be attributed to the absence of crenarchaeol in these samples, which also

implies harsh conditions in the (upper) water column, sufficiently stressful to hamper the survival of Thaumarchaeota. Thus, the combined presence of archaeol and extended archaeol, in combination with a high degree of sulfurization of the extracted organic matter, suggests that sulfidic and possibly even hypersaline conditions may have been present in the Piedmont basin during deposition of the PLG unit. However, because the exact source of the DGDs remains uncertain, the possibility remains that these lipids might have been produced by non-halophilic Prokarya (*sensu* Natalicchio *et al.,* 2017). Nevertheless, stratification seems to have been stronger during precession minima (see **section 8.3**), whereas archaeol and extended archaeol concentrations peak during or close to periods of gypsum deposition (precession maxima), suggesting that lesser freshwater input favors the source organisms that biosynthesized archaeol and extended archaeol.

Remarkably, gypsum samples and laminated shales that are typified by relatively high abundances in DGDs and/or a high GDGT-0/crenarchaeol ratio also reveal high abundances of two relatively unknown sterols; 4-methyl-ergosta-14-en-3β-ol and ergosta-7-en-3β-ol (**Fig. 20**). Unfortunately, the exact origin of these enigmatic sterols is difficult to track down, since these compounds are hardly, if at all, described in scientific literature, especially 4-methyl-ergosta-14-en-3β-ol. Intuitively, the expected microbial source for lipid biomarkers in hypersaline paleoenvironments would probably be prokaryotic (most likely halophilic bacteria or archaea) or perhaps algae. However, the enigmatic sterols identified in this study could possibly have a fungal origin, because ergosta-7-en-3β-ol (fungisterol) has first been isolated from ergot fungi (Tanret, 1908), and more recently in e.g. yeast strains (Kamilova and Ekhvalova, 1989) and wild mushroom species (Baraza *et al.,* 2007). Although marine fungi might not be the usual suspects one might think of as the producers of these enigmatic sterols, halophilic fungi have in fact been isolated from several hypersaline environments, including hypersaline waters, microbial mats in high-salinity environments, and even from the depositional environments of Mediterranean solar salterns (Méjanelle *et al.,* 2000). Among the halophilic fungi in hypersaline environments are mostly yeast-like (Gunde-Cimerman *et al.,* 2000) and filamentous fungi (Gunde-Cimerman *et al.,* 1997; Tepšič *et al.,* 1997). Recently, anaerobic consortia of filamentous fungi have been associated with sulfate reducing bacteria in the deep biosphere (Drake *et al.,* 2017). This illustrates that

fungi are able to thrive in extreme environments and that a microeukaryotic origin of these enigmatic sterols is perhaps not as farfetched as it might intuitively seem.

Traditionally, ergosterol (ergosta-5,7,22-trien-3β-ol) has been used as a diagnostic biomarker to indicate the presence of fungi and to assess fungal biomass (Seitz *et al.,* 1977; Stahl and Parkin, 1996; Gessner, 2020), as it is almost exclusively biosynthesized by fungi. Ergosterol is an essential sterol in fungal cell membranes, representing over 80% of all sterols in fungal strains (Gutiérrez *et al.,* 2020). However, not all fungi are able to biosynthesize ergosterol, like many fungi within the division Chytridiomycota (Newell, 2001). Since it was usually assumed that they play an insignificant role, marine (pelagic) fungi have been poorly studied thus far, so their ecological and biogeochemical significance remains largely enigmatic at this point (Grossart *et al.,* 2020). Nevertheless, it has been recently suggested that fungi might play an important role in many pelagic biogeochemical cycles after all (Morales *et al.,* 2019; Baltar *et al.,* 2021). Thus, even though ergosterol was not identified in any of the Pollenzo sediment, this does not necessarily exclude a fungal origin for the enigmatic sterols, since ergosterol is not produced by all fungi and the fungal presence in the pelagic realm is still poorly understood. Nevertheless, it is unclear at this point what sources the enigmatic sterols and it remains to be seen whether these peculiar sterols can be used to indicate specific environmental conditions.

However, regardless of its origin, the observation that the enigmatic sterols correlate with high abundances of DGDs and/or a high GDGT-0/crenarchaeol ratio suggests that they could possibly be indicators for extreme conditions in the marine water column of the Piedmont basin. Moreover, these sterols are exclusively identified in samples where dinosterol and the C_{30} 1,15-diol are absent, and vice versa (**Fig. 20**). Dinosterol and the C_{30} 1,15-diol (produced by dinoflagellates and eustigmatophyte algae, respectively) are compounds that are usually associated with normal marine conditions in the upper water column (Withers, 1983; Rampen *et al.,* 2014). Therefore, the enigmatic sterols could perhaps be used as a molecular proxy to indicate whether or not stressful (hypersaline?) conditions might have been present in the upper water column of the Piedmont basin.

Although environmental conditions in the bottom waters appear to have been quite stressful during deposition of the PLG unit, normal marine water conditions seem to have been intermittently present in the upper water column of the Piedmont basin. This is

strongly suggested by peaks of the biomarkers dinosterol and C_{30} 1,15-diol, which appear during shale intervals in most of the analyzed PLG cycles (**Fig. 20**). Both dinosterol and the C_{30} 1,15-diol have probably been biosynthesized by primary producers that lived in the upper water column, such as dinoflagellates (dinosterol; Withers, 1983; Volkman *et al.,* 1993; 1999) and eustigmatophyte algae (C_{30} 1,15-diol; Volkman *et al.,* 1992; Rampen *et al.,* 2014). Even though dinosterol is usually the dominant sterol in dinoflagellate species (Amo *et al.,* 2010), it should be noted that is it rarely found in other algae (Volkman *et al.,* 1993). The role of eustigmatophyte algae as producers of the C_{30} 1,15-diol in the marine realm has more uncertainty (Rampen *et al.,* 2014; Balzano *et al.,* 2018). Nevertheless, it seems plausible that phytoplankton species are responsible for the peaks in dinosterol and C_{30} 1,15-diol production, which is probably related to changes in the upper water column towards relatively normal marine conditions. This is also suggested by the correlation of the peaks in dinosterol and C_{30} 1,15-diol abundance with lower BIT values (0.29-0.69; see **Fig. 20** and **Table 2**). The lower BIT values indicate a relative increase in the production of crenarchaeol and thus the presence of Thaumarchaeota, even though the riverine input of brGDGTs remained a relevant factor (**Fig. 23**). These findings suggest that an increased input of freshwater from the catchment area, most likely related to precession minima (insolation maxima), reduced the salinity of the upper water column in the Piedmont basin, leading to a re-establishment of normal marine conditions in the upper water column. The return of normal marine conditions in the upper water column, possibly in combination with an increased supply of nutrients to the Piedmont basin (i.e. eutrophication), resulted in pulses of primary productivity and the recurrence of Thaumarchaeota in the upper water column. However, the question remains how the primary producers were able to reoccupy the upper water column of the Piedmont basin. If the basin was completely isolated during precession maxima, the increase of freshwater to the basin might have resulted in a reconnection of the Piedmont basin with the main Mediterranean water body, allowing the return of organisms that are typical for normal marine conditions. An alternative hypothesis is that a freshening of the upper water column during precession minima led to more hospitable conditions in the entire Mediterranean basin and that Thaumarchaeota, dinoflagellates and eustigmatophyte algae were reintroduced from Atlantic waters.

8.5) Paleoenvironmental information deduced from gypsum morphology

Although a gradual restriction of the marginal sub-basins or an increase in salinity seems the most probable reason for the basin-wide sharp lithofacies change during the 6th PLG cycle, a unifying mechanism that explains the contemporaneous deposition of branching selenite and laminar gypsum has yet to be identified. The lipid-based evidence in this thesis by itself is not strong enough to suggest a model for the concurrent precipitation of branching selenite and laminar gypsum. However, even though petrographic evidence is not included in this thesis, the larger scale morphology of branching selenite and laminar gypsum may hint at some clues related to specific paleoenvironmental conditions during the deposition of these types of gypsum lithofacies.

To begin with, it is important to apprehend that the precipitation of gypsum from brines is related to supersaturation with respect to Ca^{2+} and SO_4^{2-} ions. Thus, the precipitation of gypsum in seawater is not necessarily related to a high salinity (total amount of dissolved salt), which is mostly indicative for high Na^+ and Cl^- ions, as they are the most abundant ions in modern seawater (Brennan *et al.,* 2013). In fact, it has been suggested that Messinian selenitic gypsum precipitated from seawater which was depleted in Na^+ and Cl^- ions compared to modern seawater (Natalicchio *et al.,* 2014; Evans *et al.,* 2015; Costanzo *et al.,* 2019). Besides brine composition, other factors such as ionic strength (the concentration of ionic charge in a solution) and thermodynamic settings also control the precipitation of gypsum (Reiss *et al.,* 2021). Although understanding the effects of brine composition on the morphology of gypsum crystals can obviously help in determining the paleoenvironmental conditions during gypsum deposition, only a limited number of studies have thus far explored the effects of brine composition on the morphology of gypsum under hypersaline conditions, especially at the microscopic level. Thus, further research is most certainly required before the morphology of gypsum crystals (i.e. the relative growth rate of the different crystal faces) can be applied as a tool for paleoenvironmental reconstructions, in particular when they concern paleosalinity reconstructions.

However, regarding the studies on this topic performed to date, the Ca^{2+}/SO_4^{2-} molar ratio seems to be one of the crucial factors that influences the morphology of gypsum crystals

(and thus gypsum facies). Unfortunately, this mechanism has yet to be fully understood, since the Ca^{2+}/SO_4^{2-} ratio seems to cause opposing effects depending on salinity (Reiss *et al.,* 2021). According to Reiss *et al.* (2019), lower Ca^{2+}/SO_4^{2-} molar ratios result in more elongated gypsum crystals (acicular morphology) under hypersaline conditions, whereas in solutions with lower ionic strengths, a higher ratio of Ca^{2+} to SO_4^{2-} ions favors the growth of more elongated crystals (Mbogoro *et al.,* 2017). Another important factor appears to be the distance from equilibrium conditions regarding the saturation state of a solution. The precipitation of needle-like crystals afloat in solution appears to be favored in experiments conducted further from equilibrium conditions, i.e. within solutions at higher supersaturation (Reiss *et al.,* 2019).

Thus, taking into account the results from these experimental studies and the suggested increase in paleosalinity during deposition of the 6th PLG cycle, the deposition of the needle-like crystals (i.e. laminar gypsum) might possibly be related to elevated concentrations of SO_4^{2-} in a hypersaline water column. This could perhaps be related to a mechanism that is similar to the one responsible for the observation of so-called "gypsum blooms" in the present-day Salton Sea (Tiffany *et al.,* 2007). Here, gypsum crystals spontaneously precipitate in the upper water column due to episodically returning sulfide interruptions, during which sulfide species reach the mixed layer where they react with molecular oxygen, as a consequence of severe anoxia in bottom waters (Tiffany *et al.,* 2007). Thus, the deposition of laminar gypsum in the Piedmont basin could have possibly been promoted by the interaction of sulfur redox reactions, including bacterial sulfate reduction and the re-oxidation of H_2S to SO_4^{2-}. In fact, bacterial sulfate reduction and the associated production of H_2S during the MSC has been proposed by several studies (De Lange and Krijgsman, 2010; Garcia-Veigas *et al.,* 2018; Sabino *et al.,* 2021). Another factor that might have theoretically influenced the precipitation of needle-like crystals could have been an increase of major cations in the gypsum parent water, in particular Mg^{2+}, which has been reported to favor the precipitation of more elongated crystals (Rabizadeh *et al.,* 2017).

Besides the influence of inorganic compounds, also organic molecules are able to influence the morphology of gypsum crystals (e.g. Rabizadeh *et al.,* 2014). This may be an important factor to consider, since significant amounts of organic matter have been deposited in the

Mediterranean marginal sub-basins, and as this study clearly indicates, also during the deposition of gypsum. Especially if the residence time of seawater in marginal sub-basins increased due to the gradual restriction of the Mediterranean, dissolved organic carbon concentrations in gypsum parent water might have increased. Interestingly, it has been shown that dissolved organic compounds inhibit the growth of gypsum crystals at specific crystal faces, possibly due to the adsorption of polar organic compouds (Barcelona and Atwood, 1978). Tannic acid, a ubiquitous humic compound related to terrestrial plants, has also been shown to influence the crystal habit of gypsum, with higher concentrations of organic acid causing a flattening of the gypsum crystals (Cody and Cody, 1988), which reminds of the flattened conical structures of branching selenite. Another aspect that could be of importance for gypsum crystal morphology is the dominant mechanism of gypsum nucleation (i.e. homogeneous vs. heterogeneous nucleation), which has been shown to affect the size of gypsum crystals (e.g. Ahmi and Gadri, 2004). As such, a lower degree of saturation seems to favor the growth of larger crystals, while higher concentrations favor the growth of smaller crystals (Ahmi and Gadri, 2004). This factor could explain the significant reduction in crystal size from massive selenite on the one hand, and branching selenite and laminar gypsum on the other hand. However, although (1) the degree of supersaturation, (2) brine composition and (3) dissolved organic matter could have all played a role in the abrupt change of gypsum lithofacies, further petrographic and geochemical research is necessary to elucidate the unifying mechanism that is able to explain the synchronous appearance of branching selenite and laminar gypsum from the 6th PLG cycle onwards. Future research should focus on the role of biogeochemical sulfur cycling in marginal Mediterranean basins, which could possibly provide the missing link that is able to explain the contemporaneous deposition of branching selenite and laminar gypsum.

8.6) Implications for deposition of the PLG unit: insights from the Pollenzo section

The combination of the stratigraphic and lipid biomarker dataset allowed to formulate a sound scenario for the deposition of the PLG unit in Piedmont basin, in which the paleoenvironmental reconstruction of terrestrial climate and the marine water column are integrated. Following the interpretation of the TOC (see **section 8.1**) and long-chain *n*-

alkane data (see **section 8.2**) of the Pollenzo sediments, the sedimentary cyclicity of the PLG unit can be ascribed to precessional forcing, with a shale hemicycle linked to precession minima (insolation maxima) and gypsum hemicycle linked to precession maxima (insolation minima) (**Fig. 27**). Regardless of the precessional phase, the Piedmont basin water column has probably been subject to persisting stratification, controlled by a vertically oscillating chemocline, as suggested by tetrahymanol abundances throughout the analyzed strata of the Pollenzo section (see **section 8.3**). Modern-day deep- and intermediate water formation in the Mediterranean mainly occurs in relatively shallow and restricted sub-basins along the northern edges, such as the Adriatic Sea and Aegean Sea (Tsimplis *et al.,* 2006). Such regions are also areas where the strongest annual heat loss takes place due to cold and dry winds from the north, indicating that besides salinity, convection is a major driver that charges the Mediterranean thermohaline overturning circulation (Lascaratos *et al.,* 1999; Tsimplis *et al.,* 2006; Simon and Meijer, 2017). However, if overturning circulation was present in the Piedmont basin, this may have been temporarily suppressed during precession minima if the input of riverine freshwater was high enough, a mechanism that has been suggested to be a recurrent event in the Eastern Mediterranean related to the formation of post-MSC sapropels (Rohling *et al.,* 2015; Andersen *et al.,* 2018). Such a strong runoff would have favored intensified stratification of the water column (and the expansion of anoxic conditions), as well as the accumulation and preservation of organic matter, which is supported by the lipid biomarker data in the shale hemicycle of the PLG cycles (see **section 8.4**). These data indicate that during precession minima, normal marine conditions in the upper water column episodically returned, triggering pulses of primary productivity in a basin where otherwise harsh conditions seem to have been present during deposition of the PLG unit. Intense stratification and primary productivity in the upper water column during shale deposition (precession minima) agree with paleoenvironmental reconstructions concerning deposition of the PLG unit in the Vena del Gesso basin (Sinninghe Damsté *et al.,* 1995b; Kenig *et al.,* 1995). Unfortunately, the obtained data does not provide a definite answer concerning the connectivity of the Piedmont basin with the main Mediterranean water body during deposition of the PLG unit. However, a persisting connection seems to be the most likely situation, since outflowing water appears to be necessary in order to counterbalance the salt influx in marginal basins during gypsum deposition (De Lange and Krijgsman, 2010).

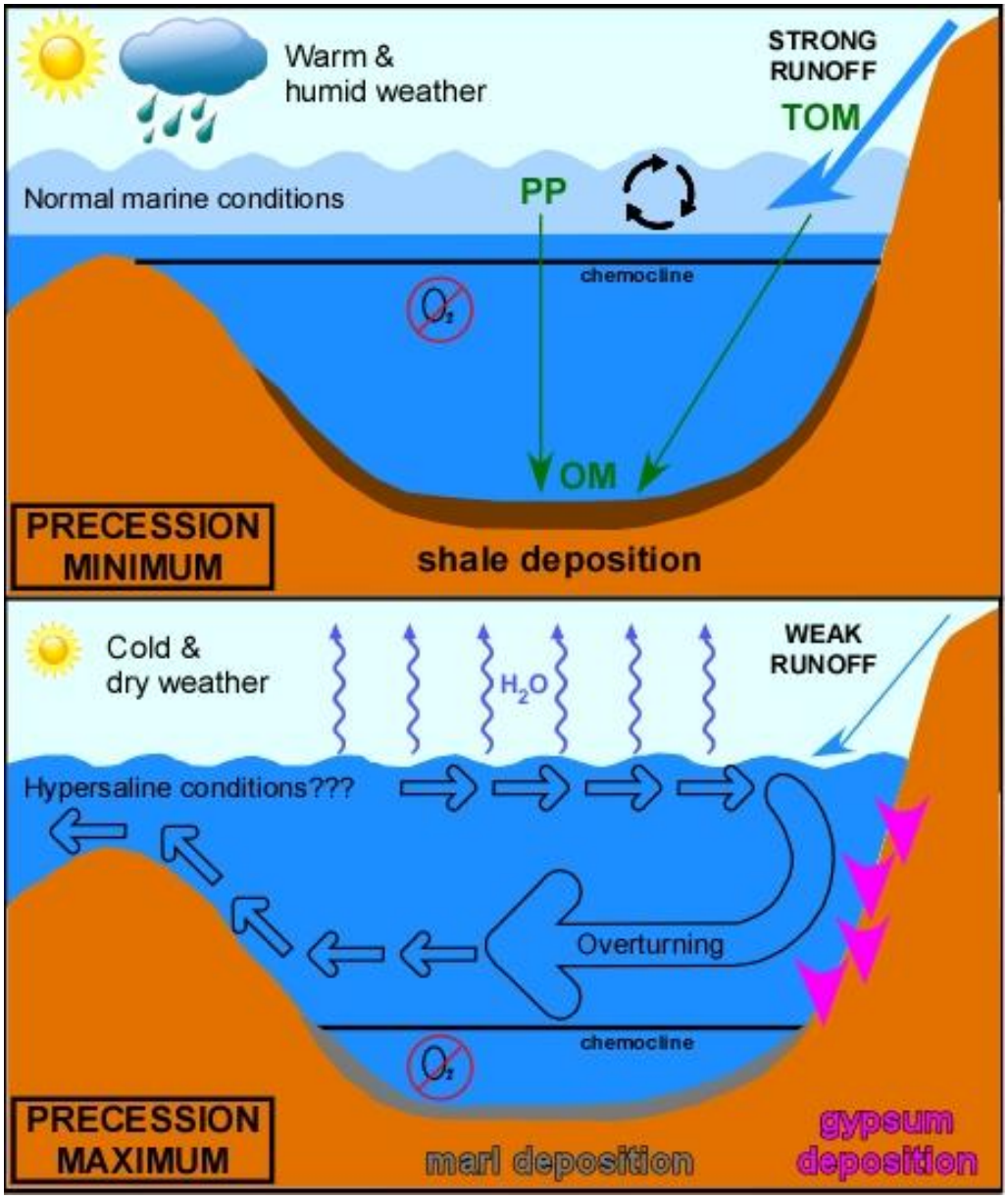

(Fig. 27): Simplified reconstruction of the water column in the Piedmont basin. (**TOP**) Sketch that depicts the situation during precession minima (insolation maxima), when laminated shales are deposited in the entire basin. (**BOTTOM**) Sketch that depicts the situation during precession maxima (insolation minima), when gypsum is deposited at the basinal margin and marls in the deeper basin. Note that these sketches are not to scale. OM = organic matter; PP = primary productivity; TOM = terrestrial organic matter.

During precession minima, warmer and more humid climate conditions caused a stronger runoff from the continent, increasing the input of freshwater to the Piedmont basin. A stronger runoff brings more terrestrial organic matter and nutrients to the basin, of which the latter is favorable for primary productivity in the upper water column. If the input of freshwater to the basin is high enough to disrupt the overturning circulation in the

Piedmont basin, a low-salinity lid may have formed, which could have resulted in a density-stratified water column. The combined effect of an increased flux of organic matter to the seafloor and a ceased overturning circulation in a restricted basin are suitable for the upward expansion of anoxic/euxinic conditions and an associated shallowing of the chemocline. These paleoenvironmental conditions in the Piedmont basin likely resulted in the deposition of shales from the basinal margin to the deeper basin.

During precession maxima, colder and dryer weather conditions likely resulted in a weaker runoff from the continent, reducing the freshwater input to the Piedmont basin. Reduced freshwater input caused a decrease in the amount of terrestrial organic matter and nutrients to the basin, of which the latter is unfavorable for primary productivity. Furthermore, a weaker runoff probably resulted in the reestablishment of the overturning circulation. The downwelling of dense and oxygenated waters to deeper transects would have resulted in a deepening of the chemocline. As the mineral-rich (Ca^{2+} and SO_4^{2-}) oxygenated waters were transported along the basin margin, gypsum was able to precipitate, while marls were deposited in the deeper part of the basin (Sabino *et al.,* 2020; 2021).

The circumstance that the input of freshwater had a strong influence in the Piedmont basin was already implied by the salinities of fluid inclusions from selenite gypsum, which are even lower than modern Mediterranean seawater (Natalicchio *et al.,* 2014). This finding is remarkable in the sense that it is in contrast with the classical view that Messinian gypsum was deposited under strictly hypersaline conditions. However, the biomarker data of this study are in apparent contradiction with such low salinities during gypsum precipitation, because the lipid biomarker inventory of gypsum samples is (1) absent of biomarkers that are unambiguously diagnostic for normal or brackish marine conditions, (2) generally predominated by DGDs (particularly archaeol accompanied by extended archaeol) and (3) typified by high GDGT-0/crenarchaeol ratios (see **section 8.4**). Nevertheless, because there are no other independent salinity indicators (lithological features nor other lipid biomarkers), it must be considered that there could be source organisms other than hypersaline Euryarchaeota responsible for the biosynthesis of high abundances of DGDs and GDGT-0 (Natalicchio *et al.,* 2017). Although these findings seem to indicate an apparent contradiction concerning the paleosalinity during gypsum deposition, it might simply reflect

a change towards more saline paleoenvironmental conditions, evidenced by the sharp gypsum lithofacies change that occurs in the 6th PLG cycle (Dela Pierre *et al.,* 2011). After all, from the 6th PLG cycle onwards, the massive selenite that was deposited in the lowest five PLG cycles, is replaced by the branching selenite and laminar gypsum lithofacies, a change that appears to have occurred synchronously in the sub-basins of the western Mediterranean (Lugli *et al.,* 2010). Especially concerning the large scale on which this lithofacies change seems to have taken place, it makes sense to link it to a chemophysical parameter that was able to impact the entire western Mediterranean.

The most plausible reason that could explain the apparent change in paleosalinity during the 6th PLG cycle is an abrupt change in the Mediterranean thermohaline overturning circulation, related to the gradual isolation of the Mediterranean basin. In fact, the stepwise closure of the different Atlantic-Mediterranean gateways (Blanc-Valleron *et al.,* 2002; Van Assen *et al.,* 2006) is thought to have lasted well into the MSC (Benson *et al.,* 1991; Govers, 2009), although the exact timing of the final gateway closure is unknown. However, the thickness of the evaporite deposits in the PLG unit can only be explained with a continuous influx of Atlantic waters (Meijer and Krijgsman, 2005; Govers, 2009) and model results show that the Mediterranean thermohaline circulation and salinity strongly depend on the sill depth of the Atlantic-Mediterranean gateway (Alhammoud *et al.,* 2010). If the sill depth shallows and the intensity of the inflow-outflow system is reduced, the residence time of seawater in the Mediterranean increases, resulting in an elevated basin salinity (Alhammoud *et al.,* 2010). Furthermore, the tuning of PLG cycles with the astronomical curve of Laskar *et al.* 2004 suggests that deposition of the 6th PLG cycle coincided with an eccentricity minimum (Manzi *et al.,* 2013), associated with a cooling phase and global sea level fall (Van der Laan *et al.,* 2012; Miller *et al.,* 2011). Thus, the interaction of these processes in combination with a continuous tectonic activity in the Atlantic-Mediterranean gateway (Govers, 2009) may have resulted in a gradual reduction of the sill depth and the inflow-outflow intensity of the Atlantic-Mediterranean gateway. As a consequence, the marginal Mediterranean sub-basins would have experienced an ongoing restriction and an associated increase in paleosalinity, which could possibly explain the dramatic facies change from massive selenite, to branching selenite and laminar gypsum.

Conclusions

Since the early 2000s, numerous studies based on astronomical tuning, climatic modeling and sedimentary cyclicity have indicated that orbital forcing must have been the main climatic driver during deposition of the PLG unit. These findings have now been confirmed by this study, by performing compound specific carbon stable isotope measurements on long-chain *n*-alkanes, which indicate significant $\delta^{13}C$-excursions over the course of individual PLG cycles (up to ~6‰). These $\delta^{13}C$-excursions confirm that the cyclic precession of Earth's axis of rotation controlled the deposition of the PLG unit. Thus, superimposed on the Late Miocene global cooling trend, the Mediterranean basin also endured significant climatic fluctuations driven by precessional forcing. Precession and its direct effect on insolation and precipitation, affected the freshwater budget of the Piedmont basin, ultimately resulting in deposition of the shale/gypsum couplets of the Pollenzo section. Tetrahymanol abundances suggest that stratification was likely often present during deposition of the studied strata of the Pollenzo section, although it appears to have been more pronounced during precession minima, probably as a result of increased freshwater input during these periods. The combined effect of the ongoing restriction of the Mediterranean and the fluctuating input of freshwater might have temporarily suppressed the overturning circulation in the Piedmont basin, resulting in vertical oscillations of the chemocline. Normal marine conditions episodically returned during deposition of the shale hemicycle, as evidenced by peaks in the abundances of dinosterol, C_{30} 1,15-diol and crenarchaeol, indicating primary productivity pulses and the possible reestablishment of thaumarchaeotal communities in the upper water column. The appearance of the branching selenite and laminar gypsum in the 6th PLG cycle, never observed in underlying PLG cycles, possibly reflects a critical reduction of the sill depth in the Atlantic-Mediterranean gateway, and an associated increase in paleosalinity. The latter is suggested by the lipid biomarker inventory of the gypsum hemicycles, indicating an absence of diagnostic biomarkers for normal or brackish marine conditions, as well as the combined predominance of archaeol in association with extended archaeol, supported by very high GDGT-0/crenarchaeol ratios. The proposed increase in paleosalinity could possibly explain the dramatic facies change from massive selenite to branching selenite and laminar gypsum during the 6th PLG cycle.

References

Aerts, J., Röling, W., Elsaesser, A., & Ehrenfreund, P. (2014). Biota and biomolecules in extreme environments on earth: implications for life detection on Mars. *Life*, *4*(4), 535–565. https://doi.org/10.3390/life4040535

Ahmi, F., & Gadri, A. (2004). Kinetics and morphology of formed gypsum. *Desalination*, *166*, 427–434. https://doi.org/10.1016/j.desal.2004.06.097

Alhammoud, B., Meijer, P. T., & Dijkstra, H. A. (2010). Sensitivity of Mediterranean thermohaline circulation to gateway depth: A model investigation. *Paleoceanography*, *25*(2). https://doi.org/10.1029/2009PA001823

Amo, M., Suzuki, N., Kawamura, H., Yamaguchi, A., Takano, Y., & Horiguchi, T. (2010). Sterol composition of dinoflagellates: Different abundance and composition in heterotrophic species and resting cysts. *Geochemical Journal*, *44*(3), 225–231. https://doi.org/10.2343/geochemj.1.0063

Andersen, N., Paul, H. A., Bernasconi, S. M., McKenzie, J. A., Behrens, A., Schaeffer, P., & Albrecht, P. (2001). Large and rapid climate variability during the Messinian salinity crisis: Evidence from deuterium concentrations of individual biomarkers. *Geology*, *29*(9), 799–802. https://doi.org/10.1130/0091-7613(2001)029<0799:LARCVD>2.0.CO;2

Andersen, M. B., Matthews, A., Vance, D., Bar-Matthews, M., Archer, C., & de Souza, G. F. (2018). A 10-fold decline in the deep Eastern Mediterranean thermohaline overturning circulation during the last interglacial period. *Earth and Planetary Science Letters*, *503*, 58–67. https://doi.org/10.1016/j.epsl.2018.09.013

Auguet, J.-C., Barberan, A., & Casamayor, E. O. (2010). Global ecological patterns in uncultured Archaea. *The ISME Journal*, *4*(2), 182–190. https://doi.org/10.1038/ismej.2009.109

Bąbel, M. (1999). History of sedimentation of the Nida Gypsum deposits (middle Miocene, Carpathian Foredeep, southern Poland). *Geological Quarterly*, *43*(4), 429-447.

Bąbel, M. (2002). Brine palaeocurrent analysis based on oriented selenite crystals in the Nida Gypsum deposits (Badenian, southern Poland). *Geological Quarterly*, *46*(4), 435-448.

Bąbel, M. (2004). Models for evaporite, selenite and gypsum microbialite deposition in ancient saline basins. *Acta Geologica Polonica*, *54*(2), 219–249.

Bąbel, M., & Becker, A. (2006). Cyclonic brine-flow pattern recorded by oriented gypsum crystals in the Badenian evaporite basin of the Northern Carpathian foredeep. *Journal of Sedimentary Research*, *76*(7), 996–1011. https://doi.org/10.2110/jsr.2006.090

Bąbel, M. (2007). Depositional environments of a salina-type evaporite basin recorded in the Badenian gypsum facies in the northern Carpathian Foredeep. *Geological Society, London, Special Publications*, *285*(1), 107–142. https://doi.org/10.1144/SP285.7

Bąbel, M., & Bogucki, A. (2007). The Badenian evaporite basin of the northern Carpathian Foredeep as a model of a meromictic selenite basin. *Geological Society, London, Special Publications*, *285*(1), 219–246. https://doi.org/10.1144/SP285.13

Bąbel, M., & Schreiber, B. C. (2014). Geochemistry of Evaporites and Evolution of Seawater. In *Treatise on Geochemistry* (pp. 483–560). Elsevier. https://doi.org/10.1016/B978-0-08-095975-7.00718-X

Bache, F., Popescu, S.-M., Rabineau, M., Gorini, C., Suc, J.-P., Clauzon, G., Olivet, J.-L., Rubino, J.-L., Melinte-Dobrinescu, M. C., Estrada, F., Londeix, L., Armijo, R., Meyer, B., Jolivet, L., Jouannic, G., Leroux, E., Aslanian, D., Reis, A. T. D., Mocochain, L., … Çakır, Z. (2012). A two-step process for the reflooding of the Mediterranean after the Messinian Salinity Crisis. *Basin Research*, *24*(2), 125–153. https://doi.org/10.1111/j.1365-2117.2011.00521.x

Bai, Y., Azamdzhon, M., Wang, S., Fang, X., Guo, H., Zhou, P., Chen, C., Liu, X., Jia, S., & Wang, Q. (2019). An evaluation of biological and climatic effects on plant n-alkane distributions and δ2Halk in a field experiment conducted in central Tibet. *Organic Geochemistry*, *135*, 53–63. https://doi.org/10.1016/j.orggeochem.2019.06.003

Baltar, F., Zhao, Z., & Herndl, G. J. (2021). Potential and expression of carbohydrate utilization by marine fungi in the global ocean. *Microbiome*, *9*(1), 106. https://doi.org/10.1186/s40168-021-01063-4

Banta, A. B., Wei, J. H., & Welander, P. V. (2015). A distinct pathway for tetrahymanol synthesis in bacteria. *Proceedings of the National Academy of Sciences*, *112*(44), 13478–13483. https://doi.org/10.1073/pnas.1511482112

Baraza, L. D., Joseph, C. C., Moshi, M. J., & Nkunya, M. H. H. (2007). Chemical constituents and biological activity of three Tanzanian wild mushroom species. *Tanzania Journal of Science*, *33*. https://doi.org/10.4314/tjs.v33i1.44280

Barcelona, M. J., & Atwood, D. K. (1978). Gypsum-organic interactions in natural seawater: Effect of organics on precipitation kinetics and crystal morphology. *Marine Chemistry*, *6*(2), 99–115. https://doi.org/10.1016/0304-4203(78)90021-X

Barrett, S. M., Volkman, J. K., Dunstan, G. A., & LeRoi, J.-M. (1995). Sterols of 14 Species of Marine Diatoms (bacillariophyta)1. *Journal of Phycology*, *31*(3), 360–369. https://doi.org/10.1111/j.0022-3646.1995.00360.x

Bassetti, M. A., Miculan, P., & Sierro, F. J. (2006). Evolution of depositional environments after the end of Messinian Salinity Crisis in Nijar basin (SE Betic Cordillera). *Sedimentary Geology*, *188–189*, 279–295. https://doi.org/10.1016/j.sedgeo.2006.03.009

Bataglion, G. A., Koolen, H. H. F., Weber, R. R., & Eberlin, M. N. (2016). Quantification of Sterol and Triterpenol Biomarkers in Sediments of the Cananéia-Iguape Estuarine-Lagoonal System (Brazil) by UHPLC-MS/MS. *International Journal of Analytical Chemistry*, *2016*, 1–8. https://doi.org/10.1155/2016/8361375

Baumann, L. M. F., Taubner, R.-S., Bauersachs, T., Steiner, M., Schleper, C., Peckmann, J., Rittmann, S. K.-M. R., & Birgel, D. (2018). Intact polar lipid and core lipid inventory of the hydrothermal vent

methanogens Methanocaldococcus villosus and Methanothermococcus okinawensis. *Organic Geochemistry*, *126*, 33–42. https://doi.org/10.1016/j.orggeochem.2018.10.006

Benson, R. H., Bied, K. R.-E., & Bonaduce, G. (1991). An important current reversal (influx) in the Rifian Corridor (Morocco) at the Tortonian-Messinian boundary: The end of Tethys Ocean. *Paleoceanography*, *6*(1), 165–192. https://doi.org/10.1029/90PA00756

Birgel, D., Guido, A., Liu, X., Hinrichs, K.-U., Gier, S., & Peckmann, J. (2014). Hypersaline conditions during deposition of the Calcare di Base revealed from archaeal di- and tetraether inventories. *Organic Geochemistry*, *77*, 11–21. https://doi.org/10.1016/j.orggeochem.2014.09.002

Birgel, D., Thiel, V., Hinrichs, K.-U., Elvert, M., Campbell, K. A., Reitner, J., Farmer, J. D., & Peckmann, J. (2006). Lipid biomarker patterns of methane-seep microbialites from the Mesozoic convergent margin of California. *Organic Geochemistry*, *37*(10), 1289–1302. https://doi.org/10.1016/j.orggeochem.2006.02.004

Blaga, C. I., Reichart, G.-J., Heiri, O., & Sinninghe Damsté, J. S. (2009). Tetraether membrane lipid distributions in water-column particulate matter and sediments: A study of 47 European lakes along a north–south transect. *Journal of Paleolimnology*, *41*(3), 523–540. https://doi.org/10.1007/s10933-008-9242-2

Blanc-Valleron, M.-M., Pierre, C., Caulet, J. P., Caruso, A., Rouchy, J.-M., Cespuglio, G., Sprovieri, R., Pestrea, S., & Di Stefano, E. (2002). Sedimentary, stable isotope and micropaleontological records of paleoceanographic change in the Messinian Tripoli Formation (Sicily, Italy). *Palaeogeography, Palaeoclimatology, Palaeoecology*, *185*(3–4), 255–286. https://doi.org/10.1016/S0031-0182(02)00302-4

Blumenberg, M., Seifert, R., Reitner, J., Pape, T., & Michaelis, W. (2004). Membrane lipid patterns typify distinct anaerobic methanotrophic consortia. *Proceedings of the National Academy of Sciences*, *101*(30), 11111–11116. https://doi.org/10.1073/pnas.0401188101

Boon, J. J., Rijpstra, W. I. C., De Lange, F., De Leeuw, J. W., Yoshioka, M., & Shimizu, Y. (1979). Black Sea sterol—A molecular fossil for dinoflagellate blooms. *Nature*, *277*(5692), 125–127. https://doi.org/10.1038/277125a0

Bosmans, J. H. C., Drijfhout, S. S., Tuenter, E., Hilgen, F. J., Lourens, L. J., & Rohling, E. J. (2015). Precession and obliquity forcing of the freshwater budget over the Mediterranean. *Quaternary Science Reviews*, *123*, 16–30. https://doi.org/10.1016/j.quascirev.2015.06.008

Bouvier, P., Rohmer, M., Benveniste, P., & Ourisson, G. (1976). Δ8(14)-steroids in the bacterium Methylococcus capsulatus. *Biochemical Journal*, *159*(2), 267–271. https://doi.org/10.1042/bj1590267

Braga, J. C., Martín, J. M., Riding, R., Aguirre, J., Sánchez-Almazo, I. M., & Dinarès-Turell, J. (2006). Testing models for the Messinian salinity crisis: The Messinian record in Almería, SE Spain. *Sedimentary Geology*, *188–189*, 131–154. https://doi.org/10.1016/j.sedgeo.2006.03.002

Braitsch, O. (1971). Salt Deposits. Their Origin and Composition, pp. 1–297 (translated from German edition, Springer, Berlin 1962, updated by A. G. Herrmann). Berlin: Springer.

Bray, E. E., & Evans, E. D. (1961). Distribution of n-paraffins as a clue to recognition of source beds. *Geochimica et Cosmochimica Acta*, *22*(1), 2–15. https://doi.org/10.1016/0016-7037(61)90069-2

Brennan, S. T., Lowenstein, T. K., & Cendón, D. I. (2013). The major-ion composition of Cenozoic seawater: The past 36 million years from fluid inclusions in marine halite. *American Journal of Science*, *313*(8), 713–775. https://doi.org/10.2475/08.2013.01

Briggs, D. E. G., & Summons, R. E. (2014). Ancient biomolecules: Their origins, fossilization, and role in revealing the history of life: Prospects & Overviews. *BioEssays*, *36*(5), 482–490. https://doi.org/10.1002/bies.201400010

Brochier-Armanet, C., Boussau, B., Gribaldo, S., & Forterre, P. (2008). Mesophilic crenarchaeota: Proposal for a third archaeal phylum, the Thaumarchaeota. *Nature Reviews Microbiology*, *6*(3), 245–252. https://doi.org/10.1038/nrmicro1852

Brock, T. D., & Freeze, H. (1969). Thermus aquaticus gen. N. And sp. N., a Nonsporulating Extreme Thermophile. *Journal of Bacteriology*, *98*(1), 289–297.

Brocks, J. J., Buick, R., Logan, G. A., & Summons, R. E. (2003). Composition and syngeneity of molecular fossils from the 2.78 to 2.45 billion-year-old Mount Bruce Supergroup, Pilbara Craton, Western Australia. *Geochimica et Cosmochimica Acta*, *67*(22), 4289–4319. https://doi.org/10.1016/S0016-7037(03)00208-4

Brocks, J. J., & Summons, R. E. (2005). Sedimentary Hydrocarbons. *Biogeochemistry*, *8*, 63.

Brocks, J. J. (2011). Biomarkers (molecular fossils). *Encyclopaedia of Biogeology*, 147-167.

Bush, R. T., & McInerney, F. A. (2013). Leaf wax n-alkane distributions in and across modern plants: Implications for paleoecology and chemotaxonomy. *Geochimica et Cosmochimica Acta*, *117*, 161–179. https://doi.org/10.1016/j.gca.2013.04.016

Bush, R. T., & McInerney, F. A. (2015). Influence of temperature and C 4 abundance on n -alkane chain length distributions across the central USA. *Organic Geochemistry*, *79*, 65–73. https://doi.org/10.1016/j.orggeochem.2014.12.003

Butler, R. W. H., Lickorish, W. H., Grasso, M., Pedley, H. M., & Ramberti, L. (1995). Tectonics and sequence stratigraphy in Messinian basins, Sicily: Constraints on the initiation and termination of the Mediterranean salinity crisis. *GSA Bulletin*, *107*(4), 425–439. https://doi.org/10.1130/0016-7606(1995)107<0425:TASSIM>2.3.CO;2

Caforio, A., & Driessen, A. J. M. (2017). Archaeal phospholipids: Structural properties and biosynthesis. *Biochimica et Biophysica Acta (BBA) - Molecular and Cell Biology of Lipids*, *1862*(11), 1325–1339. https://doi.org/10.1016/j.bbalip.2016.12.006

Camerlenghi, A., & Aloisi, V. (2020). Uncovering the Mediterranean Salt Giant (MEDSALT)—Scientific Networking as Incubator of Cross-disciplinary Research in Earth Sciences. *European Review*, *28*(1), 40–61. https://doi.org/10.1017/S1062798719000255

Capella, W., Flecker, R., Hernández-Molina, F. J., Simon, D., Meijer, P. Th., Rogerson, M., Sierro, F. J., & Krijgsman, W. (2019). Mediterranean isolation preconditioning the Earth System for late Miocene climate cooling. *Scientific Reports*, *9*(1), 3795. https://doi.org/10.1038/s41598-019-40208-2

Carnevale, G., Caputo, D., & Landini, W. (2006). Late Miocene fish otoliths from the Colombacci Formation (Northern Apennines, Italy): Implications for the Messinian 'Lago-mare' event. *Geological Journal*, *41*(5), 537–555. https://doi.org/10.1002/gj.1055

Carnevale, G., Gennari, R., Lozar, F., Pellegrino, L., Pellegrino, L., & Dela Pierre, F. (2019). Living in a deep desiccated Mediterranean Sea: An overview of the Italian fossil record of the Messinian salinity crisis. *Bollettino Della Società Paleontologica Italiana*, *1*, 109–140. https://doi.org/10.4435/BSPI.2019.04

Carnevale, G., Longinelli, A., Caputo, D., Barbieri, M., & Landini, W. (2008). Did the Mediterranean marine reflooding precede the Mio–Pliocene boundary? Paleontological and geochemical evidence from upper Messinian sequences of Tuscany, Italy. *Palaeogeography, Palaeoclimatology, Palaeoecology*, *257*(1), 81–105. https://doi.org/10.1016/j.palaeo.2007.09.005

Casamayor, E. O., Massana, R., Benlloch, S., Øvreås, L., Díez, B., Goddard, V. J., Gasol, J. M., Joint, I., Rodríguez-Valera, F., & Pedrós-Alió, C. (2002). Changes in archaeal, bacterial and eukaryal assemblages along a salinity gradient by comparison of genetic fingerprinting methods in a multipond solar saltern. *Environmental Microbiology*, *4*(6), 338–348. https://doi.org/10.1046/j.1462-2920.2002.00297.x

Caselle, C., Bonetto, S., Colombero, C., & Comina, C. (2019). Mechanical properties of microcrystalline branching selenite gypsum samples and influence of constituting factors. *Journal of Rock Mechanics and Geotechnical Engineering*, *11*(2), 228–241. https://doi.org/10.1016/j.jrmge.2018.09.003

Castaneda, I. S., Mulitza, S., Schefuss, E., Lopes dos Santos, R. A., Sinninghe Damste, J. S., & Schouten, S. (2009). Wet phases in the Sahara/Sahel region and human migration patterns in North Africa. *Proceedings of the National Academy of Sciences*, *106*(48), 20159–20163. https://doi.org/10.1073/pnas.0905771106

Chu, G., Sun, Q., Xie, M., Lin, Y., Shang, W., Zhu, Q., Shan, Y., Xu, D., Rioual, P., Wang, L., & Liu, J. (2014). Holocene cyclic climatic variations and the role of the Pacific Ocean as recorded in varved sediments from northeastern China. *Quaternary Science Reviews*, *102*, 85–95. https://doi.org/10.1016/j.quascirev.2014.08.008

CIESM (2008). The Messinian salinity crisis from mega-deposits to microbiology. In: Briand, F. (Ed.), A consensus report, in 33ème CIESM Workshop Monographs, 33. CIESM, 16, bd de Suisse, MC-98000, Monaco, pp. 1–168.

Clauzon, G., Suc, J.-P., Gautier, F., Berger, A., & Loutre, M.-F. (1996). Alternate interpretation of the Messinian salinity crisis: Controversy resolved? *Geology*, *24*(4), 363–366. https://doi.org/10.1130/0091-7613(1996)024<0363:AIOTMS>2.3.CO;2

Cody, R. D., & Cody, A. M. (1988). Gypsum nucleation and crystal morphology in analog saline terrestrial environments. *Journal of Sedimentary Research*, *58*(2), 247–255. https://doi.org/10.1306/212F8D69-2B24-11D7-8648000102C1865D

Collins, J. A., Schefuß, E., Heslop, D., Mulitza, S., Prange, M., Zabel, M., Tjallingii, R., Dokken, T. M., Huang, E., Mackensen, A., Schulz, M., Tian, J., Zarriess, M., & Wefer, G. (2011). Interhemispheric symmetry of the tropical African rainbelt over the past 23,000 years. *Nature Geoscience*, *4*(1), 42–45. https://doi.org/10.1038/ngeo1039

Collister, J. W., Rieley, G., Stern, B., Eglinton, G., & Fry, B. (1994). Compound-specific δ 13C analyses of leaf lipids from plants with differing carbon dioxide metabolisms. *Organic Geochemistry*, *21*(6), 619–627. https://doi.org/10.1016/0146-6380(94)90008-6

Conte, M. H., & Weber, J. C. (2002). Long-range atmospheric transport of terrestrial biomarkers to the western North Atlantic: ATMOSPHERIC TRANSPORT. *Global Biogeochemical Cycles*, *16*(4), 89-1-89–17. https://doi.org/10.1029/2002GB001922

Cordova-Gonzalez, A., Birgel, D., Kappler, A., & Peckmann, J. (2020). Carbon stable isotope patterns of cyclic terpenoids: A comparison of cultured alkaliphilic aerobic methanotrophic bacteria and methane-seep environments. *Organic Geochemistry*, *139*, 103940. https://doi.org/10.1016/j.orggeochem.2019.103940

Costanzo, A., Cipriani, M., Feely, M., Cianflone, G., & Dominici, R. (2019). Messinian twinned selenite from the Catanzaro Trough, Calabria, Southern Italy: Field, petrographic and fluid inclusion perspectives. *Carbonates and Evaporites*, *34*(3), 743–756. https://doi.org/10.1007/s13146-019-00516-0

Cranwell, P. A. (1973). Chain-length distribution of n-alkanes from lake sediments in relation to post-glacial environmental change. *Freshwater Biology*, *3*(3), 259–265. https://doi.org/10.1111/j.1365-2427.1973.tb00921.x

Danise, S., Twitchett, R. J., & Little, C. T. S. (2015). Environmental controls on Jurassic marine ecosystems during global warming. *Geology*, *43*(3), 263–266. https://doi.org/10.1130/G36390.1

Dawson, K. S., Freeman, K. H., & Macalady, J. L. (2012). Molecular characterization of core lipids from halophilic archaea grown under different salinity conditions. *Organic Geochemistry*, *48*, 1–8. https://doi.org/10.1016/j.orggeochem.2012.04.003

De Bar, M. W., Stolwijk, D. J., McManus, J. F., Sinninghe Damsté, J. S., & Schouten, S. (2018). A Late Quaternary climate record based on long-chain diol proxies from the Chilean margin. *Climate of the Past*, *14*(11), 1783-1803. De Lange, G. J., & Krijgsman, W. (2010). Messinian salinity crisis: A novel

unifying shallow gypsum/deep dolomite formation mechanism. *Marine Geology*, *275*(1), 273–277. https://doi.org/10.1016/j.margeo.2010.05.003

De Lange, G. J., Thomson, J., Reitz, A., Slomp, C. P., Speranza Principato, M., Erba, E., & Corselli, C. (2008). Synchronous basin-wide formation and redox-controlled preservation of a Mediterranean sapropel. *Nature Geoscience*, *1*(9), 606–610. https://doi.org/10.1038/ngeo283

De Rosa, M., Esposito, E., Gambacorta, A., Nicolaus, B., & Bu'Lock, J. D. (1980). Effects of temperature on ether lipid composition of Caldariella acidophila. *Phytochemistry*, *19*(5), 827–831. https://doi.org/10.1016/0031-9422(80)85120-X

De Rosa, M., & Gambacorta, A. (1988). The lipids of archaebacteria. *Progress in Lipid Research*, *27*(3), 153–175. https://doi.org/10.1016/0163-7827(88)90011-2

Degermendzhy, A. G., Zadereev, E. S., Rogozin, D. Yu., Prokopkin, I. G., Barkhatov, Y. V., Tolomeev, A. P., Khromechek, E. B., Janse, J. H., Mooij, W. M., & Gulati, R. D. (2010). Vertical stratification of physical, chemical and biological components in two saline lakes Shira and Shunet (South Siberia, Russia). *Aquatic Ecology*, *44*(3), 619–632. https://doi.org/10.1007/s10452-010-9336-6

Dela Pierre, F., Festa, A., & Irace, A. (2007). Interaction of tectonic, sedimentary, and diapiric processes in the origin of chaotic sediments: An example from the Messinian of Torino Hill (Tertiary Piedmont Basin, northwestern Italy). *GSA Bulletin*, *119*(9–10), 1107–1119. https://doi.org/10.1130/B26072.1

Dela Pierre, F., Bernardi, E., Cavagna, S., Clari, P., Gennari, R., Irace, A., Lozar, F., Lugli, S., Manzi, V., Natalicchio, M., Roveri, M., & Violanti, D. (2011). The record of the Messinian salinity crisis in the Tertiary Piedmont Basin (NW Italy): The Alba section revisited. *Palaeogeography, Palaeoclimatology, Palaeoecology*, *310*(3–4), 238–255. https://doi.org/10.1016/j.palaeo.2011.07.017

Dela Pierre, F., Clari, P., Bernardi, E., Natalicchio, M., Costa, E., Cavagna, S., Lozar, F., Lugli, S., Manzi, V., Roveri, M., & Violanti, D. (2012). Messinian carbonate-rich beds of the Tertiary Piedmont Basin (NW

Italy): Microbially-mediated products straddling the onset of the salinity crisis. *Palaeogeography, Palaeoclimatology, Palaeoecology*, *344–345*, 78–93. https://doi.org/10.1016/j.palaeo.2012.05.022

Dela Pierre, F., Clari, P., Natalicchio, M., Ferrando, S., Giustetto, R., Lozar, F., Lugli, S., Manzi, V., Roveri, M., & Violanti, D. (2014). Flocculent layers and bacterial mats in the mudstone interbeds of the Primary Lower Gypsum unit (Tertiary Piedmont basin, NW Italy): Archives of palaeoenvironmental changes during the Messinian salinity crisis. *Marine Geology*, *355*, 71–87. https://doi.org/10.1016/j.margeo.2014.05.010

Dela Pierre, F., Natalicchio, M., Ferrando, S., Giustetto, R., Birgel, D., Carnevale, G., Gier, S., Lozar, F., Marabello, D., & Peckmann, J. (2015). Are the large filamentous microfossils preserved in Messinian gypsum colorless sulfide-oxidizing bacteria? *Geology*, *43*(10), 855–858. https://doi.org/10.1130/G37018.1

Dela Pierre, F., Natalicchio, M., Lozar, F., Bonetto, S., Carnevale, G., Cavagna, S., Colombero, S., Sabino, M., & Violanti, D. (2016). The northernmost record of the Messinian salinity crisis. *Geological Field Trips*, 58.

DeLong, E. F., King, L. L., Massana, R., Cittone, H., Murray, A., Schleper, C., & Wakeham, S. G. (1998). Dibiphytanyl Ether Lipids in Nonthermophilic Crenarchaeotes. *Applied and Environmental Microbiology*, *64*(3), 1133–1138. https://doi.org/10.1128/AEM.64.3.1133-1138.1998

Diefendorf, A. F., Freeman, K. H., Wing, S. L., Currano, E. D., & Mueller, K. E. (2015a). Paleogene plants fractionated carbon isotopes similar to modern plants. *Earth and Planetary Science Letters*, *429*, 33–44. https://doi.org/10.1016/j.epsl.2015.07.029

Diefendorf, A. F., Leslie, A. B., & Wing, S. L. (2015b). Leaf wax composition and carbon isotopes vary among major conifer groups. *Geochimica et Cosmochimica Acta*, *170*, 145–156. https://doi.org/10.1016/j.gca.2015.08.018

Diefendorf, A. F., Sberna, D. T., & Taylor, D. W. (2015c). Effect of thermal maturation on plant-derived terpenoids and leaf wax n-alkyl components. *Organic Geochemistry*, *89–90*, 61–70. https://doi.org/10.1016/j.orggeochem.2015.10.006

Diefendorf, A. F., & Freimuth, E. J. (2017). Extracting the most from terrestrial plant-derived n-alkyl lipids and their carbon isotopes from the sedimentary record: A review. *Organic Geochemistry*, *103*, 1–21. https://doi.org/10.1016/j.orggeochem.2016.10.016

Diester-Haass, L., Billups, K., & Emeis, K. C. (2006). Late Miocene carbon isotope records and marine biological productivity: Was there a (dusty) link? *Paleoceanography*, *21*(4). https://doi.org/10.1029/2006PA001267

Do Couto, D., Gumiaux, C., Jolivet, L., Augier, R., Lebret, N., Folcher, N., Jouannic, G., Suc, J.-P., & Gorini, C. (2015). 3D modelling of the Sorbas Basin (Spain): New constraints on the Messinian Erosional Surface morphology. *Marine and Petroleum Geology*, *66*, 101–116. https://doi.org/10.1016/j.marpetgeo.2014.12.011

Drake, H., Ivarsson, M., Bengtson, S., Heim, C., Siljeström, S., Whitehouse, M. J., Broman, C., Belivanova, V., & Åström, M. E. (2017). Anaerobic consortia of fungi and sulfate reducing bacteria in deep granite fractures. *Nature Communications*, *8*(1), 55. https://doi.org/10.1038/s41467-017-00094-6

Dronkert, H. (1977). The evaporites of the Sorbas basin. Inst. Invest. Geol. Diput. Prov. Univ. Barcelona, 32, 55–76.

Dronkert, H. (1985). Evaporite models and sedimentology of Messinian and recent evaporites. GUA Pap. Geol. Ser.1 (24), 283.

Duggen, S., Hoernle, K., van den Bogaard, P., Rüpke, L., & Phipps Morgan, J. (2003). Deep roots of the Messinian salinity crisis. *Nature*, *422*(6932), 602–606. https://doi.org/10.1038/nature01553

Edwards, E. J., Osborne, C. P., Strömberg, C. A. E., Smith, S. A., & Consortium, C. G. (2010). The Origins of C4 Grasslands: Integrating Evolutionary and Ecosystem Science. *Science*, *328*(5978), 587–591. https://doi.org/10.1126/science.1177216

Eglinton, G., Gonzalez, A. G., Hamilton, R. J., & Raphael, R. A. (1962). Hydrocarbon constituents of the wax coatings of plant leaves: A taxonomic survey. *Phytochemistry*, *1*(2), 89–102. https://doi.org/10.1016/S0031-9422(00)88006-1

Eglinton, G., & Hamilton, R. J. (1963). Chemical plant taxonomy. *T. Swain, Academic Press, London and New York*, 187.

Eglinton, G., & Hamilton, R. J. (1967). Leaf Epicuticular Waxes. *Science*, *156*(3780), 1322–1335. https://doi.org/10.1126/science.156.3780.1322

Eglinton, G., & Logan, G. A. (1991). Molecular preservation. *Philosophical Transactions of the Royal Society of London. Series B: Biological Sciences*, *333*(1268), 315–328. https://doi.org/10.1098/rstb.1991.0081

Eglinton, T. I., & Eglinton, G. (2008). Molecular proxies for paleoclimatology. *Earth and Planetary Science Letters*, *275*(1–2), 1–16. https://doi.org/10.1016/j.epsl.2008.07.012

Eley, Y. L., & Hren, M. T. (2018). Reconstructing vapor pressure deficit from leaf wax lipid molecular distributions. *Scientific Reports*, *8*(1), 3967. https://doi.org/10.1038/s41598-018-21959-w

Elling, F. J., Könneke, M., Nicol, G. W., Stieglmeier, M., Bayer, B., Spieck, E., Torre, J. R. de la, Becker, K. W., Thomm, M., Prosser, J. I., Herndl, G. J., Schleper, C., & Hinrichs, K.-U. (2017). Chemotaxonomic characterisation of the thaumarchaeal lipidome. *Environmental Microbiology*, *19*(7), 2681–2700. https://doi.org/10.1111/1462-2920.13759

Elshahed, M. S., Savage, K. N., Oren, A., Gutierrez, M. C., Ventosa, A., & Krumholz, L. R. (2004). Haloferax sulfurifontis sp. Nov., a halophilic archaeon isolated from a sulfide- and sulfur-rich spring.

International Journal of Systematic and Evolutionary Microbiology, *54*(6), 2275–2279. https://doi.org/10.1099/ijs.0.63211-0

Evans, N. P., Turchyn, A. V., Gázquez, F., Bontognali, T. R. R., Chapman, H. J., & Hodell, D. A. (2015). Coupled measurements of δ18O and δD of hydration water and salinity of fluid inclusions in gypsum from the Messinian Yesares Member, Sorbas Basin (SE Spain). *Earth and Planetary Science Letters*, *430*, 499–510. https://doi.org/10.1016/j.epsl.2015.07.071

Falk, H., & Wolkenstein, K. (2017). Natural product molecular Fossils. In A. D. Kinghorn, H. Falk, S. Gibbons, & J. Kobayashi (Eds.), *Progress in the Chemistry of Organic Natural Products 104* (Vol. 104, pp. 1–126). Springer International Publishing. https://doi.org/10.1007/978-3-319-45618-8_1

Flecker, R., de Villiers, S., & Ellam, R. M. (2002). Modelling the effect of evaporation on the salinity–87Sr/86Sr relationship in modern and ancient marginal-marine systems: The Mediterranean Messinian Salinity Crisis. *Earth and Planetary Science Letters*, *203*(1), 221–233. https://doi.org/10.1016/S0012-821X(02)00848-8

Flecker, R., Krijgsman, W., Capella, W., de Castro Martíns, C., Dmitrieva, E., Mayser, J. P., Marzocchi, A., Modestou, S., Ochoa, D., Simon, D., Tulbure, M., van den Berg, B., van der Schee, M., de Lange, G., Ellam, R., Govers, R., Gutjahr, M., Hilgen, F., Kouwenhoven, T., … Yousfi, M. Z. (2015). Evolution of the Late Miocene Mediterranean–Atlantic gateways and their impact on regional and global environmental change. *Earth-Science Reviews*, *150*, 365–392. https://doi.org/10.1016/j.earscirev.2015.08.007

Forster, A., Schouten, S., Baas, M., & Damsté, J. S. S. (2007). Mid-Cretaceous (Albian–Santonian) sea surface temperature record of the tropical Atlantic Ocean. *Geology*, *35*(10), 919–922. https://doi.org/10.1130/G23874A.1

Fortuin, A. R., & Krijgsman, W. (2003). The Messinian of the Nijar Basin (SE Spain): Sedimentation, depositional environments and paleogeographic evolution. *Sedimentary Geology*, *160*(1), 213–242. https://doi.org/10.1016/S0037-0738(02)00377-9

Freeman, K. H., & Pancost, R. D. (2014). Biomarkers for terrestrial plants and climate. In *Treatise on Geochemistry* (pp. 395–416). Elsevier. https://doi.org/10.1016/B978-0-08-095975-7.01028-7

Gaines, S. M., Eglinton, G., & Rullkotter, J. (2009). *Echoes of life: what fossil molecules reveal about earth history*. Oxford University Press.

Garcia-Castellanos, D., & Villaseñor, A. (2011). Messinian salinity crisis regulated by competing tectonics and erosion at the Gibraltar arc. *Nature*, *480*(7377), 359–363. https://doi.org/10.1038/nature10651

García-Veigas, J., Cendón, D. I., Gibert, L., Lowenstein, T. K., & Artiaga, D. (2018). Geochemical indicators in Western Mediterranean Messinian evaporites: Implications for the salinity crisis. *Marine Geology*, *403*, 197–214. https://doi.org/10.1016/j.margeo.2018.06.005

Garrett, D. E. (1970). The chemistry and origin of potash deposits. In: Rau JL and Dellwig LF (eds.) 3rd Symposium on Salt, Cleveland, April 21–24, 1969, vol. 1, pp. 211–222. Cleveland, OH: Northern Ohio Geological Society.

Gennari, R., Lozar, F., Turco, E., Dela Pierre, F., Lugli, S., Manzi, V., Natalicchio, M., Roveri, M., Schreiber, B. C., & Taviani, M. (2018). Integrated stratigraphy and paleoceanographic evolution of the pre-evaporitic phase of the Messinian salinity crisis in the Eastern Mediterranean as recorded in the Tokhni section (Cyprus island). *Newsletters on Stratigraphy*, *51*(1), 33–55. https://doi.org/10.1127/nos/2017/0350

Gessner, M.O. (2020) Ergosterol as a Measure of Fungal Biomass. In: Bärlocher F., Gessner M., Graça M. (eds) *Methods to Study Litter Decomposition*. Springer, Cham. https://doi.org/10.1007/978-3-030-30515-4_27

Goad, J., & Akihisa, T. (2012). *Analysis of sterols*. Springer Science & Business Media.

Govers, R. (2009). Choking the Mediterranean to dehydration: The Messinian salinity crisis. *Geology*, *37*(2), 167–170. https://doi.org/10.1130/G25141A.1

Grant, K. M., Grimm, R., Mikolajewicz, U., Marino, G., Ziegler, M., & Rohling, E. J. (2016). The timing of Mediterranean sapropel deposition relative to insolation, sea-level and African monsoon changes. *Quaternary Science Reviews*, *140*, 125–141. https://doi.org/10.1016/j.quascirev.2016.03.026

Grice, K., Schouten, S., Nissenbaum, A., Charrach, J., & Sinninghe Damsté, J. S. (1998). Isotopically heavy carbon in the C21 to C25 regular isoprenoids in halite-rich deposits from the Sdom Formation, Dead Sea Basin, Israel. *Organic Geochemistry*, *28*(6), 349–359. https://doi.org/10.1016/S0146-6380(98)00006-0

Grossart, H.-P., Massana, R., McMahon, K. D., & Walsh, D. A. (2020). Linking metagenomics to aquatic microbial ecology and biogeochemical cycles. *Limnology and Oceanography*, *65*(S1), S2–S20. https://doi.org/10.1002/lno.11382

Grothe, A., Andreetto, F., Reichart, G.-J., Wolthers, M., Van Baak, C. G. C., Vasiliev, I., Stoica, M., Sangiorgi, F., Middelburg, J. J., Davies, G. R., & Krijgsman, W. (2020). Paratethys pacing of the Messinian Salinity Crisis: Low salinity waters contributing to gypsum precipitation? *Earth and Planetary Science Letters*, *532*, 116029. https://doi.org/10.1016/j.epsl.2019.116029

Grothe, A., Brinkhuis, Henk, Krijgsman, Wout, Sangiorgi, Francesca, & University Utrecht. (2016). *The Messinian Salinity Crisis: A Paratethyan perspective* [UU Dept. of Earth Sciences]. https://dspace.library.uu.nl/handle/1874/333994

Guilbert, J.M. & Park, C.F. (1986). The Geology of Ore Deposits. W.H. Freeman and Co., 985 pp

Guhl, B. E., & Finlay, B. J. (1993). Anaerobic predatory ciliates track seasonal migrations of planktonic photosynthetic bacteria. *FEMS Microbiology Letters*, *107*(2–3), 313–316. https://doi.org/10.1111/j.1574-6968.1993.tb06049.x

Gunde-Cimerman, N., Zalar, P., & Cimerman, A., (1997) Diversity of fungal community in high salt marine environments. *Proceedings of International Symposium Environmental Biotechnology* (Verachtert H. Verstraete W., Eds.), pp. 189–191. EFB, Oostende.

Gunde-Cimerman, N., Zalar, P., de Hoog, S., & Plemenitaš, A. (2000). Hypersaline waters in salterns – natural ecological niches for halophilic black yeasts. *FEMS Microbiology Ecology*, *32*(3), 235–240. https://doi.org/10.1111/j.1574-6941.2000.tb00716.x

Güneş, P., Aksu, A. E., & Hall, J. (2018). Internal seismic stratigraphy of the Messinian evaporites across the northern sector of the eastern Mediterranean Sea. *Marine and Petroleum Geology*, *91*, 297–320. https://doi.org/10.1016/j.marpetgeo.2018.01.016

Guo, N., Gao, J., He, Y., Zhang, Z., & Guo, Y. (2014). Variations in leaf epicuticular n-alkanes in some Broussonetia, Ficus and Humulus species. *Biochemical Systematics and Ecology*, *54*, 150–156. https://doi.org/10.1016/j.bse.2014.02.005

Gutiérrez, M. H., Vera, J., Srain, B., Quiñones, R. A., Wörmer, L., Hinrichs, K.-U., & Pantoja-Gutiérrez, S. (2020). Biochemical fingerprints of marine fungi: Implications for trophic and biogeochemical studies. *Aquatic Microbial Ecology*, *84*, 75–90. https://doi.org/10.3354/ame01927

Haq, B., Gorini, C., Baur, J., Moneron, J., & Rubino, J.-L. (2020). Deep Mediterranean's Messinian evaporite giant: How much salt? *Global and Planetary Change*, *184*, 103052. https://doi.org/10.1016/j.gloplacha.2019.103052

Hardie, L. A. (1967). The Gypsum—Anhydrite Equilibrium at One Atmosphere Pressure. *American Mineralogist*, *52*(1–2), 171–200.

Hardie, L. A., & Lowenstein, T. K. (2004). Did the Mediterranean Sea dry out during the Miocene? A Reassessment of the Evaporite Evidence from DSDP Legs 13 and 42A Cores. *Journal of Sedimentary Research*, *74*(4), 453–461. https://doi.org/10.1306/112003740453

Hartman, G., & Danin, A. (2010). Isotopic values of plants in relation to water availability in the Eastern Mediterranean region. *Oecologia*, *162*(4), 837–852. https://doi.org/10.1007/s00442-009-1514-7

Harvey, H. R., Bradshaw, S. A., O'Hara, S. C. M., Eglinton, G., & Corner, E. D. S. (1988). Lipid composition of the marine dinoflagellate Scrippsiella trochoidea. *Phytochemistry*, *27*(6), 1723–1729. https://doi.org/10.1016/0031-9422(88)80432-1

Harvey, H. R., & Mcmanus, G. B. (1991). Marine ciliates as a widespread source of tetrahymanol and hopan-3β-ol in sediments. *Geochimica et Cosmochimica Acta*, *55*(11), 3387–3390. https://doi.org/10.1016/0016-7037(91)90496-R\

Hayes, J. M., Takigiku, R., Ocampo, R., Callot H.J., & Albrecht P. (1987). Isotopic compositions and probable origins of organic molecules in the Eocene Messel shale. *Nature*, 48–51. https://doi.org/10.1038/329048a0, http://dx.doi.org/10.1038/329048a0

Hayes, J. M., Freeman, K. H., Popp, B. N., & Hoham, C. H. (1990). Compound-specific isotopic analyses: A novel tool for reconstruction of ancient biogeochemical processes. *Organic Geochemistry*, *16*(4), 1115–1128. https://doi.org/10.1016/0146-6380(90)90147-R

Herbert, T. D., Lawrence, K. T., Tzanova, A., Peterson, L. C., Caballero-Gill, R., & Kelly, C. S. (2016). Late Miocene global cooling and the rise of modern ecosystems. *Nature Geoscience*, *9*(11), 843–847. https://doi.org/10.1038/ngeo2813

Herfort, L., Schouten, S., Veldhuis, M., Coolen, M.J.L., Wuchter, C., Boon, J.P., Herndl, G.J., Sinninghe Damsté, J.S. (2007). Ecology and physiology of marine Archaea in the North Sea. *FEMS Microbial Ecology*, 62, 242–257.

Hershberger, K. L., Barns, S. M., Reysenbach, A.-L., Dawson, S. C., & Pace, N. R. (1996). Wide diversity of Crenarchaeota. *Nature*, *384*(6608), 420–420. https://doi.org/10.1038/384420a0

Hilgen, F. J., Krijgsman, W., Langereis, C. G., Lourens, L. J., Santarelli, A., & Zachariasse, W. J. (1995). Extending the astronomical (polarity) time scale into the Miocene. *Earth and Planetary Science Letters*, *136*(3–4), 495–510. https://doi.org/10.1016/0012-821X(95)00207-S

Hilgen, F. J., & Krijgsman, W. (1999). Cyclostratigraphy and astrochronology of the Tripolo diatomite formation pre-evaporite Messinian, Sicily, italy. *Terra Nova*, *11*(1), 16-22. http://localhost/handle/1874/1655

Hilgen, F., Kuiper, K., Krijgsman, W., Snel, E., & van der Laan, E. (2007). Astronomical tuning as the basis for high resolution chronostratigraphy: the intricate history of the Messinian Salinity Crisis. *Stratigraphy*, *4*(2–3), 231-238.

Hinrichs, K.-U., Hayes, J. M., Sylva, S. P., Brewer, P. G., & DeLong, E. F. (1999). Methane-consuming archaebacteria in marine sediments. *Nature*, *398*(6730), 802–805. https://doi.org/10.1038/19751

Hoffmann, B., Kahmen, A., Cernusak, L. A., Arndt, S. K., & Sachse, D. (2013). Abundance and distribution of leaf wax n-alkanes in leaves of Acacia and Eucalyptus trees along a strong humidity gradient in northern Australia. *Organic Geochemistry*, *62*, 62–67. https://doi.org/10.1016/j.orggeochem.2013.07.003

Holbourn, A. E., Kuhnt, W., Clemens, S. C., Kochhann, K. G. D., Jöhnck, J., Lübbers, J., & Andersen, N. (2018). Late Miocene climate cooling and intensification of southeast Asian winter monsoon. *Nature Communications*, *9*(1), 1584. https://doi.org/10.1038/s41467-018-03950-1

Holland, H. D. (1984). The Chemical Evolution of the Atmosphere and Oceans: Princeton, Princeton University Press, 582 p.

Hopmans, E. C., Weijers, J. W. H., Schefuß, E., Herfort, L., Sinninghe Damsté, J. S., & Schouten, S. (2004). A novel proxy for terrestrial organic matter in sediments based on branched and isoprenoid tetraether lipids. *Earth and Planetary Science Letters*, *224*(1–2), 107–116. https://doi.org/10.1016/j.epsl.2004.05.012

Hren, M. T., Pagani, M., Erwin, D. M., & Brandon, M. (2010). Biomarker reconstruction of the early Eocene paleotopography and paleoclimate of the northern Sierra Nevada. *Geology*, *38*(1), 7–10. https://doi.org/10.1130/G30215.1

Hsü, K. J., Montadert, L., Bernoulli, D., Cita, M. B., Erickson, A., Garrison, R. E., Kidd, R. B., Mèlierés, F., Müller, C., & Wright, R. (1977). History of the Mediterranean salinity crisis. *Nature*, *267*(5610), 399–403. https://doi.org/10.1038/267399a0

Hsü, K., Ryan, W., & Cita, M. (1973a). Late Miocene Desiccation of the Mediterranean. *Nature*, *242*, 240. https://doi.org/10.1038/242240a0

Hsü, K. J., Cita, M. B., & Ryan, W. B. F. (1973b). The origin of the Mediterranean evaporites. In: Initial Reports of the Deep Sea Drilling Project 13, Part 2. U.S. Government Printing Office, Washington D.C., pp. 1203–1231.

Huang, Y., Dupont, L., Sarnthein, M., Hayes, J. M., & Eglinton, G. (2000). Mapping of C4 plant input from North West Africa into North East Atlantic sediments. *Geochimica et Cosmochimica Acta*, *64*(20), 3505–3513. https://doi.org/10.1016/S0016-7037(00)00445-2

Hughes, W. B., Holba, A. G., & Dzou, L. I. P. (1995). The ratios of dibenzothiophene to phenanthrene and pristane to phytane as indicators of depositional environment and lithology of petroleum source rocks. *Geochimica et Cosmochimica Acta*, *59*(17), 3581–3598. https://doi.org/10.1016/0016-7037(95)00225-O

Huguet, A., Wiesenberg, G. L. B., Gocke, M., Fosse, C., & Derenne, S. (2012). Branched tetraether membrane lipids associated with rhizoliths in loess: Rhizomicrobial overprinting of initial biomarker record. *Organic Geochemistry*, *43*, 12–19. https://doi.org/10.1016/j.orggeochem.2011.11.006

Huguet, C., Hopmans, E. C., Febo-Ayala, W., Thompson, D. H., Sinninghe Damsté, J. S., & Schouten, S. (2006). An improved method to determine the absolute abundance of glycerol dibiphytanyl glycerol

tetraether lipids. *Organic Geochemistry*, *37*(9), 1036–1041. https://doi.org/10.1016/j.orggeochem.2006.05.008

Huybers, P., & Aharonson, O. (2010). Orbital tuning, eccentricity, and the frequency modulation of climatic precession. *Paleoceanography*, *25*(4). https://doi.org/10.1029/2010PA001952

Iaccarino, S.M., Castradori, D., Cita, M.B., Di Stefano, E., Gaboardi, S., Mckenzie, J.A., Spezzaferri, S., Sprovieri, R., (1999). The Miocene/Pliocene boundary and the significance of the earliest Pliocene flooding in the Mediterranean. Memorie della *Società Geoligica Italiana*, 54, 109–131.

Isaji, Y., Kawahata, H., Takano, Y., Ogawa, N. O., Kuroda, J., Yoshimura, T., Lugli, S., Manzi, V., Roveri, M., & Ohkouchi, N. (2019). Diazotrophy Drives Primary Production in the Organic-Rich Shales Deposited Under a Stratified Environment During the Messinian Salinity Crisis (Vena del Gesso, Italy). *Frontiers in Earth Science*, *7*, 85. https://doi.org/10.3389/feart.2019.00085

Jansen, B., & Wiesenberg, G. L. B. (2017). Opportunities and limitations related to the application of plant-derived lipid molecular proxies in soil science. *SOIL*, *3*(4), 211–234. https://doi.org/10.5194/soil-3-211-2017

Jeng, W.-L. (2006). Higher plant n-alkane average chain length as an indicator of petrogenic hydrocarbon contamination in marine sediments. *Marine Chemistry*, *102*(3–4), 242–251. https://doi.org/10.1016/j.marchem.2006.05.001

Jenkyns, H. C., Forster, A., Schouten, S., & Sinninghe Damsté, J. S. (2004). High temperatures in the Late Cretaceous Arctic Ocean. *Nature*, *432*(7019), 888–892. https://doi.org/10.1038/nature03143

Jenkyns, H. C., Schouten-Huibers, L., Schouten, S., & Sinninghe Damsté, J. S. (2012). Warm Middle Jurassic–Early Cretaceous high-latitude sea-surface temperatures from the Southern Ocean. *Climate of the Past*, *8*(1), 215–226. https://doi.org/10.5194/cp-8-215-2012

Kamilova, T. A., & Ekhvalova, T. V. (1989). Episterol and fungisterol from mutant strains of the yeast Saccharomyces cerevisiae. *Chemistry of Natural Compounds*, *25*(5), 624–625. https://doi.org/10.1007/BF00598097

Keely, B. J., Blake, S. R., Schaeffer, P., & Maxwell, J. R. (1995). Distributions of pigments in the organic matter of marls from the Vena del Gesso evaporitic sequence. *Organic Geochemistry*, *23*(6), 527–539. https://doi.org/10.1016/0146-6380(95)00046-H

Kendall, A.C. (1992) Evaporites. In: Facies Models: Response to sea level change (eds R.G. Walker and N.P. James), pp. 375–409. Geological Association of Canada, St John, Newfoundland.

Kenig, F., Sinninghe Damsté, J. S., Frewin, N. L., Hayes, J. M., & De Leeuw, J. W. (1995). Molecular indicators for palaeoenvironmental change in a Messinian evaporitic sequence (Vena del Gesso, Italy). II: High-resolution variations in abundances and 13C contents of free and sulphur-bound carbon skeletons in a single marl bed. *Organic Geochemistry*, *23*(6), 485–526. https://doi.org/10.1016/0146-6380(95)00049-K

Kennicutt II, M. C., Barker, C., Brooks, J. M., DeFreitas, D. A., & Zhu, G. H. (1987). Selected organic matter source indicators in the Orinoco, Nile and Changjiang deltas. *Organic Geochemistry*, *11*(1), 41-51.

Khromechek, E. B., Barkhatov, Y. V., & Rogozin, D. Y. (2010). Densities and distribution of flagellates and ciliates in the chemocline of saline, meromictic Lake Shunet (Siberia, Russia). *Aquatic Ecology*, *44*(3), 497–511. https://doi.org/10.1007/s10452-010-9332-x

Kim, J.-H., Schouten, S., Hopmans, E. C., Donner, B., & Sinninghe Damsté, J. S. (2008). Global sediment core-top calibration of the TEX86 paleothermometer in the ocean. *Geochimica et Cosmochimica Acta*, *72*(4), 1154–1173. https://doi.org/10.1016/j.gca.2007.12.010

Kim, J.-H., van der Meer, J., Schouten, S., Helmke, P., Willmott, V., Sangiorgi, F., Koç, N., Hopmans, E. C., & Damsté, J. S. S. (2010). New indices and calibrations derived from the distribution of crenarchaeal

isoprenoid tetraether lipids: Implications for past sea surface temperature reconstructions. *Geochimica et Cosmochimica Acta*, *74*(16), 4639–4654. https://doi.org/10.1016/j.gca.2010.05.027

Kleemann, G., Poralla, K., Englert, G., Kjøsen, H., Liaaen-Jensen, S., Neunlist, S., & Rohmer, M. (1990). Tetrahymanol from the phototrophic bacterium Rhodopseudomonas palustris: First report of a gammacerane triterpene from a prokaryote. *Microbiology, 136*(12), 2551–2553. https://doi.org/10.1099/00221287-136-12-2551

Koga, Y., & Morii, H. (2007). Biosynthesis of Ether-Type Polar Lipids in Archaea and Evolutionary Considerations. *Microbiology and Molecular Biology Reviews*, *71*(1), 97–120. https://doi.org/10.1128/MMBR.00033-06

Koga, Y., Morii, H., Akagawa-Matsushita, M., & Ohga, M. (1998). Correlation of polar lipid composition with 16S rRNA phylogeny in methanogens. Further analysis of lipid component parts. *Bioscience, Biotechnology, and Biochemistry*, *62*(2), 230–236. https://doi.org/10.1271/bbb.62.230

Koga, Y., Nishihara, M., Morii, H., & Akagawa-Matsushita, M. (1993). Ether polar lipids of methanogenic bacteria: Structures, comparative aspects, and biosyntheses. *Microbiology and Molecular Biology Reviews*, *57*(1), 164–182.

Kouwenhoven, T. J., Hilgen, F. J., & van der Zwaan, G. J. (2003). Late Tortonian–early Messinian stepwise disruption of the Mediterranean–Atlantic connections: Constraints from benthic foraminiferal and geochemical data. *Palaeogeography, Palaeoclimatology, Palaeoecology*, *198*(3), 303–319. https://doi.org/10.1016/S0031-0182(03)00472-3

Kouwenhoven, T. J., Seidenkrantz, M.-S., & van der Zwaan, G. J. (1999). Deep-water changes: The near-synchronous disappearance of a group of benthic foraminifera from the Late Miocene Mediterranean1NSG Paper No. 99037.1. *Palaeogeography, Palaeoclimatology, Palaeoecology*, *152*(3), 259–281. https://doi.org/10.1016/S0031-0182(99)00065-6

Kouwenhoven, T. J., Morigi, C., Negri, A., Giunta, S., Krijgsman, W., & Rouchy, J.-M. (2006). Paleoenvironmental evolution of the eastern Mediterranean during the Messinian: Constraints from integrated microfossil data of the Pissouri Basin (Cyprus). *Marine Micropaleontology*, *60*(1), 17–44. https://doi.org/10.1016/j.marmicro.2006.02.005

Kouwenhoven, T. J., & van der Zwaan, G. J. (2006). A reconstruction of late Miocene Mediterranean circulation patterns using benthic foraminifera. *Palaeogeography, Palaeoclimatology, Palaeoecology*, *238*(1), 373–385. https://doi.org/10.1016/j.palaeo.2006.03.035

Krijgsman, W., Hilgen, F. J., Raffi, I., Sierro, F. J., & Wilson, D. S. (1999). Chronology, causes and progression of the Messinian salinity crisis. *Nature*, *400*(6745), 652–655. https://doi.org/10.1038/23231

Krijgsman, W., Fortuin, A. R., Hilgen, F. J., & Sierro, F. J. (2001). Astrochronology for the Messinian Sorbas basin (SE Spain) and orbital (precessional) forcing for evaporite cyclicity. *Sedimentary Geology*, *140*(1–2), 43–60. https://doi.org/10.1016/S0037-0738(00)00171-8

Krijgsman, W., Blanc-Valleron, M.-M., Flecker, R., Hilgen, F. J., Kouwenhoven, T. J., Merle, D., Orszag-Sperber, F., & Rouchy, J.-M. (2002). The onset of the Messinian salinity crisis in the Eastern Mediterranean (Pissouri Basin, Cyprus). *Earth and Planetary Science Letters*, *194*(3–4), 299–310. https://doi.org/10.1016/S0012-821X(01)00574-X

Krijgsman, W., Stoica, M., Vasiliev, I., & Popov, V. V. (2010). Rise and fall of the Paratethys Sea during the Messinian Salinity Crisis. *Earth and Planetary Science Letters*, *290*(1), 183–191. https://doi.org/10.1016/j.epsl.2009.12.020

Kutzbach, J. E., Chen, G., Cheng, H., Edwards, R. L., & Liu, Z. (2014). Potential role of winter rainfall in explaining increased moisture in the Mediterranean and Middle East during periods of maximum orbitally-forced insolation seasonality. *Climate Dynamics*, *42*(3–4), 1079–1095. https://doi.org/10.1007/s00382-013-1692-1

Kuypers, M. M. M., Blokker, P., Erbacher, J., Kinkel, H., Pancost, R. D., Schouten, S., & Damsté, J. S. S. (2001). Massive expansion of marine Archaea during a Mid-Cretaceous Oceanic Anoxic Event. *Science*, *293*(5527), 92–95. https://doi.org/10.1126/science.1058424

LaRowe, D. E., & Van Cappellen, P. (2011). Degradation of natural organic matter: A thermodynamic analysis. *Geochimica et Cosmochimica Acta*, *75*(8), 2030–2042. https://doi.org/10.1016/j.gca.2011.01.020

Lascaratos, A., Roether, W., Nittis, K., & Klein, B. (1999). Recent changes in deep water formation and spreading in the eastern Mediterranean Sea: A review. *Progress in Oceanography*, *44*(1–3), 5–36. https://doi.org/10.1016/S0079-6611(99)00019-1

Laskar, J., Robutel, P., Joutel, F., Gastineau, M., Correia, A. C. M., & Levrard, B. (2004). A long-term numerical solution for the insolation quantities of the Earth. *Astronomy & Astrophysics*, *428*(1), 261–285. https://doi.org/10.1051/0004-6361:20041335

Lofi, J., Gorini, C., Berné, S., Clauzon, G., Tadeu Dos Reis, A., Ryan, W. B. F., & Steckler, M. S. (2005). Erosional processes and paleo-environmental changes in the Western Gulf of Lions (SW France) during the Messinian Salinity Crisis. *Marine Geology*, *217*(1), 1–30. https://doi.org/10.1016/j.margeo.2005.02.014

Lofi, J., Sage, F., Déverchère, J., Loncke, L., Maillard, A., Gaullier, V., Thinon, I., Gillet, H., Guennoc, P., & Gorini, C. (2011a). Refining our knowledge of the Messinian salinity crisis records in the offshore domain through multi-site seismic analysis. *Bulletin de La Société Géologique de France*, *182*(2), 163–180. https://doi.org/10.2113/gssgfbull.182.2.163

Lofi, J., Déverchère, J., Gaullier, V., Gillet, H., Gorini, C., Guennoc, P., Loncke, L., Maillard, A., Sage, F., & Thinon, I. (2011b). Seismic Atlas of the Messinian Salinity Crisis markers in the Mediterranean and Black Seas. In *Mémoire de la Société Géologique n.s.: Vol. t. 179* (p. 1). Société Géologique de France. https://hal-brgm.archives-ouvertes.fr/hal-00593502

Logan, B.W. (1987). The MacLeod evaporite basin, western Australia. Holocene environments, sediments and geological evolution. *AAPG Memoir*, 44: 1–140.

Lozar, F., Violanti, D., Pierre, F. D., Bernardi, E., Cavagna, S., Clari, P., Irace, A., Martinetto, E., & Trenkwalder, S. (2010). Calcareous nannofossils and foraminifers herald the Messinian Salinity Crisis: The Pollenzo section (Alba, Cuneo; NW Italy). *Geobios*, *43*(1), 21–32. https://doi.org/10.1016/j.geobios.2009.07.002

Lozar, F., Violanti, D., Bernardi, E., Dela Pierre, F., & Natalicchio, M. (2018). Identifying the onset of the Messinian salinity crisis: A reassessment of the biochronostratigraphic tools (Piedmont Basin, NW Italy). *Newsletters on Stratigraphy*, *51*(1), 11–31. https://doi.org/10.1127/nos/2017/0354

Lozar, F., & Negri, A. (2019). A review of basin-wide calcareous nannofossil bioevents in the Mediterranean at the onset of the Messinian salinity crisis. *Marine Micropaleontology*, *151*, 101752. https://doi.org/10.1016/j.marmicro.2019.101752

Lugli, S., Vinicio, M., Marco, R., & Charlotte, S. B. (2010). The Primary Lower Gypsum in the Mediterranean: A new facies interpretation for the first stage of the Messinian salinity crisis. *Palaeogeography, Palaeoclimatology, Palaeoecology*, *297*(1), 83–99. https://doi.org/10.1016/j.palaeo.2010.07.017

Lugli, S., Manzi, V., Roveri, M., & Schreiber, B. C. (2015). The deep record of the Messinian salinity crisis: Evidence of a non-desiccated Mediterranean Sea. *Palaeogeography, Palaeoclimatology, Palaeoecology*, *433*, 201–218. https://doi.org/10.1016/j.palaeo.2015.05.017

Luo, G., Yang, H., Algeo, T. J., Hallmann, C., & Xie, S. (2019). Lipid biomarkers for the reconstruction of deep-time environmental conditions. *Earth-Science Reviews*, *189*, 99–124. https://doi.org/10.1016/j.earscirev.2018.03.005

Ma, J.-Y., Sun, W., Liu, X.-N., & Chen, F.-H. (2012). Variation in the Stable Carbon and Nitrogen Isotope Composition of Plants and Soil along a Precipitation Gradient in Northern China. *PLOS ONE*, *7*(12), e51894. https://doi.org/10.1371/journal.pone.0051894

MacElroy, R. D. (1974). Some comments on the evolution of extremophiles. *Biosystems*, *6*(1), 74-75.

MacGregor, B. J., Moser, D. P., Alm, E. W., Nealson, K. H., & Stahl, D. A. (1997). Crenarchaeota in Lake Michigan sediment. *Applied and Environmental Microbiology*, *63*(3), 1178–1181.

Mallory, F. B., Gordon, J. T., & Conner, R. L. (1963). The isolation of a pentacyclic triterpenoid alcohol from a protozoan. *Journal of the American Chemical Society*, *85*(9), 1362-1363. https://doi.org/10.1021/ja00892a042

Mancini, A. M., Gennari, R., Ziveri, P., Mortyn, P. G., Stolwijk, D. J., & Lozar, F. (2020). Calcareous nannofossil and foraminiferal trace element records in the Sorbas Basin: A new piece of the Messinian Salinity Crisis onset puzzle. *Palaeogeography, Palaeoclimatology, Palaeoecology*, 109796. https://doi.org/10.1016/j.palaeo.2020.109796

Manzi, V., Lugli, S., Lucchi, F. R., & Roveri, M. (2005). Deep-water clastic evaporites deposition in the Messinian Adriatic foredeep (northern Apennines, Italy): Did the Mediterranean ever dry out? *Sedimentology*, *52*(4), 875–902. https://doi.org/10.1111/j.1365-3091.2005.00722.x

Manzi, V., Roveri, M., Gennari, R., Bertini, A., Biffi, U., Giunta, S., Iaccarino, S. M., Lanci, L., Lugli, S., Negri, A., Riva, A., Rossi, M. E., & Taviani, M. (2007). The deep-water counterpart of the Messinian Lower Evaporites in the Apennine foredeep: The Fanantello section (Northern Apennines, Italy). *Palaeogeography, Palaeoclimatology, Palaeoecology*, *251*(3–4), 470–499. https://doi.org/10.1016/j.palaeo.2007.04.012

Manzi, V., Lugli, S., Roveri, M., & Schreiber, B. C. (2009). A new facies model for the Upper Gypsum of Sicily (Italy): Chronological and palaeoenvironmental constraints for the Messinian salinity crisis in

the Mediterranean. *Sedimentology*, *56*(7), 1937–1960. https://doi.org/10.1111/j.1365-3091.2009.01063.x

Manzi, V., Lugli, S., Roveri, M., Schreiber, B. C., & Gennari, R. (2011). The Messinian "Calcare di Base" (Sicily, Italy) revisited. *Geological Society of America Bulletin*, *123*(1–2), 347–370. https://doi.org/10.1130/B30262.1

Manzi, V., Gennari, R., Lugli, S., Roveri, M., Scafetta, N., & Schreiber, B. C. (2012). High-frequency cyclicity in the Mediterranean Messinian evaporites: evidence for solar–lunar climate forcing. *Journal of Sedimentary Research*, *82*(12), 991-1005. https://doi.org/10.2110/jsr.2012.81

Manzi, V., Gennari, R., Hilgen, F., Krijgsman, W., Lugli, S., Roveri, M., & Sierro, F. J. (2013). Age refinement of the Messinian salinity crisis onset in the Mediterranean. *Terra Nova*, *25*(4), 315–322. https://doi.org/10.1111/ter.12038

Mariotti, A., Struglia, M. V., Zeng, N., & Lau, K.-M. (2002). The Hydrological Cycle in the Mediterranean Region and Implications for the Water Budget of the Mediterranean Sea. *Journal of Climate*, *15*(13), 1674–1690. https://doi.org/10.1175/1520-0442(2002)015<1674:THCITM>2.0.CO;2

Mayser, J. P., Flecker, R., Marzocchi, A., Kouwenhoven, T. J., Lunt, D. J., & Pancost, R. D. (2017). Precession driven changes in terrestrial organic matter input to the Eastern Mediterranean leading up to the Messinian Salinity Crisis. *Earth and Planetary Science Letters*, *462*, 199–211. https://doi.org/10.1016/j.epsl.2017.01.029

Mbogoro, M. M., Peruffo, M., Adobes-Vidal, M., Field, E. L., O'Connell, M. A., & Unwin, P. R. (2017). Quantitative 3D Visualization of the Growth of Individual Gypsum Microcrystals: Effect of Ca2+:SO42– Ratio on Kinetics and Crystal Morphology. *The Journal of Physical Chemistry C*, *121*(23), 12726–12734. https://doi.org/10.1021/acs.jpcc.7b01566

McCaffrey, M. A., Lazar, B., & Holland, H. D. (1987). The evaporation path of seawater and the coprecipitation of Br (super -) and K (super +) with halite. *Journal of Sedimentary Research*, *57*(5), 928–937. https://doi.org/10.1306/212F8CAB-2B24-11D7-8648000102C1865D

McCallister, S. L., Bauer, J. E., Ducklow, H. W., & Canuel, E. A. (2006). Sources of estuarine dissolved and particulate organic matter: A multi-tracer approach. *Organic Geochemistry*, *37*(4), 454–468. https://doi.org/10.1016/j.orggeochem.2005.12.005

McCulloch, M. T., & Deckker, P. D. (1989). Sr isotope constraints on the Mediterranean environment at the end of the Messinian salinity crisis. *Nature*, *342*(6245), 62–65. https://doi.org/10.1038/342062a0

McInerney, F. A., & Wing, S. L. (2011). The Paleocene-Eocene Thermal Maximum: A perturbation of carbon cycle, climate, and biosphere with implications for the future. *Annual Review of Earth and Planetary Sciences*, *39*(1), 489–516. https://doi.org/10.1146/annurev-earth-040610-133431

Medeiros, P. M., & Simoneit, B. R. T. (2008). Multi-biomarker characterization of sedimentary organic carbon in small rivers draining the Northwestern United States. *Organic Geochemistry*, *39*(1), 52–74. https://doi.org/10.1016/j.orggeochem.2007.10.001

Mei, X., Li, R., Zhang, X., Wang, Z., & Zhang, Y., (2019). Reconstruction of phytoplankton productivity and community structure in the South Yellow Sea. *China Geology*, *2*(3), 313–322. https://doi.org/10.31035/cg2018091

Meijer, P. Th., & Krijgsman, W. (2005). A quantitative analysis of the desiccation and re-filling of the Mediterranean during the Messinian Salinity Crisis. *Earth and Planetary Science Letters*, *240*(2), 510–520. https://doi.org/10.1016/j.epsl.2005.09.029

Meijer, P. Th., & Tuenter, E. (2007). The effect of precession-induced changes in the Mediterranean freshwater budget on circulation at shallow and intermediate depth. *Journal of Marine Systems*, *68*(3), 349–365. https://doi.org/10.1016/j.jmarsys.2007.01.006

Menzel, D., Hopmans, E. C., Schouten, S., & Sinninghe Damsté, J. S. (2006). Membrane tetraether lipids of planktonic Crenarchaeota in Pliocene sapropels of the eastern Mediterranean Sea. *Palaeogeography, Palaeoclimatology, Palaeoecology*, *239*(1), 1–15. https://doi.org/10.1016/j.palaeo.2006.01.002

Menzel, D., van Bergen, P. F., Schouten, S., & Sinninghe Damsté, J. S. (2003). Reconstruction of changes in export productivity during Pliocene sapropel deposition: A biomarker approach. *Palaeogeography, Palaeoclimatology, Palaeoecology*, *190*, 273–287. https://doi.org/10.1016/S0031-0182(02)00610-7

Micallef, A., Camerlenghi, A., Garcia-Castellanos, D., Cunarro Otero, D., Gutscher, M.-A., Barreca, G., Spatola, D., Facchin, L., Geletti, R., Krastel, S., Gross, F., & Urlaub, M. (2018). Evidence of the Zanclean megaflood in the eastern Mediterranean Basin. *Scientific Reports*, *8*(1), 1078. https://doi.org/10.1038/s41598-018-19446-3

Miller, K. G., Mountain, G. S., Wright, J. D., & Browning, J. V. (2011). A 180-million-year record of sea level and ice volume variations from continental margin and deep-sea isotopic records. *Oceanography*, *24*(2), 40–53.

Modestou, S., Simon, D., Gutjahr, M., Marzocchi, A., Kouwenhoven, T. J., Ellam, R. M., & Flecker, R. (2017). Precessional variability of 87Sr/86Sr in the late Miocene Sorbas Basin: An interdisciplinary study of drivers of interbasin exchange. *Paleoceanography*, *32*(6), 531–552. https://doi.org/10.1002/2016PA003061

Morales, S. E., Biswas, A., Herndl, G. J., & Baltar, F. (2019). Global Structuring of Phylogenetic and Functional Diversity of Pelagic Fungi by Depth and Temperature. *Frontiers in Marine Science*, *6*, 131. https://doi.org/10.3389/fmars.2019.00131

Moreau, R. A., Whitaker, B. D., & Hicks, K. B. (2002). Phytosterols, phytostanols, and their conjugates in foods: Structural diversity, quantitative analysis, and health-promoting uses. *Progress in Lipid Research*, *41*(6), 457–500. https://doi.org/10.1016/S0163-7827(02)00006-1

Mosca, P., Polino, R., Rogledi, S., & Rossi, M. (2010). New data for the kinematic interpretation of the Alps–Apennines junction (Northwestern Italy). *International Journal of Earth Sciences*, *99*(4), 833–849. https://doi.org/10.1007/s00531-009-0428-2

Mouradian, M., Panetta, R. J., Vernal, A. de, & GÉlinas, Y. (2007). Dinosterols or dinocysts to estimate dinoflagellate contributions to marine sedimentary organic matter? *Limnology and Oceanography*, *52*(6), 2569–2581. https://doi.org/10.4319/lo.2007.52.6.2569

Myher, J. J., & Kuksis, A. (1995). General strategies in chromatographic analysis of lipids. *Journal of Chromatography B: Biomedical Sciences and Applications*, *671*(1), 3–33. https://doi.org/10.1016/0378-4347(95)00178-L

Naafs, B. D. A., Hefter, J., Acton, G., Haug, G. H., Martínez-Garcia, A., Pancost, R., & Stein, R. (2012). Strengthening of North American dust sources during the late Pliocene (2.7Ma). *Earth and Planetary Science Letters*, *317–318*, 8–19. https://doi.org/10.1016/j.epsl.2011.11.026

Naafs, B. D. A., Inglis, G. N., Blewett, J., McClymont, E. L., Lauretano, V., Xie, S., Evershed, R. P., & Pancost, R. D. (2019). The potential of biomarker proxies to trace climate, vegetation, and biogeochemical processes in peat: A review. *Global and Planetary Change*, *179*, 57–79. https://doi.org/10.1016/j.gloplacha.2019.05.006

Nash, D., Clemow, L., Leeming, R., Hannah, M., Halliwell, D., & Allen, D. (2004). Sterols and other alcohols in overland flow from grazing land and possible source materials. SuperSoil 2004: 3rd Australian New Zealand Soils Conference, 5 – 9 December 2004, University of Sydney, Australia.

Natalicchio, M., Birgel, D., Peckmann, J., Lozar, F., Carnevale, G., Liu, X., Hinrichs, K.-U., & Dela Pierre, F. (2017). An archaeal biomarker record of paleoenvironmental change across the onset of the Messinian salinity crisis in the absence of evaporites (Piedmont Basin, Italy). *Organic Geochemistry*, *113*, 242–253. https://doi.org/10.1016/j.orggeochem.2017.08.014

Natalicchio, M., Dela Pierre, F., Birgel, D., Brumsack, H., Carnevale, G., Gennari, R., Gier, S., Lozar, F., Pellegrino, L., Sabino, M., Schnetger, B., & Peckmann, J. (2019). Paleoenvironmental change in a precession-paced succession across the onset of the Messinian salinity crisis: Insight from element geochemistry and molecular fossils. *Palaeogeography, Palaeoclimatology, Palaeoecology*, *518*, 45–61. https://doi.org/10.1016/j.palaeo.2019.01.009

Natalicchio, M., Dela Pierre, F., Lugli, S., Lowenstein, T. K., Feiner, S. J., Ferrando, S., Manzi, V., Roveri, M., & Clari, P. (2014). Did Late Miocene (Messinian) gypsum precipitate from evaporated marine brines? Insights from the Piedmont Basin (Italy). *Geology*, *42*(3), 179–182. https://doi.org/10.1130/G34986.1

Newell, S. Y. (2001). Fungal biomass and productivity. In *Methods in Microbiology* (Vol. 30, pp. 357–372). Academic Press. https://doi.org/10.1016/S0580-9517(01)30053-3

Niessen, W. M. (2006). *Liquid chromatography-mass spectrometry*. CRC press.

Nishimura, M. (1978). Geochemical characteristics of the high reduction zone of stenols in Suwa sediments and the environmental factors controlling the conversion of stenols into stanols. *Geochimica et Cosmochimica Acta*, *42*(4), 349–357. https://doi.org/10.1016/0016-7037(78)90265-X

Orszag-Sperber, F. (2006). Changing perspectives in the concept of "Lago-Mare" in Mediterranean Late Miocene evolution. *Sedimentary Geology*, *188–189*, 259–277. https://doi.org/10.1016/j.sedgeo.2006.03.008

Orti Cabo, F., Pueyo Mur, J. J., Geisler-Cussey, D., & Dulau, N. (1984). Evaporitic sedimentation in the coastal salinas of Santa Pola, Alicante, Spain. *Evaporitic Sedimentation in the Coastal Salinas of Santa Pola, Alicante, Spain*, *38–39*, 169–220.

Otto, A., & Wilde, V. (2001). Sesqui-, di-, and triterpenoids as chemosystematic markers in extant conifers—A review. *The Botanical Review*, *67*(2), 141–238. https://doi.org/10.1007/BF02858076

Pagani, M., Freeman, K.H., Arthur, M.A. (1999). Late Miocene Atmospheric CO2 Concentrations and the Expansion of C4 Grasses. *Science*, *285*(5429), 876–879. https://doi.org/10.1126/science.285.5429.876

Pancost, R. D., & Boot, C. S. (2004). The palaeoclimatic utility of terrestrial biomarkers in marine sediments. *Marine Chemistry*, *92*(1), 239–261. https://doi.org/10.1016/j.marchem.2004.06.029

Pancost, R. D., Freeman, K. H., Herrmann, A. D., Patzkowsky, M. E., Ainsaar, L., & Martma, T. (2013). Reconstructing Late Ordovician carbon cycle variations. *Geochimica et Cosmochimica Acta*, *105*, 433–454. https://doi.org/10.1016/j.gca.2012.11.033

Pancost, R. D., Geel, B. van, Baas, M., & Damsté, J. S. S. (2000). Δ13C values and radiocarbon dates of microbial biomarkers as tracers for carbon recycling in peat deposits. *Geology*, *28*(7), 663–666. https://doi.org/10.1130/0091-7613(2000)28<663:CVARDO>2.0.CO;2

Pancost, R. D., Hopmans, E. C., & Sinninghe Damsté, J. S. (2001). Archaeal lipids in Mediterranean cold seeps: Molecular proxies for anaerobic methane oxidation. *Geochimica et Cosmochimica Acta*, *65*(10), 1611–1627. https://doi.org/10.1016/S0016-7037(00)00562-7

Pancost, R. D., Zhang, C. L., Tavacoli, J., Talbot, H. M., Farrimond, P., Schouten, S., Sinninghe Damsté, J. S., & Sassen, R. (2005). Lipid biomarkers preserved in hydrate-associated authigenic carbonate rocks of the Gulf of Mexico. *Palaeogeography, Palaeoclimatology, Palaeoecology*, *227*(1), 48–66. https://doi.org/10.1016/j.palaeo.2005.04.035

Pancost, R. D., McClymont, E. L., Bingham, E. M., Roberts, Z., Charman, D. J., Hornibrook, E. R. C., Blundell, A., Chambers, F. M., Lim, K. L. H., & Evershed, R. P. (2011). Archaeol as a methanogen biomarker in ombrotrophic bogs. *Organic Geochemistry*, *42*(10), 1279–1287. https://doi.org/10.1016/j.orggeochem.2011.07.003

Panieri, G., Lugli, S., Manzi, V., Roveri, M., Schreiber, B. C., & Palinska, K. A. (2010). Ribosomal RNA gene fragments from fossilized cyanobacteria identified in primary gypsum from the late Miocene, Italy. *Geobiology*, *8*(2), 101–111. https://doi.org/10.1111/j.1472-4669.2009.00230.x

Patterson, G. W., & Nes, W. D. (Eds.). (1991). *Physiology and biochemistry of sterols*. The American Oil Chemists Society.

Peters, K. E., & Moldowan, J. M. (1993). The biomarker guide: interpreting molecular fossils in petroleum and ancient sediments.

Peterse, F., Kim, J.-H., Schouten, S., Kristensen, D. K., Koç, N., & Sinninghe Damsté, J. S. (2009). Constraints on the application of the MBT/CBT palaeothermometer at high latitude environments (Svalbard, Norway). *Organic Geochemistry*, *40*(6), 692–699. https://doi.org/10.1016/j.orggeochem.2009.03.004

Peterse, F., van der Meer, J., Schouten, S., Weijers, J. W. H., Fierer, N., Jackson, R. B., Kim, J.-H., & Sinninghe Damsté, J. S. (2012). Revised calibration of the MBT–CBT paleotemperature proxy based on branched tetraether membrane lipids in surface soils. *Geochimica et Cosmochimica Acta*, *96*, 215–229. https://doi.org/10.1016/j.gca.2012.08.011

Philp, R. P., & Lewis, C. A. (1987). Organic geochemistry of biomarkers. *Annual Review of Earth and Planetary Sciences*, *15*(1), 363-395.

Pitcher, A., Wuchter, C., Siedenberg, K., Schouten, S., & Damsté, J. S. S. (2011). Crenarchaeol tracks winter blooms of ammonia-oxidizing Thaumarchaeota in the coastal North Sea. *Limnology and Oceanography*, *56*(6), 2308–2318. https://doi.org/10.4319/lo.2011.56.6.2308

Plumb, J. J., Gibbs, B., Stott, M. B., Robertson, W. J., Gibson, J. A. E., Nichols, P. D., Watling, H. R., & Franzmann, P. D. (2002). Enrichment and characterisation of thermophilic acidophiles for the bioleaching of mineral sulphides. *Minerals Engineering*, *15*(11), 787–794. https://doi.org/10.1016/S0892-6875(02)00117-6

Poynter, J. G., Farrimond, P., Robinson, N., & Eglinton, G. (1989). Aeolian-Derived Higher Plant Lipids in the Marine Sedimentary Record: Links with Palaeoclimate. In M. Leinen & M. Sarnthein (Eds.), *Paleoclimatology and Paleometeorology: Modern and Past Patterns of Global Atmospheric Transport* (pp. 435–462). Springer Netherlands. https://doi.org/10.1007/978-94-009-0995-3_18

Poynter, J., Eglinton, G. (1990). Molecular composition of three sediments from Hole 717C: the Bengal Fan. In: Cochran, J.R., Stow, D.A.V. (Eds.), Proc. ODP, Sci. Results. vol 116. pp. 155–161 College Station, TX (Ocean Drilling Program).

Prahl, F. G., & Wakeham, S. G. (1987). Calibration of unsaturation patterns in long-chain ketone compositions for palaeotemperature assessment. *Nature*, *330*(6146), 367–369. https://doi.org/10.1038/330367a0

Prartono, T., & Wolff, G. A. (1998). Organic geochemistry of lacustrine sediments: A record of the changing trophic status of Rostherne Mere, U.K. *Organic Geochemistry*, *28*(11), 729–747. https://doi.org/10.1016/S0146-6380(98)00016-3

Rabizadeh, T., Peacock, C. L., & Benning, L. G. (2014). Carboxylic acids: Effective inhibitors for calcium sulfate precipitation? *Mineralogical Magazine*, *78*(6), 1465–1472. https://doi.org/10.1180/minmag.2014.078.6.13

Rabizadeh, T., Stawski, T. M., Morgan, D. J., Peacock, C. L., & Benning, L. G. (2017). The Effects of Inorganic Additives on the Nucleation and Growth Kinetics of Calcium Sulfate Dihydrate Crystals. *Crystal Growth & Design*, *17*(2), 582–589. https://doi.org/10.1021/acs.cgd.6b01441

Rampen, S. W., Schouten, S., Wakeham, S. G., & Sinninghe Damsté, J. S. (2007). Seasonal and spatial variation in the sources and fluxes of long chain diols and mid-chain hydroxy methyl alkanoates in the Arabian Sea. *Organic Geochemistry*, *38*(2), 165–179. https://doi.org/10.1016/j.orggeochem.2006.10.008

Rampen, S. W., Abbas, B. A., Schouten, S., & Sinninghe Damste, J. S. (2010). A comprehensive study of sterols in marine diatoms (Bacillariophyta): Implications for their use as tracers for diatom productivity. *Limnology and Oceanography*, *55*(1), 91–105. https://doi.org/10.4319/lo.2010.55.1.0091

Rampen, S. W., Willmott, V., Kim, J.-H., Uliana, E., Mollenhauer, G., Schefuß, E., Sinninghe Damsté, J. S., & Schouten, S. (2012). Long chain 1,13- and 1,15-diols as a potential proxy for palaeotemperature reconstruction. *Geochimica et Cosmochimica Acta*, *84*, 204–216. https://doi.org/10.1016/j.gca.2012.01.024

Rampen, S. W., Datema, M., Rodrigo-Gámiz, M., Schouten, S., Reichart, G.-J., & Sinninghe Damsté, J. S. (2014). Sources and proxy potential of long chain alkyl diols in lacustrine environments. *Geochimica et Cosmochimica Acta*, *144*, 59–71. https://doi.org/10.1016/j.gca.2014.08.033

Reghizzi, M., Gennari, R., Douville, E., Lugli, S., Manzi, V., Montagna, P., Roveri, M., Sierro, F. J., & Taviani, M. (2017). Isotope stratigraphy (87Sr/86Sr, δ18O, δ13C) of the Sorbas basin (Betic Cordillera, Spain): Paleoceanographic evolution across the onset of the Messinian salinity crisis. *Palaeogeography, Palaeoclimatology, Palaeoecology*, *469*, 60–73. https://doi.org/10.1016/j.palaeo.2016.12.039

Reghizzi, M., Lugli, S., Manzi, V., Rossi, F. P., & Roveri, M. (2018). Orbitally Forced Hydrological Balance During the Messinian Salinity Crisis: Insights From Strontium Isotopes (87Sr/86Sr) in the Vena del Gesso Basin (Northern Apennines, Italy). *Paleoceanography and Paleoclimatology*, *33*(7), 716–731. https://doi.org/10.1029/2018PA003395

Reiss, A. G., Ganor, J., & Gavrieli, I. (2019). Size distribution and morphology of gypsum crystals precipitating from hypersaline solutions. *Crystal Growth & Design*, *19*(12), 6954–6962. https://doi.org/10.1021/acs.cgd.9b00735

Reiss, A. G., Gavrieli, I., Rosenberg, Y. O., Reznik, I. J., Luttge, A., Emmanuel, S., & Ganor, J. (2021). Gypsum Precipitation under Saline Conditions: Thermodynamics, Kinetics, Morphology, and Size Distribution. *Minerals*, *11*(2), 141. https://doi.org/10.3390/min11020141

Rinke, C., Rubino, F., Messer, L. F., Youssef, N., Parks, D. H., Chuvochina, M., Brown, M., Jeffries, T., Tyson, G. W., Seymour, J. R., & Hugenholtz, P. (2019). A phylogenomic and ecological analysis of the globally abundant Marine Group II archaea (Ca. Poseidoniales ord. Nov.). *The ISME Journal*, *13*(3), 663–675. https://doi.org/10.1038/s41396-018-0282-y

Rivas-Marin, E., Stettner, S., Gottshall, E. Y., Santana-Molina, C., Helling, M., Basile, F., Ward, N. L., & Devos, D. P. (2019). Essentiality of sterol synthesis genes in the planctomycete bacterium Gemmata obscuriglobus. *Nature Communications*, *10*(1), 2916. https://doi.org/10.1038/s41467-019-10983-7

Robinson, N., Cranwell, P. A., Eglinton, G., & Jaworski, G. H. M. (1987). Lipids of four species of freshwater dinoflagellates. *Phytochemistry*, *26*(2), 411–421. https://doi.org/10.1016/S0031-9422(00)81423-5

Robinson, N., Eglinton, G., Brassell, S. C., & Cranwell, P. A. (1984). Dinoflagellate origin for sedimentary 4α-methylsteroids and 5α (H)-stanols. *Nature*, *308*(5958), 439-442.

Rohling, E. J., & Hilgen, F. J. (2007). The eastern Mediterranean climate at times of sapropel formation: a review. *Netherlands Journal of Geosciences / Geologie en Mijnbouw*. http://localhost/handle/1874/28551

Rohling, E. J., Marino, G., & Grant, K. M. (2015). Mediterranean climate and oceanography, and the periodic development of anoxic events (sapropels). *Earth-Science Reviews*, *143*, 62–97. https://doi.org/10.1016/j.earscirev.2015.01.008

Rommerskirchen, F., Eglinton, G., Dupont, L., Güntner, U., Wenzel, C., & Rullkötter, J. (2003). A north to south transect of Holocene southeast Atlantic continental margin sediments: Relationship between aerosol transport and compound-specific δ13C land plant biomarker and pollen records. *Geochemistry, Geophysics, Geosystems*, *4*(12). https://doi.org/10.1029/2003GC000541

Rommerskirchen, F., Plader, A., Eglinton, G., Chikaraishi, Y., & Rullkötter, J. (2006a). Chemotaxonomic significance of distribution and stable carbon isotopic composition of long-chain alkanes and alkan-1-ols in C4 grass waxes. *Organic Geochemistry*, *37*(10), 1303–1332. https://doi.org/10.1016/j.orggeochem.2005.12.013

Rommerskirchen, F., Eglinton, G., Dupont, L., & Rullkötter, J. (2006b). Glacial/interglacial changes in southern Africa: Compound-specific δ13C land plant biomarker and pollen records from southeast Atlantic continental margin sediments. *Geochemistry, Geophysics, Geosystems*, *7*(8). https://doi.org/10.1029/2005GC001223

Rosell, L., Orti, F., Kasprzyk, A., Playa, E., & Peryt, T. M. (1998). Strontium Geochemistry of Miocene Primary Gypsum: Messinian of Southeastern Spain and Sicily and Badenian of Poland. *Journal of Sedimentary Research*, *68*(1). http://archives.datapages.com/data/sepm/journals/v66-67/data/068/068001/0063.HTM

Rosell-Melé, A. (1998). Interhemispheric appraisal of the value of alkenone indices as temperature and salinity proxies in high-latitude locations. *Paleoceanography*, *13*(6), 694–703. https://doi.org/10.1029/98PA02355

Rossi, M. (2017). Outcrop and seismic expression of stratigraphic patterns driven by accommodation and sediment supply turnarounds: Implications on the meaning and variability of unconformities in syn-orogenic basins. *Marine and Petroleum Geology*, *87*, 112–127. https://doi.org/10.1016/j.marpetgeo.2017.03.032

Rossi, M., Mosca, P., Riccardo, P., Rogledi, S., & Biffi, U. (2009). New outcrop and subsurface data in the tertiary piedmont basin (NW-Italy): Unconformity-bounded stratigraphic units and their relationships with basin-modification phases. *Rivista Italiana Di Paleontologia e Stratigrafia*, *115*, 305–335. https://doi.org/10.13130/2039-4942/6386

Rothschild, L. J., & Mancinelli, R. L. (2001). Life in extreme environments. *Nature*, *409*(6823), 1092–1101. https://doi.org/10.1038/35059215

Rouchy, J.M., (1982). La genèse des évaporites messiniennes de Méditerranée. *Bulletin du Muséum National d'Histoire Naturelle Paris*, Science de la Terre, pp. 1–280.

Rouchy, J. M., & Monty, C. (2000). Gypsum Microbial Sediments: Neogene and Modern Examples. In R. E. Riding & S. M. Awramik (Eds.), *Microbial Sediments* (pp. 209–216). Springer. https://doi.org/10.1007/978-3-662-04036-2_23

Rouchy, J. M., & Caruso, A. (2006). The Messinian salinity crisis in the Mediterranean basin: A reassessment of the data and an integrated scenario. *Sedimentary Geology*, *188–189*, 35–67. https://doi.org/10.1016/j.sedgeo.2006.02.005

Roveri, M., Bertini, A., Stefano, A. D., Gennari, R., Gliozzi, E., Grossi, F., Iaccarino, S. M., Lugli, S., Manzi, V., & Taviani, M. (2008). A high-resolution stratigraphic framework for the latest Messinian events in the Mediterranean area. *Stratigraphy*, *5*(3–4), 323-342.

Roveri, M., Flecker, R., Krijgsman, W., Lofi, J., Lugli, S., Manzi, V., Sierro, F. J., Bertini, A., Camerlenghi, A., De Lange, G., Govers, R., Hilgen, F. J., Hübscher, C., Meijer, P. Th., & Stoica, M. (2014). The Messinian Salinity Crisis: Past and future of a great challenge for marine sciences. *Marine Geology*, *352*, 25–58. https://doi.org/10.1016/j.margeo.2014.02.002

Ryan, W. B. F. (1976). Quantitative evaluation of the depth of the western Mediterranean before, during and after the Late Miocene salinity crisis. *Sedimentology*, *23*(6), 791–813. https://doi.org/10.1111/j.1365-3091.1976.tb00109.x

Sabino, M., Schefuß, E., Natalicchio, M., Dela Pierre, F., Birgel, D., Bortels, D., Schnetger, B., & Peckmann, J. (2020). Climatic and hydrologic variability in the northern Mediterranean across the onset of the Messinian salinity crisis. *Palaeogeography, Palaeoclimatology, Palaeoecology*, *545*, 109632. https://doi.org/10.1016/j.palaeo.2020.109632

Sabino, M., Natalicchio, M., Birgel, D., Dela Pierre, F., & Peckmann, J. (2021). Environmental change across the onset of the Messinian salinity crisis in the northern Mediterranean (Piedmont Basin, NW Italy). *EGU General Assembly Conference Abstracts*, EGU21-1475.

Saccà, A., Borrego, C. M., Renda, R., Triadó-Margarit, X., Bruni, V., & Guglielmo, L. (2009). Predation impact of ciliated and flagellated protozoa during a summer bloom of brown sulfur bacteria in a meromictic coastal lake. *FEMS Microbiology Ecology*, *70*(1), 42–53. https://doi.org/10.1111/j.1574-6941.2009.00735.x

Sachs, J. P., Pahnke, K., Smittenberg, R., & Zhang, Z. (2013). PALEOCEANOGRAPHY, BIOLOGICAL PROXIES | Biomarker Indicators of Past Climate. In *Encyclopedia of Quaternary Science* (pp. 775–782). Elsevier. https://doi.org/10.1016/B978-0-444-53643-3.00280-6

Sachse, D., Radke, J., & Gleixner, G. (2004). Hydrogen isotope ratios of recent lacustrine sedimentary n-alkanes record modern climate variability. *Geochimica et Cosmochimica Acta*, *68*(23), 4877–4889. https://doi.org/10.1016/j.gca.2004.06.004

Sachse, D., Billault, I., Bowen, G. J., Chikaraishi, Y., Dawson, T. E., Feakins, S. J., Freeman, K. H., Magill, C. R., McInerney, F. A., van der Meer, M. T. J., Polissar, P., Robins, R. J., Sachs, J. P., Schmidt, H.-L., Sessions, A. L., White, J. W. C., West, J. B., & Kahmen, A. (2012). Molecular Paleohydrology: Interpreting the Hydrogen-Isotopic Composition of Lipid Biomarkers from Photosynthesizing Organisms. *Annual Review of Earth and Planetary Sciences*, *40*(1), 221–249. https://doi.org/10.1146/annurev-earth-042711-105535

Sampalmieri, G., Iadanza, A., Cipollari, P., Cosentino, D., & Mastro, S. L. (2010). Palaeoenvironments of the Mediterranean Basin at the Messinian hypersaline/hyposaline transition: Evidence from natural radioactivity and microfacies of post-evaporitic successions of the Adriatic sub-basin. *Terra Nova*, *22*(4), 239–250. https://doi.org/10.1111/j.1365-3121.2010.00939.x

Schaeffer, P., Harrison, W. N., Keely, B. J., & Maxwell, J. R. (1995). Product distributions from chemical degradation of kerogens from a marl from a Miocene evaporitic sequence (Vena del Gesso, N. Italy). *Organic Geochemistry*, *23*(6), 541–554. https://doi.org/10.1016/0146-6380(95)00033-B

Schefuß, E., Eglinton, T. I., Spencer-Jones, C. L., Rullkötter, J., De Pol-Holz, R., Talbot, H. M., Grootes, P. M., & Schneider, R. R. (2016). Hydrologic control of carbon cycling and aged carbon discharge in the Congo River basin. *Nature Geoscience*, *9*(9), 687–690. https://doi.org/10.1038/ngeo2778

Schefuß, E., Ratmeyer, V., Stuut, J.-B. W., Jansen, J. H. F., & Sinninghe Damsté, J. S. (2003). Carbon isotope analyses of n-alkanes in dust from the lower atmosphere over the central eastern Atlantic. *Geochimica et Cosmochimica Acta*, *67*(10), 1757–1767. https://doi.org/10.1016/S0016-7037(02)01414-X

Schefuß, E., Schouten, S., & Schneider, R. R. (2005). Climatic controls on central African hydrology during the past 20,000 years. *Nature*, *437*(7061), 1003–1006. https://doi.org/10.1038/nature03945

Schlünz, B., & Schneider, R. R. (2000). Transport of terrestrial organic carbon to the oceans by rivers: Re-estimating flux- and burial rates. *International Journal of Earth Sciences*, *88*(4), 599–606. https://doi.org/10.1007/s005310050290

Schoell, M., Hwang, R. J., Carlson, R. M. K., & Welton, J. E. (1994). Carbon isotopic composition of individual biomarkers in gilsonites (Utah). *Organic Geochemistry*, *21*(6), 673–683. https://doi.org/10.1016/0146-6380(94)90012-4

Schouten, S., Rijpstra, W. I. C., Kok, M., Hopmans, E. C., Summons, R. E., Volkman, J. K., & Sinninghe Damsté, J. S. (2001). Molecular organic tracers of biogeochemical processes in a saline meromictic lake (Ace Lake). *Geochimica et Cosmochimica Acta*, *65*(10), 1629–1640. https://doi.org/10.1016/S0016-7037(00)00627-X

Schouten, S., Hopmans, E. C., Schefuß, E., & Sinninghe Damsté, J. S. (2002). Distributional variations in marine crenarchaeotal membrane lipids: A new tool for reconstructing ancient sea water

temperatures? *Earth and Planetary Science Letters*, *204*(1), 265–274. https://doi.org/10.1016/S0012-821X(02)00979-2

Schouten, S., Hopmans, E. C., Forster, A., Breugel, Y. van, Kuypers, M. M. M., & Damsté, J. S. S. (2003). Extremely high sea-surface temperatures at low latitudes during the middle Cretaceous as revealed by archaeal membrane lipids. *Geology*, *31*(12), 1069–1072. https://doi.org/10.1130/G19876.1

Schouten, S., Hopmans, E. C., & Sinninghe Damsté, J. S. (2004). The effect of maturity and depositional redox conditions on archaeal tetraether lipid palaeothermometry. *Organic Geochemistry*, *35*(5), 567–571. https://doi.org/10.1016/j.orggeochem.2004.01.012

Schouten, S., Meer, M. T. J. van der, Hopmans, E. C., Rijpstra, W. I. C., Reysenbach, A.-L., Ward, D. M., & Damsté, J. S. S. (2007). Archaeal and Bacterial Glycerol Dialkyl Glycerol Tetraether Lipids in Hot Springs of Yellowstone National Park. *Applied and Environmental Microbiology*, *73*(19), 6181–6191. https://doi.org/10.1128/AEM.00630-07

Schouten, S., Hopmans, E. C., & Sinninghe Damsté, J. S. (2013). The organic geochemistry of glycerol dialkyl glycerol tetraether lipids: A review. *Organic Geochemistry*, *54*, 19–61. https://doi.org/10.1016/j.orggeochem.2012.09.006

Schreiber, B. C., Friedman, G. M., Decima, A., & Schreiber, E. (1976). Depositional environments of Upper Miocene (Messinian) evaporite deposits of the Sicilian Basin*. *Sedimentology*, *23*(6), 729–760. https://doi.org/10.1111/j.1365-3091.1976.tb00107.x

Schreiber, B. C., & Tabakh, M. E. (2000). Deposition and early alteration of evaporites. *Sedimentology*, *47*(s1), 215–238. https://doi.org/10.1046/j.1365-3091.2000.00002.x

Schroeder, W. W., Dinnel, S. P., & Wiseman, W. J. (1990). Salinity stratification in a river-dominated estuary. *Estuaries*, *13*(2), 145–154. https://doi.org/10.2307/1351583

Schwarzbauer, J., & Jovančićević, B. (2016). *From biomolecules to chemofossils*. Springer International Publishing.

Seitz, L. M., Mohr, H. E., Burroughs, R., & Sauer, D. B. (1977). Ergosterol as an indicator of fungal invasion in grains. *Cereal Chemistry*.

Selli, R. (1960). Il Messiniano Mayer-Eymar 1867. Proposta di un neostratotipo. Giornale di Geologia 28, 1–33.

Sessions, A. L. (2016). Factors controlling the deuterium contents of sedimentary hydrocarbons. *Organic Geochemistry*, *96*, 43–64. https://doi.org/10.1016/j.orggeochem.2016.02.012

Sierro, F. J., Flores, J. A., Zamarreño, I., Vázquez, A., Utrilla, R., Francés, G., Hilgen, F., & Krijgsman, W. (1996). *Astronomical cyclicity and sapropels in the pre-evaporitic Messinian of the Sorbas basin (Western Mediterranean)*. http://rabida.uhu.es/dspace/handle/10272/11075

Sierro, F. J., Flores, J. A., Zamarreño, I., Vázquez, A., Utrilla, R., Francés, G., Hilgen, F. J., & Krijgsman, W. (1999). Messinian pre-evaporite sapropels and precession-induced oscillations in western Mediterranean climate. *Marine Geology*, *153*(1–4), 137–146. https://doi.org/10.1016/S0025-3227(98)00085-1

Sierro, F. J., Flores, J. A., Francés, G., Vazquez, A., Utrilla, R., Zamarreño, I., Erlenkeuser, H., & Barcena, M. A. (2003). Orbitally-controlled oscillations in planktic communities and cyclic changes in western Mediterranean hydrography during the Messinian. *Palaeogeography, Palaeoclimatology, Palaeoecology*, *190*, 289–316. https://doi.org/10.1016/S0031-0182(02)00611-9

Simon, D., & Meijer, P. (2015). Dimensions of the Atlantic–Mediterranean connection that caused the Messinian Salinity Crisis. *Marine Geology*, *364*, 53–64. https://doi.org/10.1016/j.margeo.2015.02.004

Simon, D., Marzocchi, A., Flecker, R., Lunt, D. J., Hilgen, F. J., & Meijer, P. Th. (2017). Quantifying the Mediterranean freshwater budget throughout the late Miocene: New implications for sapropel formation and the Messinian Salinity Crisis. *Earth and Planetary Science Letters*, *472*, 25–37. https://doi.org/10.1016/j.epsl.2017.05.013

Simon, D., & Meijer, P. Th. (2017). Salinity stratification of the Mediterranean Sea during the Messinian crisis: A first model analysis. *Earth and Planetary Science Letters*, *479*, 366–376. https://doi.org/10.1016/j.epsl.2017.09.045

Sinninghe Damsté, J. S., Wakeham, S. G., Kohnen, M. E. L., Hayes, J. M., & de Leeuw, J. W. (1993). A 6,000–year sedimentary molecular record of chemocline excursions in the Black Sea. *Nature*, *362*(6423), 827–829. https://doi.org/10.1038/362827a0

Sinninghe Damsté, J. S., Kenig, F., Koopmans, M. P., Köster, J., Schouten, S., Hayes, J. M., & de Leeuw, J. W. (1995a). Evidence for gammacerane as an indicator of water column stratification. *Geochimica et Cosmochimica Acta*, *59*(9), 1895–1900. https://doi.org/10.1016/0016-7037(95)00073-9

Sinninghe Damsté, J. S., Frewin, N. L., Kenig, F., & De Leeuw, J. W. (1995b). Molecular indicators for palaeoenvironmental change in a Messinian evaporitic sequence (Vena del Gesso, Italy). I: Variations in extractable organic matter of ten cyclically deposited marl beds. *Organic Geochemistry*, *23*(6), 471–483. https://doi.org/10.1016/0146-6380(95)00040-L

Sinninghe Damsté, J. S., Hopmans, E. C., Pancost, R. D., Schouten, S., & Geenevasen, J. A. J. (2000). Newly discovered non-isoprenoid glycerol dialkylglycerol tetraether lipids in sediments. *Chemical Communications*, *17*, 1683–1684. https://doi.org/10.1039/B004517I

Sinninghe Damsté, J. S., Schouten, S., Hopmans, E. C., van Duin, A. C. T., & Geenevasen, J. A. J. (2002a). Crenarchaeol: The characteristic core glycerol dibiphytanyl glycerol tetraether membrane lipid of cosmopolitan pelagic crenarchaeota. *Journal of Lipid Research*, *43*(10), 1641–1651. https://doi.org/10.1194/jlr.M200148-JLR200

Sinninghe Damsté, J.S., Rijpstra, W.I.C., Hopmans, E.C., Prahl, F.G., Wakeham, S.G., and Schouten, S. (2002b). Distribution of membrane lipids of planktonic Crenarchaeota in the Arabian Sea. *Applied and Environmental Microbiology*. 68, 2997–3002. https://journals.asm.org/doi/abs/10.1128/AEM.68.6.2997-3002.2002

Sinninghe Damsté, J. S., & Schouten, S. (2006). Biological markers for anoxia in the photic zone of the water column. In J. K. Volkman (Ed.), *Marine Organic Matter: Biomarkers, Isotopes and DNA* (Vol. 2N, pp. 127–163). Springer-Verlag. https://doi.org/10.1007/698_2_005

Sinninghe Damsté, J. S., Rijpstra, W. I. C., Hopmans, E. C., Weijers, J. W. H., Foesel, B. U., Overmann, J., & Dedysh, S. N. (2011a). 13,16-dimethyl octacosanedioic acid (iso-diabolic acid), a common membrane-spanning lipid of Acidobacteria subdivisions 1 and 3. *Applied and Environmental Microbiology*, *77*(12), 4147–4154. https://doi.org/10.1128/AEM.00466-11

Sinninghe Damsté, J. S., Verschuren, D., Ossebaar, J., Blokker, J., van Houten, R., van der Meer, M. T. J., Plessen, B., & Schouten, S. (2011b). A 25,000-year record of climate-induced changes in lowland vegetation of eastern equatorial Africa revealed by the stable carbon-isotopic composition of fossil plant leaf waxes. *Earth and Planetary Science Letters*, *302*(1), 236–246. https://doi.org/10.1016/j.epsl.2010.12.025

Sinninghe Damsté, J. S., Rijpstra, W. I. C., Hopmans, E. C., Jung, M.-Y., Kim, J.-G., Rhee, S.-K., Stieglmeier, M., & Schleper, C. (2012). Intact polar and core glycerol dibiphytanyl glycerol tetraether lipids of group I.1a and I.1b Thaumarchaeota in soil. *Applied and Environmental Microbiology*, *78*(19), 6866–6874. https://doi.org/10.1128/AEM.01681-12

Sinninghe Damsté, J. S., Rijpstra, W. I. C., Hopmans, E. C., den Uijl, M. J., Weijers, J. W. H., & Schouten, S. (2018). The enigmatic structure of the crenarchaeol isomer. *Organic Geochemistry*, *124*, 22–28. https://doi.org/10.1016/j.orggeochem.2018.06.005

Słowakiewicz, M., Whitaker, F., Thomas, L., Tucker, M. E., Zheng, Y., Gedl, P., & Pancost, R. D. (2016). Biogeochemistry of intertidal microbial mats from Qatar: New insights from organic matter characterisation. *Organic Geochemistry*, *102*, 14–29. https://doi.org/10.1016/j.orggeochem.2016.09.006

Sollai, M., Villanueva, L., Hopmans, E. C., Keil, R. G., & Sinninghe Damsté, J. S. (2019). Archaeal sources of intact membrane lipid biomarkers in the oxygen deficient zone of the Eastern Tropical South Pacific. *Frontiers in Microbiology*, *10*, 765. https://doi.org/10.3389/fmicb.2019.00765

Spang, A., Hatzenpichler, R., Brochier-Armanet, C., Rattei, T., Tischler, P., Spieck, E., Streit, W., Stahl, D. A., Wagner, M., & Schleper, C. (2010). Distinct gene set in two different lineages of ammonia-oxidizing archaea supports the phylum Thaumarchaeota. *Trends in Microbiology*, *18*(8), 331–340. https://doi.org/10.1016/j.tim.2010.06.003

Stadnitskaia, A., Bouloubassi, I., Elvert, M., Hinrichs, K.-U., & Sinninghe Damsté, J. S. (2008). Extended hydroxyarchaeol, a novel lipid biomarker for anaerobic methanotrophy in cold seepage habitats. *Organic Geochemistry*, *39*(8), 1007–1014. https://doi.org/10.1016/j.orggeochem.2008.04.019

Stahl, P. D., & Parkin, T. B. (1996). Relationship of soil ergosterol concentration and fungal biomass. *Soil Biology and Biochemistry*, *28*(7), 847–855. https://doi.org/10.1016/0038-0717(96)00061-2

Stern, J. (2009). Sulfur-bound biomarkers of a Monterey shale and a Greenland lake sediment. *Nature Precedings*, 1–1. https://doi.org/10.1038/npre.2009.3325.1

Sturani C. (1973). A fossil eel (Anguilla sp.) from the Messinian of Alba (tertiary Piedmontese basin). Palaeoenvironmental and palaeographic implications. In: Drooger, C.W. (Ed.), *Messinian Events in the Mediterranean*. K. Nederl. Akad. Wetensch, Amsterdam, pp. 243–255.

Suess, E. (1980). Particulate organic carbon flux in the oceans—Surface productivity and oxygen utilization. *Nature*, *288*(5788), 260–263. https://doi.org/10.1038/288260a0

Sun, M.-Y., & Wakeham, S. G. (1994). Molecular evidence for degradation and preservation of organic matter in the anoxic Black Sea Basin. *Geochimica et Cosmochimica Acta*, *58*(16), 3395–3406. https://doi.org/10.1016/0016-7037(94)90094-9

Tachibana, A. (1994). A novel prenyltransferase, farnesylgeranyl diphosphate synthase, from the haloalkaliphilic archaeon, Natronobacterium pharaonis. *FEBS Letters*, *341*(2–3), 291–294. https://doi.org/10.1016/0014-5793(94)80475-3

Tanret, M.C. (1908). Sur l'ergostérine et la fongistérine. C.R.Hebd. Seances Acad. Sci., 147, 75–77.

Tegelaar, E. W., de Leeuw, J. W., Derenne, S., & Largeau, C. (1989). A reappraisal of kerogen formation. *Geochimica et Cosmochimica Acta*, *53*(11), 3103–3106. https://doi.org/10.1016/0016-7037(89)90191-9

Teixidor, P., Grimait, J. O., Pueyo, J. J., & Rodriguez-Valera, F. (1993). Isopranylglycerol diethers in non-alkaline evaporitic environments. *Geochimica et Cosmochimica Acta*, *57*(18), 4479–4489. https://doi.org/10.1016/0016-7037(93)90497-K

Ten Haven, H. L., Rohmer, M., Rullkötter, J., & Bisseret, P. (1989). Tetrahymanol, the most likely precursor of gammacerane, occurs ubiquitously in marine sediments. *Geochimica et Cosmochimica Acta*, *53*(11), 3073–3079. https://doi.org/10.1016/0016-7037(89)90186-5

Tepšič, K., Gunde-Cimerman, N., & Frisvad, J. C. (1997). Growth and mycotoxin production by Aspergillus fumigatus strains isolated from a saltern. *FEMS Microbiology Letters*, *157*(1), 9–12. https://doi.org/10.1111/j.1574-6968.1997.tb12745.x

Tierney, J. E., Russell, J. M., Huang, Y., Damsté, J. S. S., Hopmans, E. C., & Cohen, A. S. (2008). Northern Hemisphere Controls on Tropical Southeast African Climate During the Past 60,000 Years. *Science*, *322*(5899), 252–255. https://doi.org/10.1126/science.1160485

Tierney, J. E., & Russell, J. M. (2009). Distributions of branched GDGTs in a tropical lake system: Implications for lacustrine application of the MBT/CBT paleoproxy. *Organic Geochemistry*, *40*(9), 1032–1036. https://doi.org/10.1016/j.orggeochem.2009.04.014

Tierney, J. E., Russell, J. M., & Huang, Y. (2010). A molecular perspective on Late Quaternary climate and vegetation change in the Lake Tanganyika basin, East Africa. *Quaternary Science Reviews*, *29*(5), 787–800. https://doi.org/10.1016/j.quascirev.2009.11.030

Tipple, B. J., Meyers, S. R., & Pagani, M. (2010). Carbon isotope ratio of Cenozoic CO2: A comparative evaluation of available geochemical proxies. *Paleoceanography*, *25*(3). https://doi.org/10.1029/2009PA001851

Tipple, B. J., & Pagani, M. (2010). A 35Myr North American leaf-wax compound-specific carbon and hydrogen isotope record: Implications for C4 grasslands and hydrologic cycle dynamics. *Earth and Planetary Science Letters*, *299*(1–2), 250–262. https://doi.org/10.1016/j.epsl.2010.09.006

Topper, R. P. M., Flecker, R., Meijer, P. Th., & Wortel, M. J. R. (2011). A box model of the Late Miocene Mediterranean Sea: Implications from combined ^{87}Sr/^{86}Sr and salinity data: BOX MODEL OF THE MESSINIAN MEDITERRANEAN. *Paleoceanography*, *26*(3), n/a-n/a. https://doi.org/10.1029/2010PA002063

Topper, R. P. M., & Meijer, P. Th. (2013). A modeling perspective on spatial and temporal variations in Messinian evaporite deposits. *Marine Geology*, *336*, 44–60. https://doi.org/10.1016/j.margeo.2012.11.009

Topper, R. P. M., Lugli, S., Manzi, V., Roveri, M., & Meijer, P. Th. (2014). Precessional control of Sr ratios in marginal basins during the Messinian Salinity Crisis? *Geochemistry, Geophysics, Geosystems*, *15*(5), 1926–1944. https://doi.org/10.1002/2013GC005192

Topper, R. P. M., & Meijer, P. Th. (2015). The precessional phase lag of Messinian gypsum deposition in Mediterranean marginal basins. *Palaeogeography, Palaeoclimatology, Palaeoecology*, *417*, 6–16. https://doi.org/10.1016/j.palaeo.2014.10.025

Toucanne, S., Angue Minto'o, C. M., Fontanier, C., Bassetti, M.-A., Jorry, S. J., & Jouet, G. (2015). Tracking rainfall in the northern Mediterranean borderlands during sapropel deposition. *Quaternary Science Reviews*, *129*, 178–195. https://doi.org/10.1016/j.quascirev.2015.10.016

Tribovillard, N., Algeo, T. J., Lyons, T., & Riboulleau, A. (2006). Trace metals as paleoredox and paleoproductivity proxies: An update. *Chemical Geology*, *232*(1), 12–32. https://doi.org/10.1016/j.chemgeo.2006.02.012

Tsimplis, M. N., Zervakis, V., Josey, S. A., Peneva, E. L., Struglia, M. V., Stanev, E. V., Theocharis, A., Lionello, P., Malanotte-Rizzoli, P., Artale, V., Tragou, E., & Oguz, T. (2006). Chapter 4 Changes in the oceanography of the Mediterranean Sea and their link to climate variability. In P. Lionello, P. Malanotte-Rizzoli, & R. Boscolo (Eds.), *Developments in Earth and Environmental Sciences* (Vol. 4, pp. 227–282). Elsevier. https://doi.org/10.1016/S1571-9197(06)80007-8

Turich, C., Freeman, K. H., Bruns, M. A., Conte, M., Jones, A. D., & Wakeham, S. G. (2007). Lipids of marine Archaea: Patterns and provenance in the water-column and sediments. *Geochimica et Cosmochimica Acta*, *71*(13), 3272–3291. https://doi.org/10.1016/j.gca.2007.04.013

Turich, C., & Freeman, K. H. (2011). Archaeal lipids record paleosalinity in hypersaline systems. *Organic Geochemistry*, S0146638011001598. https://doi.org/10.1016/j.orggeochem.2011.06.002

Twitchett, R. J. (2006). The palaeoclimatology, palaeoecology and palaeoenvironmental analysis of mass extinction events. *Palaeogeography, Palaeoclimatology, Palaeoecology*, *232*(2), 190–213. https://doi.org/10.1016/j.palaeo.2005.05.019

Uda, I., Sugai, A., Itoh, Y. H., & Itoh, T. (2001). Variation in molecular species of polar lipids from Thermoplasma acidophilum depends on growth temperature. *Lipids*, *36*(1), 103–105. https://doi.org/10.1007/s11745-001-0914-2

Usiglio, J. (1849a). Analyse de l'eau de la Me´diterrane´e sur les coˆtes de France. *Annales de Chimie et de Physique 3e`me se´r*. 27: 92–107.

Usiglio, J. (1849b). Etudes sur la composition de l'eau de la Me´diterrane´e et sur l'exploitation des sels qu'elle contient. *Annales de Chimie et de Physique 3e`me se´r*. 27: 172–191.

Vai, G. B., & Lucchi, F. R. (1977). Algal crusts, autochthonous and clastic gypsum in a cannibalistic evaporite basin: A case history from the Messinian of Northern Apennines. *Sedimentology*, *24*(2), 211–244. https://doi.org/10.1111/j.1365-3091.1977.tb00255.x

Valentine, D. L. (2007). Adaptations to energy stress dictate the ecology and evolution of the Archaea. *Nature Reviews Microbiology*, *5*(4), 316–323. https://doi.org/10.1038/nrmicro1619

Van Assen, E., Kuiper, K. F., Barhoun, N., Krijgsman, W., & Sierro, F. J. (2006). Messinian astrochronology of the Melilla Basin: Stepwise restriction of the Mediterranean–Atlantic connection through Morocco. *Palaeogeography, Palaeoclimatology, Palaeoecology*, *238*(1), 15–31. https://doi.org/10.1016/j.palaeo.2006.03.014

Van Couvering, J. A., Castradori, D., Cita, M. B., Hilgen, F. J., & Rio, D. (2000). The base of the Zanclean Stage and of the Pliocene Series. *Episodes*, *23*(3), 179-187. https://doi.org/10.18814/epiiugs/2000/v23i3/005

Van der Laan, E., Hilgen, F. J., Lourens, L. J., de Kaenel, E., Gaboardi, S., & Iaccarino, S. (2012). Astronomical forcing of Northwest African climate and glacial history during the late Messinian (6.5–5.5Ma). *Palaeogeography, Palaeoclimatology, Palaeoecology*, *313–314*, 107–126. https://doi.org/10.1016/j.palaeo.2011.10.013

Van der Meer, M. T. J., Baas, M., Rijpstra, W. I. C., Marino, G., Rohling, E. J., Sinninghe Damsté, J. S., & Schouten, S. (2007). Hydrogen isotopic compositions of long-chain alkenones record freshwater flooding of the Eastern Mediterranean at the onset of sapropel deposition. *Earth and Planetary Science Letters*, *262*(3), 594–600. https://doi.org/10.1016/j.epsl.2007.08.014

Vasiliev, I., Reichart, G.-J., & Krijgsman, W. (2013). Impact of the Messinian Salinity Crisis on Black Sea hydrology—Insights from hydrogen isotopes analysis on biomarkers. *Earth and Planetary Science Letters*, *362*, 272–282. https://doi.org/10.1016/j.epsl.2012.11.038

Vasiliev, I., Reichart, G.-J., Grothe, A., Sinninghe Damsté, J. S., Krijgsman, W., Sangiorgi, F., Weijers, J. W. H., & van Roij, L. (2015). Recurrent phases of drought in the upper Miocene of the Black Sea region. *Palaeogeography, Palaeoclimatology, Palaeoecology*, *423*, 18–31. https://doi.org/10.1016/j.palaeo.2015.01.020

Vasiliev, I., Mezger, E. M., Lugli, S., Reichart, G.-J., Manzi, V., & Roveri, M. (2017). How dry was the Mediterranean during the Messinian salinity crisis? *Palaeogeography, Palaeoclimatology, Palaeoecology*, *471*, 120–133. https://doi.org/10.1016/j.palaeo.2017.01.032

Vasiliev, I., Reichart, G.-J., Krijgsman, W., & Mulch, A. (2019). Black Sea rivers capture significant change in catchment-wide mean annual temperature and soil pH during the Miocene-to-Pliocene transition. *Global and Planetary Change*, *172*, 428–439. https://doi.org/10.1016/j.gloplacha.2018.10.016

Vetriani, C., Reysenbach, A.-L., & Doré, J. (1998). Recovery and phylogenetic analysis of archaeal rRNA sequences from continental shelf sediments. *FEMS Microbiology Letters*, *161*(1), 83–88. https://doi.org/10.1111/j.1574-6968.1998.tb12932.x

Violanti, D., Lozar, F., & Natalicchio, M. (2013). Stress-tolerant microfossils of a Messinian succession from the Northern Mediterranean basin (Pollenzo section, Piedmont, northwestern Italy). *Bollettino Della Società Paleontologica Italiana*, *1*, 45–54. https://doi.org/10.4435/BSPI.2013.09

Vogts, A., Moossen, H., Rommerskirchen, F., & Rullkötter, J. (2009). Distribution patterns and stable carbon isotopic composition of alkanes and alkan-1-ols from plant waxes of African rain forest and savanna C3 species. *Organic Geochemistry*, *40*(10), 1037–1054. https://doi.org/10.1016/j.orggeochem.2009.07.011

Vogts, A., Schefuß, E., Badewien, T., & Rullkötter, J. (2012). N-Alkane parameters from a deep sea sediment transect off southwest Africa reflect continental vegetation and climate conditions. *Organic Geochemistry*, *47*, 109–119. https://doi.org/10.1016/j.orggeochem.2012.03.011

Volkman, J. K. (1986). A review of sterol markers for marine and terrigenous organic matter. *Organic Geochemistry*, *9*(2), 83–99. https://doi.org/10.1016/0146-6380(86)90089-6

Volkman, J. K., Barrett, S. M., Dunstan, G. A., & Jeffrey, S. W. (1992). C30–C32 alkyl diols and unsaturated alcohols in microalgae of the class Eustigmatophyceae. *Organic Geochemistry*, *18*(1), 131–138. https://doi.org/10.1016/0146-6380(92)90150-V

Volkman, J. K., Barrett, S. M., Dunstan, G. A., & Jeffrey, S. W. (1993). Geochemical significance of the occurrence of dinosterol and other 4-methyl sterols in a marine diatom. *Organic Geochemistry*, *20*(1), 7–15. https://doi.org/10.1016/0146-6380(93)90076-N

Volkman, J. K., Barrett, S. M., Blackburn, S. I., Mansour, M. P., Sikes, E. L., & Gelin, F. (1998). Microalgal biomarkers: A review of recent research developments. *Organic Geochemistry*, *29*(5–7), 1163–1179. https://doi.org/10.1016/S0146-6380(98)00062-X

Volkman, J. K., Rijpstra, W. I. C., de Leeuw, J. W., Mansour, M. P., Jackson, A. E., & Blackburn, S. I. (1999). Sterols of four dinoflagellates from the genus Prorocentrum. *Phytochemistry*, *52*(4), 659–668. https://doi.org/10.1016/S0031-9422(99)00251-4

Volkman, J. (2003). Sterols in microorganisms. *Applied Microbiology and Biotechnology*, *60*(5), 495–506. https://doi.org/10.1007/s00253-002-1172-8

Volkman, J. K. (2005). Sterols and other triterpenoids: Source specificity and evolution of biosynthetic pathways. *Organic Geochemistry*, *36*(2), 139–159. https://doi.org/10.1016/j.orggeochem.2004.06.013

Wakeham, S. G., & Canuel, E. A. (2006). Degradation and Preservation of Organic Matter in Marine Sediments. In J. K. Volkman (Ed.), *Marine Organic Matter: Biomarkers, Isotopes and DNA* (Vol. 2N, pp. 295–321). Springer-Verlag. https://doi.org/10.1007/698_2_009

Walker, C. B., Torre, J. R. de la, Klotz, M. G., Urakawa, H., Pinel, N., Arp, D. J., Brochier-Armanet, C., Chain, P. S. G., Chan, P. P., Gollabgir, A., Hemp, J., Hügler, M., Karr, E. A., Könneke, M., Shin, M., Lawton, T. J., Lowe, T., Martens-Habbena, W., Sayavedra-Soto, L. A., … Stahl, D. A. (2010). Nitrosopumilus maritimus genome reveals unique mechanisms for nitrification and autotrophy in globally distributed marine crenarchaea. *Proceedings of the National Academy of Sciences*, *107*(19), 8818–8823. https://doi.org/10.1073/pnas.0913533107

Wang, G., Kawamura, K., Xie, M., Hu, S., Gao, S., Cao, J., An, Z., & Wang, Z. (2009). Size-distributions of n-alkanes, PAHs and hopanes and their sources in the urban, mountain and marine atmospheres over East Asia. *Atmospheric Chemistry and Physics*, *9*(22), 8869–8882. https://doi.org/10.5194/acp-9-8869-2009

Wang, H., Liu, W., Zhang, C. L., Jiang, H., Dong, H., Lu, H., & Wang, J. (2013). Assessing the ratio of archaeol to caldarchaeol as a salinity proxy in highland lakes on the northeastern Qinghai–Tibetan Plateau. *Organic Geochemistry*, *54*, 69–77. https://doi.org/10.1016/j.orggeochem.2012.09.011

Wang, Q., Li, W., Yang, H., Liu, Y., Cao, H., Dornmayr-Pfaffenhuemer, M., Stan-Lotter, H., & Guo, G. (2007). Halococcus qingdaonensis sp. Nov., a halophilic archaeon isolated from a crude sea-salt sample. *International Journal of Systematic and Evolutionary Microbiology*, *57*(3), 600–604. https://doi.org/10.1099/ijs.0.64673-0

Wang, R. (1998). Acyclic isoprenoids – molecular indicators of archaeal activity in contemporary and ancient Chinese saline/hypersaline environments. *Hydrobiologia*, *381*(1), 59–76. https://doi.org/10.1023/A:1003223506939

Warren, J. K. (2010). Evaporites through time: Tectonic, climatic and eustatic controls in marine and nonmarine deposits. *Earth-Science Reviews*, *98*(3), 217–268. https://doi.org/10.1016/j.earscirev.2009.11.004

Wei, J. H., Yin, X., & Welander, P. V. (2016). Sterol Synthesis in Diverse Bacteria. *Frontiers in Microbiology*, *7*. https://doi.org/10.3389/fmicb.2016.00990

Weijers, J. W. H., Schouten, S., Spaargaren, O. C., & Sinninghe Damsté, J. S. (2006). Occurrence and distribution of tetraether membrane lipids in soils: Implications for the use of the TEX86 proxy and the BIT index. *Organic Geochemistry*, *37*(12), 1680–1693. https://doi.org/10.1016/j.orggeochem.2006.07.018

Weijers, J. W. H., Schouten, S., van den Donker, J. C., Hopmans, E. C., & Sinninghe Damsté, J. S. (2007). Environmental controls on bacterial tetraether membrane lipid distribution in soils. *Geochimica et Cosmochimica Acta*, *71*(3), 703–713. https://doi.org/10.1016/j.gca.2006.10.003

Weijers, J. W. H., Panoto, E., Bleijswijk, J. van, Schouten, S., Rijpstra, W. I. C., Balk, M., Stams, A. J. M., & Damsté, J. S. S. (2009). Constraints on the Biological Source(s) of the Orphan Branched Tetraether Membrane Lipids. *Geomicrobiology Journal*, *26*(6), 402–414. https://doi.org/10.1080/01490450902937293

Weijers, J. W. H., Lim, K. L. H., Aquilina, A., Damsté, J. S. S., & Pancost, R. D. (2011). Biogeochemical controls on glycerol dialkyl glycerol tetraether lipid distributions in sediments characterized by diffusive methane flux. *Geochemistry, Geophysics, Geosystems*, *12*(10). https://doi.org/10.1029/2011GC003724

Withers, N. (1983). Chapter 3—Dinoflagellate Sterols. In P. J. Scheuer (Ed.), *Marine Natural Products* (pp. 87–130). Academic Press. https://doi.org/10.1016/B978-0-12-624005-4.50010-0

Withers, N. (1987) Dinoflagellate sterols. In: Taylor FJR (ed) The biology of dinoflagellates. *Biological monographs*, vol 21. Blackwell Scientific, Oxford, pp 316–359

Wuchter, C. (2006). *Ecology and membrane lipid distribution of marine Crenarchaeota: Implications for TEX86 paleothermometry*. Faculty of Geosciences, Utrecht University].

Xing, L., Zhang, R., Liu, Y., Zhao, X., Liu, S., Shi, X., & Zhao, M. (2011). Biomarker records of phytoplankton productivity and community structure changes in the Japan Sea over the last 166 kyr. *Quaternary Science Reviews*, *30*(19–20), 2666–2675. https://doi.org/10.1016/j.quascirev.2011.05.021

Zang, J., Lei, Y., & Yang, H. (2018). Distribution of glycerol ethers in Turpan soils: Implications for use of GDGT-based proxies in hot and dry regions. *Frontiers of Earth Science*, *12*(4), 862–876. https://doi.org/10.1007/s11707-018-0722-z

Zell, C., Kim, J.-H., Balsinha, M., Dorhout, D., Fernandes, C., Baas, M., & Sinninghe Damsté, J. S. (2014). Transport of branched tetraether lipids from the Tagus River basin to the coastal ocean of the Portuguese margin: Consequences for the interpretation of the MBT'/CBT paleothermometer. *Biogeosciences*, *11*(19), 5637–5655. https://doi.org/10.5194/bg-11-5637-2014

Zell, C., Kim, J.-H., Dorhout, D., Baas, M., & Sinninghe Damsté, J. S. (2015). Sources and distributions of branched tetraether lipids and crenarchaeol along the Portuguese continental margin: Implications for the BIT index. *Continental Shelf Research*, *96*, 34–44. https://doi.org/10.1016/j.csr.2015.01.006

Zhang, Y. G., Zhang, C. L., Liu, X.-L., Li, L., Hinrichs, K.-U., & Noakes, J. E. (2011). Methane Index: A tetraether archaeal lipid biomarker indicator for detecting the instability of marine gas hydrates. *Earth and Planetary Science Letters*, *307*(3), 525–534. https://doi.org/10.1016/j.epsl.2011.05.031

Zhang, Z., Smittenberg, R. H., & Bradley, R. S. (2016). GDGT distribution in a stratified lake and implications for the application of TEX86 in paleoenvironmental reconstructions. *Scientific Reports*, *6*(1), 34465. https://doi.org/10.1038/srep34465

Zhao, M., Mercer, J. L., Eglinton, G., Higginson, M. J., & Huang, C.-Y. (2006). Comparative molecular biomarker assessment of phytoplankton paleoproductivity for the last 160kyr off Cap Blanc, NW Africa. *Organic Geochemistry*, *37*(1), 72–97. https://doi.org/10.1016/j.orggeochem.2005.08.022

Zhu, C., Weijers, J. W. H., Wagner, T., Pan, J.-Ming., Chen, J.-F., & Pancost, R. D. (2011). Sources and distributions of tetraether lipids in surface sediments across a large river-dominated continental margin. *Organic Geochemistry*, *42*(4), 376–386. https://doi.org/10.1016/j.orggeochem.2011.02.002

Ziegler, M., Tuenter, E., & Lourens, L. J. (2010). The precession phase of the boreal summer monsoon as viewed from the eastern Mediterranean (ODP Site 968). *Quaternary Science Reviews*, *29*(11), 1481–1490. https://doi.org/10.1016/j.quascirev.2010.03.011

Zink, K.-G., Vandergoes, M. J., Mangelsdorf, K., Dieffenbacher-Krall, A. C., & Schwark, L. (2010). Application of bacterial glycerol dialkyl glycerol tetraethers (GDGTs) to develop modern and past temperature estimates from New Zealand lakes. *Organic Geochemistry*, *41*(9), 1060–1066. https://doi.org/10.1016/j.orggeochem.2010.03.004

Zubkov, M. V., Sazhin, A. F., & Flint, M. V. (1992). The microplankton organisms at the oxic-anoxic interface in the pelagial of the Black Sea. *FEMS Microbiology Letters*, *101*(4), 245–250. https://doi.org/10.1111/j.1574-6968.1992.tb05781.x

Supplementary Information

The leftmost column of each table indicated the sample names. The first number that is indicated in the sample names (i.e. after the acronym), refers to the cycle to which it belongs (Pg3 to Pg9), while the second number refers to stratigraphic position within the cycle itself (from oldest to youngest). Shaded colours in the leftmost column indicate lithology (green = laminated shale; grey = homogenous marl; pink = branching selenite; orange = laminar gypsum).

	isoGDGTs (ug / g TOC)	brGDGTs (ug / g TOC)	Archaeol (ug / g TOC)	Ext. archaeol (ug / g TOC)	Tetra-hymanol (ug / g TOC)	Ergosta-7-en-ol (ug / g TOC)	%	4-Me-ergosta-14-en-ol (ug / g TOC)	%	Enigmatic sterols (ug / g TOC)	%	Dinosterol (ug / g TOC)	C30 1,15-diol (ug / g TOC)	GDGT-0 Cren. ratio	BIT index
PZD.9.5	542,82	257,26	514,9	30,6	0,0	36,2	24	111,7	76	147,93	100	0,00	0,00	49,6	0,96
PZD.9.3	151,29	47,25	693,3	44,6	9,7	105,4	44	135,1	56	240,47	100	0,00	0,00	3,3	0,62
PZD.9.2	22,92	15,47	76,6	6,0	30,5	0,00	0	0,00	0	0,00	0	673,62	186,4	86,0	0,98
PZD.9.1	0,03	0,00	1487,5	106,1	19,9	927,7	49	949,6	51	1877,27	100	0,00	0,00	no cren	no brGDGTs
PZD.8.5	1064,30	144,49	565,1	36,7	2,2	63,8	30	149,0	70	212,78	100	0,00	0,00	441,3	0,98
PZD.8.4	90,36	39,44	2158,8	177,9	0,0	255,4	34	486,8	66	742,19	100	0,00	0,00	144,0	0,99
PZD.8.3	179,18	58,73	1352,0	82,1	33,0	258,5	35	484,6	65	1122,34	100	0,00	0,00	3,7	0,65
PZD.8.2	142,58	37,68	289,9	37,9	3,8	0,00	0	0,00	0	0,00	0	2357,31	0,00	212,7	0,98
PZD.8.1	0,00	0,00	891,6	138,4	81,2	0,00	0	0,00	0	0,00	0	1388,58	0,00	no cren	no brGDGTs
PZD.7.9	0,16	0,00	1055,1	65,6	1,9	151,8	34	299,8	66	451,57	100	0,00	0,00	no cren	no brGDGTs
PZD.7.8	22,52	14,63	2690,4	194,4	13,6	921,6	37	1585,2	63	2506,75	100	0,00	0,00	117,8	0,99
PZD.7.6	0,20	0,00	1003,8	63,0	23,4	240,0	43	321,4	57	561,36	100	0,00	0,00	no cren	no brGDGTs
PZD.7.5	17,81	2,38	431,5	27,5	15,3	53,5	52	49,0	48	102,55	100	0,00	0,00	no cren	no cren
PZD.7.4	23,55	7,48	848,5	80,7	227,4	82,9	34	157,5	66	240,40	100	0,00	0,00	173,7	0,98
PZD.7.2	101,13	9,56	21,1	3,4	91,3	0,00	0	0,00	0	0,00	0	1561,02	84,7	2,0	0,30
PZD.7.1	0,09	0,00	58,5	3,9	0,0	0,00	0	0,00	0	0,00	0	913,49	160,8	256,1	no brGDGTs
PZD.6.10	483,12	18,84	399,1	31,6	0,9	38,2	29	93,2	71	131,37	100	0,00	0,00	394,1	0,94
PZD.6.9	159,04	9,42	1116,1	74,8	0,0	72,9	29	178,2	71	251,13	100	0,00	0,00	415,7	0,96
PZD.6.8	0,00	0,00	428,1	38,5	1,5	55,9	27	150,3	73	206,17	100	0,00	0,00	no cren	no brGDGTs
PZD.6.7	39,61	4,74	999,5	79,4	47,9	150,4	30	348,3	70	498,69	100	0,00	0,00	148,3	0,95
PZD.6.6	30,58	0,00	175,2	19,0	4,4	56,4	77	16,8	23	73,21	100	0,00	0,00	140,3	no brGDGTs
PZD.6.5	9,31	0,00	203,4	66,2	25,5	0,00	0	0,00	0	0,00	0	302,11	0,00	26,8	no brGDGTs
PZD.6.4	102,47	10,74	44,0	3,8	0,0	0,00	0	0,00	0	0,00	0	702,90	142,9	1,8	0,29
PZD.6.2	31,21	13,17	67,8	5,0	41,9	0,00	0	0,00	0	0,00	0	973,13	352,1	3,8	0,71
PZD.6.1	21,85	4,43	1231,3	79,8	7,6	463,7	56	368,9	44	832,66	100	0,00	0,00	323,7	0,99
PZD.5.8	0,00	0,00	600,5	39,6	1,8	33,6	43	44,0	57	77,61	100	0,00	0,00	no cren	no brGDGTs
PZD.5.7	65,86	13,16	1613,8	115,2	0,0	662,6	50	655,0	50	1317,64	100	0,00	0,00	3,6	0,54
PZD.5.6	0,00	0,00	122,1	8,5	1,6	8,6	38	14,1	62	22,67	100	0,00	0,00	no cren	no brGDGTs
PZD.5.5	14,37	0,57	660,6	57,0	3,1	180,5	30	416,9	70	597,35	100	0,00	0,00	no cren	no cren
PZD.5.3	11,03	3,32	2107,7	158,9	0,0	387,1	36	686,4	64	1073,53	100	0,00	0,00	169,4	0,98

PZD.5.2	0,08	0,00	31,0	12,4	2,3	0,00	0	0,00	0	0,00	0	53,73	0,00	no cren	no brGDGTs
PZD.5.1	15,96	4,13	1599,9	85,5	0,0	468,9	51	444,1	49	913,00	100	0,00	0,00	341,7	0,99
PZD.4.13	0,74	0,00	546,8	31,8	3,7	334,2	48	369,2	52	703,38	100	0,00	0,00	no cren	no brGDGTs
PZD.4.12	0,18	0,00	722,2	49,1	3,6	154,8	31	345,9	69	500,71	100	0,00	0,00	no cren	no brGDGTs
PZD.4.10	0,00	0,00	350,4	24,7	23,8	180,1	38	292,5	62	472,57	100	0,00	0,00	no cren	no brGDGTs
PZD.4.9	0,00	0,00	59,7	9,1	2,4	0,00	0	0,00	0	0,00	0	15,57	0,00	no cren	no brGDGTs
PZD.4.8	54,17	10,82	73,7	3,4	20,8	0,00	0	0,00	0	0,00	0	368,75	70,8	3,6	0,54
PZD.4.7	5,63	0,00	74,9	4,6	4,1	0,00	0	0,00	0	0,00	0	26,11	17,0	60,9	no brGDGTs
PZD.4.6	0,00	0,00	169,7	31,0	8,0	0,00	0	0,00	0	0,00	0	0,00	0,00	no cren	no brGDGTs
PZD.4.2	9,89	6,62	9,8	1,5	21,6	0,00	0	0,00	0	0,00	0	350,70	0,00	101,8	0,99
PZD.4.1	10,11	2,01	199,2	42,7	10,1	0,00	0	0,00	0	0,00	0	182,85	0,00	0,2	0,85
PZD.3.16	0,00	0,00	421,7	31,3	5,3	38,5	29	93,4	71	131,84	100	0,00	0,00	no cren	no brGDGTs
PZD.3.15	0,00	0,00	765,2	59,1	10,8	84,6	32	183,5	68	268,13	100	0,00	0,00	no cren	no brGDGTs
PZD.3.13	280,15	25,71	2543,6	132,7	45,0	2332,7	38	3886,9	62	6219,64	100	0,00	0,00	1043,5	0,99
PZD.3.12	7,69	0,00	721,1	31,0	3,3	50,7	33	105,0	67	155,73	100	0,00	0,00	no cren	no brGDGTs
PZD.3.11	702,25	82,24	2870,1	111,0	17,7	378,0	27	1001,2	73	1379,16	100	0,00	0,00	516,2	0,98
PZD.3.10	0,68	0,00	363,8	17,0	7,6	38,9	31	86,1	69	124,99	100	0,00	0,00	3,7	no brGDGTs
PZD.3.8	0,00	0,00	76,8	5,7	3,2	0,00	0	0,00	0	0,00	0	21,70	0,00	no cren	no brGDGTs
PZD.3.7	25,69	10,20	45,4	7,4	24,9	0,00	0	0,00	0	0,00	0	833,03	0,00	10,9	0,84
PZD.3.6	22,05	12,09	31,1	4,0	35,8	0,00	0	0,00	0	0,00	0	947,39	344,4	5,6	0,80
PZD.3.4	82,27	5,49	46,4	5,6	19,1	0,00	0	0,00	0	0,00	0	1005,16	250,4	609,8	0,98
PZD.3.3	18,66	9,37	703,0	106,9	36,6	0,00	0	0,00	0	0,00	0	870,15	0,00	20,3	0,92
PZD.3.1	106,77	44,06	50,0	2,6	7,9	0,00	0	0,00	0	0,00	0	1138,96	362,6	3,3	0,69

(Table 2): Lipid biomarker abundances and calculated proxies of the fifty-three analysed samples from the studied interval of the Pollenzo section. Columns indicate from left to right: **1)** total isoprenoid GDGT abundance (µg/g TOC) (see **Table 3**), **2)** total branched GDGT abundance (µg/g TOC); Sum of brGDGT-I, brGDGT-II and brGDGT-III **3)** archaeol ($C_{20,20}$) abundance (µg/g TOC), **4)** extended archaeol ($C_{20,25}$) abundance (µg/g TOC), **5)** tetrahymanol abudance (µg/g TOC), **6)** ergosta-7-en-ol abundance(µg/g TOC), **7)** 4-methyl-ergosta-14-en-ol abundance (µg/g TOC), **8)** Sum of 7-ergosta-en-ol and 4-methyl-ergosta-14-en-ol (µg/g TOC); **9)** Dinosterol abundance (µg/g TOC), **10)** C_{30} 1,15-diol abundance (µg/g TOC), **11)** GDGT-0/Crenarchaeol ratio (Turich *et al.*, 2007) **12)** Branched and Isoprenoid Tetraether index (BIT; Hopmans *et al.*, 2004).

	GDGT-0		GDGT-1		GDGT-2		GDGT-3		GDGT-4		Crenarchaeol		Crenarchaeol'		Total isoGDGTs
	(µg / g TOC)	%	(µg / g TOC)	%	(µg / g TOC)	%	(µg / g TOC)	%	(µg / g TOC)	%	(µg / g TOC)	%	(µg / g TOC)	%	(µg / g TOC)
PZD.9.5	509,49	93,9	15,57	2,9	4,07	0,7	2,13	0,4	0,00	0,00	10,27	1,9	1,30	0,2	**542,82**
PZD.9.3	96,02	63,5	7,34	4,8	12,83	8,5	2,76	1,8	0,00	0,00	28,69	19,0	3,65	2,4	**151,29**
PZD.9.2	22,12	96,5	0,54	2,3	0,00	0,0	0,00	0,0	0,00	0,00	0,26	1,1	0,00	0,0	**22,92**
PZD.9.1	0,03	100,0	0,00	0,0	0,00	0,0	0,00	0,0	0,00	0,00	0,00	0,0	0,00	0,0	**0,03**
PZD.8.5	1025,49	96,4	29,36	2,8	5,05	0,5	1,52	0,1	0,00	0,00	2,32	0,2	0,56	0,1	**1064,30**
PZD.8.4	81,47	90,2	3,83	4,2	4,19	4,6	0,18	0,2	0,00	0,00	0,57	0,6	0,12	0,1	**90,36**
PZD.8.3	116,30	64,9	11,17	6,2	15,55	8,7	2,67	1,5	0,00	0,00	31,31	17,5	2,17	1,2	**179,18**
PZD.8.2	138,59	97,2	2,41	1,7	0,53	0,4	0,15	0,1	0,00	0,00	0,65	0,5	0,25	0,2	**142,58**

PZD.8.1	0,00	0,0	0,00	0,0	0,00	0,0	0,00	0,0	0,00	0,00	0,00	0,0	0,00	0,0	0,00
PZD.7.9	0,16	100,0	0,00	0,0	0,00	0,0	0,00	0,0	0,00	0,00	0,00	0,0	0,00	0,0	0,16
PZD.7.8	20,55	91,3	1,01	4,5	0,78	3,5	0,00	0,0	0,00	0,00	0,17	0,8	0,00	0,0	22,52
PZD.7.6	0,20	100,0	0,00	0,0	0,00	0,0	0,00	0,0	0,00	0,00	0,00	0,0	0,00	0,0	0,20
PZD.7.5	17,48	98,1	0,33	1,9	0,00	0,0	0,00	0,0	0,00	0,00	0,00	0,0	0,00	0,0	17,81
PZD.7.4	22,24	94,5	0,92	3,9	0,17	0,7	0,08	0,4	0,00	0,00	0,13	0,5	0,00	0,0	23,55
PZD.7.2	44,29	43,8	6,42	6,3	9,59	9,5	3,00	3,0	13,49	13,34	21,85	21,6	2,49	2,5	101,13
PZD.7.1	0,09	97,0	0,00	2,6	0,00	0,0	0,00	0,0	0,00	0,00	0,0003	0,4	0,00	0,0	0,09
PZD.6.10	467,62	96,8	12,15	2,5	1,78	0,4	0,00	0,0	0,00	0,00	1,19	0,2	0,38	0,1	483,12
PZD.6.9	155,53	97,8	3,02	1,9	0,00	0,0	0,00	0,0	0,00	0,00	0,37	0,2	0,11	0,1	159,04
PZD.6.8	0,00	0,0	0,00	0,0	0,00	0,0	0,00	0,0	0,00	0,00	0,00	0,0	0,00	0,0	0,00
PZD.6.7	34,87	88,0	1,78	4,5	2,59	6,6	0,08	0,2	0,00	0,00	0,24	0,6	0,05	0,1	39,61
PZD.6.6	29,15	95,3	0,95	3,1	0,25	0,8	0,00	0,0	0,00	0,00	0,21	0,7	0,03	0,1	30,58
PZD.6.5	7,57	81,3	0,82	8,8	0,46	4,9	0,14	1,5	0,00	0,00	0,28	3,0	0,04	0,4	9,31
PZD.6.4	47,91	46,8	9,92	9,7	12,73	12,4	2,90	2,8	0,00	0,00	26,02	25,4	3,00	2,9	102,47
PZD.6.2	20,56	65,9	1,98	6,3	2,41	7,7	0,49	1,6	0,00	0,00	5,36	17,2	0,42	1,3	31,21
PZD.6.1	21,32	97,6	0,38	1,8	0,07	0,3	0,00	0,0	0,00	0,00	0,07	0,3	0,00	0,0	21,85
PZD.5.8	0,00	0,0	0,00	0,0	0,00	0,0	0,00	0,0	0,00	0,00	0,00	0,0	0,00	0,0	0,00
PZD.5.7	40,33	61,2	4,88	7,4	6,61	10,0	1,53	2,3	0,00	0,00	11,36	17,2	1,15	1,7	65,86
PZD.5.6	0,00	0,0	0,00	0,0	0,00	0,0	0,00	0,0	0,00	0,00	0,00	0,0	0,00	0,0	0,00
PZD.5.5	12,87	89,6	0,82	5,7	0,68	4,7	0,00	0,0	0,00	0,00	0,00	0,0	0,00	0,0	14,37
PZD.5.3	10,75	97,4	0,13	1,2	0,06	0,5	0,00	0,0	0,00	0,00	0,06	0,6	0,03	0,3	11,03
PZD.5.2	0,08	100,0	0,00	0,0	0,00	0,0	0,00	0,0	0,00	0,00	0,00	0,0	0,00	0,0	0,08
PZD.5.1	15,58	97,7	0,33	2,1	0,00	0,0	0,00	0,0	0,00	0,00	0,05	0,3	0,00	0,0	15,96
PZD.4.13	0,74	100,0	0,00	0,0	0,00	0,0	0,00	0,0	0,00	0,00	0,00	0,0	0,00	0,0	0,74
PZD.4.12	0,18	100,0	0,00	0,0	0,00	0,0	0,00	0,0	0,00	0,00	0,00	0,0	0,00	0,0	0,18
PZD.4.10	0,00	0,0	0,00	0,0	0,00	0,0	0,00	0,0	0,00	0,00	0,00	0,0	0,00	0,0	0,00
PZD.4.9	0,00	0,0	0,00	0,0	0,00	0,0	0,00	0,0	0,00	0,00	0,00	0,0	0,00	0,0	0,00
PZD.4.8	33,17	61,2	4,01	7,4	5,44	10,0	1,26	2,3	0,00	0,00	9,34	17,2	0,94	1,7	54,17
PZD.4.7	5,14	91,3	0,25	4,4	0,13	2,3	0,03	0,6	0,00	0,00	0,08	1,5	0,00	0,0	5,63
PZD.4.6	0,00	0,0	0,00	0,0	0,00	0,0	0,00	0,0	0,00	0,00	0,00	0,0	0,00	0,0	0,00
PZD.4.2	9,44	95,5	0,24	2,4	0,09	0,9	0,02	0,2	0,00	0,00	0,09	0,9	0,00	0,0	9,89
PZD.4.1	0,08	0,8	9,22	91,2	0,30	2,9	0,09	0,9	0,00	0,00	0,35	3,5	0,06	0,6	10,11
PZD.3.16	0,00	0,0	0,00	0,0	0,00	0,0	0,00	0,0	0,00	0,00	0,00	0,0	0,00	0,0	0,00
PZD.3.15	0,00	0,0	0,00	0,0	0,00	0,0	0,00	0,0	0,00	0,00	0,00	0,0	0,00	0,0	0,00
PZD.3.13	275,06	98,2	4,01	1,4	0,58	0,2	0,24	0,1	0,00	0,00	0,26	0,1	0,00	0,0	280,15
PZD.3.12	7,47	97,1	0,22	2,9	0,00	0,0	0,00	0,0	0,00	0,00	0,00	0,0	0,00	0,0	7,69
PZD.3.11	683,80	97,4	12,72	1,8	3,17	0,5	1,06	0,2	0,00	0,00	1,32	0,2	0,18	0,0	702,25
PZD.3.10	0,44	64,6	0,00	0,0	0,06	8,2	0,00	0,0	0,07	9,85	0,12	17,4	0,00	0,0	0,68
PZD.3.8	0,00	0,0	0,00	0,0	0,00	0,0	0,00	0,0	0,00	0,00	0,00	0,0	0,00	0,0	0,00
PZD.3.7	21,77	84,7	0,84	3,3	1,00	3,9	0,09	0,3	0,00	0,00	2,00	7,8	0,00	0,0	25,69
PZD.3.6	16,68	75,6	1,21	5,5	0,88	4,0	0,23	1,0	0,00	0,00	2,97	13,5	0,08	0,4	22,05
PZD.3.4	80,17	97,4	1,64	2,0	0,27	0,3	0,00	0,0	0,00	0,00	0,13	0,2	0,06	0,1	82,27
PZD.3.3	16,40	87,9	0,75	4,0	0,44	2,3	0,21	1,1	0,00	0,00	0,81	4,3	0,06	0,3	18,66
PZD.3.1	66,34	62,1	9,46	8,9	6,45	6,0	3,04	2,8	0,00	0,00	20,23	18,9	1,25	1,2	106,77

(Table 3): GDGT abundance in all fifty-three analysed samples from the studied interval of the Pollenzo section. The rightmost column indicates the total abundance of isoGDGTs, the summed abundance of the seven common isoGDGTs in the middle columns. Green shades in the GDGT-0 column indicate >90% weight percentage of the total GDGT abundance. Blue shades in the crenarchaeol column indicate >10% weight percentage of the total GDGT abundance. Red shades indicate that the compound in question is undetected.

	brGDGT-I (ug / g TOC)	%	brGDGT-II (ug / g TOC)	%	brGDGT-III (ug / g TOC)	%	brGDGT I + II + III (ug / g TOC)
PZD.9.5	70,33	27,3	99,20	38,6	87,72	34,1	257,26
PZD.9.3	12,49	26,4	17,09	36,2	17,67	37,4	47,25
PZD.9.2	3,80	24,6	5,57	36,0	6,10	39,4	15,47
PZD.9.1	0,00	0,00	0,00	0,0	0,00	0,00	0,00
PZD.8.5	34,80	24,1	54,35	37,6	55,33	38,3	144,49
PZD.8.4	7,71	19,5	14,44	36,6	17,29	43,8	39,44
PZD.8.3z	17,39	29,6	24,67	42,0	16,67	28,4	58,73
PZD.8.2	8,89	23,6	14,26	37,8	14,52	38,6	37,68
PZD.8.1	0,00	0,00	0,00	0,0	0,00	0,00	0,00
PZD.7.9	0,00	0,00	0,00	0,0	0,00	0,00	0,00
PZD.7.8	3,06	20,9	5,97	40,8	5,60	38,3	14,63
PZD.7.6	0,00	0,00	0,00	0,0	0,00	0,00	0,00
PZD.7.5	0,71	29,6	0,82	34,3	0,86	36,1	2,38
PZD.7.4	2,02	27,1	2,62	35,1	2,84	37,9	7,48
PZD.7.2	0,74	7,7	3,97	41,5	4,85	50,7	9,56
PZD.7.1	0,00	0,00	0,00	0,00	0,00	0,00	0,00
PZD.6.10	4,65	24,7	9,10	48,3	5,09	27,0	18,84
PZD.6.9	2,95	31,4	3,69	39,2	2,77	29,4	9,42
PZD.6.8	0,00	0,00	0,00	0,00	0,00	0,00	0,00
PZD.6.7z	0,00	0,00	2,72	57,4	2,02	42,6	4,74
PZD.6.6	0,00	0,00	0,00	0,00	0,00	0,00	0,00
PZD.6.5	0,00	0,00	0,00	0,00	0,00	0,00	0,00
PZD.6.4z	2,84	26,5	3,83	35,6	4,07	37,9	10,74
PZD.6.2	3,06	23,2	4,54	34,4	5,58	42,4	13,17
PZD.6.1	0,96	21,6	1,67	37,7	1,80	40,6	4,43
PZD.5.8	0,00	0,00	0,00	0,00	0,00	0,00	0,00
PZD.5.7	4,63	35,2	4,35	33,1	4,18	31,7	13,16
PZD.5.6	0,00	0,00	0,00	0,00	0,00	0,00	0,00
PZD.5.5	0,21	37,1	0,19	33,1	0,17	29,9	0,57
PZD.5.3	0,87	26,3	1,29	38,9	1,15	34,8	3,32
PZD.5.2	0,00	0,00	0,00	0,00	0,00	0,00	0,00
PZD.5.1	0,90	21,8	1,72	41,5	1,52	36,6	4,13
PZD.4.13	0,00	0,00	0,00	0,00	0,00	0,00	0,00
PZD.4.12	0,00	0,00	0,00	0,00	0,00	0,00	0,00

PZD.4.10	0,00	0,00	0,00	0,00	0,00	0,00	0,00
PZD.4.9	0,00	0,00	0,00	0,00	0,00	0,00	0,00
PZD.4.8	3,81	35,2	3,58	33,1	3,44	31,7	10,82
PZD.4.7	0,00	0,00	0,00	0,00	0,00	0,00	0,00
PZD.4.6	0,00	0,00	0,00	0,00	0,00	0,00	0,00
PZD.4.2	1,68	25,3	2,49	37,6	2,46	37,1	6,62
PZD.4.1	0,56	27,8	0,78	38,6	0,68	33,6	2,01
PZD.3.16	0,00	0,00	0,00	0,00	0,00	0,00	0,00
PZD.3.15	0,00	0,00	0,00	0,00	0,00	0,00	0,00
PZD.3.13	4,67	18,2	10,13	39,4	10,91	42,4	25,71
PZD.3.12	0,00	0,00	0,00	0,00	0,00	0,00	0,00
PZD.3.11	17,69	21,5	27,48	33,4	37,06	45,1	82,24
PZD.3.10	0,00	0,00	0,00	0,00	0,00	0,00	0,00
PZD.3.8	0,00	0,00	0,00	0,00	0,00	0,00	0,00
PZD.3.7	0,81	7,9	3,99	39,1	5,41	53,0	10,20
PZD.3.6	2,97	24,5	4,03	33,3	5,09	42,1	12,09
PZD.3.4	1,61	29,4	2,24	40,9	1,63	29,8	5,49
PZD.3.3	2,01	21,4	2,97	31,7	4,39	46,9	9,37
PZD.3.1	13,54	30,7	18,01	40,9	12,50	28,4	44,06

(Table 4): The abundance of brGDGTs in all fifty-three analysed samples from the studied interval of the Pollenzo section. The rightmost column indicates the summed abundance of the three detected brGDGTs in the middle column. Red shades indicate that the compound in question is undetected. Light blue shades indicate lowest abundances and yellow shades indicate highest abundances.

	Archaeol (ug / g TOC)	**Extended archaeol** (ug / g TOC)	**DGDs** (ug / g TOC)	%	**isoGDGTs** (ug / g TOC)	%	**brGDGTs** (ug / g TOC)	%
PZD.9.5	514,92	30,60	545,53	**40,54**	542,82	**40,34**	257,26	**19,12**
PZD.9.3	693,27	44,57	737,84	**78,80**	151,29	**16,16**	47,25	**5,05**
PZD.9.2	76,59	5,98	82,56	**68,26**	22,92	**18,95**	15,47	**12,79**
PZD.9.1	1487,51	106,08	1593,60	100,00	0,03	0,00	0,00	0,00
PZD.8.5	565,11	36,70	601,81	**33,24**	1064,30	**58,78**	144,49	**7,98**
PZD.8.4	2158,80	177,92	2336,72	94,74	90,36	3,66	39,44	1,60
PZD.8.3z	1351,97	82,07	1434,05	85,77	179,18	10,72	58,73	3,51
PZD.8.2	289,87	37,91	327,78	**64,52**	142,58	**28,06**	37,68	**7,42**
PZD.8.1	891,60	138,39	1029,99	100,00	0,00	0,00	0,00	0,00
PZD.7.9	1055,10	65,57	1120,68	99,99	0,16	0,01	0,00	0,00
PZD.7.8	2690,38	194,41	2884,79	98,73	22,52	0,77	14,63	0,50
PZD.7.6	1003,81	63,03	1066,83	99,98	0,20	0,02	0,00	0,00

PZD.7.5	431,45	27,54	458,99	95,79	17,81	3,72	2,38	0,50
PZD.7.4	848,54	80,67	929,21	96,77	23,55	2,45	7,48	0,78
PZD.7.2	21,13	3,38	24,51	**18,13**	101,13	**74,80**	9,56	**7,07**
PZD.7.1	58,46	3,85	62,32	99,85	0,09	0,15	0,00	0,00
PZD.6.10	399,10	31,60	430,71	46,18	483,12	51,80	18,84	2,02
PZD.6.9	1116,13	74,80	1190,92	87,61	159,04	11,70	9,42	0,69
PZD.6.8	428,13	38,48	466,61	100,00	0,00	0,00	0,00	0,00
PZD.6.7z	999,53	79,40	1078,93	96,05	39,61	3,53	4,74	0,42
PZD.6.6	175,18	18,97	194,15	86,39	30,58	13,61	0,00	0,00
PZD.6.5	203,40	66,20	269,60	96,66	9,31	3,34	0,00	0,00
PZD.6.4z	43,96	3,84	47,80	**29,69**	102,47	**63,64**	10,74	**6,67**
PZD.6.2	67,79	4,96	72,75	**62,11**	31,21	**26,64**	13,17	**11,25**
PZD.6.1	1231,33	79,76	1311,09	98,04	21,85	1,63	4,43	0,33
PZD.5.8	600,50	39,61	640,11	100,00	0,00	0,00	0,00	0,00
PZD.5.7	1613,76	115,24	1729,00	95,63	65,86	3,64	13,16	0,73
PZD.5.6	122,07	8,47	130,54	100,00	0,00	0,00	0,00	0,00
PZD.5.5	660,57	57,01	717,58	97,96	14,37	1,96	0,57	0,08
PZD.5.3	2107,72	158,86	2266,58	99,37	11,03	0,48	3,32	0,15
PZD.5.2	31,00	12,36	43,35	99,82	0,08	0,18	0,00	0,00
PZD.5.1	1599,93	85,50	1685,43	98,82	15,96	0,94	4,13	0,24
PZD.4.13	546,78	31,77	578,54	99,87	0,74	0,13	0,00	0,00
PZD.4.12	722,23	49,12	771,35	99,98	0,18	0,02	0,00	0,00
PZD.4.10	350,39	24,75	375,13	100,00	0,00	0,00	0,00	0,00
PZD.4.9	59,67	9,05	68,72	100,00	0,00	0,00	0,00	0,00
PZD.4.8	73,68	3,37	77,05	**54,25**	54,17	**38,13**	10,82	**7,62**
PZD.4.7	74,88	4,57	79,45	93,38	5,63	6,62	0,00	0,00
PZD.4.6	169,71	30,97	200,69	100,00	0,00	0,00	0,00	0,00
PZD.4.2	9,77	1,51	11,28	**40,58**	9,89	**35,59**	6,62	**23,84**
PZD.4.1	199,24	42,71	241,95	95,23	10,11	3,98	2,01	0,79
PZD.3.16	421,73	31,28	453,01	100,00	0,00	0,00	0,00	0,00
PZD.3.15	765,15	59,06	824,21	100,00	0,00	0,00	0,00	0,00
PZD.3.13	2543,62	132,69	2676,31	89,74	280,15	9,39	25,71	0,86
PZD.3.12	721,06	31,03	752,08	98,99	7,69	1,01	0,00	0,00
PZD.3.11	2870,08	110,99	2981,07	79,17	702,25	18,65	82,24	2,18
PZD.3.10	363,78	16,95	380,74	99,82	0,68	0,18	0,00	0,00
PZD.3.8	76,79	5,68	82,47	100,00	0,00	0,00	0,00	0,00
PZD.3.7	45,40	7,39	52,79	**59,52**	25,69	**28,97**	10,20	**11,51**
PZD.3.6	31,10	4,00	35,10	**50,70**	22,05	**31,84**	12,09	**17,46**
PZD.3.4	46,37	5,63	52,00	37,21	82,27	58,87	5,49	3,93
PZD.3.3	702,99	106,95	809,93	96,65	18,66	2,23	9,37	1,12
PZD.3.1	49,95	2,56	52,52	**25,83**	106,77	**52,51**	44,06	**21,67**

(Table 5): The (relative) abundances of DGDs (archaeol + extended archaeol), isoGDGTs and brGDGTs in all fifty-three analysed samples from the studied interval of the Pollenzo section. The thirteen samples that are highlighted contain a relatively high proportion of both isoGDGTs and brGDGTs. Blue shades indicate a relatively high proportion of isoGDGTs and brown shades indicate a relatively high proportion of brGDGTs. Red shades indicate that the compound in question is undetected.